

Microwave-to-Optical Transduction with Gallium Phosphide Electro-Optomechanical Devices

Présentée le 30 septembre 2021

Faculté des sciences et techniques de l'ingénieur
Laboratoire de photonique et mesures quantiques (STI/SB)
Programme doctoral en photonique

pour l'obtention du grade de Docteur ès Sciences

par

Simon Benjamin Klaus HÖNL

Acceptée sur proposition du jury

Prof. E. Charbon, président du jury
Prof. T. Kippenberg, Dr P. F. Seidler, directeurs de thèse
Prof. S. Gröblacher, rapporteur
Prof. J. Fink, rapporteur
Prof. N. Grandjean, rapporteur

One never notices what has been done,
one can only see what remains to be done.

— Marie Curie

To my parents, who have always supported me in all my endeavors ...

Acknowledgements

I have been very fortunate to have worked with many fantastic people during my PhD, and I believe that I could not have achieved anything of merit were it not for the support and mentorship of my colleagues. First, I would like to express my deepest gratitude to Paul Seidler for his continued mentorship, and who has given me the opportunity to work on this exciting topic in a great environment during the last four years, and who always had an open ear for me. I also want to express my gratitude to Katharina Schmeing and Dalziel Wilson, with whom I had the pleasure of working with in the lab and who have taught me so much about science and life. I would also like to thank Lukas Czornomaz, Heinz Schmid and Yannick Baumgartner for their continued support and for many illuminating discussions on epitaxial growth and semiconductor devices. Furthermore, I would like to thank Daniele Caimi, Darius Urbonas, Thilo Stöferle, Andreas Fuhrer, Matthias Mergenthaler, and the entire Quantum team at IBM Research in Zurich, Laura Bégon-Lours, Youri Popoff, Bernd Gotsmann, Alan Molinari, Ute Drechsler, Diana Davila, Antonis Olziersky, and the operations team of the Binnig-Rohrer Nanotechnology Center, Preksha Tiwari, Svenja Mauthe, Charles Möhl, Thomas Karg, Walter Riess and Heike Riel for supporting me. I would also like to thank Gary Steele for numerous insightful discussions on piezoelectric equivalent circuits. Furthermore, I would like to thank Alberto Beccari, Mohammad Berehyi, Junqiu Liu and the team of Prof. Kippenberg, as well as my fellow members of the ITN Optomechanical Technologies for many inspiring discussions. Last but not least, I would also like to express my deep gratitude towards Tobias Kippenberg, from whom I have always received excellent advice and guidance.

Zurich, August 30, 2021

S. H.

Abstract

Quantum computing is one of the great scientific challenges of the 21st century. Small-scale systems today promise to surpass classical computers in the coming years and to enable the solution of classically intractable computational tasks in the fields of quantum chemistry, optimization, cryptography and more.

In contrast to classical computers, quantum computers based on superconducting quantum bits (qubits) can to date not be linked over long distance in a network to improve their computing capacity, since devices, which preserve the quantum state when it is transferred from one machine to another, are not available. Several approaches are being pursued to realize such a component, one of the most promising to date makes use of an intermediary, micromechanical element that enables quantum coherent conversion between the information present in the quantum computer and an optical fiber, without compromising the quantum nature of the information, via optomechanical interaction. This approach could allow fiber-optic quantum networks between separate quantum computers based on superconducting qubits in the future.

In this work a platform for such a microwave-to-optic link was developed based on the piezoelectric material gallium phosphide. This III-V semiconductor offers not only a piezoelectric coupling between the electric field of a microwave circuit and a mechanical mode, but also a wide optical bandgap $E_g = 2.26\text{ eV}$ which reduces nonlinear optical absorption in the device and a large refractive index $n(1550\text{ nm}) = 3.01$ which allows strong optical confinement at near-infrared wavelengths.

Importantly and in contrast to other approaches with gallium phosphide, an epitaxially grown, single crystal thin film of the material is integrated directly on a silicon wafer with pre-structured niobium electrodes by direct wafer-bonding. This opens up the possibility of integrating the device design presented here directly with superconducting qubits fabricated with this material system.

A microwave-to-optical transducer design was simulated and fabricated in the gallium phosphide-on-silicon platform. The device was found to exhibit large vacuum optomechanical coupling rates $g_0/2\pi \approx 290\text{ kHz}$ and a high intrinsic optical quality factor $Q > 10^5$ while at the same time permitting electromechanical coupling to a microwave electrode. Coherent microwave-to-optical transduction was shown at room temperature for this device and the electromechanical coupling rate could be extracted from a model derived by input-output theory.

The electromechanical coupling between the electro-optomechanical device and a superconducting qubit was estimated to be $g/2\pi = \mathcal{O}(200\text{ kHz})$ which indicates that strong coupling

Abstract

between the here presented device and a superconducting transmon qubit is achievable. In addition, superconducting microwave cavities with high quality factor at single photon energy $Q \sim 5 \times 10^5$ were fabricated and measured to verify that fabrication process of the microwave-to-optical transducer is compatible with high-quality superconducting microwave circuits.

Keywords

Optomechanics, microwave-to-optical transduction, superconducting circuits, gallium phosphide, integrated photonics.

Zusammenfassung

Quanten-Computing ist eine der großen wissenschaftlichen Herausforderungen des ein- und zwanzigsten Jahrhunderts. Experimente mit heutigen kleinen Systemen versprechen klassische Rechensysteme in naher Zukunft zu übertreffen und bisher unlösbare Probleme in Forschungsbereichen wie Quanten-Chemie, Optimierung, Kryptographie und mehr zu erlauben.

Im Gegensatz zu klassischen Computern, Quanten Computer basierend auf supraleitenden Quanten Bits (Qubits), können bisher nicht über lange Distanz in einem Netzwerk verbunden werden um ihre Rechenleistung zu erhöhen, da es an Apparaten fehlt, die den Quanten Zustand eines Qubits bewahren können, wenn er von einer Maschine zur anderen übertragen wird. Mehrere Ansätze werden derzeit erforscht, um einen solchen Apparat zu realisieren, einer der vielversprechendsten bisher nutzt ein mikromechanisches Element, welches die quanten-kohärente Umwandlung der Information in einem supraleitenden Quanten Computer und einer optischen Faser erlaubt, ohne die Quanten Natur der Information dabei zu beeinträchtigen. Diese Methode könnte es in Zukunft erlauben, supraleitende Quanten Computer über ein optisches Netzwerk über lange Distanzen zu verbinden.

In dieser Arbeit wurde eine Plattform für eine solche Mikrowellen-optische Verbindung auf der Basis des piezoelektrischen Materials Gallium Phosphid entwickelt. Dieser III-V Halbleiter bietet nicht nur eine piezoelektrische Kopplung, sondern auch eine große optische Bandlücke von $E_g = 2.26 \text{ eV}$, was nichtlineare Absorption in optischen Elementen reduziert sowie einen großen Brechungsindex $n(1550 \text{ nm}) = 3.01$, der ein hohes optisches Confinement bei Wellenlängen im nah-infraroten Bereich gewährleistet.

Von großer Bedeutung und im Gegensatz zu anderen Ansätzen mit Gallium Phosphid ist bei der hier vorgestellten Plattform, dass ein epitaktisch gewachsener, ein-kristalliner Dünnschicht des Materials direkt auf einem Silizium Wafer mit vorstrukturierten Elektroden über direktes Wafer-Bonding integriert wird. Dieser Umstand eröffnet die Möglichkeit, die hier entwickelten Elemente direkt mit supraleitenden Qubits auf dieser Plattform zu integrieren.

Ein Design für einen Mikrowellen-zu-Optik Umwandler wurde im Rahmen dieser Arbeit entwickelt und basierend auf der Gallium Phosphid-auf-Silizium Plattform hergestellt. Optomechanische Vakuumkopplungsraten des hergestellten Elements im Bereich $g_0/2\pi \approx 290 \text{ kHz}$ wurden gemessen bei einem intrinsischen optischen Qualitätsfaktor $Q > 10^5$, während gleichzeitig eine elektromechanische Kopplung mit einer integrierten Elektrode möglich war. Kohärente Mikrowellen-zu-Optik Umwandlung für dieses Element wurde bei Raumtemperatur demonstriert und die elektromechanische Kopplungsrate konnte aus den Messungen extra-

Zusammenfassung

hiert werden über ein Modell, das aus Input-Output Theorie hergeleitet wurde.

Die elektromechanische Kopplung zwischen dem elektro-optomechanischen Element und einem supraleitenden Qubit wurde als $g/2\pi = \mathcal{O}(200\text{ kHz})$ abgeschätzt, was indiziert, dass eine starke Kopplung zwischen dem mechanischen Element und einem supraleitenden Transmon Qubit möglich sein sollte.

Zusätzlich wurden supraleitende Mikrowellenkavitäten mit einem Qualitätsfaktor bei Energien auf dem Niveau eines einzelnen Mikrowellenphotons von $Q \sim 5 \times 10^5$ auf der Basis des entwickelten Prozesses hergestellt und charakterisiert um die Kompatibilität zwischen dem Mikrowellen-optischen Wandler und supraleitenden Mikrowellenschaltkreisen von hoher Qualität zu bestätigen.

Stichwörter

Optomechanik, Mikrowellen-zu-Optik Umwandlung, supraleitende Schaltkreise, Gallium Phosphid, Integrierte Photonics.

Contents

Acknowledgements	i
Abstract (English/Deutsch)	iii
Introduction	1
Quantum Networks	2
Cavity Optomechanics – Mediator between Light and Darkness	4
Circuit Quantum Acousto-Dynamics	8
Gallium Phosphide	9
Building a Microwave-Optical Link	9
 I Theoretical Background	 11
 1 Resonators	 13
1.1 Input-Output Formalism	13
1.2 Optical Cavities	14
1.3 Superconducting Microwave Resonators	15
1.4 Mechanical Oscillators	16
 2 Superconducting Qubits	 19
2.1 Josephson Nonlinear Inductance	19
2.2 Cooper-Pair Box Hamiltonian	20
2.3 Transmon Limit	20
2.4 Interaction between a Transmon and a Linear LC Resonator	21
 3 Cavity-Optomechanics	 23
3.1 Optomechanical Hamiltonian	23
3.2 Optomechanical Coupling in Optomechanical Crystal Cavities	24
3.2.1 Moving Boundary Effect	25
3.2.2 Photoelastic Effect	25
3.2.3 Vacuum Optomechanical Coupling Rate	26
3.3 Optomechanical equations of motion	26
3.4 Direct Optical Detection	27
3.5 Dynamical Backaction	29

Contents

3.6	Estimation of the Vacuum Optomechanical Coupling Rate via Noise calibration and the Fluctuation Dissipation Theorem	32
3.6.1	Fluctuation Dissipation Theorem	32
3.6.2	Relation to the Vacuum Optomechanical Coupling Rate	33
3.6.3	Phase Noise Calibration	33
3.6.4	Inference of the Vacuum Optomechanical Coupling Rate	34
3.7	Microwave-to-optical transduction in the Low-Cooperativity Limit	34
II	Device Design	39
4	Optomechanical Design	41
4.1	Photonic Crystal Supermode Resonator	41
4.2	Photonic and Phononic Crystal Design	42
4.2.1	Phoxonic Mirror	42
4.2.2	Defect Cell	43
4.2.3	Waveguide Mirror	43
4.2.4	Phononic End-Reflector	44
4.2.5	Photonic Crystal	44
4.2.6	Localized Optical Mode	45
4.2.7	Mechanical Supermodes	46
4.3	Optomechanical Coupling	48
5	Piezoelectric Coupling	53
5.1	Simulation Setup	54
5.2	Estimation of Circuit Parameters	55
5.3	Results for Coplanar Electrode Configuration	56
5.3.1	Coupling to a Transmon Qubit	57
5.4	Top-Bottom Electrode Configuration	58
III	Device Fabrication and Integration	63
6	Growth of Gallium Phosphide with Metal-Organic Vapor Phase Epitaxy	67
6.1	Metal-Organic Vapor Phase Epitaxy	67
6.2	Growth Dynamics of Gallium Phosphide	68
6.3	Suppression of Defect Formation due to Growth Along Higher Order Crystal Planes	70
6.4	Optimized Growth	72
6.5	Growth on Silicon	73
7	Fabrication of Nb and NbN Superconducting Circuits on Silicon	75
7.1	Deposition of Superconducting Nb and NbN Layers by Magnetron Sputtering	75
7.1.1	Reactive Sputtering of NbN	76

7.2	Characterization of NbN	76
7.2.1	X-Ray Diffraction	76
7.2.2	Critical Temperature and Kinetic Inductance	77
7.3	Fabrication of Superconducting Nb and NbN Devices	79
8	Silicon Recess and Planarization	83
8.1	Silicon Recess	83
8.2	Planarization	84
8.2.1	Compensation Etch	85
8.2.2	Chemical Mechanical Polishing	85
8.2.3	Improvements with Filler Pattern	86
9	Hybrid Materials Integration via Direct Wafer-Bonding	89
9.1	Prerequisites for Direct Wafer-Bonding	90
9.2	GaP Hillock Planarization with Ion Beam Milling	90
9.3	Donor Wafer Removal	91
9.3.1	Selective Dry-Etching of Gallium Phosphide	91
10	Fabrication of GaP Integrated Photonic Circuit	95
10.1	Electron Beam Lithography	95
10.2	Device Etch	95
10.3	Device Release	96
10.4	Integration of Top Electrode	97
IV	Classical Microwave-to-Optical Transduction in a Gallium Phosphide Optomechanical Device	101
11	Experimental Setup	103
11.1	Setup for Microwave-to-optical Transduction	103
11.1.1	Broadband Optical Spectroscopy	103
11.1.2	Optical Alignment	103
11.1.3	Narrowband Optical Spectroscopy	105
11.1.4	Measurement of Thermomechanical Noise Spectrum	105
11.1.5	Phase Modulator Calibration	105
11.1.6	Dynamical Backaction	106
11.1.7	Microwave-to-Optical Transduction	106
12	Cavity Optomechanics	109
12.1	Optical Spectroscopy	109
12.2	Determination of the Vacuum Optomechanical Coupling Rate via a Noise Calibration Measurement	110
12.3	Dynamical Backaction	112
12.3.1	Optomechanically Induced Absorption	112

Contents

12.3.2 Optomechanically Induced Transparency	114
13 Microwave-to-Optical Transduction	117
13.1 Microwave-to-Optical Transduction Spectrum	117
13.2 Continuous-Wave Transduction	117
13.2.1 Nonlinear Behavior	120
13.3 Transduction Calibration and Phase-Coherent Transduction Spectrum	123
13.3.1 Setup Calibration	123
13.3.2 Frequency Response – Red Detuning	124
13.3.3 Frequency Response – Blue Detuning	125
13.3.4 Inference of the Electromechanical Coupling Rate	126
V Superconducting Microwave Cavities	127
14 Superconducting Nb and NbN Coplanar Waveguide Cavities	129
14.1 Setup for Measurement of Superconducting Microwave Cavities	129
14.2 Results	130
14.3 Nb Resonators	131
14.3.1 TLS Model Fit	133
14.4 NbN Resonators	134
14.4.1 Kinetic Inductance	135
14.5 Conclusion	136
VI Outlook	137
15 Towards Quantum Optomechanics and Quantum Acoustics	139
15.1 State of the Art	139
15.2 Quantum Acoustics	139
15.2.1 Dielectric loss in GaP-Transmon Hybrid Devices	139
15.2.2 Dielectric Loss due to Defects in GaP	140
15.3 Quantum Optomechanics	140
15.4 Improvements to GaP Platform	141
16 Integration of Superconducting Qubits	143
16.1 Transmon Design	144
A Gallium Phosphide Nonlinear Integrated Photonics	145
A.1 Resonator Design	146
A.2 Fabrication	150
A.3 Resonator Quality	151
B Design of Adiabatic Waveguide Coupler	153
C Fabrication of Etched Tapered Fibers	157

C.1 Etching Rig	157
C.2 Impact of Differential Etch Rate	158
C.3 Etching procedure	159
C.4 Post Processing	161
D Fiber mounting and optical alignment	163
E Fiber Packaging	165
E.1 Etching of Ultra-High NA Fibers	165
E.2 Packaging Procedure and UV Curing	166
E.2.1 Primary Fixation	167
E.2.2 Secondary fixation	167
Bibliography	177

Introduction

Building a universal quantum computer is one of the great challenges of modern-age physics and computer science. While small prototype machines have been demonstrated in various implementations, the grand goal of a universal, fault tolerant machine that exceeds classical counterparts in practical usecases such as quantum chemistry remains out of reach. Several physical implementations are currently being pursued, one of the most prominent is based on superconducting qubits. In this quickly growing field, recent advances in device integration, materials science and control have enabled a rapid development of machines with ever growing capabilities [56, 57]. While boundaries are shattered at many fronts, one essential ingredient to powerful quantum supercomputers continues to evade the physical realization, quantum networks.

In the scope of this work, I introduced a new platform for a key ingredient of a quantum network, a microwave-to-optical link, based on the piezoelectric material gallium phosphide, that is integrated on a Si/Nb platform for superconducting qubits. The link comprises an optomechanical photonic crystal resonator with an engineered phononic mode spectrum that introduces distributed mechanical supermodes. This design was then fabricated and tested in a prototype setting at room-temperature to demonstrate the coherent conversion of microwave photons to optical photons. In addition, the experiment allowed the comparison between simulated and experimental electromechanical coupling and a clear path towards the implementation of strong coupling between a superconducting qubit and the optomechanically coupled breathing supermodes. In the scope of the project, superconducting microwave resonators were fabricated on separate samples with the techniques employed during fabrication of the link and tested. The resonators were found to exhibit appreciable quality factors which demonstrates the compatibility of the fabrication process with that employed for the fabrication of the IBM superconducting qubit platform.

It is important to me to define a clear path towards the implementation of a quantum network, so that the motivation behind figures of merit and development strategies are transparent to the reader. Therefore, I will commence with a more qualitative, general discussion about the overall goal of the project, the implementation of a quantum network, and narrow the discussion down to the presented platform, so as to set the presented work in the context of ongoing research.

Quantum Networks

One aspect that makes classical supercomputers exceedingly powerful is the ability to distribute computational tasks across a large number of individual machines in a network. This is an aspect which has so far remained largely unfeasible for quantum devices based on superconducting qubits, which is mainly related to the low energy of the qubits' excited state of only $\sim 20\mu\text{eV}$ that requires the devices to be operated at cryogenic temperatures to keep the thermal occupation of the qubits at bay. Similarly, information that is being sent from one qubit to another must also be protected from thermal interference. This generally leaves two possibilities for a quantum interconnect, either lowering the temperature of the interconnect far below the energy of the microwave qubits, or encoding the information in a state with much higher energy such that thermal occupation at room temperature is of no concern. Both approaches are being pursued and have their own merits and shortcomings.

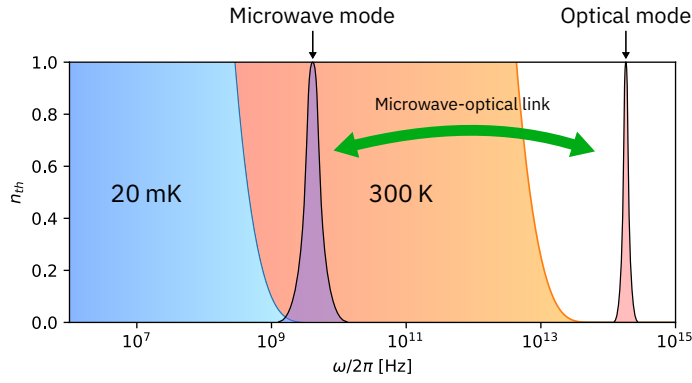


Figure 1: Thermal occupation at 20 mK (blue line) and 300 K (orange line) and indicated typical microwave and optical frequencies.

How to Build a Quantum Network

In order to better illustrate what is required of a quantum interconnect, it is instructive to give a specific example on how a quantum network could operate. First and foremost, the network should link nodes without significant loss of information, and second, the network should enable exchange of information between nodes on the time-scales at which operations are typically carried out in the quantum processor.

A fine example of such information exchange is quantum teleportation [10], where two nodes share a reservoir of Bell-pairs, that can be used to exchange quantum information faithfully via local operations on the Bell-pairs and classical communication. This method is faithful in that it relies only on the purity of the shared entangled states, and it is fast in that all operations that must be performed are implemented via a small number (≤ 4) of quantum gates, two qubit measurements and the exchange of two bits of classical information, all of which can be achieved on time-scales much shorter than the coherence time of modern superconducting

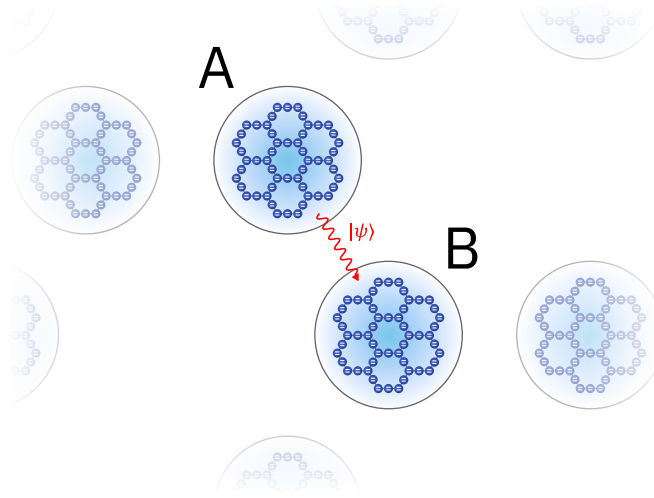


Figure 2: Illustration of network of modular quantum processors. A quantum state $|\psi\rangle$ is sent from node A to node B.

qubits [92]. The key element of such a network is the distribution of Bell-pairs between nodes. Therefore, the main requirement to a 'quantum interconnect' apparatus would be in this case that it produces such Bell-pairs at a sufficient rate and with sufficient fidelity to be used as a resource for teleportation. To the latter point it is worth noting that 'impure' Bell-pairs, or mixed entangled states, may be distilled into a smaller number of states with higher purity [11, 12], so the apparatus may make up for infidelity by producing states at a high rate. I also want to note here that this example is a special case of quantum transduction, often referred to as entanglement-based quantum transduction (EQT). Other approaches based on direct quantum transduction (DQT) [46] and adaptive quantum transduction (AQT) are also being pursued.

Benefits of Going Optical

As mentioned before, one might employ two different design philosophies in realizing a quantum interconnect, either lowering the temperature to avoid thermal noise or converting the quantum state into a medium with higher energy that is insensitive to thermal noise. For the latter, optical photons at near-infrared frequencies in the telecommunications bands are particularly attractive as they allow entanglement distribution via optical fiber networks [60]. A quantum interconnect at microwave frequencies has recently been demonstrated by connecting two dilution refrigerators, each housing a superconducting quantum processor, with a cryogenic bridge that was cooled to millikelvin temperatures and accommodated a superconducting microwave waveguide, that allowed the preparation of a Bell-pair between qubits in each of the quantum processors [64]. With regard to the introduced network interaction via quantum teleportation this method has the appeal that Bell-pairs can be produced at relatively high fidelity $\mathcal{F} = 79.5\%$, and at a high rate, limited only by the gate and qubit reset times, both of which are highly optimized components of the circuit quantum electrodynamics (circuit

QED) toolbox. However, this approach comes with the disadvantage that the implementation of a sufficiently isolated and thermalized cryogenic bridge between dilution refrigerators is not trivial, and probably limits the distribution to relatively short distances on the order of meters.

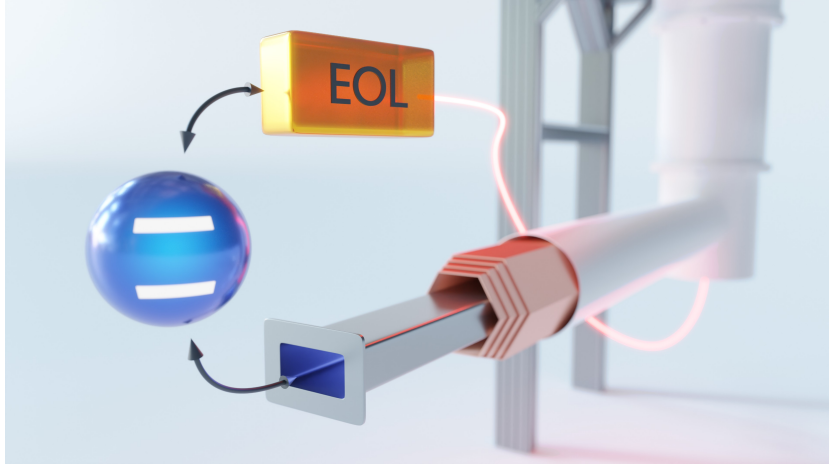


Figure 3: Illustration of alternative approaches to quantum interconnects, qubit state transduced via microwaves (bottom) and via electro-optic link (EOL) (top).

The second design paradigm, implementing a quantum interconnect via optical photons, has gained particular traction in recent years and is being developed in several platforms, two of the most mature and for this work most relevant methods are via an intermediary mechanical element [3, 49, 4, 8, 15, 67, 49, 52, 45, 42, 44, 43, 88], and via the electro-optic effect [50, 65, 35, 73, 103, 32, 36, 91, 79, 47, 101]. The incentive to implement an optical interconnect instead of one that is based on microwaves is motivated by a plethora of attractive properties. Most importantly, optical photons, having a frequency $\sim 10^4$ times higher than microwave photons, do not require cooling or radiation shielding from a room-temperature environment to conserve quantum information. Additionally, the high flexibility of fiber networks makes the implementation of an interconnect much more straight forward than with a rigid microwave waveguide.

Cavity Optomechanics – Mediator between Light and Darkness

At this point, I would like to focus the discussion on cavity optomechanical implementations of a microwave-to-optical link, as, between optomechanical and direct electro-optic implementations, the former is by far the more mature and the one in which significant progress has been demonstrated in recent years [3, 7, 52, 67, 77, 78, 43, 88]. The canonical picture of optomechanical coupling employs a Fabry-Pérot cavity, as illustrated in Figure 4, of which one mirror is suspended on a spring.

Radiation pressure exerted on the suspended mirror by photons circulating in the cavity creates a driving force on the mirror that produces a mechanical displacement of the mirror.

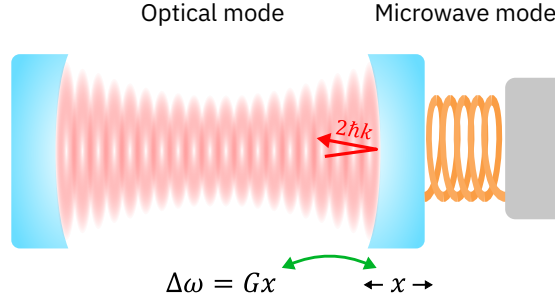


Figure 4: Optomechanical coupling. n cavity photons lead to radiation pressure force on mirror $F_{\text{rad}} = 2\hbar k \cdot n/\tau_c$ with photon roundtrip time τ_c . Mirror displaced by x due to force creates cavity frequency shift $\Delta\omega$.

The mirror displacement leads to a dispersive shift of the optical frequency, thus realizing a parametric coupling between the mechanical and optical modes. Optomechanics offers the opportunity of implementing a quantum link in two fundamentally different ways, via parametric down-conversion (two-mode squeezer interaction) or by direct transduction (beam-splitter interaction). An introduction to the topic is given by Aspelmeyer et al. [6].

Direct Transduction

Direct transduction can be viewed in analogy to the microwave link discussed before. In this case, a Bell-state could be prepared in a circuit QED system and one half of the pair would then be converted into an optical photon by means of a pump pulse (detuned from the optical resonance frequency by the mechanical frequency $-\Omega_m$) that swaps the state of the mechanical oscillator with that of the cavity mode, and back into a microwave photon on the other end of the connection. A simplified example of this protocol is shown in Figure 5

While appealing at first sight, being in close analogy to classical datacom, this approach has some important shortcomings. First, the fidelity of the link is made fundamentally dependent on noise, such as optically-induced thermal noise and backaction noise, and loss in the transmission channel, for example fiber-chip coupling loss. Classical fiber-optic networks can sustain high loss as weak signals can be amplified and loss can be compensated by higher optical power. However, it is not possible to amplify a quantum state and non-trivial to produce one that is insensitive to loss. Second, deterministic transduction typically requires a strong optical parametric drive to obtain sufficient cooperativity for appreciable transduction efficiency. This poses several technical problems with the operation of a circuit QED system. First, dilution refrigerators typically only provide $\mathcal{O}(10\mu\text{W})$ of cooling power at the baseplate temperature of 10 mK, a strong optical pump which would likely have some amount of scattering into the refrigerator would inevitably create an excessive amount of heating, increasing the thermal occupation of the devices. Second, optical photons are regarded with discomfort by the research community of superconducting qubits, as they have sufficient energy to overcome the pairing energy of a cooper-pair in the superconductor, such that optical absorption can lead to the introduction of de-paired electron-electron pairs (quasi-particles) which can

Entanglement Distribution with Cavity Optomechanics

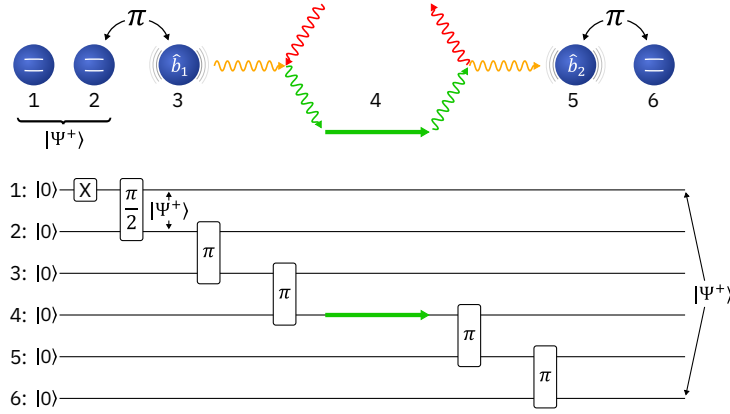


Figure 5: Simplified example of entanglement via direct transduction. Orange wavy lines indicate phonons at the mechanical frequency, green wavy lines indicate photons at the optical cavity resonance frequency, and red wavy lines indicate photons detuned from the optical resonance by the mechanical frequency. 1,2 and 6 are superconducting qubits, 3 and 5 are mechanical modes of optomechanical system. 4 is optical channel. Optomechanical interaction is symbolized with scattering process, red and green lines are photons, orange lines are phonons. Bell-state $|\Psi^+\rangle$ is prepared in qubit pair 1,2. State of 2 and 3 are swapped, optomechanical beam-splitter pulse swaps 3 and 4, optical photon is transmitted, 4 and 5 are swapped, and 5 and 6 are swapped. 1 and 6 end up in $|\Psi^+\rangle$.

introduce unwanted state transitions in the qubit. For that reason, dilution refrigerators are typically heavily shielded against thermal radiation, even against that at higher cryogenic temperature. Introducing a large number of optical photons deliberately into this carefully shielded area seems unwise.

Entanglement Distribution with Cavity Optomechanics

The second possibility of implementing a quantum interconnect with an optomechanical device is based on the two-particle process named the 'two-mode squeezer' interaction. Here, a higher-energy pump photon (detuned from the optical cavity resonance frequency by the mechanical frequency Ω_m) scatters into a lower-energy photon on resonance with the optical cavity while producing a phonon in the mechanical resonator in the process. The extraction and measurement of the produced photon then permits the projection of the mechanical oscillator into a single-phonon quantum state [77]. In extension to this, the scattered photons from two devices can be mixed on a beam-splitter to erase the information about the origin of the scattered photons. A subsequent measurement of the scattered photons then projects the system of the two mechanical devices into a Bell-state [78]. A simplified picture of this protocol is shown in Figure 6

The success of this probabilistic protocol (DLCZ [28]) is conditioned to a low probability of the scattering process to occur, to avoid multi-scattering processes due to the classical nature of the pump field. However, if the heralding photon produced by the scattering event is detected,

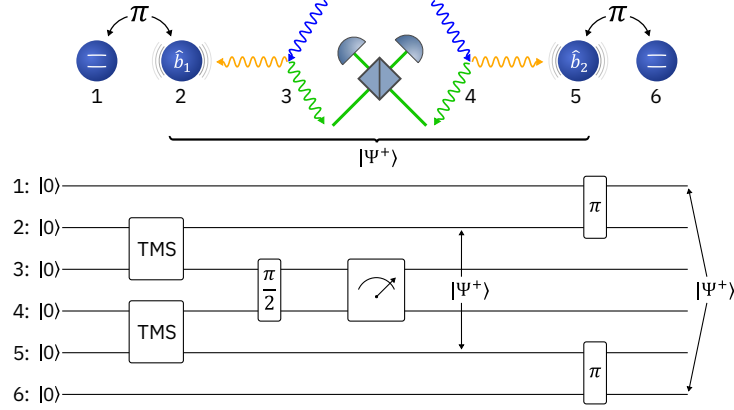


Figure 6: Example of entanglement via two-mode squeezer interaction, notation as in Figure 5. 3 and 4 are pumped with a weak, blue-detuned pump pulse to drive two-mode squeezer interaction (TMS). Scattered photons are sent through beam-splitter (indicated in the schematic by $\pi/2$) and subsequently measured. Positive measurement outcome projects 2 and 5 into $|\Psi^+\rangle$, 1 and 2, and 5 and 6 are swapped, 1 and 6 end up in $|\Psi^+\rangle$.

the probability of finding the system in a bell-state is comparatively high (exact fidelities are not given by Riedinger et al. [78], typical fidelity for single-phonon Fock state is $\sim 88\%$ [77]). This protocol can produce Bell-pairs in the mechanical resonators that may be housed inside different dilution refrigerators at a rate that is determined by the repetition rate of the experiment and the success rate of the heralding process. Importantly, the fidelity of the produced Bell-pair is not determined by loss in the optical path, only by diagonal elements in the density matrix that do not correspond to the creation of a single-phonon state, e.g. the remaining probability of a two-photon scattering event, and false positives created by the single-photon detectors. Optical loss merely leads to a reduced success rate. Although to date, the rate at which Bell-pairs can be produced with this protocol is low [78], one can envision a clear path on how to improve on the existing protocols to obtain a sufficient rate of Bell-pairs for a teleportation protocol, such as active resonator reset and multiple devices operating in parallel.

Optomechanical Design

Optomechanical coupling is realized in a wide range of physical implementations [6]. Most progress towards an entanglement distribution scheme as described above to date has been made in one-dimensional photonic crystal cavities [77, 78] that support an optical mode that is co-localized with mechanical modes with frequencies in the gigahertz range. These devices experience high optomechanical vacuum coupling rates $g_0/2\pi = \mathcal{O}(1 \text{ MHz})$ and recent experiments have demonstrated astonishing phonon lifetimes [62]. Mechanical frequencies in the gigahertz range make this system appealing for resonant coupling to superconducting qubits [67]. All these properties make this system a promising candidate for the optomechanical component in a microwave-to-optical link.

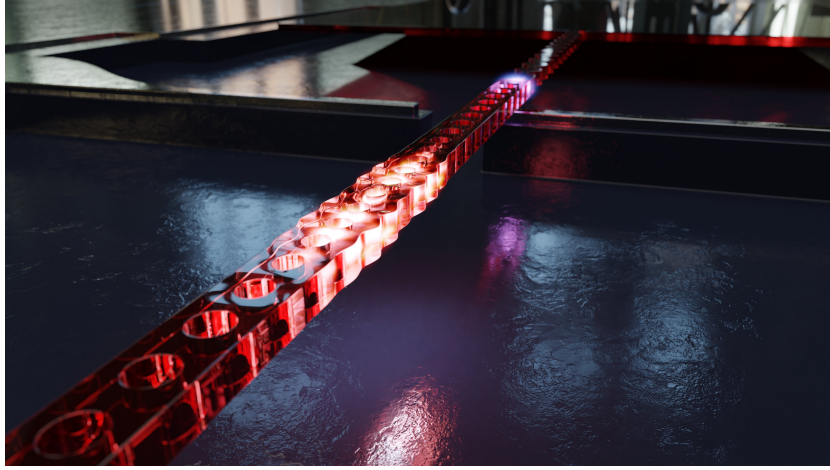


Figure 7: Artistic representation of photonic crystal cavity integrated on superconducting circuit.

Circuit Quantum Acousto-Dynamics

Preparing a Bell-pair in a pair of mechanical resonators is only half of the recipe to success. The other half consists of moving the Bell-pair from the resonators to a set of qubits, where it may be further processed, either by moving it into a quantum memory, or by performing a teleportation protocol on it. The emerging field of circuit quantum acousto-dynamics, i.e. coupling superconducting qubits to mechanical oscillators, has seen big strides in the past decade. Numerous systems have been introduced which allow swapping the state of the mechanical oscillator with that of the qubit [72], notably phononic crystal resonators [5], surface-acoustic wave resonators [82, 13] and high-overtone bulk acoustic resonators [20, 21], and a state swap of a single phonon state can be achieved with a fidelity $\sim 86\%$ [21], even at moderate coupling rates between qubit and mechanical resonator $g/2\pi \sim 350\text{ kHz}$. The important prerequisite for a state-swap with high fidelity is strong coupling between the mechanical and qubit modes, and so one major design goal for a physical implementation of the quantum acoustic component of the microwave-to-optical link is to realize at least a moderate coupling rate between the superconducting qubit and the mechanical resonator $\mathcal{O}(100\text{ kHz})$.

Piezoelectric Coupling

Most quantum-acoustic platforms, especially those with mechanical modes in the gigahertz regime, realize electromechanical coupling between the qubit and mechanical resonator via the piezoelectric effect. Functional materials such as AlN [21, 71], LiNbO₃ [5, 82] or GaAs [8] are therefore required to enable the electromechanical coupling. Typically, the geometry of the mechanical resonator is chosen carefully to engineer the electromechanical coupling between the mechanical mode of interest and the qubit, and suppress the coupling to other

mechanical modes such as bulk phonons, which pose a considerable source of loss for the qubit.

Gallium Phosphide

Gallium phosphide was chosen as a material for the presented platform as it experiences a large optical bandgap $E_g = 2.26\text{ eV}$ compared to that of silicon ($E_g = 1.14\text{ eV}$), a typical material for photonic crystal cavities such as the ones discussed here [29, 18, 19, 77, 78, 62, 75]. This promises better thermal properties, while gallium phosphide at the same time has a non-centrosymmetric crystal structure, which provides piezoelectric coupling to an external electric field, albeit a small one [68]. At IBM, GaP was previously integrated on SiO_2 to realize photonic integrated circuits [84] and photonic crystal cavities with optomechanical coupling rates that are comparable to those in Si devices [85]. Recently, GaP has also been used for quantum optomechanical experiments [93] where the thermal properties, especially with regard to delayed heating, were shown to compare favorably to those of similar III-V semiconductors such as GaAs. Importantly, mechanical quality factors $> 2 \times 10^5$ were shown at single phonon energies, which indicates that quantum optomechanical experiments analogous to those performed with silicon devices [77, 78] are possible.

Building a Microwave-Optical Link

To conclude this introduction, I would like to outline the the work presented here. First, I present the theoretical background necessary to describe the simulated and experimental results. Then, I will present the design of the electro-optomechanical device with estimations of the optomechanical and electromechanical coupling rates. In Part III I present a novel fabrication process that I developed which allows, for the first time, the integration of a single-crystal piezoelectric film on a wafer on which a superconducting circuit was previously fabricated. In Part IV I present results on microwave-to-optical transduction in the classical domain with the discussed design and finally, I present results for superconducting cavities that were fabricated with the developed process flow to show that the employed process has no detrimental effect on the superconducting devices. I conclude this work with an outlook on future improvements of the platform and with a perspective on the integration of superconducting qubits with this platform.

Theoretical Background **Part I**

1 Resonators

In this chapter I will introduce the description of optical, mechanical, and microwave resonators in the framework of input-output theory. I will only briefly sketch the derivation of the input-output relations and the equation of motion for a harmonic oscillator. A more exhaustive description can be found in [37].

1.1 Input-Output Formalism

The interaction of a harmonic oscillator (cavity) with the environment, e.g. a heat bath or a drive, can be described as the interaction of the cavity mode with 'bath modes' (annihilation operator \hat{c}), a large number of harmonic oscillator modes with frequency ω_q that are coupled bi-linearly to the cavity mode. The Hamiltonian then reads

$$\hat{H} = \hat{H}_{\text{sys}} + \hat{H}_{\text{bath}} + \hat{H}_{\text{int}} \quad (1.1)$$

where \hat{H}_{sys} is the system Hamiltonian with annihilation operator \hat{a} , and

$$\begin{aligned} \hat{H}_{\text{bath}} &= \hbar \sum_q \omega_q \hat{c}_q^\dagger \hat{c}_q \\ \hat{H}_{\text{int}} &= -i\hbar \sum_q f_q \hat{a}^\dagger \hat{c}_q - f_q^* \hat{a} \hat{c}_q^\dagger \end{aligned} \quad (1.2)$$

are the bath Hamiltonian, and the interaction Hamiltonian of the bath with the cavity with coupling rates f_q . The Heisenberg equation of motion

$$\dot{\hat{a}} = \frac{i}{\hbar} [\hat{H}, \hat{a}] \quad (1.3)$$

which describes the time evolution of the system annihilation operator \hat{a} , can then be solved assuming the Markov approximation. This means the bath modes are assumed to have a very short correlation time τ_C compared to the coupling rates f_q , which implies that:

1. All bath modes are coupled equally to the cavity: $f_q = f = \text{const.}$
2. The density of bath modes is a continuum with a constant density of states ρ .
3. The coupling rate to the bath κ can be derived from f via Fermi's golden rule.

$\dot{\hat{a}}$ can then be found as [37]

$$\dot{\hat{a}} = \frac{i}{\hbar} [\hat{H}_{\text{sys}}, \hat{a}] - \frac{\kappa}{2} \hat{a} - \sqrt{\kappa} \hat{c}_{\text{in}} \quad (1.4)$$

and

$$\hat{c}_{\text{out}} = \hat{c}_{\text{in}} + \sqrt{\kappa} \hat{a}, \quad (1.5)$$

where \hat{c}_{in} and \hat{c}_{out} are respectively the input and output fields.

The relevant case for this work is the description of the harmonic oscillator with the system Hamiltonian

$$\hat{H}_{\text{sys}} = \hbar\omega_0 \hat{a}^\dagger \hat{a} \quad (1.6)$$

where ω_0 is the oscillator's eigenfrequency. We neglect the ground state energy of the harmonic oscillator in this case as this term commutes with the annihilation operator and consequently does not appear in the equations of motion, and is therefore inconsequential for the system dynamics.

We obtain the equation of motion

$$\dot{\hat{a}} = -i\omega_0 \hat{a} - \frac{\kappa}{2} \hat{a} - \sqrt{\kappa} \hat{c}_{\text{in}}. \quad (1.7)$$

In case of a driven resonator it is convenient to separate the interaction with the mode of the incoming driving field \hat{a}_{in} with the coupling rate κ_{ex} from the contributions of the remaining bath \hat{f}_{in} that couples to the resonator with an intrinsic decay rate κ_0 , such that the equation of motion reads

$$\dot{\hat{a}} = -i\omega_0 \hat{a} - \frac{\kappa}{2} \hat{a} - \sqrt{\kappa_{\text{ex}}} \hat{a}_{\text{in}} - \sqrt{\kappa_0} \hat{\delta}_{\text{in}}. \quad (1.8)$$

$\hat{\delta}_{\text{in}}$ is a noise operator, which has some important properties:

$$\begin{aligned} \langle \hat{\delta}(t) \rangle &= 0 \\ \langle \hat{\delta}^\dagger(t) \hat{\delta}(t') \rangle &= \bar{n}_{\text{th}} \delta(t - t') \\ \langle \hat{\delta}(t) \hat{\delta}^\dagger(t') \rangle &= (\bar{n}_{\text{th}} + 1) \delta(t - t') \end{aligned} \quad (1.9)$$

1.2 Optical Cavities

We can solve Equation 1.8 for a classical optical input field, the relevant solution for the work presented here, by replacing the operators \hat{a} , \hat{a}_{in} , and $\hat{\delta}_{\text{in}}$ by their expectation values for a

coherent state $|\alpha\rangle$:

$$\begin{aligned}\langle \hat{a} \rangle &= \alpha \\ \langle \hat{a}_{\text{in}} \rangle &= \alpha_{\text{in}} \\ \langle \hat{\delta}_{\text{in}} \rangle &= 0\end{aligned}\tag{1.10}$$

where α_{in} is the amplitude of the coherent input state $|\alpha\rangle$.

$$\dot{\alpha} = -\left(i\omega_0 + \frac{\kappa}{2}\right)\alpha - \sqrt{\kappa_{\text{ex}}}\alpha_{\text{in}}.\tag{1.11}$$

For a cavity driven at a laser frequency ω_L we find the solution as

$$\alpha = -\frac{\sqrt{\kappa_{\text{ex}}}}{\frac{\kappa}{2} - i(\omega_L - \omega_0)}\alpha_{\text{in}} = -\frac{\sqrt{\kappa_{\text{ex}}}}{\frac{\kappa}{2} - i\Delta}\alpha_{\text{in}}\tag{1.12}$$

with the cavity detuning $\Delta = \omega_L - \omega_0$. The frequency response the cavity at a frequency Ω offset from the laser is given as

$$\alpha(\Omega) = -\frac{\sqrt{\kappa_{\text{ex}}}}{\kappa/2 - i(\Delta + \Omega)}\alpha_{\text{in}}(\Omega) = -\chi_{\text{opt}}(\Omega)\sqrt{\kappa_{\text{ex}}}\alpha_{\text{in}}(\Omega)\tag{1.13}$$

where the optical susceptibility is defined as

$$\chi_{\text{opt}}(\Omega) = \frac{1}{\kappa/2 - i(\Delta + \Omega)}.\tag{1.14}$$

We can easily find the intracavity photon number

$$\bar{n}_{\text{cav}} = |\alpha|^2 = \frac{\kappa_{\text{ex}}}{\kappa^2/4 + \Delta^2}|\alpha_{\text{in}}|^2 = \frac{\kappa_{\text{ex}}}{\kappa^2/4 + \Delta^2} \frac{P_{\text{in}}}{\hbar\omega_L}.\tag{1.15}$$

1.3 Superconducting Microwave Resonators

We can treat a superconducting microwave resonator analogously to an optical cavity where β denotes the resonator amplitude and β_{in} the microwave input field and solve Equation 1.11 to find

$$\beta = -\chi_{\text{mw}}(\Omega)\sqrt{\kappa_{\text{ex}}}\beta_{\text{in}}\tag{1.16}$$

with

$$\chi_{\text{mw}}(\Omega) = \frac{1}{\frac{\kappa}{2} - i(\Omega - \Omega_{\text{mw}})}\tag{1.17}$$

where Ω_{mw} is the resonator's eigenfrequency. We will later analyze scattering data from a vector network analyzer to characterize the loss rate $\kappa_0 = \kappa - \kappa_{\text{ex}}$ and eigenfrequency Ω_{mw} of superconducting resonators, in particular the transmission S_{21} between the two ports of the transmission line that the resonator is coupled to. We can derive this simply by analyzing the

output field β_{out} of the cavity

$$\begin{aligned}\beta_{\text{out}}(\Omega) &= \beta_{\text{in}}(\Omega) + \sqrt{\kappa_{\text{ex}}}\beta(\Omega) \\ &= \beta_{\text{in}}(\Omega) (1 - \kappa_{\text{ex}}\chi_{\text{mw}}(\Omega)).\end{aligned}\tag{1.18}$$

The relevant scattering parameter is defined as $S_{21}(\Omega) = \frac{V_{\text{out}}(\Omega)}{V_{\text{in}}(\Omega)} = \frac{\beta_{\text{out}}(\Omega)}{\beta_{\text{in}}(\Omega)}$ [74]. We can express the loss and gain of the measurement system with a global detection gain factor Γ_{D} . In addition, the electronic delay τ of the system leads to an accumulated phase $\omega\tau$, as well as a phase offset θ . The scattering parameter then reads

$$S_{21}(\Omega) = \Gamma_{\text{D}} (1 - \kappa_{\text{ex}}\chi_{\text{mw}}(\Omega)) e^{i(\Omega\tau + \theta)}.\tag{1.19}$$

1.4 Mechanical Oscillators

In the context of the work discussed here, where the displacement of the mechanical oscillator is not of particular interest, and not even unambiguously defined, it is more useful to describe the oscillator in terms of its amplitude \hat{b} , where the displacement would be given as $\hat{x} = x_{\text{ZPF}}(\hat{b} + \hat{b}^\dagger)$. We can then use the identical description as for a microwave cavity derived in the previous section, such that we find, for a coherent input state $|\beta_{\text{in}}\rangle$, the classical amplitude $\beta = \langle \hat{b} \rangle$ as

$$\beta(\Omega) = -\chi_{\text{m}}(\Omega) \sqrt{\Gamma_{\text{ex}}}\beta_{\text{in}}(\Omega)\tag{1.20}$$

with

$$\chi_{\text{m}}(\Omega) = \frac{1}{\frac{\Gamma_{\text{m}}}{2} - i(\Omega - \Omega_{\text{m}})}.\tag{1.21}$$

with the mechanical damping rate Γ_{m} , the mechanical eigenfrequency Ω_{m} and the coupling rate Γ_{ex} to the incoming microwave field $\beta_{\text{in}}(\Omega) = \langle \hat{b}_{\text{in}} \rangle = \beta_{\text{in},0} e^{-i\Omega t}$ where $\beta_{\text{in},0} = |V_0|/\sqrt{2Z_0\hbar\Omega}$ is the rate of incident microwave photons, $Z_0 = 50\Omega$ is the characteristic impedance of the microwave transmission line, and V_0 is the voltage amplitude of the incident microwave in the transmission line. This description has the added benefit that we can easily perform a circuit decomposition of the piezoelectrically coupled oscillator, as soon as Γ_{ex} and the capacitance of the coupling electrodes C_0 are known.

Circuit Decomposition of a Piezoelectrically Coupled Mechanical Oscillator

Equation 1.20 being in a general form of a harmonic oscillator and not specific to a mechanical resonator, we can consider it from the viewpoint of the microwave input signal as an equivalent parallel LC resonator with eigenfrequency $\Omega_{\text{m}} = 1/\sqrt{LC}$ with inductance L and capacitance C , that is coupled to a transmission line – the microwave drive port – via a small coupling capacitor $C_0 \ll C$. This form is useful as it simplifies the description of a system in which the mechanical resonator is piezoelectrically coupled to a superconducting qubit.

In order to find the coupling rate Γ_{ex} to the transmission line, we can consider a situation

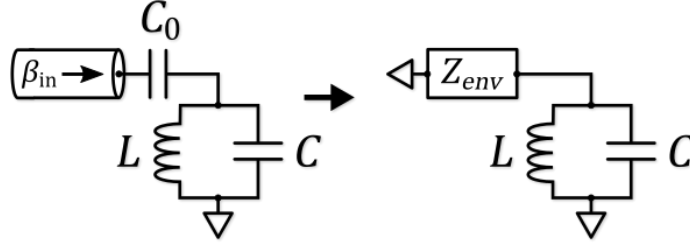


Figure 1.1: Equivalent circuit of a parallel LC resonator coupled to a semi-infinite transmission line via a coupling capacitor C_0 (left) and representation of coupling capacitor and transmission line as environmental load impedance Z_{env} on the LC resonator.

where the LC resonator has no additional loss and the decay rate of the circuit is determined by the impedance of the environment

$$Z_{env} = Z_0 + \frac{1}{i\Omega C_0} \quad (1.22)$$

presented by the transmission line. Here, $Z_0 = 50\Omega$ is the reference impedance of the transmission line. In the spirit of input-output theory we can again make the Markov approximation, and assume that photons which couple from the LC circuit into the transmission line are lost, and do not couple back into the resonator – i.e. a semi-infinite transmission line [37].

The impact of the environment on the resonator is given by its admittance $Y_{env} = 1/Z_{env}$ and we may identify the real part of the Y_{env} with a resistive load R on the oscillator with

$$R = \frac{1}{\Re\{Y_{env}\}} \approx \frac{1}{Z_0 \Omega^2 C_0^2} \quad (1.23)$$

for $C_0 \ll C \frac{Z_{res}}{Z_0}$, where Z_{res} is the resonator impedance. The damping rate Γ_{ex} is now given as

$$\Gamma_{ex} = \frac{1}{R(C + C_0)} = \frac{C_0^2 Z_0 \Omega^2}{C + C_0} \quad (1.24)$$

We can then determine

$$C = \frac{C_0^2 Z_0 \Omega_m^2}{\Gamma_{ex}} - C_0 \quad (1.25)$$

and consequently

$$L = \frac{1}{\Omega_m^2 C}. \quad (1.26)$$

In the case where C_0 is on the order of C , the imaginary part of Y_{env} introduces a dispersive shift of the resonator. In the case of the piezoelectric devices discussed here ($C \sim 10^6 C_0$) this shift can be neglected.

2 Superconducting Qubits

At this point, I want to briefly introduce superconducting qubits, to the extend that we can understand dynamics of a superconducting qubit coupled to a mechanical oscillator. An excellent and expansive treatment of superconducting qubits is given in [37] and an overview over the topic and several implementations is given in [26].

2.1 Josephson Nonlinear Inductance

Electrons in a normal conductor occupy a macroscopic number of individual states, which makes a quantum-mechanical description intractable. In a superconductor however, at frequencies Ω and temperatures T well below the superconducting bandgap – $k_B T, \hbar\Omega \ll 2\Delta$ – the charges in the metal pair into Cooper pairs and condense into a global, non-degenerate ground-state, which makes a quantum mechanical description feasible. If two islands made of a superconductor are connected with an insulating barrier, Cooper pairs can hop from one island to another with a characteristic energy

$$E_J = \frac{1}{2} \frac{h}{(2e)^2} G_N \Delta, \quad (2.1)$$

where e is the elementary charge, Δ is the superconducting bandgap, and G_N is a normal state conductance. This equation is called the Ambegaokar-Baratoff relation [2] and is a useful method to estimate the Josephson energy E_J by measuring the resistance of the junction at room temperature.

The tunneling is described by the two Josephson-relations. The first of which links the current that flows through the junction to the phase-difference of the order parameter between the two islands φ as

$$I(\varphi) = I_C \sin(\varphi), \quad (2.2)$$

where $I_C = 2\pi E_J / \Phi_0$ is the geometry-dependent critical current of the junction, with the flux quantum Φ_0 . The second Josephson relation describes the time derivative of the phase φ with

a voltage V between the two islands:

$$V = \frac{\Phi_0}{2\pi} \dot{\varphi} \quad (2.3)$$

One can now plug the first Josephson relation into the second one to obtain

$$V = \frac{\Phi_0}{2\pi I_C \cos(\varphi)} \frac{dI}{dt}. \quad (2.4)$$

The Josephson junction can therefore be understood as a nonlinear inductor with inductance $\varphi_0 / (I_C \cos(\varphi))$.

2.2 Cooper-Pair Box Hamiltonian

In addition to the inductance that arises from the Josephson effect the number of cooper pairs tunneling between the two islands n (operator $\hat{n} = \sum n|n\rangle\langle n|$) also leads to an oscillating charge. Microscopic charges in and around the junction, or an externally applied electric field, can impose an additional offset charge n_g , such that the Hamiltonian of this cooper-pair box reads [37]

$$\hat{H}_{\text{CPB}} = 4E_C(\hat{n} + n_g)^2 - E_J \cos(\hat{\varphi}), \quad (2.5)$$

where $\hat{\varphi}$ is a dimensionless flux, $E_C = e^2/(2C)$ is the charging energy of a single electron and C is the capacitance of the junction.

2.3 Transmon Limit

Depending on the magnitude of E_C the energy of a qubit described by Equation 2.5 can lead to a strong dispersion of the qubit energy depending on the offset charge n_g . Consequently, early implementations of charge qubits were plagued by small variations in the offset charge by uncontrolled, time dependent microscopic charges in the device that lead to a shift in the qubit transition energy and consequently to decoherence of the qubit. The canonical approach nowadays is to operate in a regime where the ratio of Josephson energy to charging energy is large. This is implemented by shunting the junction with a large capacitor C_Σ , such that $E_J/E_C \gg 1$, which strongly reduces the charge dispersion of the Hamiltonian. This is the so-called Transmon limit [58]. In this limit (typically for $E_J/E_C \sim 50$), the effect of the offset charge n_g on the charging energy is negligible and Equation 2.5 can be approximated by

$$\hat{H} = 4E_C \hat{n}^2 - E_J \cos(\hat{\varphi}). \quad (2.6)$$

The Hamiltonian can be brought into a more useful form by treating the nonlinearity of the inductance perturbatively and Taylor-expanding it to second order to obtain

$$\hat{H} \approx 4E_C \hat{n}^2 + \frac{1}{2} E_J \hat{\varphi}^2 - \frac{E_J}{24} \hat{\varphi}^4 \quad (2.7)$$

2.4. Interaction between a Transmon and a Linear LC Resonator

The phase operator $\hat{\phi}$ in second quantization (with annihilation operator \hat{c}) is given as the coordinate [37]:

$$\hat{\phi} = \varphi_{\text{ZPF}}(\hat{c} + \hat{c}^\dagger) \quad (2.8)$$

with

$$\varphi_{\text{ZPF}} = \sqrt{\frac{2E_C}{E_J}}. \quad (2.9)$$

With that, we can write the Hamiltonian as

$$\hat{H} = \hbar\Omega_{\text{ge}}\hat{c}^\dagger\hat{c} - \frac{1}{24}E_J\varphi_{\text{ZPF}}^4(\hat{c}^\dagger\hat{c})^4, \quad (2.10)$$

with the qubit's first transition frequency $\Omega_{\text{ge}} = \sqrt{8E_CE_J}/\hbar$. We only keep terms from $(\hat{c}^\dagger\hat{c})^4$ that conserve energy to find

$$\hat{H} = \hbar\Omega_{\text{ge}}\hat{c}^\dagger\hat{c} - \frac{E_J}{4}\varphi_{\text{ZPF}}^4\hat{c}^{\dagger 2}\hat{c}^2 \quad (2.11)$$

and with the anharmonicity $\alpha_{\text{nl}} = E_{21} - E_{10} = -\frac{E_J\varphi_{\text{ZPF}}^4}{2}$, the difference in the transition energy of the lowest two excited states, we can write

$$\hat{H} = \hbar\Omega_{\text{ge}}\hat{c}^\dagger\hat{c} + \alpha_{\text{nl}}\hat{c}^{\dagger 2}\hat{c}^2 \quad (2.12)$$

2.4 Interaction between a Transmon and a Linear LC Resonator

The quantum-acoustic coupling between a transmon and the piezoelectric devices discussed here can be modeled as the interaction between a transmon and a linear LC resonator via a coupling capacitance C_0 , as shown in Figure 2.1. In general, it can be quite involved to calculate this coupling, especially if more than two modes are involved. This is typically achieved using black-box quantization of the circuit modes [70]. However, in this case the mechanical modes that are considered, are sufficiently well spaced in frequency and experience a sufficiently small coupling that we can consider only one mode coupling to the transmon at once. The

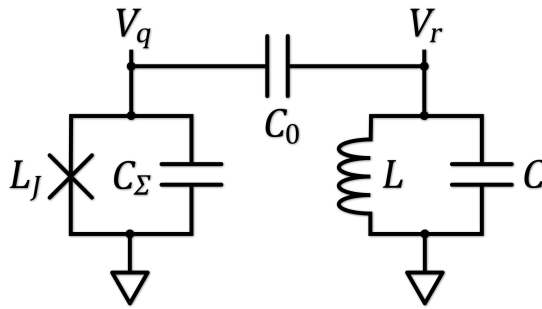


Figure 2.1: Transmon qubit coupled to a linear LC oscillator.

Chapter 2. Superconducting Qubits

derivation of the coupling rate is then trivial. We can consider the voltage at the two nodes indicated in Figure 2.1, V_q and V_r and calculate the charge on each of the capacitors C_0 , C_Σ , and C , Q_0 , Q_Σ , and Q , respectively.

We find

$$\begin{aligned}\frac{Q_\Sigma}{C_\Sigma} &= V_q \\ \frac{Q}{C} &= V_r \\ \frac{Q_0}{C_0} &= V_q - V_r = \frac{Q_\Sigma}{C_\Sigma} - \frac{Q}{C}\end{aligned}\tag{2.13}$$

Consequently, we find the electrostatic energy stored in the whole system

$$\begin{aligned}E_C &= \frac{Q_\Sigma^2}{2C_\Sigma} + \frac{Q^2}{2C} + \frac{C_0}{2} \left(\frac{Q_\Sigma}{C_\Sigma} - \frac{Q}{C} \right)^2 \\ &= \frac{Q_\Sigma^2}{2C_\Sigma} \left(1 + \frac{C_0}{C_\Sigma} \right) + \frac{Q^2}{2C} \left(1 + \frac{C_0}{C} \right) - C_0 \left(\frac{Q_\Sigma Q}{C_\Sigma C} \right).\end{aligned}\tag{2.14}$$

With the charge operators \hat{Q}_Σ and \hat{Q} in second quantization as

$$\begin{aligned}\hat{Q}_\Sigma &= \sqrt{\frac{\hbar \Omega_{ge} C_\Sigma}{2}} i(\hat{c}^\dagger - \hat{c}) \\ \hat{Q} &= \sqrt{\frac{\hbar \Omega_m C}{2}} i(\hat{b}^\dagger - \hat{b}),\end{aligned}\tag{2.15}$$

where Ω_{ge} is the qubit's first transition frequency and Ω_m is the resonator's eigenfrequency, we obtain

$$\hat{Q}_\Sigma \hat{Q} = -\frac{1}{2} \hbar \sqrt{\Omega_{ge} \Omega_m C_\Sigma C} (\hat{c}^\dagger \hat{b}^\dagger - \hat{c}^\dagger \hat{b} - \hat{c} \hat{b}^\dagger + \hat{c} \hat{b}).\tag{2.16}$$

We can then write

$$-C_0 \left(\frac{\hat{Q}_\Sigma \hat{Q}}{C_\Sigma C} \right) = -\hbar g (\hat{c}^\dagger \hat{b} + \hat{c} \hat{b}^\dagger) + \hbar g (\hat{c}^\dagger \hat{b}^\dagger + \hat{c} \hat{b})\tag{2.17}$$

with

$$g = \frac{1}{2} C_0 \sqrt{\frac{\Omega_{ge} \Omega_m}{C_\Sigma C}}.\tag{2.18}$$

Using Equation 2.12 we can then write the full system Hamiltonian as

$$\hat{H} = \hat{H}_0 + \hat{H}_{\text{int}} = \hbar \Omega_{ge} \hat{c}^\dagger \hat{c} + \alpha_{nl} \hat{c}^{\dagger 2} \hat{c}^2 + \hbar \Omega_m \hat{b}^\dagger \hat{b} - \hbar g (\hat{c}^\dagger \hat{b} + \hat{c} \hat{b}^\dagger) + \hbar g (\hat{c}^\dagger \hat{b}^\dagger + \hat{c} \hat{b}).\tag{2.19}$$

We can use the rotating-wave approximation ($\Omega_{ge} \sim \Omega_m$, $g \ll \Omega_{ge,m}$) to neglect the far off-resonant terms associated with $\hat{c}^\dagger \hat{b}^\dagger + \hat{c} \hat{b}$ such that the interaction Hamiltonian is simply given by the beam-splitter interaction

$$\hat{H}_{\text{int}} = -\hbar g (\hat{c}^\dagger \hat{b} + \hat{c} \hat{b}^\dagger).\tag{2.20}$$

3 Cavity-Optomechanics

Cavity optomechanics originates from the interaction of a cavity field with a mechanical degree of freedom via radiation pressure [6]. In the canonical picture of one mirror of a Fabry-Pérot cavity being suspended on a spring, a displacement x then leads to a shift of the cavity frequency

$$\omega = \omega_0 + \frac{\partial \omega}{\partial x} x = \omega_0 + Gx \quad (3.1)$$

where G is the dispersive shift introduced by the mirror displacement.

3.1 Optomechanical Hamiltonian

This coupling can be formulated in a Hamiltonian where two harmonic oscillators, describing the optical cavity (annihilation operator \hat{a}) and mechanical oscillator (annihilation operator \hat{b}) are coupled by the vacuum optomechanical coupling rate $g_0 = Gx_{\text{ZPF}}$, where x_{ZPF} is the zero-point fluctuation of the mechanical oscillator, in the rotating frame of the laser frequency ω_L as

$$\hat{H} = -\hbar\Delta\hat{a}^\dagger\hat{a} + \hbar\Omega_m\hat{b}^\dagger\hat{b} + \hbar g_0\hat{a}^\dagger\hat{a}(\hat{b} + \hat{b}^\dagger) \quad (3.2)$$

where Ω_m is the mechanical eigenfrequency, $\hat{x} = x_{\text{ZPF}}(\hat{b} + \hat{b}^\dagger)$, and $\Delta = \omega_L - \omega_o$ is the laser detuning from the optical resonance frequency ω_o [80]. The interaction Hamiltonian

$$\hat{H}_{\text{int}} = \hbar g_0\hat{a}^\dagger\hat{a}(\hat{b} + \hat{b}^\dagger). \quad (3.3)$$

is fundamentally nonlinear. However, we can linearize the interaction by replacing $\hat{a} \mapsto \bar{\alpha} + \delta\hat{a}$, that is, the optical field now consists of a large – in the rotating frame constant – coherent amplitude $\bar{\alpha}$ and small, time dependent fluctuations $\delta\hat{a}$. The interaction Hamiltonian then reads

$$\begin{aligned} \hat{H}_{\text{int}} &= \hbar g_0(\bar{\alpha}^* + \delta\hat{a}^\dagger)(\bar{\alpha} + \delta\hat{a})(\hat{b} + \hat{b}^\dagger) \\ &= \hbar g_0(|\alpha|^2 + \alpha^*\delta\hat{a} + \alpha\delta\hat{a}^\dagger + \delta\hat{a}^\dagger\delta\hat{a})(\hat{b} + \hat{b}^\dagger). \end{aligned} \quad (3.4)$$

The term $\hbar g_0 |\alpha|^2 (\hat{b} + \hat{b}^\dagger)$ leads to a constant radiation pressure, which can be absorbed in the Hamiltonian by redefining \hat{x} with a new equilibrium position shifted by $\Delta x = F_{\text{rad}}/k$, with the radiation pressure force F_{rad} and the spring constant k . The detuning is updated accordingly as $\Delta = \Delta + G\Delta x$. The term $\hbar g_0 (\delta \hat{a}^\dagger \delta \hat{a}) (\hat{b} + \hat{b}^\dagger)$ is smaller than other remaining terms by a factor α and can be neglected. The remaining interaction Hamiltonian then reads

$$\hat{H}_{\text{int}} = \hbar g_0 \left(\bar{\alpha}^* \delta \hat{a} + \bar{\alpha} \delta \hat{a}^\dagger \right) (\hat{b} + \hat{b}^\dagger). \quad (3.5)$$

We may choose a phase for $\bar{\alpha}$ such that $\bar{\alpha} \in \mathbb{R}$ and $\bar{\alpha} = \bar{\alpha}^*$, then we can write

$$\hat{H}_{\text{int}} = \hbar g \left(\delta \hat{a} + \delta \hat{a}^\dagger \right) (\hat{b} + \hat{b}^\dagger). \quad (3.6)$$

with $g = \bar{\alpha} g_0 = \sqrt{n_{\text{cav}}} g_0$.

It is now typical to use the rotating-wave approximation and discard far off-resonant terms in the interaction Hamiltonian, depending on the detuning Δ . For $\Delta \approx -\Omega_m$ the two-particle processes can be neglected and the interaction Hamiltonian reduces to the beam-splitter Hamiltonian:

$$\hat{H}_{\text{int}} = \hbar g \left(\delta \hat{a}^\dagger \hat{b} + \delta \hat{a} \hat{b}^\dagger \right). \quad (3.7)$$

For $\Delta \approx \Omega_m$ the beam-splitter interaction is far off-resonant and the two-particle interaction called the 'two-mode squeezer' is the dominant term such that the interaction Hamiltonian reads

$$\hat{H}_{\text{int}} = \hbar g \left(\delta \hat{a} \hat{b} + \delta \hat{a}^\dagger \hat{b}^\dagger \right) \quad (3.8)$$

and the system Hamiltonian

$$\hat{H}_{\text{sys}} = -\hbar \Delta \hat{a}^\dagger \hat{a} + \hbar \omega_m \hat{b}^\dagger \hat{b} + \hbar g \left(\delta \hat{a} \hat{b} + \delta \hat{a}^\dagger \hat{b}^\dagger \right). \quad (3.9)$$

The rotating-wave approximation typically holds in the resolved-sideband regime, where $\kappa < \Omega_m$. The devices discussed in this work typically barely fulfill this requirement with $\kappa \lesssim \Omega_m$, but it is assumed that this approximation still holds.

3.2 Optomechanical Coupling in Optomechanical Crystal Cavities

For the devices described in this thesis, the optomechanical coupling is calculated numerically from the result of a finite-element method simulation of the optical and mechanical modes. The equations from which the coupling is inferred are derived in great detail elsewhere [17, 55, 76] so I will only present the relevant equations here. We find the linear optomechanical coupling as

$$g_0 = \frac{\partial \omega}{\partial \alpha} x_{\text{ZPF}} \quad (3.10)$$

with the generalized coordinate α . The choice of α for a system such as the one discussed here is a priori arbitrary, since there is no obvious canonical definition such as for a mass on a spring, where the logical choice of the generalized coordinate would be the center of mass.

3.2. Optomechanical Coupling in Optomechanical Crystal Cavities

Instead, α can be defined ad libitum, and subsequently the effective mass m_{eff} is determined to satisfy the condition [17]

$$\frac{1}{2}\omega_m^2 \int d\mathbf{x} \rho(\mathbf{x}) |\mathbf{Q}(\mathbf{x})| = \frac{1}{2} m_{\text{eff}} \alpha^2, \quad (3.11)$$

i.e. the effective mass describes the potential energy stored in the resonator, where $\mathbf{Q}(\mathbf{x})$ is the displacement field of the mechanical oscillator and $\rho(\mathbf{x})$ the oscillators mass density at \mathbf{x} .

For a specific choice of α we can renormalize the displacement field as

$$\mathbf{q}(\mathbf{x}) = \frac{\mathbf{Q}(\mathbf{x})}{\alpha}. \quad (3.12)$$

In this case, we define α as the maximum amplitude of the displacement field \mathbf{Q} [83]. The change of the optical frequency due to the displacement α can be treated perturbatively such that

$$\frac{\partial \omega}{\partial \alpha} = -\frac{\omega_o}{2} \frac{\int d\mathbf{x} \mathbf{E}(\mathbf{x}) \frac{\partial \epsilon(\mathbf{x})}{\partial \alpha} \mathbf{E}^*(\mathbf{x})}{\int d\mathbf{x} \mathbf{E}(\mathbf{x}) \mathbf{D}(\mathbf{x})} \quad (3.13)$$

with the permittivity $\epsilon(\mathbf{x})$ and the unperturbed optical electric field $\mathbf{E}(\mathbf{x})$ and displacement field $\mathbf{D}(\mathbf{x})$.

3.2.1 Moving Boundary Effect

There are two major contributions to the optomechanical coupling in the system discussed here, the first one is due to the moving dielectric boundary between the material of the photonic crystal – gallium phosphide – and the surrounding air, due to the mechanical displacement. The resulting frequency shift can be found according to Johnson et al. [55]. For the simulations presented here, we use the form derived by Chan [17]

$$\left. \frac{\partial \omega}{\partial \alpha} \right|_{\text{mb}} = -\frac{\omega_0}{2} \frac{\oint dA(\mathbf{q}(u, v) \hat{\mathbf{n}}(u, v)) (\Delta \epsilon |\mathbf{E}(u, v)_{\parallel}|^2 - \Delta \epsilon^{-1} |\mathbf{D}(u, v)_{\perp}|^2)}{\int d\mathbf{x} \mathbf{E}(\mathbf{x}) \mathbf{D}(\mathbf{x})} \quad (3.14)$$

where $A(u, v)$ is the surface of the photonic crystal, $\hat{\mathbf{n}}$ the normal vector to the surface, and $\Delta \epsilon = \epsilon_{\text{GaP}} - \epsilon_{\text{air}}$ and $\Delta \epsilon^{-1} = \epsilon_{\text{GaP}}^{-1} - \epsilon_{\text{air}}^{-1}$ the difference in permittivity, and impermeitvity of the dielectrics, respectively.

3.2.2 Photoelastic Effect

The second major contribution to the optomechanical coupling is associated with a change in the refractive index of the dielectric due to a deformation of the material and is described by the photoelastic effect [76]. For the simulations shown here, we use again the form derived by Chan [17] where the change of the permittivity tensor ϵ is given by

$$\frac{\partial \epsilon}{\partial \alpha} = -\epsilon \left(\frac{pS}{\epsilon_0} \right) \quad (3.15)$$

where p is the photoelastic tensor and S is the strain tensor. For a dielectrically isotropic medium, as we assume is the case for gallium phosphide, this can be written as [17]

$$\frac{\partial \epsilon_{ij}}{\partial \alpha} = -\epsilon_0 n_{\text{GaP}}^4 p_{ijkl} S_{kl} \quad (3.16)$$

with the refractive index of gallium phosphide, n_{GaP} . We then find

$$\left. \frac{\partial \omega}{\partial \alpha} \right|_{\text{pe}} = \frac{\omega_o \epsilon_0 n_{\text{GaP}}^4}{2} \frac{\int d\mathbf{x} E^*(\mathbf{x}) p_{ijkl} S_{kl} \mathbf{E}(\mathbf{x})}{\int d\mathbf{x} \mathbf{E}(\mathbf{x}) \mathbf{D}(\mathbf{x})} \quad (3.17)$$

3.2.3 Vacuum Optomechanical Coupling Rate

The vacuum optomechanical coupling rate g_0 can be calculated from the contributions of the moving-boundary effect and the photoelastic effect as

$$g_0 = \left(\left. \frac{\partial \omega}{\partial \alpha} \right|_{\text{mb}} + \left. \frac{\partial \omega}{\partial \alpha} \right|_{\text{pe}} \right) x_{\text{ZPF}} \quad (3.18)$$

with $x_{\text{ZPF}} = \sqrt{\hbar/2m_{\text{eff}}\Omega_m}$.

3.3 Optomechanical equations of motion

The dynamics of the optomechanical system can be described by simply plugging the system Hamiltonian Equation 3.9 in Equation 1.4. With $\dot{\alpha} = 0$ we then obtain the equations of motion

$$\begin{aligned} \delta \dot{\hat{a}} &= -\left(\frac{\kappa}{2} - i\Delta\delta\hat{a}\right) - ig\left(\hat{b} + \hat{b}^\dagger\right) - \sqrt{\kappa_{\text{ex}}}\delta\hat{a}_{\text{in}} - \sqrt{\kappa_0}\hat{\delta}_{\text{in}} \\ \dot{\hat{b}} &= -\left(\frac{\Gamma_m}{2} + i\Omega_m\hat{b}\right) - ig\left(\delta\hat{a} + \delta\hat{a}^\dagger\right) - \sqrt{\Gamma_m}\hat{\delta}_{\text{in},m} \end{aligned} \quad (3.19)$$

where the coupling of the mechanical oscillator to the transmission line is lumped together with the overall mechanical dissipation. Since $\Gamma_{\text{ex}} \ll \Gamma_m$ we can write $\Gamma_m + \Gamma_{\text{ex}} \approx \Gamma_m$. It is also useful to derive the equations of motion with the rotating wave approximation with the reduced interaction Hamiltonian, we then obtain for $\Delta \approx -\Omega_m$:

$$\begin{aligned} \delta \dot{\hat{a}} &= -\left(\frac{\kappa}{2} - i\Delta\delta\hat{a}\right) - ig\hat{b} - \sqrt{\kappa_{\text{ex}}}\delta\hat{a}_{\text{in}} - \sqrt{\kappa_0}\hat{\delta}_{\text{in}} \\ \dot{\hat{b}} &= -\left(\frac{\Gamma_m}{2} + i\omega_m\hat{b}\right) - ig\delta\hat{a} - \sqrt{\Gamma_m}\hat{\delta}_{\text{in},m} \end{aligned} \quad (3.20)$$

and for $\Delta \approx \Omega_m$

$$\begin{aligned} \delta \dot{\hat{a}} &= -\left(\frac{\kappa}{2} - i\Delta\delta\hat{a}\right) - ig\hat{b}^\dagger - \sqrt{\kappa_{\text{ex}}}\delta\hat{a}_{\text{in}} - \sqrt{\kappa_0}\hat{\delta}_{\text{in}} \\ \dot{\hat{b}} &= -\left(\frac{\Gamma_m}{2} + i\Omega_m\hat{b}\right) - ig\delta\hat{a}^\dagger - \sqrt{\Gamma_m}\hat{\delta}_{\text{in},m} \end{aligned} \quad (3.21)$$

3.4 Direct Optical Detection

Characterization of an optomechanical device requires the detection of the optomechanically induced phase modulation. The challenge is that a photodiode typically produces a photocurrent that is proportional to the number of incident photons $n_{\text{phot}} = \frac{P_{\text{opt}}}{\hbar\omega_L}$ (with optical power P_{opt} and laser frequency ω_L):

$$I_{\text{PD}} = \eta e n_{\text{phot}} = \eta e |\alpha|^2, \quad (3.22)$$

where η is the external quantum efficiency of the detector and e the elementary charge. In other words, a photodiode measures the absolute square of an optical signal with amplitude α . Since a phase modulated signal generally has the form (provided a simple modulation scheme, i.e. no sideband suppression)

$$\alpha(t) = \alpha_0 e^{-i\phi_0 \cos(\Omega t)} \quad (3.23)$$

with $\alpha_0 \propto e^{-i\omega_L t}$, where ω_L is the laser frequency that is modulated with some modulation depth ϕ_0 and frequency Ω , the photodiode produces a constant current $I_{\text{PD}} \propto |\alpha_0|^2$, and no information is gained over the phase modulation.

A useful method to make a phase modulation visible on a photodiode is beat note detection (direct detection), which is later in this thesis also used for nearly all optical measurements. The goal of this method is to either partly suppress or otherwise vary one optical sideband from the other, such that they do not cancel out when the signal is squared on the photodiode. The method that we employ is that we probe the optical cavity with a finite optical detuning, which results in a different amplitude and phase response for the upper and the lower sideband.

In order to derive an expression for the then frequency-dependent photocurrent it is first useful to look at the phase modulation in the sideband picture. For small ϕ_0 we can express the factor $e^{-i\phi_0 \cos(\Omega t)}$ in terms of the first-order Taylor expansion around $\phi_0 = 0$:

$$\begin{aligned} e^{-i\phi_0 \cos(\Omega t)} &\approx 1 - i\phi_0 \cos(\Omega t) = 1 - \frac{i}{2}\phi_0 (e^{-i\Omega t} + e^{i\Omega t}) \\ \Rightarrow \alpha(t) &\approx \alpha_0 \left(1 - \frac{i}{2}\phi_0 (e^{-i\Omega t} + e^{i\Omega t}) \right). \end{aligned} \quad (3.24)$$

The signal consists of the carrier $\alpha_0 (\propto e^{-i\omega_L t})$, as well as an upper and lower sideband rotating at Ω and $-\Omega$ with respect to the carrier. We can assign the carrier and each sideband an amplitude $A_{0,\pm}$ and write

$$\alpha(t) \approx \alpha_0 (A_0 - A_- e^{-i\Omega t} - A_+ e^{i\Omega t}). \quad (3.25)$$

Consequently, we find the photocurrent

$$\begin{aligned}
 I_{\text{PD}} &\propto |\alpha(t)| \approx |\alpha_0|^2 \left| A_0 - A_- e^{-i\Omega t} - A_+ e^{i\Omega t} \right|^2 \\
 &= |\alpha_0|^2 \left(|A_0|^2 + |A_-|^2 + |A_+|^2 \right. \\
 &\quad - (A_0 A_-^* + A_0^* A_+) e^{i\Omega t} \\
 &\quad - (A_0 A_+^* + A_0^* A_-) e^{-i\Omega t} \\
 &\quad \left. + A_-^* A_+ e^{2i\Omega t} + A_- A_+^* e^{-2i\Omega t} \right)
 \end{aligned} \tag{3.26}$$

Given that $\phi_0 \ll 1$ we find $A_{\pm}^* A_{\mp} \ll (A_0 A_{\pm}^*)^{(*)}$ and $|A_{\pm}|^2 \ll |A_0|^2$ such that we can neglect the fast rotating terms and the sideband DC components and find

$$I_{\text{PD}} \approx \eta e |\alpha_0|^2 \left(|A_0|^2 - (A_0 A_+^* + A_0^* A_-) e^{-i\Omega t} - (A_0 A_-^* + A_0^* A_+) e^{i\Omega t} \right). \tag{3.27}$$

In our setup, we do not detect the photocurrent directly, but instead it is converted into a voltage via a trans-impedance amplifier that creates an output voltage $V_{\text{PD}} = -R_f I_{\text{PD}}$, where R_f is a feedback resistor. We then either analyze the symmetrized power spectral density

$$S_V(\Omega) = \lim_{T \rightarrow \infty} \frac{1}{T} |V_{\text{PD}}(\Omega)|^2 \tag{3.28}$$

where $\frac{1}{T}$ is the measurement bandwidth, or, in the case when the system is driven with a coherent microwave tone $V_{\text{in}}(\Omega) = |V_{\text{in}}| e^{-i\Omega t}$, we analyze the signal using a vector network analyzer (VNA). In the latter case the signal is mixed in the VNA with a local oscillator and low-pass filtered to obtain the complex scattering parameter

$$S_{23}(\Omega) = \frac{V_{\text{out}}(\Omega)}{V_{\text{in}}(\Omega)} = \frac{V_{\text{PD}}(\Omega)}{|V_{\text{in}}|} e^{i\Omega t} = \eta e |\alpha_0|^2 R_f \frac{1}{|V_{\text{in}}|} (A_0 A_+^* + A_0^* A_-) \tag{3.29}$$

where the phase modulator is connected to port 3 of the VNA. Note that in the last step only the DC components were kept, as the VNA low-pass filters the signal with a narrow bandwidth. Given that the optical setup contains several lossy components such as the fiber-chip interface, taps to monitor the optical power, etc., as well as an optical amplifier, we can define a global detection gain factor Γ_D that lumps all of these loss mechanisms together with the prefactor $\eta e |\alpha_0|^2 R_f$. This makes calibrated measurements easier in that this global gain factor can be determined easily using a calibration tone with a known modulation depth. I would like to note here that I also included $|\alpha_0|^2$ in the global gain factor, i.e. the optical power, which is justified as the carrier does not contribute to the signal except for a scaling factor, such that a measurement can be calibrated absolutely, as long as the calibration measurement was carried out at the same optical power. Of course, in the case when we perform dynamical backaction measurements, the optical power is considered for the scaling of $g = \sqrt{n_{\text{cav}}} g_0$.

$$S_{23}(\Omega) = \frac{\Gamma_D}{V_0} (A_0 A_+^*(\Omega) + A_0^* A_-(\Omega)) \tag{3.30}$$

3.5 Dynamical Backaction

A central element of cavity optomechanics is the coherent interaction of the optical and mechanical modes. One canonical experiment where this interaction can be observed is optomechanically induced transparency (OMIT) and optomechanically induced absorption (OMIA) [6]. Both effects have been observed for numerous optomechanical systems, notably in microtoroids [99] and photonic crystal cavities [80]. We follow Safavi-Naeini et al. [80] for the derivation of the output signal. We can describe the dynamics of the optomechanical system in this case completely classically where we assume a coherent state $|\alpha\rangle$ for the optical mode and we use the ansatz that the optomechanical interaction also drives the mechanical resonator in a coherent state $|\beta\rangle$. We can then describe the system dynamics in terms of the expectation values $\langle\hat{a}\rangle = \alpha$ and $\langle\hat{b}\rangle = \beta$. The optical input signal in this case consists of a strong pump that is detuned from the cavity resonance by $\Delta = \omega_o - \omega_L$, and a weak probe that is modulated on top the strong pump with a phase modulator. In the rotating frame of the laser frequency ω_L we can then write the input field as

$$\alpha_{\text{in}} = \alpha_{0,\text{in}} \left(1 - \frac{i}{2} \phi_0 \left(e^{i\Omega t} + e^{-i\Omega t} \right) \right), \quad (3.31)$$

where ϕ_0 is the modulation depth and Ω the probe frequency with respect to ω_L . For this input state we then find the intracavity field α as

$$\alpha = \alpha_0 + \alpha_- e^{i\Omega t} + \alpha_+ e^{-i\Omega t} \quad (3.32)$$

The solution of the time-independent pump field is easily found to be

$$\bar{\alpha} = \alpha_0 = \frac{\sqrt{\kappa_{\text{ex}}}}{\frac{\kappa}{2} - i\Delta} \alpha_{\text{in},0}. \quad (3.33)$$

The fluctuating field $\langle\delta\hat{a}\rangle$ is given as $\delta\alpha = \alpha_+ + \alpha_-$. At this point, it is important to make the assumption that the cavity is sideband-resolved with $\kappa < \Omega_m$, that is, that we may use the rotating-wave approximation.

In the blue-detuned case ($\Delta \approx \Omega_m$) we then find, with $\dot{\alpha}_- = i\Omega\alpha_-$, because $\alpha_- \propto e^{-i(\omega_L - \Omega)t}$, the solution to Equation 3.21 first for β_-

$$\beta_- = -\frac{ig\alpha_-^*}{\frac{\Gamma_m}{2} - i(\Omega - \Omega_m)} = -ig\alpha_-^* \chi_m(\Omega) \quad (3.34)$$

where we used the ansatz $\beta \propto e^{-i\Omega t}$, as the driving field $\alpha_-^* \propto e^{-i\Omega t}$. With this solution, we can solve for α_- to obtain

$$\alpha_- = -\frac{\sqrt{\kappa_{\text{ex}}}}{\frac{\kappa}{2} - i(\Delta - \Omega) - g^2 \chi_m^*(\Omega)} \alpha_{\text{in},-} \equiv -\sqrt{\kappa_{\text{ex}}} \alpha_{\text{in},-} \chi_{\text{om}}^-(\Omega). \quad (3.35)$$

We obtain the intracavity field as

$$\alpha = -\sqrt{\kappa_{\text{ex}}}\alpha_{\text{in},0} \left(\chi_{\text{opt}}(0) - \frac{i}{2}\phi_0\chi_{\text{om}}^-(\Omega)e^{i\Omega t} - \frac{i}{2}\phi_0\chi_{\text{om}}^-(-\Omega)e^{-i\Omega t} \right) \quad (3.36)$$

where $\chi_{\text{opt}}(0)$ is the cavity response at the laser frequency ω_L . We can then calculate the output field as

$$\alpha_{\text{out}} = \alpha_{\text{in},0} \left(1 - \kappa_{\text{ex}}\chi_{\text{opt}}(0) - \frac{i}{2}\phi_0(1 - \kappa_{\text{ex}}\chi_{\text{om}}^-(\Omega))e^{i\Omega t} - \frac{i}{2}\phi_0(1 - \kappa_{\text{ex}}\chi_{\text{om}}^-(-\Omega))e^{-i\Omega t} \right). \quad (3.37)$$

Equivalently, we find for $\Delta \approx -\Omega_m$

$$\beta_+ = -\frac{ig}{\frac{\Gamma_m}{2} - i(\Omega_m - \Omega)}\alpha_+ = -ig\alpha_+\chi_m(\Omega) \quad (3.38)$$

and

$$\alpha_+ = -\frac{\sqrt{\kappa_{\text{ex}}}}{\frac{\kappa}{2} - i(\Delta + \Omega) + g^2\chi_m(\Omega)}\alpha_{\text{in},+} \equiv -\sqrt{\kappa_{\text{ex}}}\alpha_{\text{in},+}\chi_{\text{om}}^+(\Omega). \quad (3.39)$$

Analogous to the blue-detuned case, we find the output field as

$$\alpha_{\text{out}} = \alpha_{\text{in},0} \left(1 - \kappa_{\text{ex}}\chi_{\text{opt}}(0) - \frac{i}{2}\phi_0(1 - \kappa_{\text{ex}}\chi_{\text{om}}^+(-\Omega))e^{i\Omega t} - \frac{i}{2}\phi_0(1 - \kappa_{\text{ex}}\chi_{\text{om}}^+(\Omega))e^{-i\Omega t} \right). \quad (3.40)$$

From Equation 3.37 and Equation 3.40 we can identify the clockwise rotating term $A_-(\Omega)$ and the counter-rotating term $A_+(\Omega)$ as well as the DC response A_0 . The transmission scattering parameter $S_{23}(\Omega)$ of the vector network analyzer (the phase modulator is connected to port 3 of the VNA) is then given as

$$S_{23}(\Omega) = \Gamma_D(A_0A_+^*(\Omega) + A_0^*A_-(\Omega)) \quad (3.41)$$

with

$$\begin{aligned} A_0 &= 1 - \kappa_{\text{ex}}\chi_o(0) \\ A_+(\Omega) &= -\frac{i}{2}\frac{\pi}{V_\pi}(1 - \kappa_{\text{ex}}\chi_{\text{om}}^-(\Omega)) \\ A_-(\Omega) &= -\frac{i}{2}\frac{\pi}{V_\pi}(1 - \kappa_{\text{ex}}\chi_{\text{om}}^-(-\Omega)) \end{aligned} \quad (3.42)$$

for blue detuning and

$$\begin{aligned} A_0 &= 1 - \kappa_{\text{ex}}\chi_o(0) \\ A_+(\Omega) &= -\frac{i}{2}\frac{\pi}{V_\pi}(1 - \kappa_{\text{ex}}\chi_{\text{om}}^+(-\Omega)) \\ A_-(\Omega) &= -\frac{i}{2}\frac{\pi}{V_\pi}(1 - \kappa_{\text{ex}}\chi_{\text{om}}^+(\Omega)) \end{aligned} \quad (3.43)$$

for the red-detuned case.

In either case, the optomechanical interaction between the probe field and the mechanical resonator has a strong influence on the cavity dispersion, as illustrated in Figure 3.1. In the

blue-detuned case, the mechanical oscillator is parametrically driven in phase with the probe tone and interferes constructively with it, such that at a pump-probe detuning $\Omega = \Omega_m$ the reflection from the cavity is strongly enhanced. The cavity response to the lower sideband χ_{om}^- is shown in Figure 3.1 (a,b). At high power, the parametric drive can overcome the intrinsic damping of the resonator such that small fluctuations in the mechanical oscillator are amplified strongly. This is called the parametric instability regime and occurs at a cooperativity $\mathcal{C} = \frac{4g_0^2}{\Gamma_m \kappa} > 1$ [6]. If this threshold can be determined, then the vacuum optomechanical coupling rate can be inferred via

$$\mathcal{C} = 1 = n_{\text{cav}} \frac{4g_0^2}{\Gamma_m \kappa} \Leftrightarrow g_0 = \sqrt{\frac{\Gamma_m \kappa}{4n_{\text{cav}}}} \quad (3.44)$$

For a red-detuned pump the oscillator is driven with the conjugate of the sideband amplitude, which leads to a destructive interference of the mechanically induced phase-modulation with the intracavity field. This results, at $\Omega = -\Omega_m$, in a reduced reflection, as illustrated by the cavity response for the upper sideband χ_{om}^+ shown in Figure 3.1(c-d). At $\mathcal{C} = 1$, the reflection is reduced by 1/2. In our experimental setting, χ_{om}^\pm is not directly observed. Instead, we

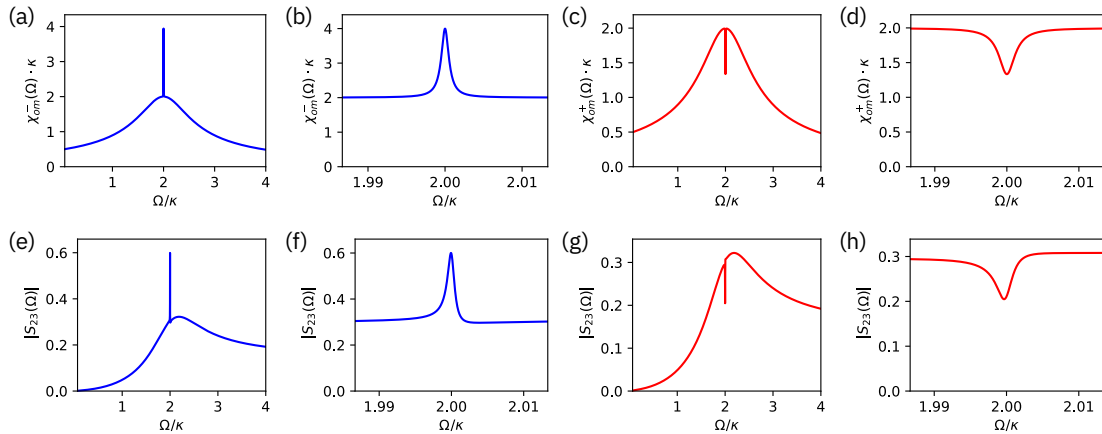


Figure 3.1: Cavity sideband response $\chi_{om}(\Omega)$ (a-d) for blue detuning $\Delta = \Omega_m$ (blue) showing amplification, and red detuning $\Delta = -\Omega_m$ (red) showing OMIT feature. Sideband resolution here is $\Omega_m/\kappa = 2$ and cooperativity $\mathcal{C} = 0.5$. Calculated transmission $|S_{23}(\Omega)|$ amplitudes for corresponding cases are shown in (e-h).

collect the light reflected off the cavity together of the input field, measure $|\alpha_{\text{out}}|^2$ on the photodetector where we obtain an RF-voltage via direct detection of the optical beat-note. This voltage is then measured by a VNA. The signal produced by this detection scheme can be calculated in terms of the scattering parameter S_{23} (cf. Equation 3.41, Equation 3.42, and Equation 3.43) which is shown below χ_{om}^\pm for the different scenarios in Figure 3.1 (e-h). The main difference is that the measured signal is slightly asymmetric. This is due to the interference of the cavity output field with the input field.

3.6 Estimation of the Vacuum Optomechanical Coupling Rate via Noise calibration and the Fluctuation Dissipation Theorem

Estimation of the vacuum optomechanical coupling rate is a key experiment for the characterization of an optomechanical device. There are several ways to perform a calibration, it can for example be inferred from dynamical backaction as derived in the previous section. However, in the case of dynamical backaction the inferred quantity is $g = \sqrt{n_{\text{cav}}} g_0$. Therefore, the intracavity photon number must be determined to obtain g_0 , which, in an integrated photonics setting, is a source of significant uncertainty. An alternative approach is the direct measurement of g_0 in the absence of dynamical backaction via the fluctuation dissipation theorem. I will sketch the derivation of the optomechanical coupling rate as presented by Gorodetsky et al. [39] here for completeness.

3.6.1 Fluctuation Dissipation Theorem

In thermal equilibrium, the fluctuation dissipation theorem links the (symmetrized) noise spectral density $S_x(\Omega)$ of the coordinate of the mechanical oscillator x to the imaginary part of its linear response $\chi_{m,x}$, which is in this case defined in terms of the coordinate x as

$$\chi_{m,x}(\Omega) = \frac{1}{m_{\text{eff}}((\Omega_m^2 - \Omega^2) - i\Omega\Gamma_m)} \quad (3.45)$$

with the effective mass of the oscillator m_{eff} [6]. The fluctuation-dissipation theorem then states [6], in the classical limit of $k_B T \gg \hbar\omega$,

$$S_x(\Omega) = 2 \frac{k_B T}{\Omega} \Im\{\chi_{m,x}(\Omega)\}. \quad (3.46)$$

With

$$\Im\{\chi_{m,x}(\Omega)\} = \frac{\Omega\Gamma_m}{m_{\text{eff}}((\Omega_m^2 - \Omega^2)^2 + \Omega^2\Gamma_m^2)} \quad (3.47)$$

we obtain

$$S_x(\Omega) = 2 \frac{k_B T}{m_{\text{eff}}} \frac{\Gamma_m}{(\Omega_m^2 - \Omega^2)^2 + \Omega^2\Gamma_m^2} \quad (3.48)$$

On the other hand, the Wiener-Khinchin theorem links the integral over the noise spectral density to the variance of the coordinate x [6] with

$$\langle x^2 \rangle = \frac{1}{2\pi} \int_{-\infty}^{\infty} S_x(\Omega) d\Omega. \quad (3.49)$$

For weak damping, the integration of $S_x(\Omega)$ yields the variance $\langle x^2 \rangle = \frac{k_B T}{m_{\text{eff}}\Omega_m^2}$.

3.6. Estimation of the Vacuum Optomechanical Coupling Rate via Noise calibration and the Fluctuation Dissipation Theorem

3.6.2 Relation to the Vacuum Optomechanical Coupling Rate

The fluctuations in the oscillator coordinate x causes frequency fluctuations of the optical cavity $\omega_o(x) = \omega_o + Gx = \omega_o + \frac{g_0}{x_{\text{ZPF}}}x$ with $x_{\text{ZPF}} = \sqrt{\hbar/2m_{\text{eff}}\Omega_m}$,

$$S_\omega(\Omega) = G^2 S_x(\Omega) \approx g_0^2 \frac{4\Omega_m}{\hbar} \frac{k_B T \Gamma_m}{(\Omega_m^2 - \Omega^2)^2 + \Omega^2 \Gamma_m^2} \quad (3.50)$$

as derived by Gorodetsky et al. [39]. Conveniently, this eliminates the effective mass m_{eff} . With Equation 3.49 the variance of the frequency fluctuations can then be calculated as

$$\langle \delta\omega_o^2 \rangle = 2\langle n_m \rangle g_0^2. \quad (3.51)$$

with $\langle n_m \rangle \approx \frac{k_B T}{\hbar\Omega_m}$. Similarly, we can use the property of the Lorentzian line-shape

$$\int_{-\infty}^{\infty} S_\omega(\Omega) d\Omega = S_\omega(\Omega_m) \frac{\Gamma_m}{2} \quad (3.52)$$

to set [39]

$$S_\omega(\Omega_m) \frac{\Gamma_m}{2} = 2\langle n_m \rangle g_0^2. \quad (3.53)$$

The frequency noise spectral density directly translates into a phase noise spectral density

$$S_\psi(\Omega) = \frac{S_\omega(\Omega)}{\Omega^2} \quad (3.54)$$

which is converted on the photoreceiver into a voltage noise spectral density [39]

$$S_V(\Omega) = K_D(\Omega) S_\psi(\Omega), \quad (3.55)$$

according to some transduction factor $K_D(\Omega)$ that is specific to the experiment. In this case, the transduction occurs via the partial suppression of one detected sideband and subsequent beat note detection. For the case discussed here, the specific value of K_D is not important, as will be shown in the next section.

3.6.3 Phase Noise Calibration

In general, the transduction function K_D is not trivial to derive, as it contains all, possibly frequency dependent, loss and gain elements in the detection chain, as well as the cavity response. This means that the measured current noise spectral density S_I is a priori uncalibrated. However, the detection chain can be completely calibrated using a phase reference with a known spectral density, such as the one produced by a phase-modulator with a known modulation depth ϕ_0 with a phase noise spectral density [39]

$$S_\phi = 2\pi \frac{1}{2} (\delta(\Omega - \Omega_{\text{mod}}) + \delta(\Omega + \Omega_{\text{mod}})) \frac{\phi_0^2}{2} \quad (3.56)$$

which translates into a total measured voltage noise spectral density [39]

$$S_V^{\text{meas}}(\Omega) = 2F(\Omega) \left(K_D(\Omega) (S_\psi(\Omega) + S_\phi(\Omega)) \right), \quad (3.57)$$

where the measured signal is convolved with the spectrum analyzer's bandwidth filter function of shape $F(\Omega)$, which is normalized such that

$$F(0)\text{ENBW} = \frac{1}{2\pi} \int_{-\infty}^{\infty} F(\Omega) d\Omega = 1, \quad (3.58)$$

where the effective noise bandwidth ENBW is defined as that of a rectangular filter function that yields the same integral as the real filter function. If the spectrum is dominated at the modulation frequency Ω_{mod} by the phase reference signal, the measured current spectral density can be approximated [39] as

$$S_V(\Omega_{\text{mod}}) = \frac{\phi_0^2}{2} K_D(\Omega_{\text{mod}}) F(0) = \frac{\phi_0^2}{2} \frac{K_D(\Omega_{\text{mod}})}{\text{ENBW}}, \quad (3.59)$$

which provides an absolute calibration of K_D at the modulation frequency Ω_{mod} .

3.6.4 Inference of the Vacuum Optomechanical Coupling Rate

Crucially, the experimental conditions in this case permit to set $K_D(\Omega_m) \approx K_D(\Omega_{\text{mod}})$, if $\Omega_{\text{mod}} - \Omega_m \ll \kappa$, where κ is the cavity decay rate. This is sufficiently true if the phase reference tone is set several mechanical linewidths $\Gamma_m/2\pi$ away from the mechanical resonance, such that the spectrum at Ω_{mod} is dominated by the phase reference. In the cases discussed here, $\Gamma_m/2\pi \approx \mathcal{O}(1 \text{ MHz})$ such that for $\Omega_{\text{mod}}/2\pi - \Omega_m/2\pi \approx \mathcal{O}(10 \text{ MHz}) \ll \kappa/2\pi \approx \mathcal{O}(1 \text{ GHz})$ is given. The vacuum optomechanical coupling rate can then be inferred as [39]

$$g_0 \approx \frac{\phi_0}{2} \Omega_m \sqrt{\frac{1}{\langle n_{\text{th}} \rangle} \frac{S_V(\Omega_m) \Gamma_m/4}{S_V(\Omega_{\text{mod}}) \text{ENBW}}}. \quad (3.60)$$

3.7 Microwave-to-optical transduction in the Low-Cooperativity Limit

Microwave-to-optical transduction is a useful reference measurement to test a given electro-optomechanical design. In this configuration, a prototype device is driven on its microwave port via a transmission line at room temperature as shown in Figure 3.2. The amplitude of the driven mechanical oscillator can then be measured via the optomechanically-induced phase modulation. This calibrated measurement of the oscillator amplitude then allows us to infer the coupling Γ_{ex} between the known drive amplitude and the resonator. On the other hand, we may infer an external coupling rate from FEM simulations presented in chapter 5 via the semi-infinite transmission line coupling derived in Equation 1.24. Γ_{ex} can then serve as a benchmark between the simulated and the experimentally realized electromechanical coupling. For this measurement the device is driven at very low optical power to avoid any

3.7. Microwave-to-optical transduction in the Low-Cooperativity Limit

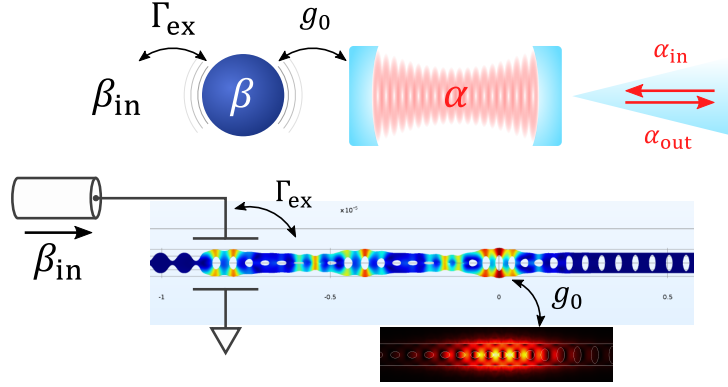


Figure 3.2: Classical microwave-to-optical transduction with transmission-line coupled device.

backaction of the optical mode on the mechanical resonator. This is important since the coherent amplitude of the resonator should be dominated by the electromechanical drive. The response of the mechanical subsystem to an incoming microwave field is well-described in the framework of input-output theory by the canonical Langevin equation of motion of the harmonic oscillator. We may then describe the optical phase modulation introduced by the mechanical amplitude and the optical output field, again, in the framework of input-output theory. Finally, we can derive an expression for the microwave field generated by the photoreceiver due to the beat note of the optical output field, and subsequently derive an expression for the scattering parameter S_{21} between the microwave port of the optomechanical device and the output of the photoreceiver.

A calibrated measurement of S_{21} then allows us to extract the electromechanical coupling rate Γ_{ex} . We can define the coherent microwave input field through the transmission line as

$$\begin{aligned}\beta_{\text{in}} &= |\beta_{\text{in}}| e^{-i\Omega t} \\ &= \frac{|V_0|}{\sqrt{2Z_0\hbar\Omega}} e^{-i\Omega t}.\end{aligned}\quad (3.61)$$

The microwave amplitude is here normalized in terms of the rate of photons arriving at the device through the transmission line. To that end, one may consider the power P_L delivered through a transmission line with impedance Z_0 to an impedance-matched termination. We may write [74]

$$P_L = \frac{1}{2Z_0} |V_0|^2 \quad (3.62)$$

where $|V_0|$ is the voltage amplitude of the incoming microwave. Analogous to the optical case, we may also express the photon flux of the microwave in terms of the delivered power

$$|\beta_{\text{in}}(\Omega)|^2 = \frac{P_L}{\hbar\Omega} = \frac{|V_0|^2}{2Z_0\hbar\Omega} \Rightarrow |\beta_{\text{in}}(\Omega)| = \frac{|V_0|}{\sqrt{2Z_0\hbar\Omega}} \quad (3.63)$$

Chapter 3. Cavity-Optomechanics

The amplitude of the mechanical resonator is then given by

$$\beta(\Omega) = -\frac{\sqrt{\Gamma_{\text{ex}}}\beta_{\text{in}}}{\frac{\Gamma_m}{2} + i(\Omega - \Omega_m)} e^{-i\phi_m} = -\chi_m(\Omega)\sqrt{\Gamma_{\text{ex}}}\beta_{\text{in}}. \quad (3.64)$$

In the absence of dynamical backaction the coherent oscillations of the mechanical oscillator with amplitude β merely lead to a phase-modulation of the optical cavity field. For an optical input field at the laser frequency ω_L we then find the modulated cavity field as

$$\alpha \propto e^{-i(\omega_L t + g_0(\beta + \beta^*))}. \quad (3.65)$$

In the limit of small modulation depth we may approximate the exponential with a first-order Taylor expansion such that

$$e^{-ig_0(\beta + \beta^*)} \approx 1 - ig_0(\beta + \beta^*). \quad (3.66)$$

We find the intracavity field for an optical input field $\alpha_{\text{in}} = \alpha_{\text{in},0}e^{-i\omega_L t}$ as

$$\alpha = -\sqrt{\kappa_{\text{ex}}}\frac{|V_0|}{\sqrt{2Z_0\hbar\Omega}}\alpha_{\text{in}}\chi_o(0)\left(1 + ig_0\chi_m(\Omega)\sqrt{\Gamma_{\text{ex}}}\chi_o(\Omega)e^{-i\Omega t} + ig_0\chi_m^*(\Omega)\sqrt{\Gamma_{\text{ex}}}\chi_o(-\Omega)e^{i\Omega t}\right) \quad (3.67)$$

where we considered the cavity response at the laser frequency ω_L as $\chi_o(0)$ and the response of at the upper and lower sideband frequencies as $\chi_o(\Omega)$ and $\chi_o(-\Omega)$, respectively. The cavity output field can be obtained via the input-output relation

$$\alpha_{\text{out}} = \alpha_{\text{in}} + \sqrt{\kappa_{\text{ex}}}\alpha \quad (3.68)$$

as

$$\alpha_{\text{out}} = \alpha_{\text{in}}\left(1 - \kappa_{\text{ex}}\chi_o(0) - i\kappa_{\text{ex}}g_0\sqrt{\Gamma_{\text{ex}}}\frac{|V_0|}{\sqrt{2Z_0\hbar\Omega}}\chi_o(0)\left(\chi_m(\Omega)\chi_o(\Omega)e^{-i\Omega t} + \chi_m^*(\Omega)\chi_o(-\Omega)e^{i\Omega t}\right)\right). \quad (3.69)$$

For the sake of brevity we write

$$\alpha_{\text{out}} = \alpha_{\text{in}}\left(A_0 - A_-e^{-i\Omega t} - A_+e^{i\Omega t}\right) \quad (3.70)$$

with

$$\begin{aligned} A_0 &= 1 - \kappa_{\text{ex}}\chi_o(0) \\ A_+ &= i\kappa_{\text{ex}}g_0\sqrt{\Gamma_{\text{ex}}}\frac{|V_0|}{\sqrt{2Z_0\hbar\Omega}}\chi_o(0)\chi_o(-\Omega)\chi_m^*(\Omega) \\ A_- &= i\kappa_{\text{ex}}g_0\sqrt{\Gamma_{\text{ex}}}\frac{|V_0|}{\sqrt{2Z_0\hbar\Omega}}\chi_o(0)\chi_o(\Omega)\chi_m(\Omega) \end{aligned} \quad (3.71)$$

We deploy the direct optical detection scheme described above, and redefine $A_{-(+)} / V_0^{(*)} \mapsto A_{-(+)}$ such that we obtain

$$S_{21} = \frac{\Gamma_D}{\sqrt{2Z_0\hbar\Omega}}(A_0A_+^* + A_0^*A_-)e^{-i(\Omega\tau + \theta)} \quad (3.72)$$

3.7. Microwave-to-optical transduction in the Low-Cooperativity Limit

with

$$\begin{aligned} A_+ &= i\kappa_{\text{ex}}g_0\sqrt{\Gamma_{\text{ex}}}\chi_o(0)\chi_o(-\Omega)\chi_m^*(\Omega) \\ A_- &= i\kappa_{\text{ex}}g_0\sqrt{\Gamma_{\text{ex}}}\chi_o(0)\chi_o(\Omega)\chi_m(\Omega). \end{aligned} \quad (3.73)$$

The electronic and optical detection delay is accounted for with an additional phase offset $\phi = \Omega\tau + \theta$. We may also write explicitly

$$\begin{aligned} S_{21} &= \frac{\Gamma_D}{\sqrt{2Z_0\hbar\Omega}}g_0\sqrt{\Gamma_{\text{ex}}}\chi_m(\Omega)i\kappa_{\text{ex}}\left(\right. \\ &\quad \left. (1 - \kappa_{\text{ex}}\chi_o^*(0))\chi_o(0)\chi_o(\Omega) \right. \\ &\quad \left. - (1 - \kappa_{\text{ex}}\chi_o(0))\chi_o^*(0)\chi_o^*(-\Omega) \right) \\ &\quad e^{-i(\Omega\tau+\theta)}. \end{aligned} \quad (3.74)$$

We may separate the contributions in Equation 3.74 that correspond to the electro-optomechanical response of the device

$$\chi_{\text{eom}}(\Omega) = g_0\sqrt{\Gamma_{\text{ex}}}\chi_m(\Omega) \quad (3.75)$$

from that which transduces the optomechanical phase modulation into the detectable beat-note signal

$$\begin{aligned} \Theta(\Omega) &= i\kappa_{\text{ex}}\left((1 - \kappa_{\text{ex}}\chi_o^*(0))\chi_o(0)\chi_o(\Omega) \right. \\ &\quad \left. - (1 - \kappa_{\text{ex}}\chi_o(0))\chi_o^*(0)\chi_o^*(-\Omega) \right) \end{aligned} \quad (3.76)$$

to obtain the more readable form

$$S_{21}(\Omega) = \Gamma_D\chi_{\text{eom}}(\Omega)\Theta(\Omega)e^{-i(\Omega\tau+\theta)}. \quad (3.77)$$

In this form, we can easily expand the model to include multiple (uncoupled) mechanical modes by adding their contributions up in the optical output field. We may then write

$$\chi_{\text{eom}}(\Omega) = \sum_n g_{0,n}\sqrt{\Gamma_{\text{ex},n}}\chi_{m,n}(\Omega)e^{-i\phi_{m,n}}, \quad (3.78)$$

where an additional, mode-dependent phase offset $\phi_m \in \{0, \pi\}$ is included to account for a phase difference of the mechanical displacement field between the microwave and optical coupling points along the nanobeam. Note that $S_{21} \propto \chi_m(\Omega)$. With prior knowledge about the detection gain Γ_D , the optomechanical coupling rate g_0 , κ , κ_{ex} and the detuning Δ , the electromechanical coupling rate Γ_{ex} can then be directly determined.

Phase-Modulated Input Signal

The microwave-to-optical transduction spectrum is experimentally calibrated by measuring the optical cavity response to a phase-modulated signal with a pre-determined modulation

depth. In this case, we find the input field as

$$\alpha_{\text{in}} = \alpha_{\text{in},0} \left(1 - \frac{i}{2} \phi_0 e^{-i(\Omega(t+\tau)+\theta)} - \frac{i}{2} \phi_0 e^{i(\Omega(t+\tau)+\theta)} \right) \quad (3.79)$$

where τ is the electronic and optical delay, and θ is a phase offset. The intracavity field is then given via the optical susceptibility $\chi_o(\Omega)$ as

$$\alpha = -\alpha_{\text{in},0} \sqrt{\kappa_{\text{ex}}} \left(\chi_o(0) - \frac{i}{2} \phi_0 \chi_o(-\Omega) e^{-i(\Omega(t+\tau)+\theta)} - \frac{i}{2} \phi_0 \chi_o(\Omega) e^{i(\Omega(t+\tau)+\theta)} \right). \quad (3.80)$$

The output field can then be calculated via

$$\alpha_{\text{out}}(\Omega) = \alpha_{\text{in}}(\Omega) + \sqrt{\kappa_{\text{ex}}} \alpha(\Omega) \quad (3.81)$$

as

$$\alpha_{\text{out}} = \alpha_{\text{in}} \left(1 - \kappa_{\text{ex}} \chi_o(0) - \frac{i}{2} (1 - \kappa_{\text{ex}} \chi_o(-\Omega)) e^{-i(\Omega(t+\tau)+\theta)} - \frac{i}{2} \phi_0 (1 - \kappa_{\text{ex}} \chi_o(\Omega)) e^{i(\Omega(t+\tau)+\theta)} \right). \quad (3.82)$$

We can then identify the upper and lower sideband amplitudes A_+ and A_- and the DC component A_0 as

$$\begin{aligned} A_0 &= 1 - \kappa_{\text{ex}} \chi_o(0) \\ A_-(\Omega) &= \frac{i}{2} \phi_0 (1 - \kappa_{\text{ex}} \chi_o(-\Omega)) e^{-i(\Omega\tau+\theta)} \\ A_+(\Omega) &= \frac{i}{2} \phi_0 (1 - \kappa_{\text{ex}} \chi_o(\Omega)) e^{i(\Omega\tau+\theta)}. \end{aligned} \quad (3.83)$$

The modulation depth can be expressed in terms of the modulator's half-wave voltage V_π and the input voltage V_0

$$\phi_0 = \frac{V_0}{V_\pi} \pi \quad (3.84)$$

such that S_{23} becomes independent of the input voltage V_0 (the phase modulator is in this case connected to port 3 of the VNA).

Device Design Part II

4 Optomechanical Design

Photonic crystal cavities with engineered mechanical mode spectrum, and especially systems called optomechanical crystals that support both, a photonic, and phononic bandgap to maximize optomechanical coupling have been used with great success for many years for a wide range of applications in classical optomechanics [29, 80], for parametric cooling to the mechanical quantum ground-state [17, 18, 75], in implementations with piezoelectric materials for microwave-to-optical transduction [15, 8, 53], and for inspiring quantum-optomechanical experiments such as the preparation of non-trivial fock states [77] and even entangled bell-states [78]. More recently, such systems were used for transduction of non-classical states [34] and most recently even for the transduction of a state prepared by a superconducting qubit [67]. In addition, optomechanical crystals fabricated from silicon have been engineered to provide exceedingly high quality factors with $Q \sim 1.5 \times 10^{10}$ and a phonon lifetime of $\tau \sim 1.5$ s [63]. We deploy a similar design for a microwave-optical link with photonic crystal cavities designed and fabricated in GaP.

4.1 Photonic Crystal Supermode Resonator

The canonical design of an optomechanical crystal [18] comprises a symmetric cavity design, that is, phonons and photons are blocked equally on either side of the cavity. In order to efficiently couple to a microwave circuit, without introducing loss in either the optical or the microwave mode it is necessary to separate the optical mode from the microwave port. This can be achieved by introducing an asymmetry to the design [8, 67] that blocks phonons on one side by, what I will refer to as a phoxonic mirror – a structure that provides a bandgap for both photons and the phonon modes of interest – and is transparent for phonons on the other side, while still providing a photonic bandgap. Such a structure allows the breathing mode to be distributed across the side without phononic bandgap, and provides the possibility to place a microwave port at some point along the ‘phononic waveguide’ sufficiently far separated from the optical mode to minimize loss in the optical mode and the generation of quasi-particles by optical absorption in the superconductor. Examples of such a device are shown in Figure 5.4 and Figure 5.7. The design of such a supermode resonator is inherently more challenging than

that of a conventional optomechanical crystal, as it requires the phonon waveguide to, on the one hand, provide a photonic bandgap that is more or less matched to that of the phoxonic mirror, and on the other hand a phonon dispersion for the breathing modes that is matched to that of the cavity center.

4.2 Photonic and Phononic Crystal Design

The propagation of waves in systems with periodic boundary conditions leads to a nonlinear dispersion relation between the frequency of the wave ω and its wave vector k as first described by Floquet [33] and later adapted for the dispersion of electrons in a solid by Bloch [14]. In a similar fashion as for electrons in solid, this nonlinear dispersion can lead to the formation of a bandgap for both photons [54], and phonons [16, 59] for structures with periodic variations of the optical and acoustic impedance. According to Bloch's theorem, it is sufficient to describe the dispersion relation for the first Brillouin zone $-\frac{\pi}{p} \leq k \leq \frac{\pi}{p}$, with the period of the structure p . Due to time reversal symmetry, it is sufficient to consider $0 \leq k \leq \frac{\pi}{p}$. This band structure can be simulated for both photons and phonons in the finite-element analysis software *COMSOL Multisphysics*® by setting the boundary condition of the faces that form the interface of the 1D periodic structure as indicated in Figure 4.1.

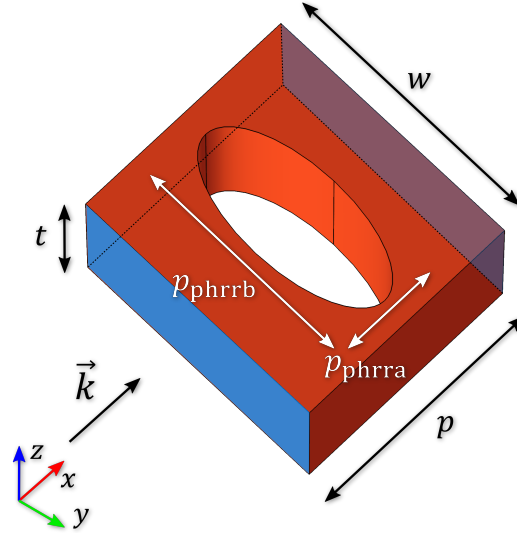


Figure 4.1: Illustration of phononic/photonic crystal unit cell. Periodic Floquet boundary conditions are indicated by blue faces.

4.2.1 Phoxonic Mirror

The first step in the design process is the definition of a suitable phoxonic end mirror. We adapt the canonical design of a rectangular unit cell with width w , height t and pitch p with an elliptical hole through the xy -plane with the semi-axis along the x -axis $a = p \cdot p_{\text{phrra}}$ and

the semi-axis along the y-axis $b = w \cdot p_{\text{phrrb}}$ (cf. Figure 4.1). The design is first optimized

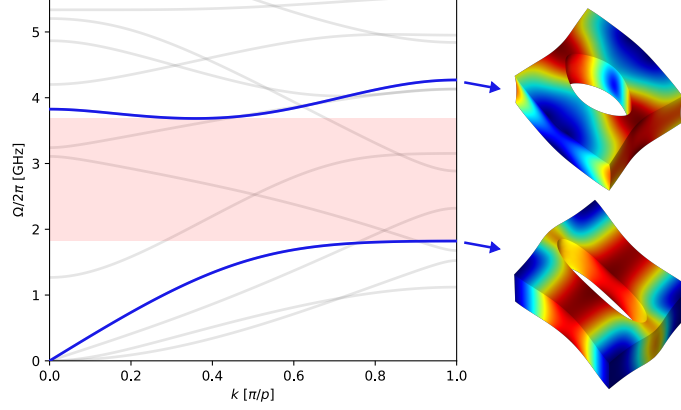


Figure 4.2: Dispersion of phonon modes in phoxonic end mirror. Breathing modes are shown in blue, respective displacement fields at $k = \pi/p$ are illustrated on the right. Color-coding corresponds to absolute displacement. The red shaded area corresponds to the bandgap for breathing modes.

for phonon dispersion at fixed w , t and p . The hole semi-axes are varied to maximize the frequency of the upper breathing mode band, as shown as upper blue line in Figure 4.2. A bandgap emerges for the breathing mode between the upper and lower mode (red shaded area in Figure 4.2). A full phononic bandgap cannot be obtained for this unit cell topology, as indicated by the gray lines in Figure 4.2 which correspond to other mechanical mode families. This, however, is not detrimental to the design as the mode of interest is a breathing mode.

4.2.2 Defect Cell

The phonon dispersion of the cavity cell is shown in Figure 4.3. It is optimized to obtain a high frequency of the breathing mode below the band edge defined by the phoxonic crystal. At the same time, the frequency of the optical dielectric band is adjusted to create a sub-bandgap state in the bandgap of the phoxonic and waveguide mirror.

4.2.3 Waveguide Mirror

The waveguide mirror is the most sensitive element of the design. It requires a photonic bandgap that is matched to that of the phoxonic crystal, while also providing a phonon dispersion of the breathing mode that is matched to that of the cavity cell. The dispersion for the breathing modes is shown in Figure 4.4. The dispersion of the defect cell and the waveguide mirror are found to be fairly well-matched if the semi-axes b of both cells are matched. The frequency of the breathing mode band and the optical bandgap are then adjusted by varying a and p .

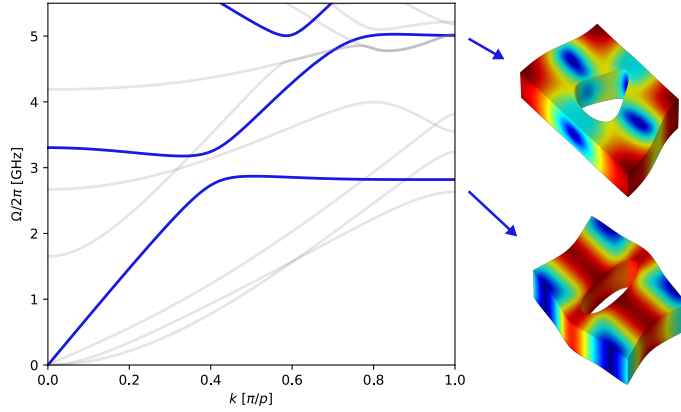


Figure 4.3: Phonon dispersion of cavity cell. Breathing modes are shown in blue, respective displacement fields at $k = \pi/p$ are illustrated on the right. Color-coding corresponds to absolute displacement.

4.2.4 Phononic End-Reflector

As the waveguide mirror has, by design, no phononic bandgap, it is crucial to terminate the waveguide with a phononic reflector to limit radiation loss. In principle, the phoxonic crystal cell could be used for this purpose. However, since the phoxonic cell is engineered for both the photonic and phononic bandgap, the design is not ideal just as a phononic reflector. First, it does not have a complete phononic bandgap, second, the design has a large surface-to-volume ratio, which might lead to excessive microwave loss at the disordered interface between gallium phosphide and air. Therefore, it is appropriate to implement a dedicated design for the end-reflector. The design is shown in Figure 4.5 on the right. The unit cell consists of a corrugation that is defined by a Bézier spline, of which the control polygon is shown in the figure in green, and supports a full phononic bandgap between 2.84 GHz and 3.51 GHz – indicated by the red-shaded area in the band-diagram shown in Figure 4.5 on the left – for a period $p = 650$ nm, $a = 0.4$ and $b = 0.15$, with a width matched to the width of the photonic crystal $w = 550$ nm.

4.2.5 Photonic Crystal

Besides the phonon dispersion, the cells must also have a matched photonic bandgap for the phoxonic mirror and the phononic waveguide mirror, while providing a sub-bandgap state for the defect cell. Simulations of the Brillouin zone are shown in Figure 4.6 for the phononic waveguide mirror (a), the defect cell (b) and the phoxonic mirror (c). The guided modes in the photonic crystal are located below the light line [54], indicated in blue in the figure. The solutions for the dielectric and air modes are shown in green as the lower and upper band, respectively. The bandgap of the waveguide and phoxonic cells are shown in (a) and (c) as red shaded areas, while the common bandgap of both cells is indicated as red shaded area in (b).

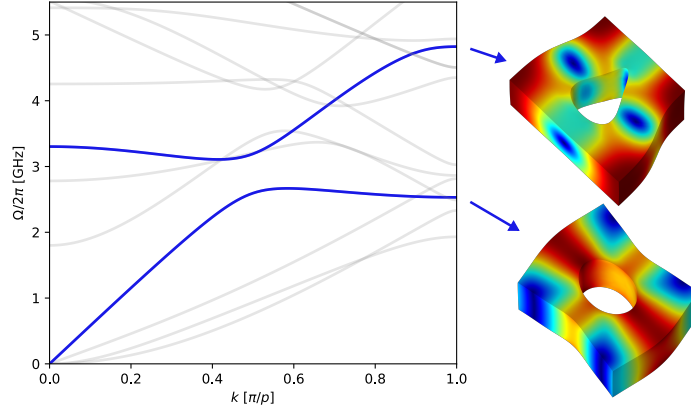


Figure 4.4: Phonon dispersion of waveguide mirror. Breathing modes are shown in blue, respective displacement fields at $k = \pi/p$ are illustrated on the right. Color-coding corresponds to absolute displacement.

Table 4.1: Cell dimensions for asymmetric photonic crystal design.

Cell type	p [nm]	w [nm]	p_{hrra}	p_{hrrb}
Phoxonic	480	550	0.4	0.8
Defect	370	550	0.65	0.35
Waveguide	470	550	0.56	0.35

This illustrates that the dielectric band of the cavity cell, (lower green line in (b)) introduces a sub-bandgap state in the photonic band structure of the photonic crystal when it is introduced as a defect.

4.2.6 Localized Optical Mode

We can introduce a defect into the nanobeam where the photonic crystal locally supports a sub-bandgap state. It is advantageous to morph the photonic crystal gradually around this defect, instead of an abrupt transition. The canonical choice for such a transition is a Gaussian defect [17], which provides the maximum adiabaticity for the optical field. For maximized optomechanical coupling it is advantageous to maximally localize the optical mode – i.e. to choose the mode volume as small as possible. This, however, contradicts the requirement of adiabaticity and leads to increased radiation (scattering) loss, for small mode volumes. Generally, there is a trade-off to be made between mode volume and radiation-limited quality factor – the smaller the mode volume, the smaller the intrinsic quality factor will ultimately be. However, in practice the quality factor of such nano-cavities is rarely radiation-limited. Instead, absorption and scattering loss at the material-air interface usually limits the achievable quality factor. In the case of gallium phosphide, we expect the intrinsic quality factor to be limited to $Q_i < 2 \times 10^5$. It is therefore justified to choose a design that limits the quality factor to $Q_{i,\text{rad}} \sim 10^6$. The width of the Gaussian defect is chosen accordingly as $\sigma_c = 1 \mu\text{m}$, which

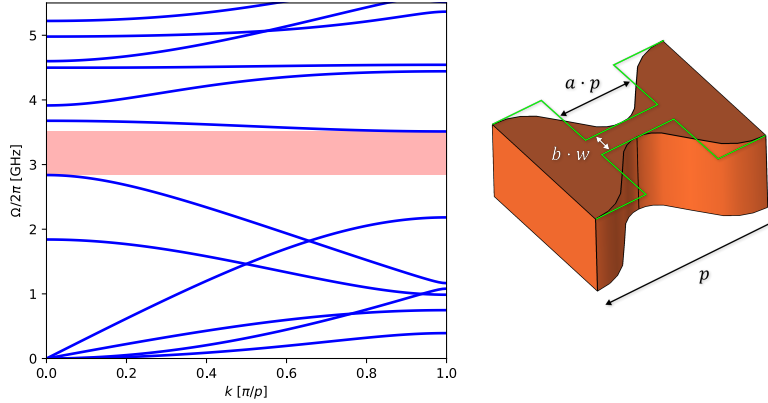


Figure 4.5: Phonon dispersion of phononic end-reflector (left) with bandgap indicated as red shaded area, and unit cell of phononic crystal (right) with Bézier control polygon indicated in green.

limits the intrinsic quality factor to $Q_{i,\text{rad}} = 1.8 \times 10^6$. The localized mode with a frequency of 193.17 THz ($\sim 1552\text{nm}$) is shown in Figure 4.7. The hole dimensions in the photonic crystal are shown in Figure 4.8 as a function of their position x along the nanobeam.

4.2.7 Mechanical Supermodes

The main advantage of this asymmetric design compared to a symmetric optomechanical crystal design is the emergence of distributed mechanical modes across the length of the beam on the side where the phonon dispersion of the waveguide is matched to that of the cavity center. The emerging modes can be viewed in analogy to a Fabry-Pérot cavity, in that they are confined on either side by the phononic bandgaps of the phoxonic mirror and the phononic end-reflector. In contrast to an optical Fabry-Pérot cavity however, the modes are not equally spaced because the phonon dispersion is not linear, or even monotonically positive. This is illustrated in Figure 4.9, where the phonon dispersions of the individual cells – the phoxonic mirror, the defect cell and the phononic waveguide mirror – are shown on the right, in blue, yellow, and red, respectively, where the red-shaded area indicates again the phononic bandgap imposed by the phoxonic mirror. A selection of the corresponding breathing-supermodes is shown in the figure on the left ascending in frequency from top to bottom. The negative dispersion is immediately clear when comparing the first and the fourth mode – the former has a lower frequency, but clearly a larger wave-vector than the latter. The fact that the dispersion is almost flat in the range $0 \leq k \leq \frac{\pi}{2p}$ also has the consequence that the higher harmonic breathing modes in this range are 'bunched' together in a fairly small frequency range, while modes with larger wave vectors are further separated. Another observation that is noteworthy here is that the defect cell is well dispersion-matched to the phononic waveguide mirror for a majority of wavevectors. Modes with $0.3 \lesssim kp/\pi \lesssim 0.45$ where the dispersion deviates show a stronger localization of the breathing mode around the optical cavity, due to a phase mismatch

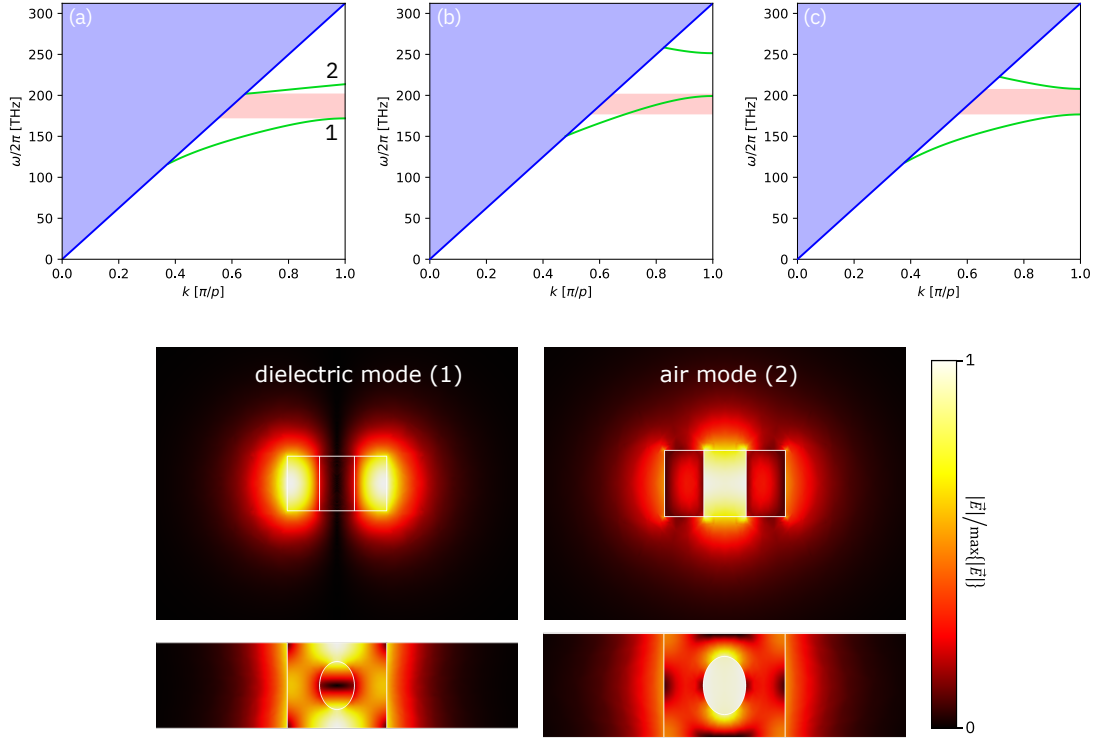


Figure 4.6: Simulation of photonic band-structure for phononic waveguide mirror (a), defect cell (b), and phoxonic mirror (c). Confined modes are shown to the right of light cone (blue shaded area). Bandgaps of waveguide and phoxonic mirror are indicated in (a) and (c) as red shaded area, and common bandgap is shown in (b) as red-shaded area. Mode profiles at the bottom (top images: side-view, bottom images: top view) show the absolute electric field of the dielectric and air modes of the waveguide mirror as indicated in (a).

with the phononic waveguide. While the mechanical energy is in these cases more localized around the optical mode, which leads to a larger optomechanical coupling, and a larger mode spacing is generally appreciated, it has a detrimental effect on the electromechanical coupling, as the mode overlap between the microwave field and the mechanical mode is reduced significantly. Therefore, since the optomechanical coupling is still appreciable for the dispersion-matched modes (cf. Table 4.3), and the microwave coupling is generally the weak link for this design, the dispersion-matched modes are the modes of interest. Finally, it is important to point out that the relative phase between the point of the displacement field where the electrode is placed as the microwave port (cf. Figure 5.4) and the point of the displacement field where the optomechanical coupling occurs – the right-hand end of the ‘Fabry-Pérot cavity’ – is not the same for all the modes shown in Figure 4.9. For example, for the first and third mode the displacement is negative at the microwave port and the optical cavity, while for the second and fourth mode the displacement is negative at the microwave port, but positive at the optical cavity. When the device is driven coherently via the microwave port, the displacement field inherits the relative phase of the incoming microwave tone. The

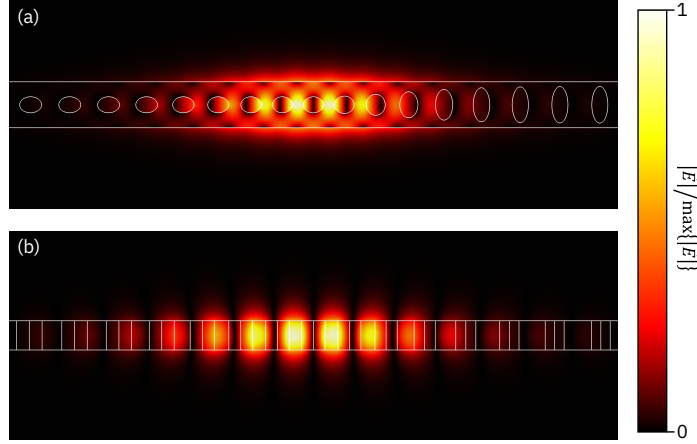


Figure 4.7: Localized optical mode. Top view (a) (xy plane) and side view (b) (yz plane). Color indicates magnitude of electric field.

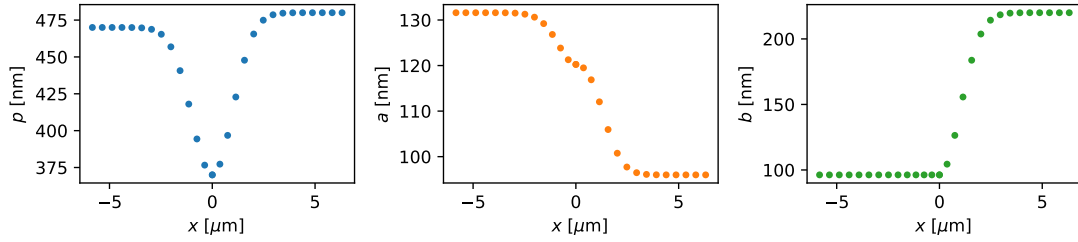


Figure 4.8: Dimensions of photonic crystal cavity along the axis of the nanobeam. Period p (left), semi-axis a of ellipse along x (center), semi-axis b of ellipse normal to x (right)

phase of the optomechanical phase modulation however is determined by the phase of the displacement field at the optical cavity. This leads to a shift of the relative phase of the optical output signal depending on which mode is actuated. This phase relationship in combination with other indicators such as the microwave coupling and the optomechanical coupling can be used to identify the modes observed in a fabricated device.

4.3 Optomechanical Coupling

The Optomechanical coupling is calculated in Comsol using Equation 3.18, where the integrals can be calculated directly in the simulation software. The photoelastic tensor can be written

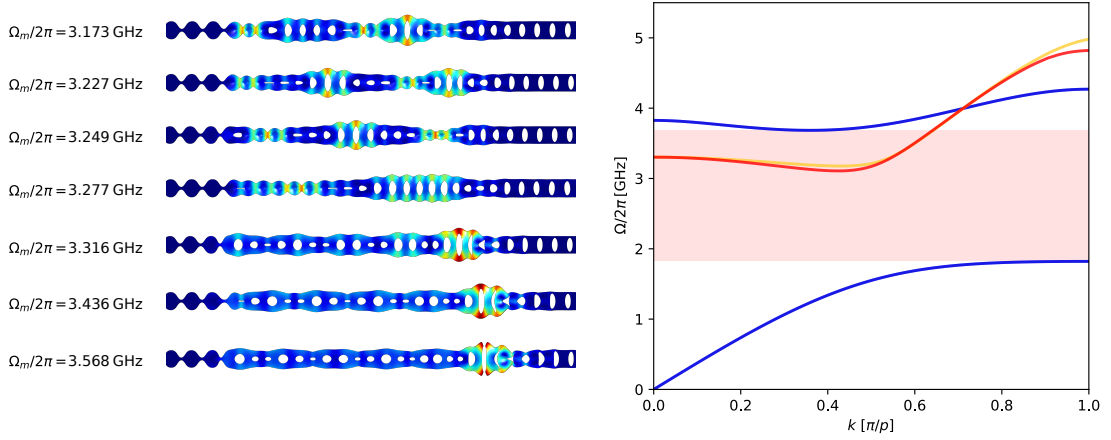


Figure 4.9: Breathing supermodes supported by asymmetric photonic crystal design. Displacement fields to several breathing modes are shown on the left with their corresponding eigenfrequencies, breathing mode dispersion of the phoxonic crystal (blue) with its bandgap indicated by red-shaded area is shown on the right together with breathing mode dispersion of the defect cell (yellow) and the waveguide cell (red), each scaled along the x-axis to fit the Brillouin zone of the phoxonic mirror cell.

in Voigt notation as

$$p = \begin{bmatrix} p_{11} & p_{12} & p_{12} & 0 & 0 & 0 \\ p_{12} & p_{11} & p_{12} & 0 & 0 & 0 \\ p_{12} & p_{12} & p_{11} & 0 & 0 & 0 \\ 0 & 0 & 0 & p_{44} & 0 & 0 \\ 0 & 0 & 0 & 0 & p_{44} & 0 \\ 0 & 0 & 0 & 0 & 0 & p_{44} \end{bmatrix} \quad (4.1)$$

and for Gallium phosphide we use the constants measured by Dixon et al. [27] given in Table 4.2. It is worth mentioning here that the photoelastic effect is strongly dependent on the wavelength, and it is stronger close to the bandgap. For gallium phosphide, the only reference, to my knowledge, for the photoelastic effect [27] obtained the photoelastic constants from an acousto-optic modulation experiment at a wavelength of $\lambda = 630 \text{ nm}$ (1.97 eV), which is much closer to the bandgap of GaP (2.26 eV), than the infrared light at $\lambda = 1550 \text{ nm}$ (0.8 eV) that is the design frequency for the devices presented here. We might therefore severely overestimate the photoelastic coupling when using these constants. The strain tensor S_{ij} can be expressed

Table 4.2: Photoelastic constants of gallium phosphide measured at $\lambda = 630 \text{ nm}$ [27].

p_{11}	p_{12}	p_{44}
-0.151	-0.082	-0.074

in Voigt notation as

$$S = \begin{bmatrix} S_1 \\ S_2 \\ S_3 \\ S_4 \\ S_5 \\ S_6 \end{bmatrix} = \begin{bmatrix} S_{xx} \\ S_{yy} \\ S_{zz} \\ 2S_{yz} \\ 2S_{xz} \\ 2S_{xy} \end{bmatrix} \quad (4.2)$$

Equation 3.17 then becomes [17]

$$\begin{aligned} \left. \frac{\partial \omega}{\partial \alpha} \right|_{\text{pe}} = & \frac{\omega_o \epsilon_0 n_{\text{GaP}}^4}{2} \int d\vec{x} \left(2\Re\{E_x^* E_y\} p_{44} S_{xy} \right. \\ & + 2\Re\{E_x^* E_x\} p_{44} S_{xz} \\ & + 2\Re\{E_y^* E_z\} p_{44} S_{yz} \\ & + |E_x|^2 (p_{11} S_{xx} + p_{12} (S_{yy} + S_{zz})) \\ & + |E_y|^2 (p_{11} S_{yy} + p_{12} (S_{xx} + S_{zz})) \\ & \left. + |E_z|^2 (p_{11} S_{zz} + p_{12} (S_{xx} + S_{yy})) \right) \bigg/ \int d\vec{x} \vec{E}(\vec{x}) \vec{D}(\vec{x}) \end{aligned} \quad (4.3)$$

The vacuum coupling rate g_0 was determined for the design presented above for 400 mechanical modes between 100 MHz and 5 GHz. Breathing modes in the frequency range between 3– and 4 GHz were selected for further study and the simulated coupling as well as other significant parameters are displayed in Table 4.3. The eigenmodes corresponding to these results are shown in Figure 4.9. Table 4.3 also lists the individual contributions to g_0 by the

Table 4.3: Calculated optomechanical coupling rate g_0 from moving boundary effect g_{mb} and photoelastic effect g_{pe} , as well as effective mass m_{eff} and zero point motion x_{ZPF} .

$\Omega_m/2\pi$ [GHz]	m_{eff} [fg]	x_{ZPF} [fm]	$g_{\text{mb}}/2\pi$ [kHz]	$g_{\text{pe}}/2\pi$ [kHz]	$g_0/2\pi$ [kHz]
3.173	702	1.94	-5.56	182	176
3.227	769	1.84	18.2	358	376
3.249	646	2.00	22.1	493	515
3.277	738	1.86	19.1	319	338
3.316	420	2.45	35.3	571	607
3.436	377	2.55	-6.88	215	209
3.568	297	2.81	9.11	120	129

moving boundary effect g_{mb} and the photoelastic effect g_{pe} that can be derived from

$$g_{\text{mb,pe}} = \left. \frac{\partial \omega}{\partial \alpha} \right|_{\text{mb,pe}} x_{\text{ZPF}}. \quad (4.4)$$

The photoelastic effect is by far the more dominant for the modes of interest, due to the large overlap of the electric field and the strain field of the mode, as is expected [17, 83]. In some instances, the moving boundary effect also has the opposite sign of the photoelastic effect,

which is also expected [83], which reduces the g_0 for the respective modes. It is also noteworthy that the effective mass is reduced for modes that are not dispersion-matched, which is due to our choice of the generalized displacement as the maximum of the displacement field. An illustration of the mode overlap between the optical mode and the mechanical mode at 3.249 GHz is shown in Figure 4.10.

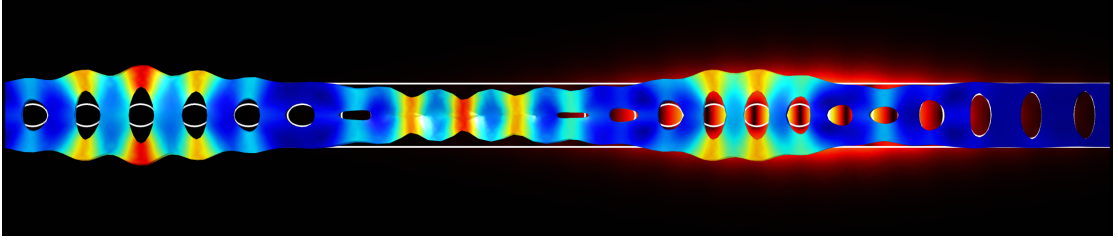


Figure 4.10: Illustration of overlap between optical and mechanical mode.

5 Piezoelectric Coupling

The piezoelectric effect describes the coupling between an electric field and the mechanical state of a non-centrosymmetric crystal, such as gallium phosphide. It is described by the two relations

$$\begin{aligned}\mathbf{D} &= \mathbf{e} \cdot \mathbf{S} + \epsilon \mathbf{E} = \mathbf{P}_{\text{pe}} + \epsilon \mathbf{E} \\ \mathbf{T} &= \mathbf{c}_E \cdot \mathbf{S} - \mathbf{e}^T \cdot \mathbf{E}.\end{aligned}\tag{5.1}$$

The first equation describes the electric displacement \mathbf{D} created by the piezoelectrically-induced polarization \mathbf{P}_{pe} by a mechanical strain \mathbf{S} in the material – often described as the ‘direct’ piezoelectric effect – while the second relation describes the stress induced in a piezoelectric material due to an externally applied electric field \mathbf{E} – often referred to as the ‘inverse’ piezoelectric effect. In Voigt notation, the piezoelectric coupling matrix \mathbf{e} can be expressed as a 3×6 matrix and the elasticity matrix \mathbf{c}_E can be expressed in terms of a 6×6 matrix.

In the zinc-blende crystal structure – the natural crystal structure for gallium phosphide – the coupling matrix has the form

$$\mathbf{e} = \begin{bmatrix} 0 & 0 & 0 & e_{14} & 0 & 0 \\ 0 & 0 & 0 & 0 & e_{14} & 0 \\ 0 & 0 & 0 & 0 & 0 & e_{14} \end{bmatrix}\tag{5.2}$$

which links a shear strain S_{ij} ($i, j = x, y, z, i \neq j$) to an electric polarization $P_{\text{pe},k}$ ($k = x, y, z, i, j \neq k$) as

$$P_{\text{pe},k} = e_{14} S_{ij}.\tag{5.3}$$

Specifically, this means that a shear strain (for example $S_{xy} > 0; S_{xz}, S_{yz} = 0$) produces an electric polarization in the orthogonal direction ($P_{\text{pe},z} > 0; P_{\text{pe},x,y} = 0$). This is illustrated in Figure 5.1. The cube represents an infinitesimal cubic volume of side length l . S_{xy} can be viewed as the fractional shift $\Delta l/l$ of the two faces orthogonal to x in y direction and, since the strain tensor \mathbf{S} is the symmetric part of the displacement tensor [23], the shift of the two faces orthogonal to y in x direction. The shear is illustrated in Figure 5.1 in the center panel, together with the piezoelectrically-induced polarization \mathbf{P}_{pe} shown out of plane along z in blue. Under a 45° rotation of the cube around the z -axis we can identify this shear displacement

with a breathing mode displacement along the x -axis. This can be realized experimentally by fabricating the photonic crystal with its long axis along the (110)-direction of the gallium phosphide lattice. For gallium phosphide the elasticity matrix is given as that of an isotropic

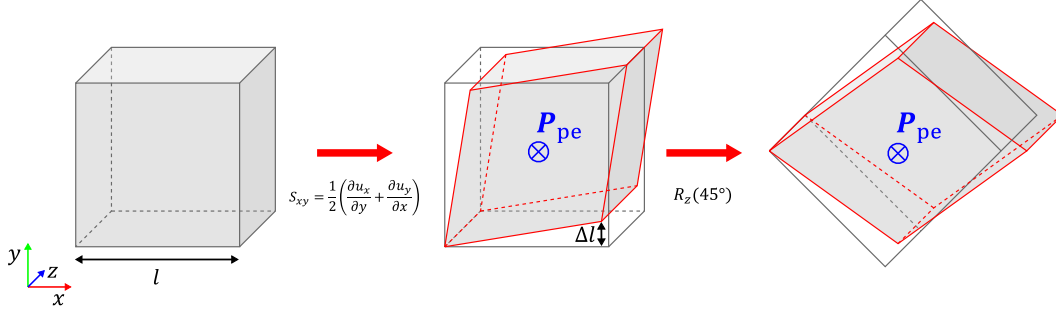


Figure 5.1: Illustration of shear strain S_{xy} and induced piezoelectric polarization \mathbf{P}_{pe} .

solid [98] with

$$\mathbf{c}_E = \begin{bmatrix} c_{11} & c_{12} & c_{12} & 0 & 0 & 0 \\ c_{12} & c_{11} & c_{12} & 0 & 0 & 0 \\ c_{12} & c_{12} & c_{11} & 0 & 0 & 0 \\ 0 & 0 & 0 & c_{44} & 0 & 0 \\ 0 & 0 & 0 & 0 & c_{44} & 0 \\ 0 & 0 & 0 & 0 & 0 & c_{44} \end{bmatrix}. \quad (5.4)$$

The piezoelectric coupling can be calculated directly in Comsol Multiphysics with a coupled

Table 5.1: Elastic [98] and piezoelectric [68] constants of gallium phosphide.

c_{11} [GPa]	c_{12} [GPa]	c_{44} [GPa]	e_{14} [C/m ²]
141.2	62.53	70.47	-0.1

solid mechanics, and electrostatics simulation. The relevant output of the simulation is the port admittance $Y = V/I$ which links the applied voltage to the current through the port.

5.1 Simulation Setup

The device is placed with a vacuum gap over two electrodes. The electrode volume is not considered for the simulation as it is field-free. The interfaces of the electrodes to the simulation domain is set to ground for one electrode, and as a terminal for the other electrode. This forms the microwave port. The boundary condition of the vacuum box is a floating potential (a perfect electric conductor).

A frequency domain study is then carried out in which the software calculates the port admittance Y . A small imaginary part ($\mathcal{O}(10^{-4})$) is introduced into the elasticity matrix of the mechanical device which introduces some spectral broadening of the mechanical resonances and allows for a lower sampling rate in the simulation.

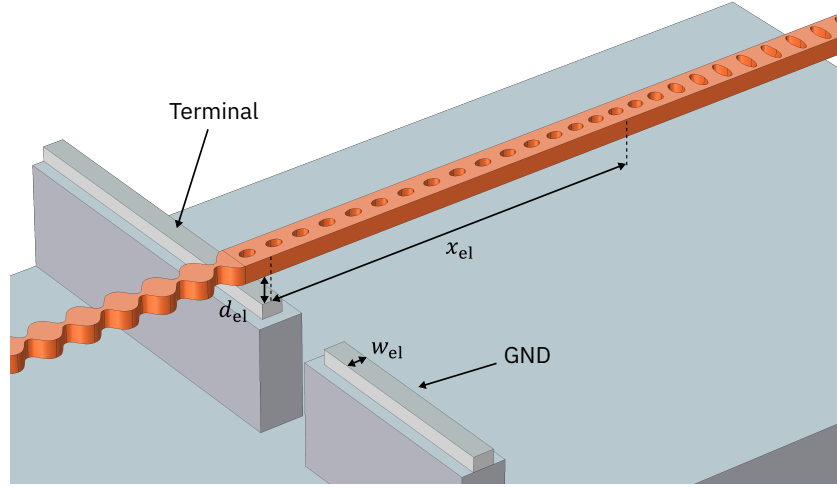


Figure 5.2: Piezoelectric simulation setup.

5.2 Estimation of Circuit Parameters

The admittance of the device can be interpreted as that of a series of parallel RLC resonators coupled to the terminal via a coupling capacitance C_0 as shown in Figure 5.3.

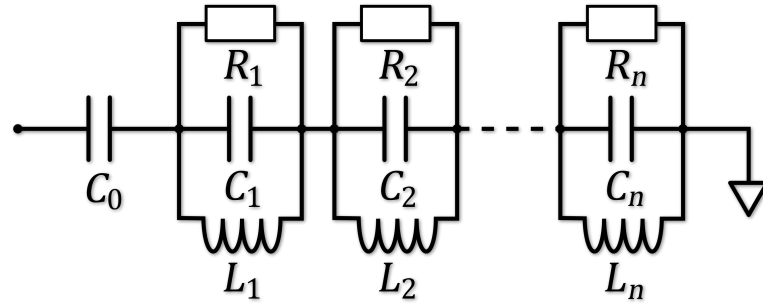


Figure 5.3: Circuit approximation of piezoelectric response.

Specifically, the admittance of the circuit is given as

$$Y(\Omega) = \frac{1}{Z(\Omega)} \quad (5.5)$$

with the circuit impedance $Z(\Omega)$. The impedance can be determined by summing up the individual series impedances as

$$Z(\Omega) = \frac{1}{i\Omega C_0} + \sum_{k=1}^n \frac{1}{Y_k(\Omega)} \quad (5.6)$$

with

$$Y_k(\Omega) = \frac{1}{R_k} + \frac{1}{i\Omega L_k} + i\Omega C_k. \quad (5.7)$$

The same photonic crystal design was simulated with two different electrode configurations. A coplanar configuration was used for the prototype device to experimentally verify the piezoelectric response. A second, optimized design is also discussed for strong coupling to superconducting qubits.

5.3 Results for Coplanar Electrode Configuration

Here, the results for a coplanar electrode configuration are shown. The dimensions of this simulated geometry correspond to the structure that was fabricated and for which the experimental results are discussed later. The electrode configuration is shown in Figure 5.4 (a) and (c). The bottom electrode gap for this device corresponds to 296 nm, which limits the coupling

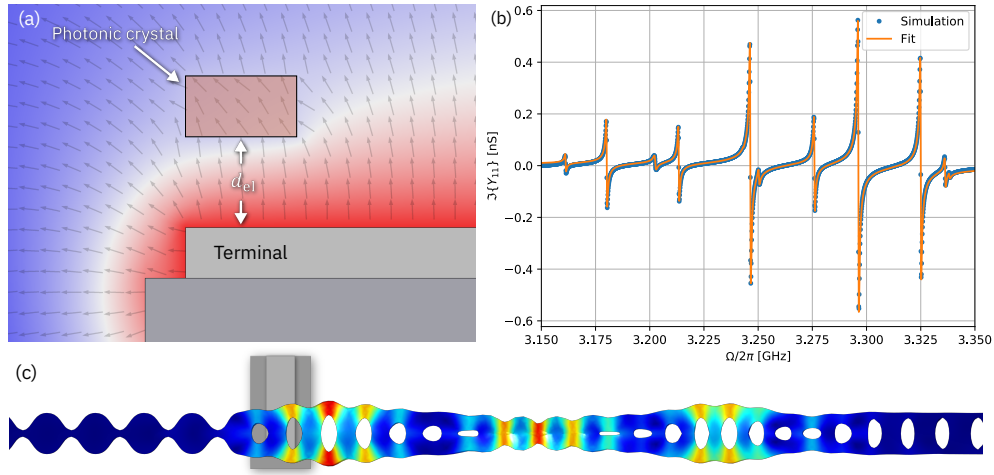


Figure 5.4: Side view of photonic crystal suspended over coplanar electrodes with electrostatic potential (red \rightarrow 1V, blue \rightarrow 0V) (a), Imaginary part of terminal admittance (blue) with fit to RLC network (orange) (electrostatic contribution due to C_0 was subtracted for clarity), and displacement field (c) with indicated position of electrode for piezoelectric response at 3.295 GHz.

efficiency. The coplanar design also results in an electric field that is not perfectly aligned along the z-axis, as indicated by the electric potential shown in Figure 5.4 (a). The piezoelectric response of the device in the frequency band from 3.15 GHz to 3.35 GHz – the range in which the optomechanically well-coupled breathing modes are located – is shown in Figure 5.4 (b). The shown data corresponds to the imaginary admittance which is fit to Equation 5.5 for a series of fourteen parallel RLC circuits. Note that the electrostatic contribution, which introduces a slope to $\Im\{Y(\Omega)\}$ was subtracted in this case to make the piezoelectric response more visible. The coupling rate to a transmission line can be estimated using Equation 1.24. The mode frequency $\Omega_m = 1/\sqrt{LC}$, the capacitance C and the transmission line coupling Γ_{ex} of the of the circuit fit are displayed in Table 5.2, the coupling capacitance is determined as $C_0 = 0.40\text{fF}$. The main takeaway of these results are the capacitances in the nF-range, which, in

5.3. Results for Coplanar Electrode Configuration

Table 5.2: Device circuit parameters.

Mode #	$\Omega_m/2\pi$ [GHz]	C [nF]	$\Gamma_{\text{ex}}/2\pi$ [Hz]
1	3.161	336	1.49×10^{-3}
2	3.180	69.83	7.27×10^{-3}
3	3.203	218.9	2.35×10^{-3}
4	3.213	83.60	6.20×10^{-3}
5	3.243	6545	8.07×10^{-5}
6	3.246	25.66	2.06×10^{-2}
7	3.250	311.6	1.70×10^{-3}
8	3.276	67.13	8.03×10^{-3}
9	3.296	21.61	2.53×10^{-2}
10	3.316	6326	8.73×10^{-6}
11	3.325	27.56	2.01×10^{-2}
12	3.336	20.49	2.73×10^{-3}
13	3.338	87.23	6.42×10^{-4}

combination with the small coupling capacitance, lead to the small transmission line coupling due to the large impedance mismatch with a load impedance $|Z_L| \sim 100 \text{ k}\Omega$. Essentially, it is not expected that the mechanical modes are actuated very efficiently when coupled to a transmission line, and the reflection coefficient $\Gamma = \frac{Z_L - Z_0}{Z_L + Z_0} > 99.999999\%$ indicates that we can also not expect to directly measure the device reflection S_{11} .

5.3.1 Coupling to a Transmon Qubit

The purpose of this design is not the efficient coupling to a transmission line, but rather to a superconducting qubit, so it is more instructive to study the quantum-acoustic coupling between a transmon qubit and the simulated design. As discussed before, the bilinear coupling between a transmon and a parallel LC circuit can be expressed as

$$g = \frac{1}{2} C_0 \sqrt{\frac{\Omega_{\text{ge}} \Omega_m}{C_\Sigma C}}, \quad (5.8)$$

where Ω_{ge} denotes the qubit's first transition frequency and C_Σ its capacitance. For a swap gate it is preferable to set the qubit frequency $\Omega_{\text{ge}} = 1/\sqrt{L_J C_\Sigma} = \Omega_m$. Additionally, it is advantageous to work in the transmon regime, such that $E_J/E_C \gg 1$. For $E_C = e^2/2C_\Sigma$ and $E_J = \varphi_0^2/L_J$ we find

$$\frac{E_J}{E_C} = 2C_\Sigma \frac{\varphi_0^2}{e^2} \frac{1}{L_J}. \quad (5.9)$$

With $L_J = 1/C_\Sigma \Omega_m^2$ we can find a shunt capacitance as a function of E_J/E_C as

$$C_\Sigma = \frac{1}{\Omega_m^2} \sqrt{\frac{E_J}{E_C} \frac{e^2}{2\varphi_0^2}} \quad (5.10)$$

Consequently, we can find g as a function of E_J/E_C and analyze at which E_J/E_C and shunt capacitance C_Σ we obtain a given coupling. Henceforth, the discussion is limited to mode 9 in Table 5.2, as it exhibits the highest admittance of the analyzed modes. The resulting coupling

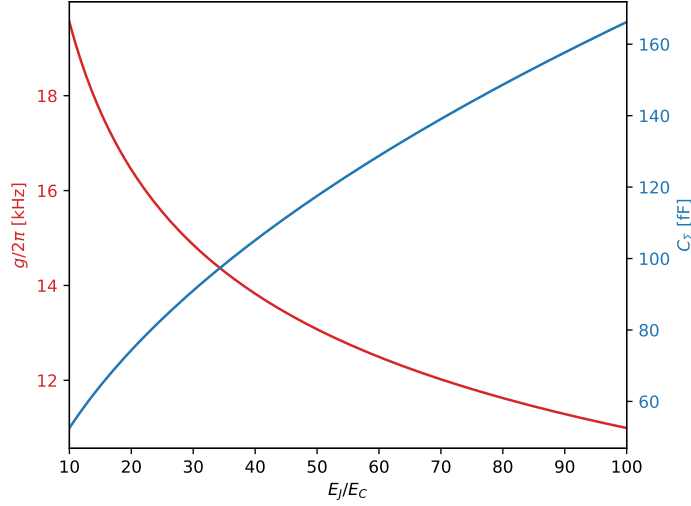


Figure 5.5: Quantum-acoustic coupling rate g and corresponding qubit shunt capacitance C_Σ as a function of E_J/E_C .

rate as well as the corresponding value of the shunt capacitance C_Σ is shown in Figure 5.5. For computational qubits it is typical to choose $E_J/E_C \sim 50$ to avoid too strong charge dispersion in the second excited state, an important consideration for the CNOT gate. Since this qubit will only be used to swap the state from the mechanical resonator into the circuit QED system, it can be justified to choose a smaller E_J/E_C for the sake of larger g , without introducing a too strong charge dispersion to the first excited state. However, an $E_J/E_C > 20$ should still be chosen. In this regime and with this geometry the achievable coupling rate is limited to $g/2\pi \sim 15$ kHz, which puts the device in the strong coupling regime for a qubit $T_1 > 10 \mu\text{s}$ and a quality factor of the mechanical oscillator $Q_m > 2.2 \times 10^5$. Both seems achievable given previously reported quantum acoustic experiments [21] and quality factors measured in gallium phosphide photonic crystal cavities measured at millikelvin temperatures [93].

5.4 Top-Bottom Electrode Configuration

The caveat with the results presented in the last section is that, although the strong coupling regime is technically achievable, it is barely so. For a Rabi-swap with significant fidelity the system must be deep in the strong coupling regime. For illustration, results of numerical simulations using the Lindblad master equation were performed with the system starting in the state $|\psi_0\rangle = |0_q 1_m\rangle$. The time evolution of the system is then simulated with representative parameters, i.e. $E_C/E_J = 20$, $T_1 = 10 \mu\text{s}$, $\alpha_{\text{nl}} = \Omega_{\text{ge}} \sqrt{\frac{E_J}{8E_C}}$, $Q_m = 2.2 \times 10^5$, and $g/2\pi = 15$ kHz. After an interaction time τ the state of the system $|\psi\rangle$ is measured and the overlap with

5.4. Top-Bottom Electrode Configuration

the target state $|\psi_1\rangle = |1_q 0_m\rangle$ is calculated to obtain the fidelity $\mathcal{F} = \langle\psi_1|\psi\rangle$. A map of the

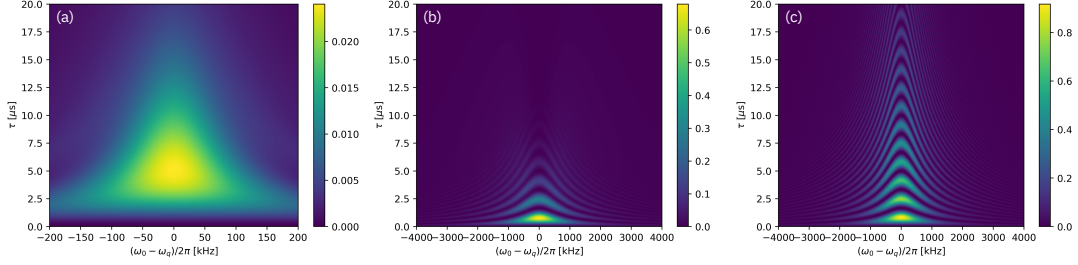


Figure 5.6: Simulated Rabi oscillation pattern for results derived in Figure 5.3.1 with a maximum fidelity of $\mathcal{F} = 2.4\%$ (a), simulation with $20\times$ enhanced g with maximum $\mathcal{F} = 67.9\%$ (b), and simulation with $20\times$ enhanced g as well as $T_1 = 40\mu\text{s}$, $Q_m = 4 \times 10^5$ with maximum $\mathcal{F} = 91.7\%$ (c). Color indicates the photon occupation of the qubit $\langle\hat{n}_q\rangle$.

simulation results with time delay τ on the y-axis and detuning of the qubit from the resonator frequency $\Omega_m - \Omega_{ge}$ on the x-axis is shown in Figure 5.6 (a). The fidelity of the Rabi swap in this case is only $\mathcal{F} = 2.4\%$. If the coupling rate can be increased by a factor 20, the fidelity increases substantially to $\mathcal{F} = 67.9\%$ (cf. Figure 5.6 (b)), and if the qubit lifetime as well as the mechanical quality factor can be improved to $T_1 = 40\mu\text{s}$ and $Q_m = 4 \times 10^5$, respectively, a fidelity of $\mathcal{F} = 91.7\%$ can be achieved.

Therefore, the motivation to improve the coupling rate is clear. The design presented in Figure 5.3.1 is by no means ideal. The electric field is not ideally aligned with respect to the crystal orientation of GaP, the gap between the photonic crystal and the bottom electrode is large, and the overlap of the electrode with the mechanical mode profile is not optimal, since the design was chosen for broad-band actuation of multiple modes and not the coupling to a specific mode. The design can be optimized by reducing the gap from 300 nm to 50 nm – a value that was demonstrated to be feasible in the planarization of the dielectric interlayer spacer during fabrication, as further discussed in subsection 8.2.3. Furthermore, a contact can be added above the photonic crystal to improve the overlap of the electric field with the relevant terms of the piezoelectric tensor, a technique that was also demonstrated to be feasible (cf. section 10.4), and finally, the geometry of the electrodes can be optimized to improve the overlap with the mechanical mode profile. An illustration of such an optimized design is shown in Figure 5.7. As in the previous section, mode 9 from Table 5.2 is chosen for further analysis. The imaginary part of the admittance is shown in Figure 5.8 together with the simulated coupling strength to a transmon qubit g and the qubit shunt capacitance C_Σ as a function of E_J/E_C . As illustrated, the coupling in this design is massively improved compared to the previous design with $g/2\pi \sim 230\text{kHz}$ for $E_J/E_C \sim 20$. This is not quite a $20\times$ improvement compared to the previous design but it is close, and if improvements to T_1 and Q_m (cf. [62]) can be made, a fidelity $> 90\%$ of a qubit-resonator state swap seems to be in reach. Simulated couplings for various gap sizes and positions of the electrode pair along the axis of the photonic crystal beam are shown in Figure 5.9.

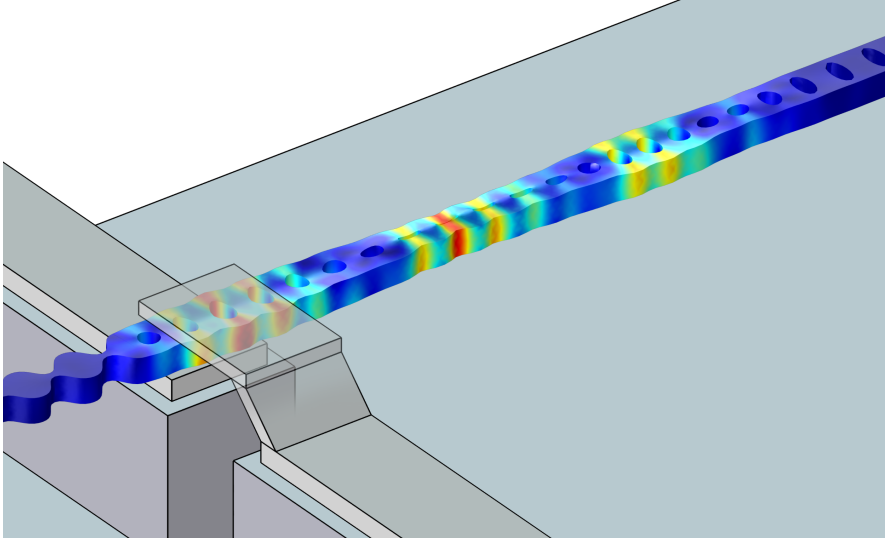


Figure 5.7: Illustration of top-bottom design.

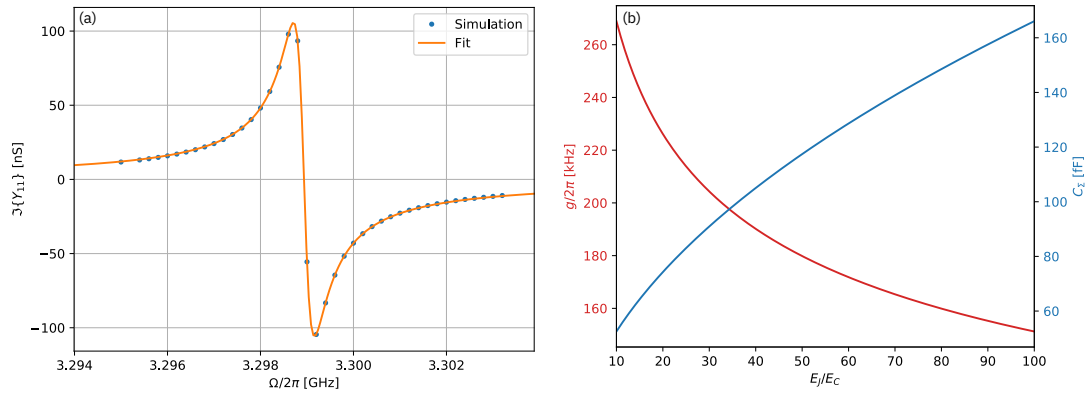


Figure 5.8: Reactance part of piezoelectric admittance of optimized design with circuit fit (a) and corresponding coupling rates g and shunt capacitance C_Σ as function of E_J/E_C (b).

5.4. Top-Bottom Electrode Configuration

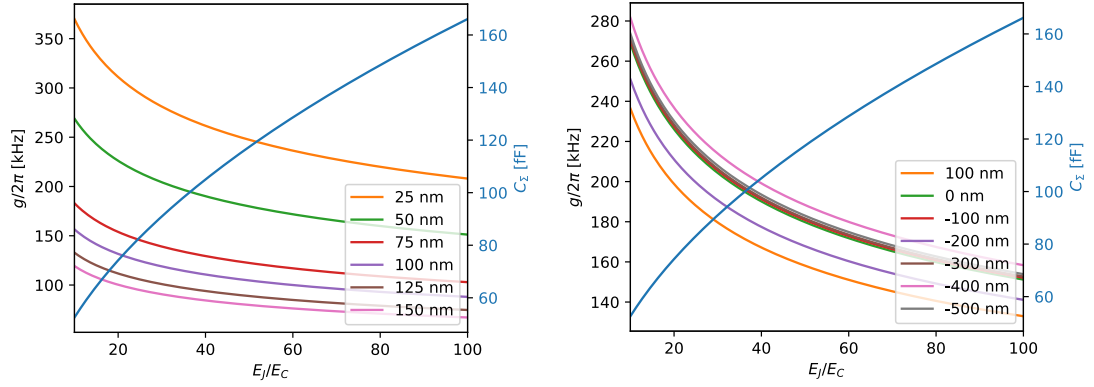


Figure 5.9: Simulated qubit coupling rates for different gap sizes between electrodes and photonic crystal (left). Simulated qubit coupling rates for various positions of the electrode pair along the photonic crystal axis (right) at a gap of 50 nm, where 0 nm is the electrode configuration shown in Figure 5.7.

Device Fabrication and Integration

Part III

This part is dedicated to the fabrication of the optomechanical hybrid device and superconducting devices. I want to especially provide a detailed description of the critical steps in the fabrication process. An overview of the process is shown in Figure 5.10 (a-d). First, the electrode pattern is fabricated on an intrinsic silicon wafer (a), discussed in chapter 7. Then, the silicon substrate is locally etched to create a sufficiently large gap between the optical cavity and the silicon substrate (b). The recess in the silicon is then filled with a sacrificial SiO_2 layer and planarized (c), as discussed in chapter 8. A gallium phosphide wafer with an epitaxially grown heterostructure comprising 300 nm GaP on 100 nm $\text{Al}_{0.1}\text{Ga}_{0.9}\text{P}$ on 100 nm GaP is then bonded to the planarized silicon wafer and the GaP growth substrate and $\text{Al}_{0.1}\text{Ga}_{0.9}\text{P}$ are removed to expose the 300 nm thick GaP device layer. The epitaxial growth of GaP is described in chapter 6 and details on the wafer bonding process and substrate removal are discussed in chapter 9. The GaP device layer is then patterned into a photonic circuit (e) and the optomechanical device is release with buffered hydrofluoric acid which removes the sacrificial SiO_2 layer (f), as discussed in chapter 10. Colorized SEM images of the finished optomechanical hybrid device are shown in Figure 5.10 (g) as an overview over the entire device and (h) as a close-up showing the optomechanical crystal cavity.

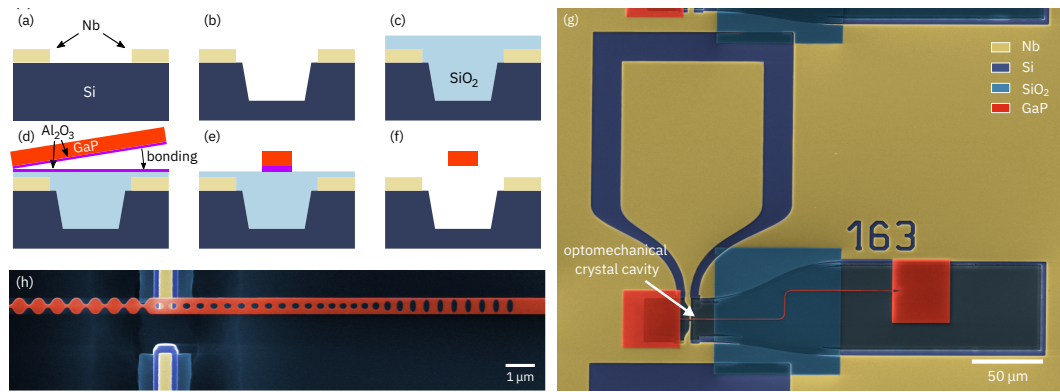


Figure 5.10: Overview of fabrication process (a-d) and colorized SEM overview image (g) with detailed view of optomechanical crystal cavity in (h).

All microfabrication steps in this work were carried out at the *Binnig and Rohrer Nanotechnology Center* (BRNC).

6 Growth of Gallium Phosphide with Metal-Organic Vapor Phase Epitaxy

For gallium phosphide to work efficiently as a piezoelectric material, it must be grown epitaxially, that is, as a single crystal. Epitaxial growth on wafer-scale is typically performed by either molecular beam epitaxy (MBE) where the precursors Ga and P are provided by effusion cells, or by metal-organic vapor phase epitaxy (MOVPE), where the precursors are bound in metal-organic compounds. In this work, a heterostructure comprising GaP/Al_xGa_(1-x)P/GaP is grown on a GaP substrate by MOVPE.

6.1 Metal-Organic Vapor Phase Epitaxy

In MOVPE, precursor atoms are bound in metal-organic compounds that dissociate during the growth process and produce elementary ad-atoms that can integrate into the crystal lattice of the substrate while the organic part of the precursor molecule desorbs due to the high temperature of the process. For GaP, the precursors that are used in this case comprise trimethylgallium (TMGa) for Ga, shown in Figure 6.1 on the right as precursor molecule containing Ga (blue), tertiarybutylphosphine (TBP) for P, shown in Figure 6.1 on the right as precursor molecule containing P (yellow) and trimethylaluminum (TMAI) for Al. The precursors are stored in liquid form and are introduced to the reactor chamber via bubblers. Hydrogen gas is injected into the precursor reservoir where the precursor vapor is entrained in the hydrogen flow. The enriched hydrogen flow is then injected into the reactor via a shower-head. When the precursor comes into contact with the heated substrate, the organic compounds break apart. The remaining elementary Ga and P are then free to integrate with the crystal lattice of the substrate, as illustrated in Figure 6.1 on the right. A typical situation in a MOVPE reactor is shown in Figure 6.1 on the left. The growth substrates (illustrated in orange) are placed on a heated chuck which rotates during the process at ~ 1000rpm while the precursor gases are dispensed with the hydrogen carrier gas by the shower head.

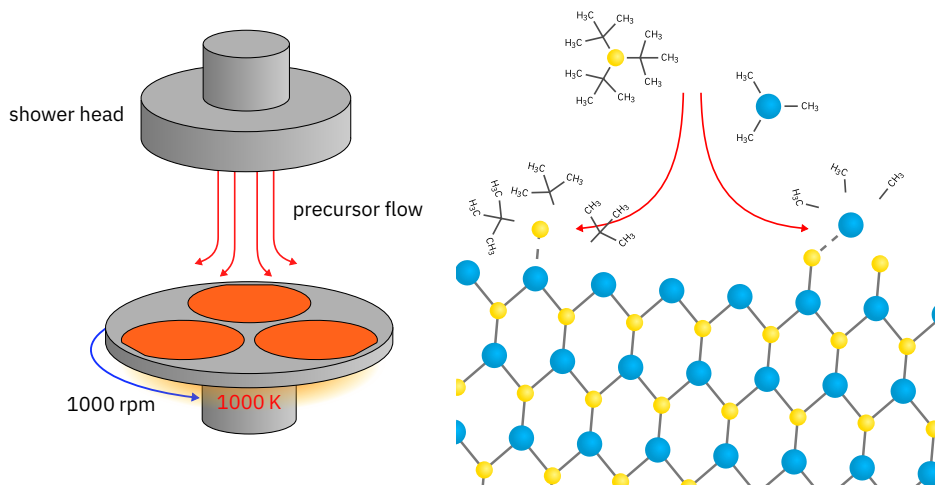


Figure 6.1: MOVPE reactor (left) and illustration of growth process (right). Shown ligands are for illustrative purposes only.

6.2 Growth Dynamics of Gallium Phosphide

As mentioned before, GaP is in this case grown homo-epitaxially on a GaP substrate. The wafer surface is polished at a slight angle to the crystal lattice to reveal the atomic layers of GaP. This assists the nucleation during growth as adatoms can arrange along these steps which allows for very ordered layer-by-layer growth. An AFM scan of a typical substrate after removal of the native oxide is shown in Figure 6.2 in a $5\mu\text{m} \times 5\mu\text{m}$ scan (left) and a $1\mu\text{m} \times 1\mu\text{m}$ scan (right). In both cases, the atomic terraces on the substrate are clearly visible. The vertical 'streaks' across the low-magnification image are due to the chemical-mechanical polishing process that is employed during the wafer fabrication. In the following, the growth dynamics of GaP are addressed to lay out the procedure with which optimized growth parameters were found. The growth of the $\text{Al}_x\text{Ga}_{1-x}\text{P}$ layer was not optimized to the same extent as it only serves as etch-stop layer for subsequent processing. Instead, the growth conditions were chosen to comply with the prioritized growth of GaP. In the future, it might be advisable to perform a similar optimization on the growth of $\text{Al}_x\text{Ga}_{1-x}\text{P}$. Suffice it to say at this point that Al has a substantially lower surface mobility than Ga such that the growth of $\text{Al}_x\text{Ga}_{1-x}\text{P}$ is conditioned at lower V-III ratio compared to that of GaP to allow for appropriate lattice arrangement.

Temperature

MOVPE growth is a process with a plethora of co-dependent parameters, the most important of which is arguably the temperature. Elevated temperature increases the surface mobility of ad-atoms such that they have a greater mean free path before they organize into the lattice, while at lower temperature the ad-atoms are more localized in the region where they first adsorb. The implications for the growth dynamics of GaP are shown in Figure 6.3 for various temperatures ranging from 550°C (a) to 730°C (f). It was found that at low temperature the ad-

6.2. Growth Dynamics of Gallium Phosphide

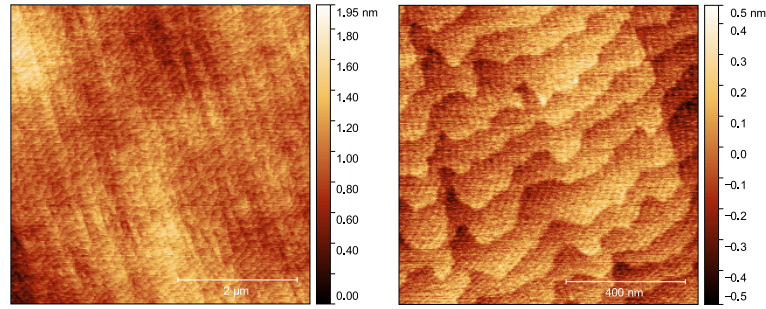


Figure 6.2: AFM measurement of GaP wafer surface prior to growth after removal of native oxide.

atoms do not have sufficient surface mobility to properly arrange along the atomic terraces. As the temperature is increased the terraces become visible. At 650 °C and 680 °C the terraces are clearly visible, but small patches of GaP are found which have not arranged completely along one step. At 700 °C we find a nearly perfect growth, while at 730 °C the ad-atoms' mobility is so high that not only growth along the (100) direction (the orientation of the growth substrate) is possible, but also along energetically more favorable higher order facets such as the (111) direction, as seen in Figure 6.3 (f) in the pyramid-like structures that emerge. We find the optimum temperature range around 700 °C-710 °C.

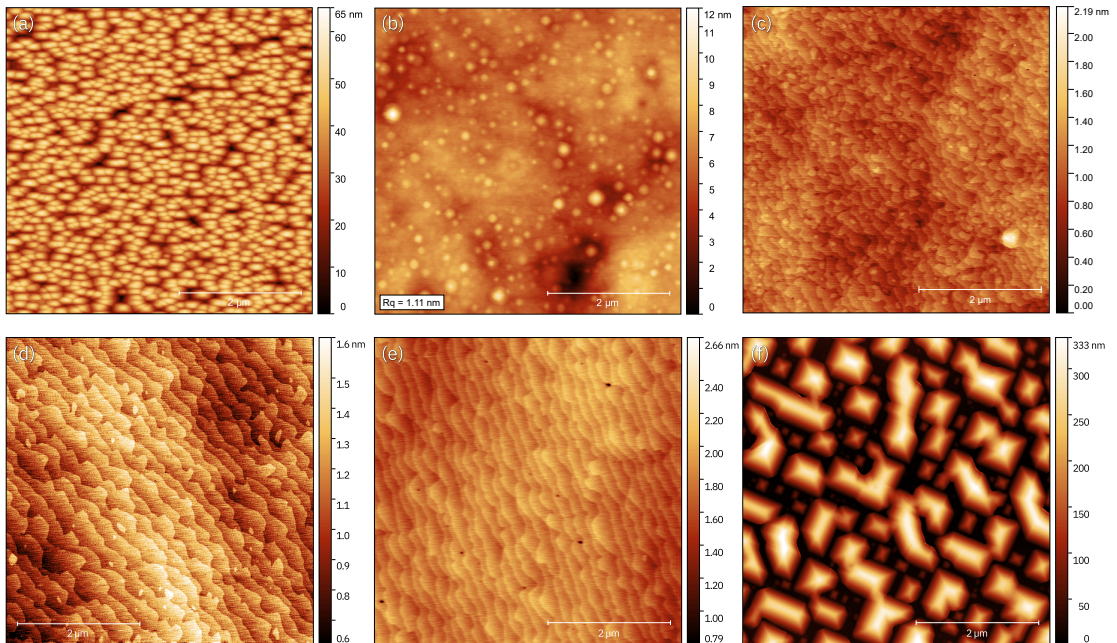


Figure 6.3: GaP surface at different growth temperatures: 550 °C (a), 600 °C (b), 650 °C (c), 680 °C (d), 700 °C (e), 730 °C (f).

Phosphorous Desorption

At elevated temperature, phosphorous may desorb from the growth substrate [94]. Ga on the other hand is much less volatile such that it remains behind. If this increased desorption is not taken into account, the Ga can form droplets on the GaP surface which can prevent a consistent growth result. Typically, the GaP substrate is heated prior to growth to remove any native oxide present on the wafer surface. An AFM scan of the GaP substrate after this treatment in a case where P desorption occurred is shown in Figure 6.4 on the left. The small particles scattered across the surface are presumed to be Ga droplets. The result for a subsequently grown GaP layer is shown in the right panel of this figure. Small holes appear where GaP is unable to nucleate due to the formation of Ga droplets. Phosphorous desorption can be prevented by establishing an overpressure of the group V element in the chamber, that is, to increase the V-III precursor molar flow ratio. However, this ratio also impacts the surface mobility of the group III material, Ga, which, at high group V overpressure more readily finds a P atom to bind to than at lower V-III ratio, thereby reducing its mean free path on the wafer surface. A strategy that has been proven useful in the development of a process was to find a minimum V-III ratio at which no more formation of Ga droplets, i.e. holes in the grown GaP layer, was observed, for each considered temperature.

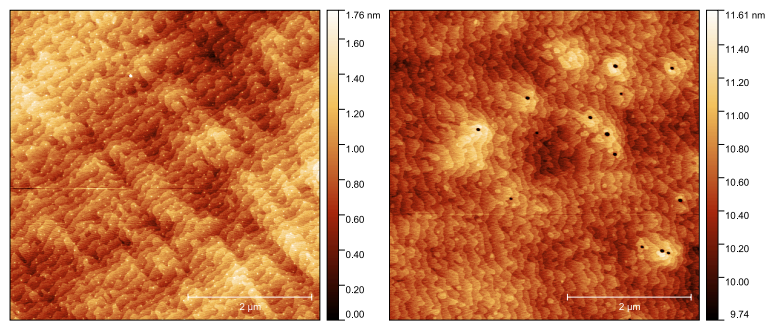


Figure 6.4: Phosphorous desorption at elevated temperature. Substrate after removal of native oxide (left) and after growth of GaP layer (right) showing the formation of holes due to the formation of Ga droplets.

6.3 Suppression of Defect Formation due to Growth Along Higher Order Crystal Planes

One major issue that we continue to struggle with during the GaP growth is the formation of hexagonal 'hillock' defects in the epi-layer. These defects are believed to form around seed particles on the substrate wafer which are a residue of the chemical-mechanical polishing process that is employed during the wafer fabrication. This form of contaminant is very difficult to remove prior to growth as the small particles with a diameter on the scale of ~ 50 nm exhibit extremely strong adhesive forces that attach them to the wafer surface. This is no fundamental issue of GaP, it is rather a result of the small production volume of GaP wafers,

6.3. Suppression of Defect Formation due to Growth Along Higher Order Crystal Planes

which limits the sourcing of substrates to companies with specialized wafer production whose quality control and fabrication techniques are not on par with that of Si or other III-V wafer foundries. A typical cluster of particles that can lead to the formation of a hillock is shown in Figure 6.5 in the SEM micrograph on the left. An optical micrograph of a typical growth result with hillocks is shown in the right panel of the figure. During growth, each aggregation of

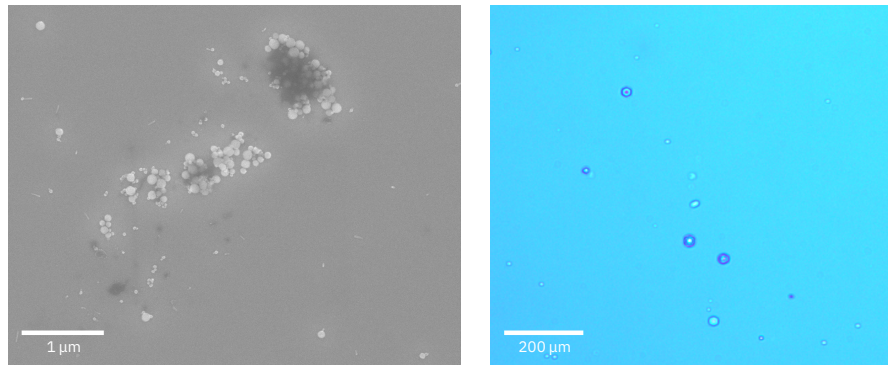


Figure 6.5: Contaminant of GaP wafer prior to growth (left) and hillock defects formed during growth (right).

contaminants on the wafer surface provides a potential seed for the growth of a GaP crystallite with a quasi-random crystal orientation. A sketch of this parasitic growth process is shown in Figure 6.6. We typically find such hillocks with a height of $0.5\text{ }\mu\text{m}$ to $1.5\text{ }\mu\text{m}$. These protrusions can locally inhibit a clean bonding interface between the GaP wafer and the substrate wafer and may, if the density of such hillocks is sufficiently high, inhibit wafer-bonding altogether [24]. The formation of a crystallite is determined by the growth conditions. If the mobility

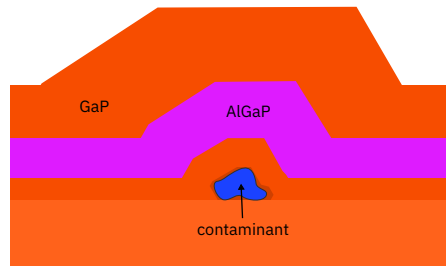


Figure 6.6: Hillock formation.

of the ad-atoms is low, it is more likely that they will adhere to the surface contaminant. At appropriate growth conditions, the hillock formation can therefore be largely suppressed. A primary goal of growth optimization was therefore to identify a growth mode of GaP in which the formation of hillocks is suppressed. An AFM micrograph of a typical hillock found after growth is shown in panels (a) and (b) of Figure 6.7, whereas an example where the formation of a hillock was suppressed is shown in panels (c) and (d) of the figure. It is important to note here again that the growth conditions were tailored for an optimal result for GaP. Since Al exhibits a generally lower surface mobility, it may still form a seed for hillocks even in a

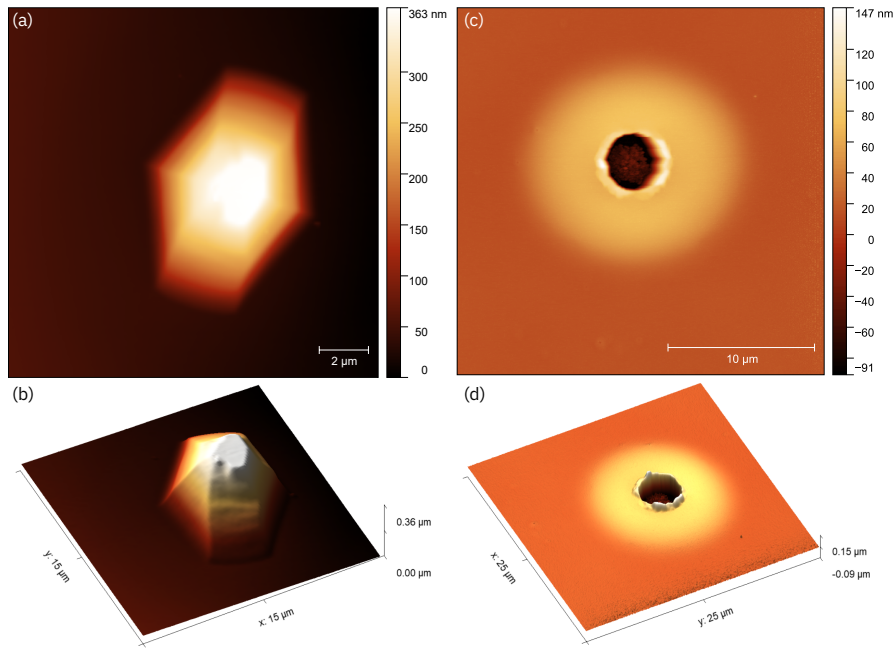


Figure 6.7: Hexagonal defect in GaP (a,b) and suppressed defect in optimized growth-mode (c,d).

growth mode where GaP does not. Since a GaP buffer layer is grown on the contaminated wafer surface prior to the AlGaP layer however, the density and height of hillocks that may form during the AlGaP growth may still be greatly reduced.

6.4 Optimized Growth

An optimized growth recipe was found with a V-III ratio of 10 during the GaP growth and 8 during the growth of $\text{Al}_{0.1}\text{Ga}_{0.9}\text{P}$ at a temperature of 710°C and a growth rate of 8 \AA/s . The individual growth steps are illustrated in Figure 6.8. A 100 nm-thick GaP buffer layer is first grown on-top of the substrate for an improved nucleation of the AlGaP layer. The surface of the buffer layer after growth is shown in Figure 6.9 (a). Subsequently, a 200 nm AlGaP etch stop layer is grown on-top of the buffer, the surface of which is shown in Figure 6.9 (b). Finally, the 300 nm GaP device layer is grown on-top, the surface of which is shown in Figure 6.9 (c). The

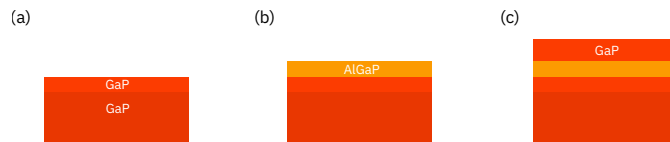


Figure 6.8: Layer stack grown by MOVPE for wafer-bonding of GaP thin-films. GaP buffer layer (a), followed by $\text{Al}_{0.1}\text{Ga}_{0.9}\text{P}$ etch stop layer (b), followed by GaP device layer (c).

as-grown GaP layer shows nearly perfect arrangement along the atomic terraces and no holes

due to phosphorous desorption were observed. The lower surface mobility of Al is indicated by an imperfect arrangement along the atomic terraces in Figure 6.9 (b) despite the lower phosphorous overpressure. The density and height of hillocks is found in this recipe to be reduced as compared to the initial growth recipe.

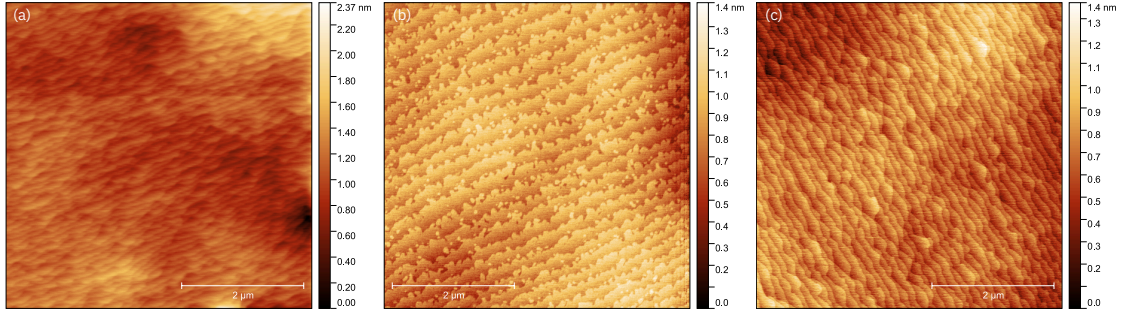


Figure 6.9: Optimized growth result. Bottom GaP buffer layer surface (a), Al_{0.1}Ga_{0.9}P etch stop layer surface (b), and GaP device layer surface (c).

6.5 Growth on Silicon

Gallium phosphide is a III-V compound semiconductor that is lattice-matched to silicon. This, in theory, opens up the possibility of growing GaP epitaxially on silicon substrates that are available at low cost and with high quality. However, since GaP is non-centrosymmetric and therefore has a polar bond polarity it requires a polar substrate to properly nucleate, which Si does not provide. While implementations of GaP on Si exist, we choose to grow GaP homo-epitaxially on a GaP substrate. The main reason for this is a more straight-forwards growth process (e.g. removal of native SiO₂ by thermal treatment of the substrate is not possible in our reactor), and the monetary incentive is, at least for now, not strong enough to justify the added complexity.

7 Fabrication of Nb and NbN Superconducting Circuits on Silicon

Superconducting qubits require low microwave loss in both substrate, and the interfaces between the superconducting film and air, the substrate and air, as well as the superconductor and the substrate. This is crucial to achieve competitive qubit lifetime [96]. Intrinsic silicon or sapphire have been shown to exhibit low microwave loss tangents at single photon energies, whereas amorphous dielectric materials such as silicon dioxide and silicon nitride have been proven to exhibit excessive loss at single photon energies [71] due to a high number of localized charge states in the bulk material. Consequently, in order to achieve a substantial qubit lifetime, the substrate of choice is either sapphire or Si for the proposed optomechanical hybrid architecture. In addition, the substrate must be machined to provide both a small gap between the superconducting electrodes and the photonic crystal, and a large gap between the optical mode and the substrate. Sapphire is an extremely resistant material and is very difficult to micro-machine, whereas a plethora of well-developed processes are available for Si. Therefore, Si was chosen as the substrate for this platform.

Two superconductors were explored in this work as platform for microwave components, Nb and NbN. The materials were chosen for their chemical and thermal stability which allow the exposure to processes with elevated temperatures and to chemical processes such as wet etching in BHF. In addition, both materials provide the added benefit of a short lifetime of optically-induced quasi-particles, a quality that might prove decisive for the operation of superconducting qubits fabricated in this material system in conjunction with optical devices. Furthermore, Nb on Si is also used as the material system for the commercial IBM quantum computing platform [56]. NbN exhibits a high kinetic inductance which opens up the possibility to fabricate quasi-linear high-impedance microwave circuits [102, 69].

7.1 Deposition of Superconducting Nb and NbN Layers by Magnetron Sputtering

Both Nb, and NbN were deposited from a Nb target by magnetron sputtering in a *Von Ardenne* system with a chamber base-pressure $p_0 \sim 10^{-7}$ mbar. In order to reduce impurities in the

Chapter 7. Fabrication of Nb and NbN Superconducting Circuits on Silicon

deposited films, 500 nm Nb was deposited in the chamber with closed shutter prior to the thin-film deposition. As Nb can act as an oxygen getter material, this reduces the base-pressure to $p_0 \sim 10^{-8}$ mbar. Native oxide was removed from the intrinsic silicon wafers (4 inch, 10 k Ω cm, Si-Mat) prior to deposition with a 1:100 diluted HF solution. In the case of Nb, a 250 nm-thick film was deposited.

Table 7.1: Parameters for deposition of Nb and NbN.

Material	Target	P_{DC}	Ar flow	N ₂ flow	Pressure	V_{DC}	Deposition rate
Nb	Nb	250 W	20 sccm	–	6×10^{-3} mbar	267 V	0.53 nm/s
NbN	Nb	100 W	32 sccm	0.6 sccm	4.5×10^{-3} mbar	279 V	0.57 nm/s

7.1.1 Reactive Sputtering of NbN

NbN can be sputtered from a Nb target by adding nitrogen to the chamber. The nitrogen then reacts with the surface of the Nb target to form, under the right conditions NbN. Since Nb and nitrogen may also form different compounds, such as Nb₄N₅ and Nb₄N₃, the choice of appropriate process conditions is critical. We followed Glowacka et al. [38] for the development of the NbN sputtering process. The Nb target is first fully saturated with nitrogen by adding a large N₂ flow to the chamber. As the flow is increased, an increased DC bias between target and electrode is observed due to the formation of nitride on the Nb surface. The measured DC bias with increasing N₂ flow is shown in Figure 7.1 in blue. At high flow, a saturation is observed. The process is kept at a high flow rate for 2 min to saturate the target. Then, the nitrogen flow is decreased until the DC bias corresponds to the half-way point between the pure Nb target and the saturated target. Glowacka et al. [38] found the highest T_C at this point which may be taken as indicator that at this point NbN is formed. A hysteresis of the DC bias is observed between increasing N₂ flow starting from the Nb target and decreasing N₂ flow starting from the saturated target (orange), similar to Glowacka et al. [38]. It should be noted here that we chose a nitrogen flow of 0.6 sccm, which is slightly higher than the half-way DC point. This is merely due to the fact that the nitrogen mass-flow controller was limited to steps of 0.2 sccm and 0.6 sccm was closest to the half-way DC point.

7.2 Characterization of NbN

Since results for our Nb deposition process regarding the critical temperature were reported elsewhere [83] only NbN will be discussed here.

7.2.1 X-Ray Diffraction

Prior to electrical measurements the NbN film was analyzed with X-ray diffraction (XRD) analysis, the results of which are shown in Figure 7.2. The film thickness was determined

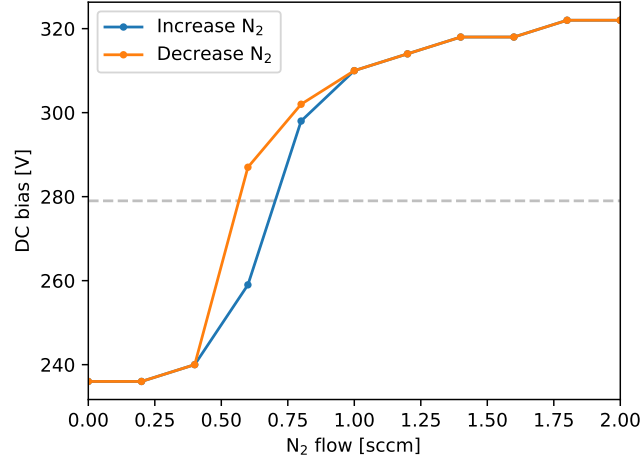


Figure 7.1: DC bias during target nitridation for different N_2 flow rates. NbN forms at half bias point, indicated by dashed gray line. DC bias also displays hysteresis.

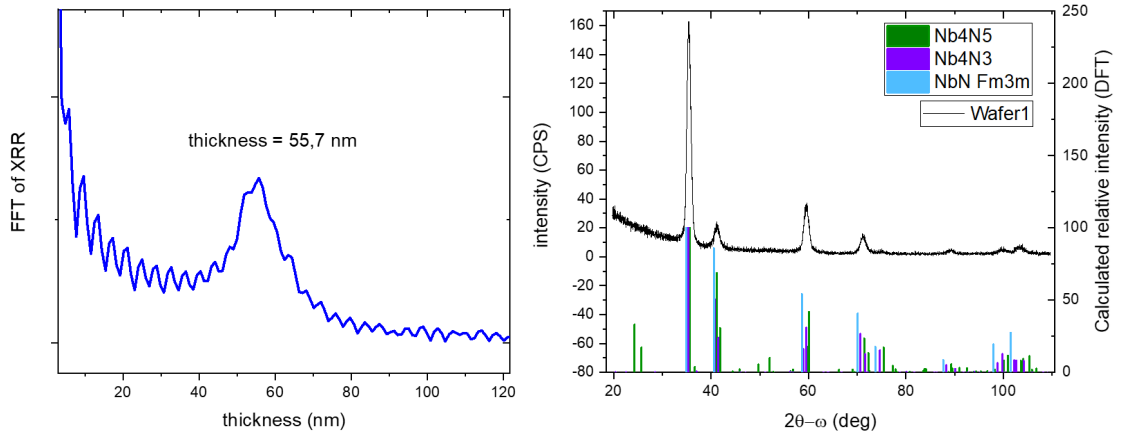


Figure 7.2: XRD analysis of NbN film. The film thickness was measured by X-ray reflectometry (left) and the crystal structure was analyzed with an $\omega - 2\theta$ measurement (right).

via X-ray reflectometry to be 55.7 nm (left panel). The crystal structure was analyzed with an $\omega - 2\theta$ Bragg-diffraction measurement, the results of which are compared to simulated relative peak intensities calculated from density functional theory (DFT) and are shown in the right panel of Figure 7.2. The best agreement between simulations and observed data was found to be with NbN in the $Fm\bar{3}m$ space group.

7.2.2 Critical Temperature and Kinetic Inductance

The kinetic sheet inductance L_k^\square of the fabricated NbN film was of special interest, as it strongly influences any microwave design. L_k^\square can be estimated from the critical temperature T_C and

the sheet resistance in the normal state R_N^\square as [69]

$$L_k^\square(0) = \frac{\hbar R_N^\square}{\pi \Delta_0}, \quad (7.1)$$

where $\Delta_0 = 2.08 k_B T_C$ is the superconducting gap. the prefactor 2.08 is an empirical factor found by Niepce et al. [69]. Both R_N^\square and T_C can be extracted from a four-point measurement of the sheet resistance close to the critical temperature. Several devices as depicted in the

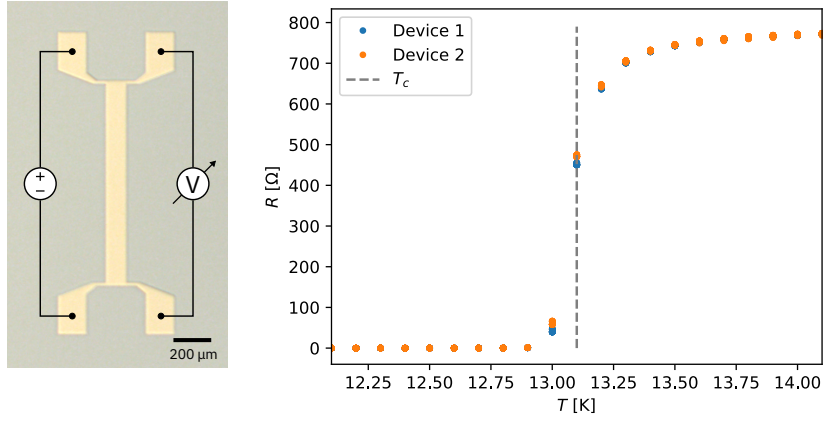


Figure 7.3: Four-point measurement of the critical temperature of NbN. Device is shown on the left, temperature-dependent resistance on the right. Critical temperature T_C is indicated by dashed gray line.

left panel of Figure 7.3 were fabricated with the process discussed below from the previously characterized NbN layer and connected for a four-point measurement as indicated. The resistance was then measured as a function of temperature in a *Quantum Design PPMS DynaCool* cryostat from 2 K to 30 K. The critical temperature was found at 13.1 K with a normal state sheet resistance at 30 K of $R_N^\square = 82.0 \Omega/\square$. The kinetic sheet inductance is then found to be $L_k^\square(0) = 7.32 \text{ pH}/\square$. Resistance measurements close to the bandgap are shown in the right panel of Figure 7.3 for two measured devices. The results for the critical temperature are very consistent with the ones found by Glowacka et al. [38].

7.3 Fabrication of Superconducting Nb and NbN Devices

Superconducting resonators, contacts and devices for four-point measurements were fabricated subtractively from Nb and NbN thin films by etching in a chlorine-based plasma using an inductively-coupled plasma reactive ion etcher (ICP-RIE). Stability of both materials at elevated temperature $\sim 300^\circ\text{C}$ permits the use of a SiO_2 hard-mask instead of a resist mask. The hard-mask is deposited with plasma-enhanced chemical vapor deposition (PECVD) and patterned with a resist mask in a reactive ion etcher (RIE). After etching the superconductor, the hard-mask is removed with buffered hydrofluoric acid (BHF). This method offers several advantages compared to using a resist mask directly for pattern transfer into the metal film. First, the Nb/NbN etching process is very aggressive and highly directional. Consequently, a resist mask must be thick in order to offer sufficient protection, which increases the critical dimension, and the remaining resist is after etching typically burnt and must be removed for example with an oxygen plasma. Since the interface between the superconductor and air is one of the critical interfaces, this is not desirable. Second, a hard-mask can be patterned in multiple steps before transferring the pattern into the metal layer. For example, fine structures can be patterned with electron-beam lithography (EBL) while large structures can be patterned with optical lithography. Patterning these structures into the hard-mask before transferring them into the metal layer can lead to a more consistent and homogeneous pattern transfer. In addition, while the superconductor is protected by a sufficiently thick SiO_2 hard-mask, the etched sample may be exposed to an O_2 plasma for additional cleaning without risking oxidation of the metal film in the masked areas.

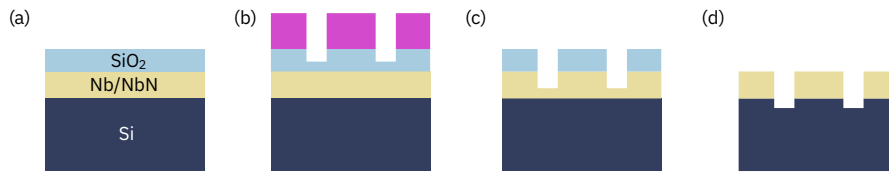


Figure 7.4: Nb/NbN electrode fabrication with SiO_2 hard-mask. Hard-mask is deposited by PECVD (a) and patterned with a resist mask (purple) with RIE (b). Nb/NbN is etched with ICP-RIE (c) and hard-mask is removed with BHF (d).

The process steps are illustrated in Figure 7.4. The thickness of the hard-mask deposited in (a) with a *Oxford Plasmalab 100* PECVD system depends on the thickness of the superconductor and the desired overetch. Etch rates of SiO_2 , Nb, NbN and the photoresist AZ1505 in the chlorine-based ICP-RIE Nb etch are given in Table 7.3. The SiO_2 thickness should be chosen with at least 20 % margin. The given etch rates are approximate and may vary. The hard-mask is patterned with a 100 W CHF_3/Ar -based process in a *Oxford NGP 80* RIE system. using a resist mask. Here, fine structures were patterned using EBL with CSAR resist, while structures with a critical dimension $> 2\mu\text{m}$ were patterned with optical lithography into AZ1505 photoresist. The resist is stripped after the RIE step for 20 min in DMSO at 110°C , in case of CSAR, and for 10 min in an ultrasonic bath in acetone in the case of AZ1505. In both cases the strip is followed by a rinse with IPA and 3 min at 600 W in a *PVA Tepla GIGAbatch 310 M* oxygen

plasma asher to remove resist residues.

Table 7.2: ICP process parameters for Nb/NbN etch.

Process parameter	Value
Pressure	3 mTorr
Cl ₂ flow	10 sccm
Ar flow	30 sccm
RF power	100 W
ICP power	500 W
DC bias	300 V

After complete pattern transfer into the hard-mask the superconductor is etched in a Cl-based process with a *Oxford PlasmaPro 100* ICP-RIE system. Process parameters are given in Table 7.2. The remaining hard-mask is removed with a BHF dip.

Table 7.3: Etch rates of Nb, NbN and SiO₂ in chlorine-based Nb etch.

Material	Etch rate
Nb	5.00 nm/s
NbN	1.89 nm/s
SiO ₂	0.70 nm/s
AZ1505	20.8 nm/s

An optomechanical hybrid device after fabrication of the electrodes is shown in Figure 7.5. An overview image of one device is shown on the left. The structure in the top left of the image is the microwave port with a pad for contact with a GS-microwave probe. A large area of silicon is exposed where the photonic crystal is integrated later. A magnified view of the bottom Nb electrodes is shown on the right. An outline is visible where EBL and optical lithography steps were overlaid.

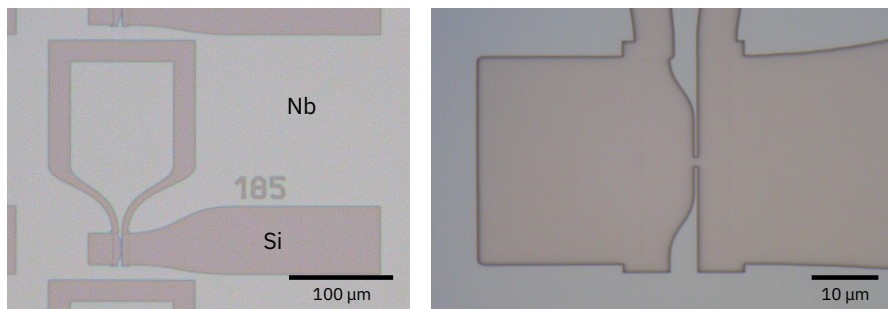


Figure 7.5: Optomechanical hybrid device after fabrication of Nb electrodes. Overview (left) and magnified view (right) of same device.

Note here that the electrodes were overetched ~ 150 nm into the silicon substrate to remove any remaining Nb grains. This is essential to prevent micromasking in the subsequent recess

7.3. Fabrication of Superconducting Nb and NbN Devices

etch. The overetching could however be achieved in two separate steps. A small overetch during the electrode patterning, and a second, longer overetch with the recess hard-mask.

8 Silicon Recess and Planarization

A critical point of the proposed design is the realization of a small gap between the superconducting electrodes and the GaP photonic crystal $\mathcal{O}(100\text{ nm})$. This can be realized by introducing a sacrificial, intermediary SiO_2 layer on-top of the superconducting circuit which can later be removed. This layer can then be planarized by chemical mechanical polishing (CMP) to achieve a surface finish sufficient for wafer-bonding. Since silicon exhibits a higher refractive index than GaP, a mode overlap between the optical cavity mode and the silicon substrate will lead to radiation loss. In order to circumvent this, pockets can be etched locally into the silicon substrate to establish a sufficient gap between the optical mode and the substrate. We found that a gap of $1.5\text{ }\mu\text{m}$ is sufficient to isolate the optical mode from the substrate. The pockets are then filled with a sacrificial oxide and the wafer is polished to an interlayer thickness between the electrode and the oxide surface $< 100\text{ nm}$, a surface roughness $S_q < 0.5\text{ nm}$ and a long-range topography $< 20\text{ nm}$. The process is outlined in Figure 8.1.

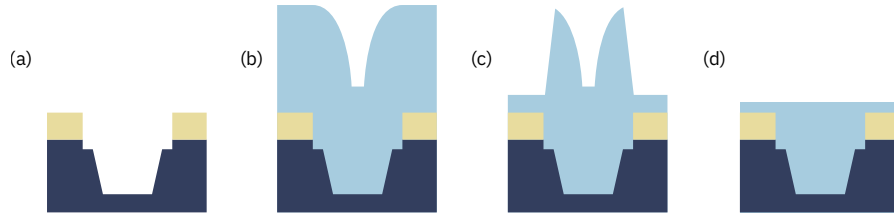


Figure 8.1: Silicon recess and planarization process. Pockets are etched into silicon with HBr (a), recess is then filled with SiO_2 (b). SiO_2 profile is planarized by compensation etch (c) and CMP (d).

8.1 Silicon Recess

First, the silicon is recessed by $\sim 1.5\text{ }\mu\text{m}$ with a HBr-based ICP-RIE process. Again, a SiO_2 hard-mask is used. It is critical for this step that the area to be recessed is cleaned from all residues or particles from previous process steps to avoid micro-masking.

Following the recess, the wafer is again cleaned with an O_2 plasma step, while the metal film

Table 8.1: Parameters of Si recess etch.

Process parameter	Value
Pressure	4 mTorr
HBr flow	37.5 sccm
O ₂ flow	3 sccm
RF power	110 W
ICP power	600 W
DC bias	290 V

remains covered by the hard-mask. A hybrid optomechanical device after recess and cleaning is shown in Figure 8.2. The mask is then removed with BHF.

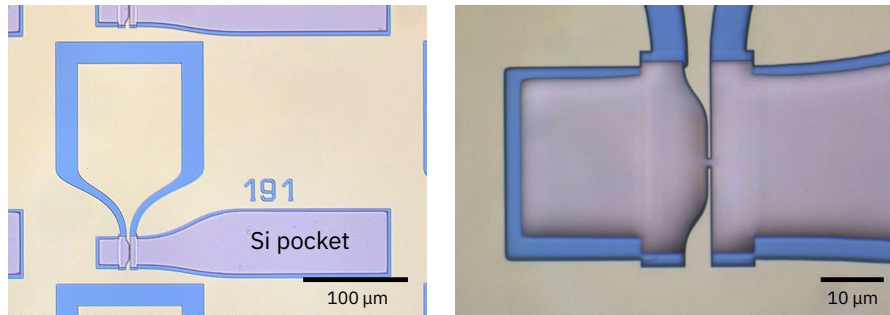


Figure 8.2: Optomechanical hybrid device after recess of silicon pocket. Overview (left) and magnified view (right) of same device.

Subsequently, the recessed pockets are filled with SiO₂ deposited by PECVD. The thickness of deposited SiO₂ is chosen such that it exceeds the overall profile, from the top of the Nb layer to the bottom of the pocket, by ~ 500 nm to enable subsequent CMP without additional oxide re-deposition. Note that a PECVD process is chosen that exhibits high uniformity $> 99\%$ across the wafer such that a small gap between the photonic crystal and the electrodes can be realized for all devices.

8.2 Planarization

Planarization of the profile depicted in Figure 8.1 is crucial for wafer-bonding and not trivial. If the topography in panel (b) were to be planarized directly, full planarization would be nearly impossible due to the steep profile and due to the fact that planarization of a negative profile is a priori difficult to achieve with CMP. Instead, a compensation etch is performed to 'level' the inner part of the pocket with the level of the SiO₂ on the Nb ground plane, as depicted in panel (c).

8.2.1 Compensation Etch

The silicon pockets are masked with a designed overlap of $\sim 5\mu\text{m}$ with a photolithographic step and the sacrificial oxide is etched with the 100 W CHF_3/Ar process used before. 3D profiles of a device before and after the compensation etch are shown in Figure 8.3 (a,b) and (c,d), respectively. Note that the height difference between the Si pocket and the Nb ground-plane is $\sim 1.9\mu\text{m}$ before the compensation etch and $\sim 0.2\mu\text{m}$ after the compensation etch. Furthermore, the profile was inverted from negative to positive, which is much more straight forward to remove during CMP. Due to the designed overlap of the compensation mask and the pocket, a ridge remains around the pocket with a height $\sim 2\mu\text{m}$. As this ridge is narrow however, such a profile can be removed with CMP.

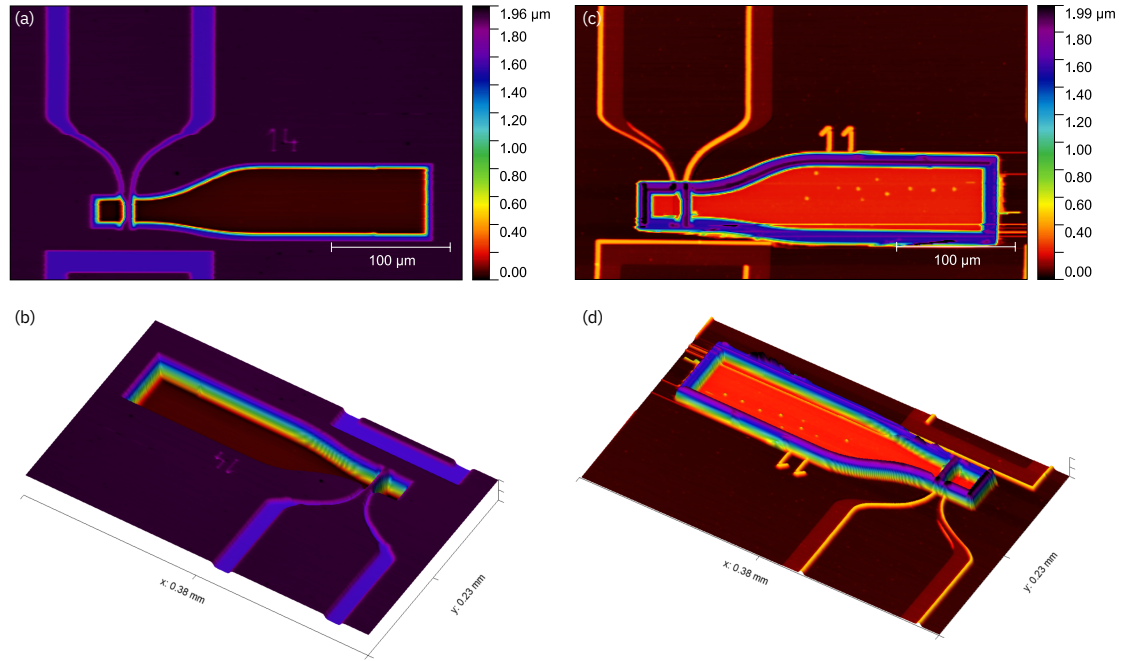


Figure 8.3: 3D profile of optomechanical hybrid device after deposition of sacrificial SiO_2 layer (a,b) and after compensation etch (c,d) measured by stylus profilometer.

8.2.2 Chemical Mechanical Polishing

The final planarization step (see Figure 8.1 (d)) to achieve a sufficient surface finish for wafer bonding and to control the gap between the photonic crystal and the electrodes is achieved by chemical mechanical polishing. During this step, the ridge remaining from the compensation etch is removed and the surface roughness is improved to $S_q < 0.5\text{ nm}$. The wafer is polished in three steps. Large-scale topography such as ridges are removed in the first step, where the oxide layer is polished from 470 nm to 300 nm. This step also reveals crevasses in the PECVD-deposited SiO_2 layer. This is typical for this process and is related to voids that form in the SiO_2 during growth along steps. Optical micrographs of a device after the first CMP step

are shown in Figure 8.4 (a,b) with AFM scans of the area indicated in (b) as red box in (c,d).

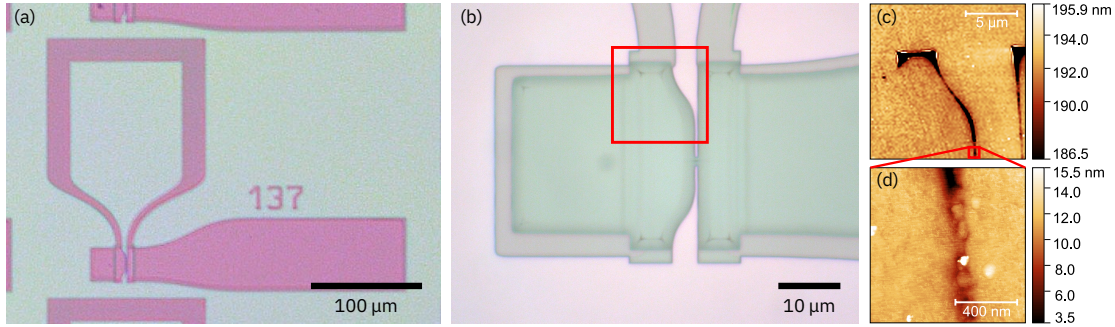


Figure 8.4: Device after first CMP step (a,b). AFM scans (c) show crevasses formed in area indicated with red box in (b). (d) shows magnified view of crevasse indicated by red box on (c)

The crevasses are clearly visible in the AFM scans, but the step between the Nb layer and the Si pocket is planarized (c). The crevasses are removed by re-deposition of 150 nm SiO_2 and a second CMP step, where 150 nm are polished. An AFM scan after this second step is shown in the right panel of Figure 8.5 with an optical micrograph indicating where the scan was taken on the left. The crevasses were completely removed, and the surface roughness $S_q = 0.52$ nm

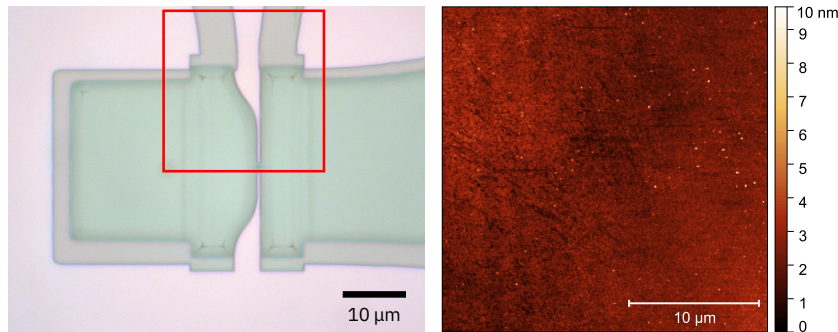


Figure 8.5: Device after second CMP step (left) and AFM scan in area indicated by red box on the left (right).

is nearly acceptable. A third CMP step is carried out after another re-deposition of 50 nm SiO_2 for further improvement of the surface finish. An AFM scan of the result is shown in Figure 8.6. The final surface roughness was measured to be $S_q = 0.47$ nm.

8.2.3 Improvements with Filler Pattern

During initial planarization runs we realized that areas on the wafer with a high density of devices were being polished at a lower rate compared to areas on the wafer without devices. This effect is related to a difference in load during the CMP due to the SiO_2 ridges around the Si pockets of the devices. This lead to a significantly higher polishing rate towards the edge of the wafer, where the oxide was eventually completely removed and the bare Nb was exposed. Nb particles can cause a massive problem during CMP, potentially damaging the

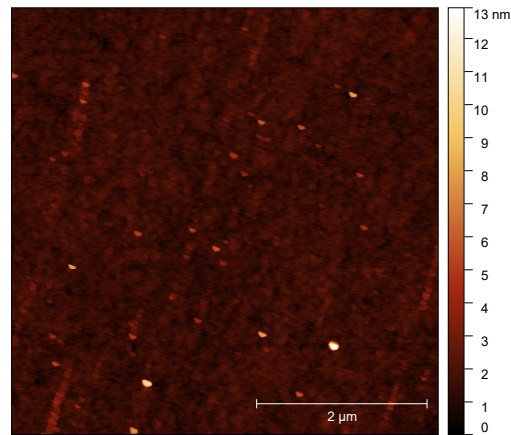


Figure 8.6: AFM scan of SiO₂ interlayer after third CMP step with surface roughness $S_q = 0.47$ nm.

wafer or even the polishing pad. For that reason, the final interlayer thickness of the devices (and therefore the gap between electrodes and photonic crystal) was limited to ~ 300 nm. To ensure a more homogeneous load for future CMP runs, a filler pattern was added to the compensation mask. The pattern is shown in blue in Figure 8.7 (a,b) in areas around the central area of the chip where devices are located. The pattern consists of horizontal and vertical bars that are arranged such that the fill-factor of the topography and the characteristic length-scales correspond to that found in the central area of the chip. Furthermore, additional oxide was added on the edges of the wafer to mitigate the risk of breaking through to the Nb layer during CMP.

The initial result without filler pattern is shown in Figure 8.7 (c), the improved result with filler pattern is shown in panel (d). While the interlayer thickness with the initial process was limited to ~ 300 nm, an interlayer thickness ~ 46 nm could be achieved with the improved process.

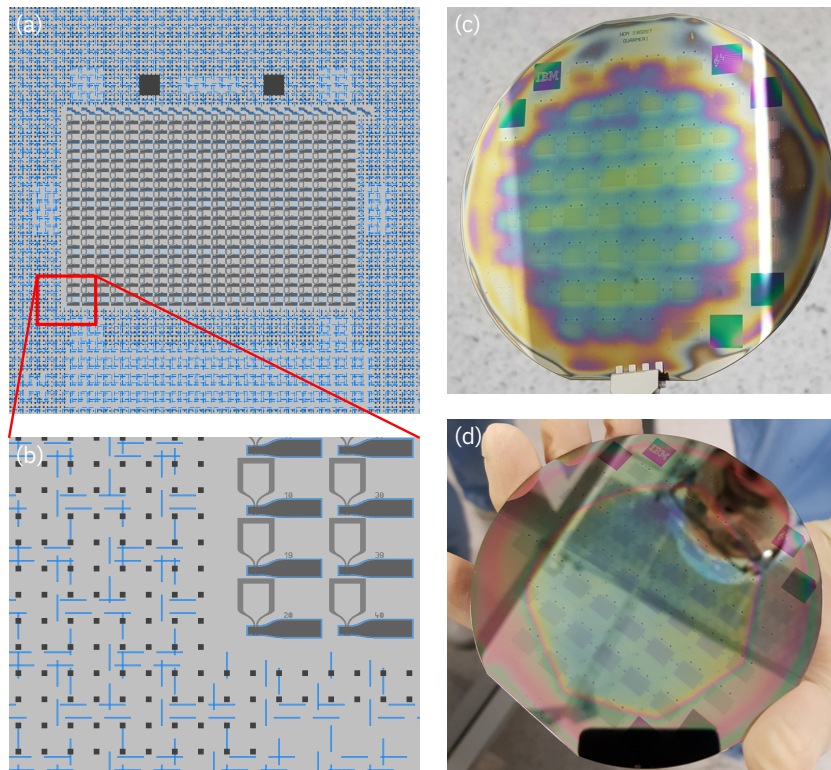


Figure 8.7: Filler pattern in areas of chip with no devices (a) improves homogeneity. Magnified view of (a) shown in (b). CMP result without filler pattern shown in (c), with filler pattern in (d)

9 Hybrid Materials Integration via Direct Wafer-Bonding

The decisive difference between the process presented here and other implementations is the monolithic integration of a single-crystalline, piezoelectric layer on-top of an arbitrary substrate on wafer-scale. This enables us to fabricate a superconducting circuit that can be optimized for low microwave loss, and integrate the piezoelectric material on wafer-level on top of this pre-fabricated circuit. While GaP is chosen as piezoelectric material for the implementation discussed here, the same method can be applied for a wide range of materials. Direct wafer-bonding (DWB) is the industry standard for, among other systems, the fabrica-

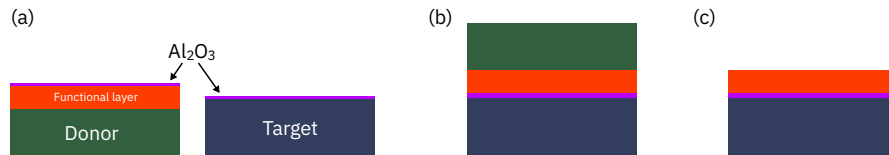


Figure 9.1: Direct wafer bonding: Target and donor wafers are coated with 5 nm Al_2O_3 layer with atomic layer deposition (a), wafers are bonded and annealed at 250 °C (b) and donor wafer is removed (c).

tion of silicon-on-insulator and lithium niobate thin-films on substrates such as silicon and sapphire. Previous work at IBM also included wafer-bonding of other functional material systems such as InGaAs for high-speed III-V transistor applications [25, 24], InGaAs/InAlAs heterostructures for integrated lasers [87, 86, 9] and barium titanate for high-speed electro-optic modulators [1, 30], and we recently demonstrated wafer-bonding of lithium niobate on a Si_3N_4 damascene platform for low-loss electro-optic modulators [22]. The DWB process is illustrated in Figure 9.1. Chemical bonding between two wafers is achieved by coating the donor and target wafers with a 5 nm Al_2O_3 layer deposited by atomic-layer deposition (a). The wafer surfaces are then brought into contact to initiate a preliminary bonding. A subsequent thermal annealing step at 250 °C then introduces a chemical bond between the Al_2O_3 layers of the donor and target wafers (b). Finally, the donor wafer is removed and the functional layer remains on the target wafer (c) [24].

9.1 Prerequisites for Direct Wafer-Bonding

DWB requires an exquisite surface finish of both the functional layer and the target wafer. In addition, any surface protrusion on either the donor or target wafers may inhibit bonding locally. The typical rule of thumb is that the RMS roughness of either surface be smaller than 0.5 nm and that a protrusion of x height inhibits bonding in a radius of $\sim 100x$ around the protrusion. A high density of protrusions, e.g. hillocks or particles, may inhibit wafer-bonding altogether. With the optimized growth recipe we find a short-range RMS roughness of the epitaxial GaP layer of $S_q = 142$ pm, well below the empirical threshold for successful wafer-bonding. Despite the optimized recipe, we still find hillock formation in the GaP/AlGaP epitaxial stack. Depending on the quality of the growth substrate, hillocks may occur at high density in random locations on the wafer. In order to ensure a reliable bonding result, a method was devised to remove hillocks prior to wafer-bonding without damaging the epitaxial GaP device layer.

9.2 GaP Hillock Planarization with Ion Beam Milling

Fundamentally, the challenge in addressing the hillocks formed on the GaP surface is that they occur randomly and at relatively high density, strongly dependent on the substrate quality. Consequently, it is unfeasible to mask individual hillocks and remove them via some conventional etching process. Instead, a self-aligned etching process is needed. This was achieved by coating the wafer surface with a sacrificial layer, either hydrogen silsesquioxane (HSQ) or a photoresist. The process is illustrated in Figure 9.2. The layer is applied by spin-coating. When applied with sufficient thickness the coating process creates a flat topography over the hillocks (b). The sacrificial layer is then milled in an argon ion mill under conditions where the etch rate of the sacrificial layer and that of GaP are matched (c). As the layer is removed, hillocks, which are now embedded into the sacrificial layer, are etched as well, while the epitaxial GaP layer remains unscathed. The etching is either monitored by periodic measurements of the remaining thickness of the sacrificial layer, or by endpoint detection via secondary-ion mass spectroscopy (SIMS). After an endpoint is reached, the remaining

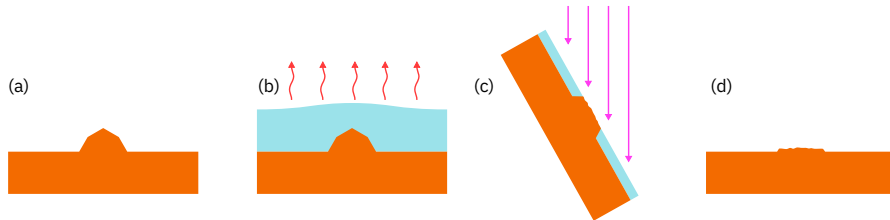


Figure 9.2: Planarization of hillock defects. GaP wafer is coated with sacrificial layer, e.g. HSQ (AZ4533), and annealed (a,b). Sacrificial layer and hillocks are etched in argon ion mill (c). Remaining sacrificial layer is removed with HF (O_2 plasma).

sacrificial layer can be removed selectively with respect to the GaP epi layer (d). In the case of HSQ, this is achieved with a short etch in hydrofluoric acid. An example of this planarization

process is shown in Figure 9.3. A typical hillock before planarization is shown in panel (a), with a height of ~ 360 nm. After application of an HSQ layer with 600 nm thickness (FOx16), the height of the hillock is reduced to ~ 20 nm (b). After planarization and removal of the sacrificial HSQ layer the top of the hillock has a flat top with a height of ~ 160 nm (c). This

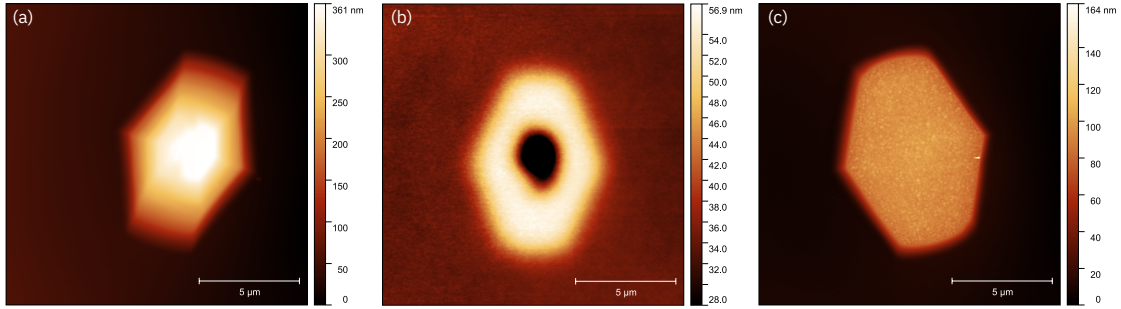


Figure 9.3: Typical hillock before planarization procedure (a), after application of a sacrificial HSQ layer (b) and after planarization (c).

result could be further improved with tighter process tolerances. However, even a reduction of the hillock height of 50 % reduces the size of the local bonding defect by 75 %.

9.3 Donor Wafer Removal

DWB is only useful if the donor wafer can be removed after bonding without damaging the functional layer. For other donor wafer materials such as GaAs, Si or InP this is fairly trivial because selective wet etching processes of the substrate with respect to the functional layer, or an epitaxial etch-stop layer are known. For GaP, this is not the case with sufficient selectivity or off-the-shelf chemicals. Fortunately, GaP is resistant to concentrated hydrochloric acid, whereas AlGaP is not. Consequently, it is possible to use AlGaP as intermediary etch stop layer. Therefore, a selective dry etching recipe had to be developed that selectively etches GaP with respect to AlGaP. The donor wafer is then removed by first removing most of the GaP wafer by either a non-selective wet etch (*Transene GaP Etchant*) comprising KOH and $\text{K}_3\text{Fe}(\text{CN})_6$ heated to 80°C , or by mechanical grinding of the GaP. The latter offers the advantage that it is much more homogeneous than the former. Lately, a combination of both proved to be best. First, the GaP wafer is ground down to a thickness of $\sim 50\mu\text{m}$ to $\sim 70\mu\text{m}$, then, the layer is thinned down further to $\sim 20\mu\text{m}$ with the non-selective wet etch. The remaining GaP is removed in a selective dry etch. The AlGaP etch stop layer is then removed in concentrated HCl.

9.3.1 Selective Dry-Etching of Gallium Phosphide

Selective etching of GaP with respect to AlGaP is the crucial process step in reliably fabricating GaP thin films by DWB. Main requirements for such an etching process are a high selectivity with respect to the etch-stop layer as well as a high etch rate. The former is necessary to

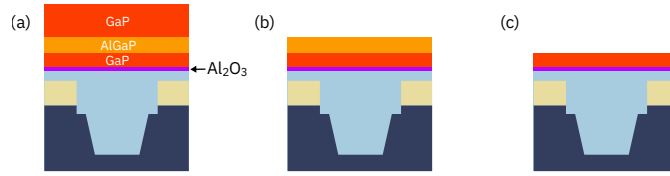


Figure 9.4: Removal of GaP donor wafer after DWB. Removal of GaP substrate (a) is carried out by combination of non-selective wet etch/mechanical grinding and a dry etch selective to AlGaP. AlGaP etch stop layer is then removed with concentrated HCl (b) to expose the GaP device layer (c).

compensate for any inhomogeneities in the thickness of the GaP that must be removed. These are typically $\sim 10\mu\text{m}$ to $\sim 30\mu\text{m}$ due to thickness variations introduced by the grinding process and by the subsequent wet etch. For an AlGaP etch stop layer with a thickness of $\sim 100\text{nm}$ this means that a selectivity $> 100 : 1$ is desirable. A high etch rate is preferable since a thickness of $\sim 20\mu\text{m}$ must be removed. In order to provide an efficient workflow an etch rate $> 1000\text{nm/min}$ is desirable. In previous work selectivities of 126:1 with respect to $\text{Al}_{0.6}\text{Ga}_{0.4}\text{P}$ [31] at an etch rate $< 100\text{nm/min}$ and 120:1 with respect to $\text{Al}_{0.36}\text{Ga}_{0.64}\text{P}$ [84] at an etch rate $\sim 270\text{nm/min}$ were achieved. In the scope of this work, a new process was introduced with a selectivity $> 1000 : 1$ with respect to $\text{Al}_{0.1}\text{Ga}_{0.9}\text{P}$ at an etch rate of $\sim 2800\text{nm/min}$ [51]. This new process provides some significant advantages compared to the one used previously in-house [84]. First, a much higher selectivity permits the use of a thinner AlGaP etch stop layer and provides a greater overall process tolerance. Second, the high etch rate – one order of magnitude higher than previously – significantly accelerates the GaP removal (etching in minutes instead of hours). Finally, the lower Al content of the etch stop layer significantly improves the quality of the GaP growth. As discussed in chapter 6, Al has a significantly lower surface mobility than Ga, which leads to a disparity of optimal growth conditions between GaP and AlGaP. If the Al content is kept low, both compounds can be grown at the same temperature with similar results and only minor adjustments of the growth parameters. The selective etching process is based on a mixture of SiCl_4 and SF_6 in an inductively-coupled plasma reactive ion etcher (ICP-RIE). The introduction of a fluorine species such as SF_6 is a typical procedure to achieve etching selectivity with respect to Al-containing compounds. The fluorine ions present in the plasma react with Al to form AlF_3 , a chemically stable, non-volatile compound, that forms a protective layer on-top of AlGaP, which prevents further chemical etching. The chlorine ions dissociated from SiCl_4 form GaCl_3 and $\text{PCl}_{3/5}$, volatile compounds that lead to the etching of GaP. Fluorine ions present in the plasma also accelerate the etching of GaP due to the formation of highly volatile $\text{PF}_{3/5}$ [51]. The process was optimized to maximize selectivity and etch rate using the design-of-experiments method with the commercial tool *JMP*. An empirical model was derived to describe the impact of the chamber pressure, ICP power, DC bias and molar fraction of SiCl_4 , f_{SiCl_4} . The etch rate of GaP and selectivity with respect to $\text{Al}_{0.1}\text{Ga}_{0.9}\text{P}$ as predicted by this model are shown in Figure 9.5 as a function of f_{SiCl_4} . An optimal selectivity is found at $f_{\text{SiCl}_4} = 60\%$, while a maximum etch rate of GaP is observed at $f_{\text{SiCl}_4} = 72\%$ [51]. Process parameters of the optimized etching recipe are listed in Table 9.1.

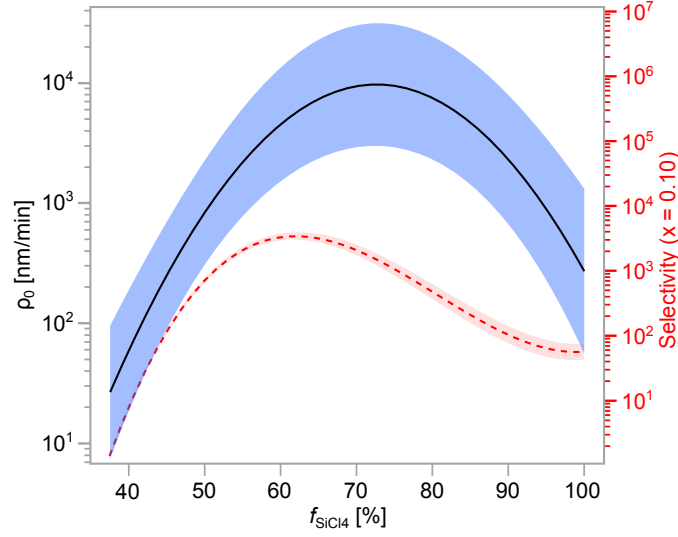


Figure 9.5: Etch rate ρ_0 of GaP and selectivity with respect to $\text{Al}_{0.1}\text{Ga}_{0.9}\text{P}$ (red dashed line) as a function of the molar fraction of SiCl_4 , f_{SiCl_4} in the gas mixture. Blue-shaded and red-shaded areas indicate 90 % confidence interval.

Table 9.1: Optimized process parameters for selective etching of GaP with respect to AlGaP.

SiCl_4 flow	SF_6 flow	DC bias	ICP power	Pressure
12.5 sccm	7.5 sccm	130 V	300 W	60 mTorr

It should be noted here that residues form during the process that condense on the etched surface once the plasma is turned off. This has two consequences. First, it is absolutely crucial that the etching is performed in one uninterrupted step, otherwise, the condensed residues lead to micro-masking of the surface in the subsequent etching. Second, the etched sample must be immersed in BHF immediately after etching to remove the residues. We observed in the past that an extended break between removal of the sample from the etcher and removal of the residues lead to crystallization which made it nearly impossible to remove the residues without damaging the underlying layers.

A device after wafer-bonding and removal of the donor wafer is shown in Figure 9.6. The GaP film is found to be bonded to the device without any voids.

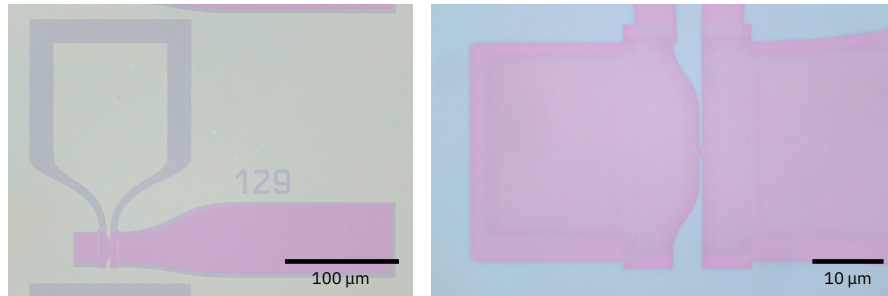


Figure 9.6: Device with bonded GaP film.

10 Fabrication of GaP Integrated Photonic Circuit

Once GaP is bonded and the donor wafer is removed, the crystalline thin-film can be patterned into a photonic circuit. This comprises the adiabatic fiber coupler, the photonic crystal and an integrated waveguide that connects the two.

10.1 Electron Beam Lithography

The integrated photonic circuit is patterned in a single EBL step with a HSQ hard-mask. HSQ exhibits poor adhesion directly on GaP. Therefore, a 3 nm SiO₂ adhesion layer is first deposited by atomic layer deposition. A 90 nm HSQ layer is applied by spin-coating. The pattern is then exposed with a 100 keV *Vistec EBPG 5200+* EBL pattern generator. Subsequently, the exposed resist is developed in a 3:1 solution of de-ionized water and AZ351B for 5 min. The SiO₂ adhesion layer is then etched with a CHF₃/O₂-based RIE process to expose the GaP device layer.

10.2 Device Etch

The photonic circuit is patterned into GaP with a chlorine-based ICP-RIE process [84]. The process is engineered to be directional and to open narrow holes in the photonic crystal design. Sidewalls are passivated during the etch with a combination of boron-containing species dissociated from BCl₃ and an organic compounds created from CH₄ that is present in the plasma. The process parameters are listed in Table 10.1 and an illustration of the process steps is shown in Figure 10.1. After the etching is completed, the passivation layer is removed with an O₂ plasma for 3 min at 600 W.

The remaining HSQ mask is removed with a brief dip in BHF. A device after removal of the HSQ is shown in Figure 10.2. Note that the sacrificial oxide that was deposited on-top of the Nb circuit with PECVD is also etched rapidly in HF. The color gradient that can be seen on the electrodes in the right panel of the figure is a consequence of the HF dip. A cross section along the axis of the photonic crystal is shown in panel (b) of Figure 10.3. The cross section reveals

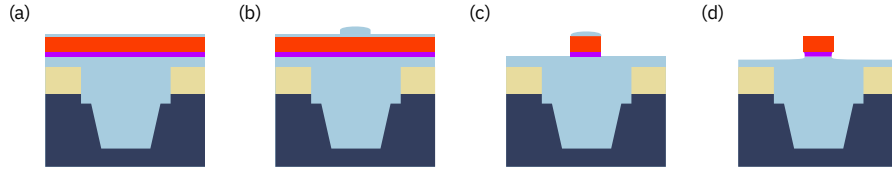


Figure 10.1: GaP photonic circuit fabrication. Deposition of SiO₂ adhesion layer (a), EBL with HSQ resist (b), adhesion layer breakthrough and GaP device etch (c) and HSQ removal with HF dip (d).

Table 10.1: Parameters of GaP device etch.

Process parameter	Value
Pressure	5 mTorr
Cl ₂ flow	10 sccm
BCl ₃ flow	10 sccm
CH ₄ flow	5 sccm
H ₂ flow	14.5 sccm
RF power	120 W
ICP power	200 W
DC bias	385 V

slightly tapered sidewalls inside the photonic crystal holes.

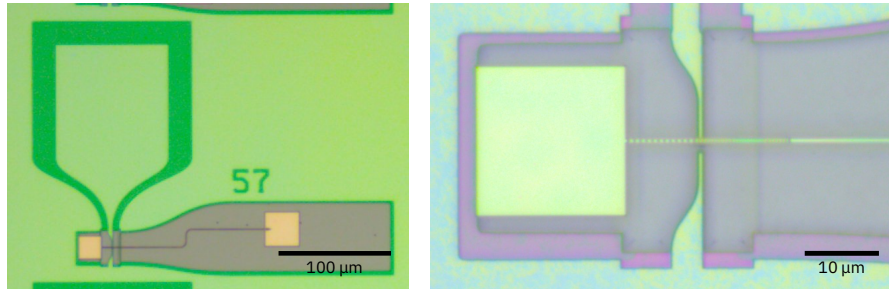


Figure 10.2: Device photonic crystal etched into GaP layer.

10.3 Device Release

The photonic crystal device must be free-standing to work according to design. This is achieved by removing the sacrificial SiO₂ layer from most of the chip with an etch in BHF. Only the photonic waveguide connecting the fiber coupler and the photonic crystal is masked with a photolithographic process (AZ1505 resist) for the release to isolate the optomechanical device from vibrations of the coupler and the tapered fiber. The masked part is indicated in Figure 10.3 (a) as white dashed box. During the release, adhesion of the photoresist to

both the substrate and the GaP waveguide is critical to prevent HF from creeping between a delaminated resist layer and the substrate. This can be best achieved by deposition of another 5 nm SiO₂ adhesion layer after removal of the HSQ. An additional hardbake at 130 °C after development of the photoresist is executed to further increase the layer adhesion. For the shown devices, only 1.5 μm SiO₂ were etched. Consequently, there is still SiO₂ left at the bottom of the Si pocket as the full thickness below the GaP layer is ~ 2.5 μm. This does not inhibit the function of the device. After the BHF etch the device must be treated with care, as freely suspended structures are sensitive to forces that arise from surface tension. When the chip is transferred from HF to water a droplet should cover the chip surface at all time. After a rinse in water, the chip is transferred to acetone to dissolve the photoresist. Then, the chip is transferred to IPA. From there, the chip can be carefully dried with a nitrogen flow at a grazing angle along the axis of the photonic crystal and coupler. This has proven to work best for the given devices. Other methods such as drying from a solvent with low surface tension (e.g. hexane) and critical point drying have proven less reliable. After release, a 5 nm Al₂O₃ layer is deposited by ALD as protective layer around the photonic crystal. This improves the long-term stability of the device and protects it from photo-induced oxidation.

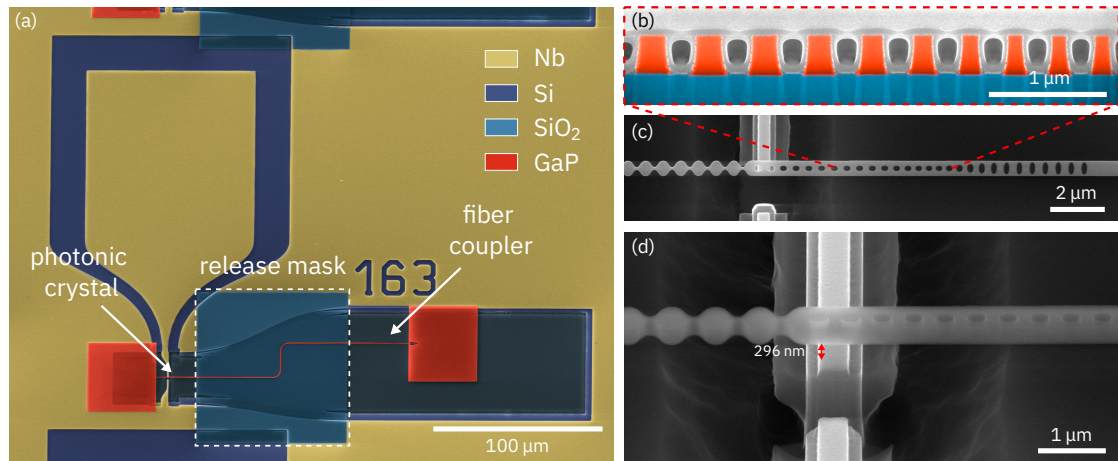


Figure 10.3: SEM micrographs of released photonic crystal device. Colorized overview image at 0° tilt (a), cross section prepared by focused ion beam milling through axis of photonic crystal (b) as illustrated in (c), gray area in image is Pt, blue area is SiO₂ and orange area is GaP. View tilted at 52° with indicated gap between electrode and photonic crystal (d).

10.4 Integration of Top Electrode

The electromechanical coupling in a GaP hybrid-optomechanical device can be optimized by fabricating a second electrode on-top of the photonic crystal as discussed in chapter 5 to realize a 'top-bottom' geometry. The process is laid out in Figure 10.4. Prior to release, a sacrificial SiO₂ layer is deposited (a), which is then planarized, e.g. by ion milling (b). A via is then etched with RIE to establish contact to the bottom Nb layer (c). Then, the top Nb contact

is structured as described in section 7.3. In a first implementation shown in Figure 10.5, the

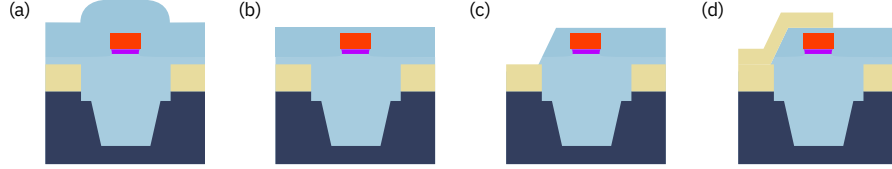


Figure 10.4: Integration of top electrode on GaP optomechanical device. Cladding of photonic circuit with SiO_2 (a), planarization (b), Etching of via to bottom Nb layer (c), deposition and patterning of top electrode (d).

SiO_2 layer was deposited by spin-coating the chip with FOx16 (HSQ) resist followed by rapid thermal annealing at 400°C for one hour, which cross-links the HSQ to a porous SiO_2 layer. The spin-coating process creates an a priori relatively flat topography over the photonic circuit. A via was then defined via EBL with a PMMA resist and etched with RIE. PMMA was chosen for its low selectivity in the RIE process, which allows the sidewalls of the via to be tapered, an important factor to ensure coverage of Nb throughout the via. Nb was then deposited and electrodes were defined with HSQ. The Nb was then etched as described above and the device was released in BHF. After release, a vacuum gap between the electrode pair and the photonic crystal is maintained, as shown by the parallax between the top view in panel (b) of Figure 10.5 and the view at a 52° angle shown in panel (c). A few aspects and areas of improvement are

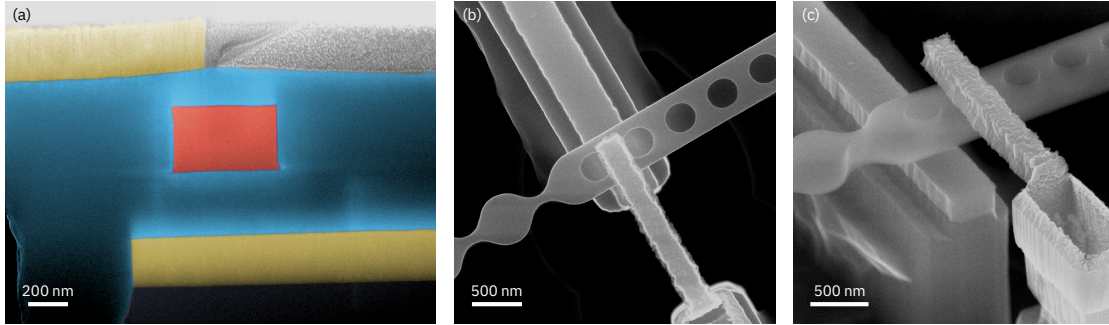


Figure 10.5: SEM micrographs of optomechanical device with top-bottom design. Color coding is analogous to Figure 10.3. Cross section orthogonal to photonic crystal axis (a). Top (b) and side (c) view of electrode pair.

worth highlighting here. First, the dimensions of the via should be chosen larger for future devices, since the RIE etch experiences severe RIE lag for a via with such high aspect ratio. Due to the relatively thick dielectric interlayer, the via has a depth of $\sim 750\text{ nm}$ in this case, whereas the via was designed with a width of only 550 nm . In addition, nearly $1\text{ }\mu\text{m}$ PMMA was used to create a tapered via, which results in an overall aspect ratio > 3 with a very narrow opening. Second, a shallower sidewall angle should be chosen for the via, since a continuous coating with Nb was achieved, but the Nb could not be removed completely from the via sidewalls, as the Nb etch is very directional, creating a 'funnel' shape as shown in Figure 10.5 (c). Finally,

despite the fact that both top and bottom electrodes were designed with the same lateral dimensions, the top electrode is significantly narrower. This can be attributed to the fact that the top electrode is fabricated on SiO_2 instead of Si. SiO_2 has a very high resistance to the etching process and does not react with the chlorine ions in the plasma. Consequently, once the etching of Nb is complete, ions from the plasma are reflected from the SiO_2 surface and impinge upon the sidewalls of the Nb electrode, undercutting the mask. For future devices this effect should be taken into account, either by considering a top electrode with increased design width or by optimizing the Nb etching process.

**Classical Microwave-to-Optical
Transduction in a Gallium Phosphide
Optomechanical Device**

Part IV

11 Experimental Setup

In this chapter I will present the optical setup used for the characterization of the optomechanical transducer.

11.1 Setup for Microwave-to-optical Transduction

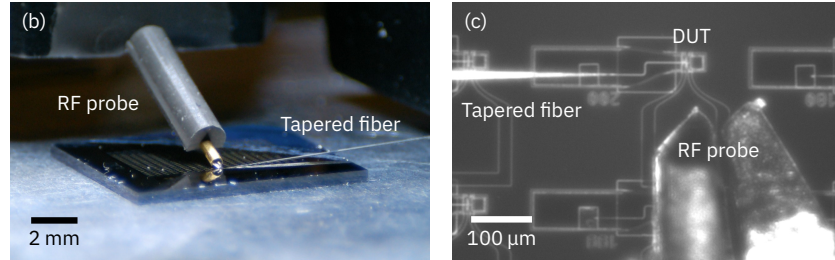
The setup configuration for microwave-to-optical transduction is shown in Figure 11.1 (a).

11.1.1 Broadband Optical Spectroscopy

For broadband optical spectroscopy of the device, the light produced by the external cavity diode laser (ECDL, Photonetics Tunic Plus) is routed through a Yenista CT400 passive component tester, which measures output power and wavelength of the laser. The light is then sent through a variable optical attenuator (Thorlabs EVOA 1550F) and subsequently through a fiber-optic beam splitter that taps 50 % of the optical power to an optical power meter (Thorlabs S154C+PM102U) for continuous measurement of the device input power. The optical signal is then sent through a circulator (Thorlabs 6015-3-APC) via a tapered optical fiber to the device under test (DUT). The reflected light is sent through the output port of the circulator through a series of FBT splitters (-13 dB) to the photoreceiver of the CT400. The component tester produces a broadband scan $\lambda \pm 15$ nm with a resolution of $\Delta\lambda = 2$ pm, which is sufficient to locate the resonance of the localized optical mode of the photonic crystal.

11.1.2 Optical Alignment

A tapered fiber is used for coupling between the fiber-optic measurement setup and the integrated photonic circuit. It is aligned using a SmarAct 3-axis slip-stick piezo positioning system (SLC-1780-D-S-HV, SLC-1750-D-S-HV, SHL-20N-10-S-HV). The fiber is first aligned via two alignment microscopes – one from the top for positioning along x- and y direction, and one from the side for positioning along z. When the fiber is not coupled to the waveguide,



(11.1)

11.1.3 Narrowband Optical Spectroscopy

Once the optical resonance is found, a high-resolution wavelength scan is performed by stepping the wavelength of the ECDL with $\Delta\lambda = 0.5$ pm steps. The reflected power is measured by power meter 1. The optical input power is reduced with the VOA until no thermal shift of the optical resonance is observed.

11.1.4 Measurement of Thermomechanical Noise Spectrum

For the measurement of the thermomechanical spectrum the laser is detuned from resonance on either the blue ($\lambda < \lambda_0$), or the red side ($\lambda > \lambda_0$). 90 % of the reflected light is then sent through an erbium-doped fiber amplifier (JDS uniphase MAP EDFA). The amplified signal is then filtered with an optical bandpass filter (DiCon SCD-0124C) with 0.8 nm bandwidth to suppress the amplified spontaneous emission of the EDFA. Following the bandpass filter, 10 % of the signal are split between an optical spectrum analyzer, which is used to center the pass-band of the bandpass filter around the laser wavelength, and power meter 3, which is used to monitor the EDFA output power. 90 % of the amplified signal are sent to the JDS uniphase RX10 fast photoreceiver with 10 GHz bandwidth. The output signal of the photoreceiver is then sent to an electrical spectrum analyzer (ESA).

11.1.5 Phase Modulator Calibration

Calibrated measurements of the optomechanical coupling and the microwave-to-optical transduction efficiency requires an independently calibrated phase-reference. Here, a lithium niobate phase modulator (Thorlabs LN65S-FC) is used to produce the reference signal with known modulation depth. In order to precisely calibrate the modulation depth of the modulator

$$\phi_0 = \frac{V_{pp}\pi}{2V_\pi}, \quad (11.2)$$

where V_{pp} is the applied peak-to-peak RF voltage, the half-wave voltage V_π must be determined. We follow a simple procedure to determine the half-wave voltage: The phase-

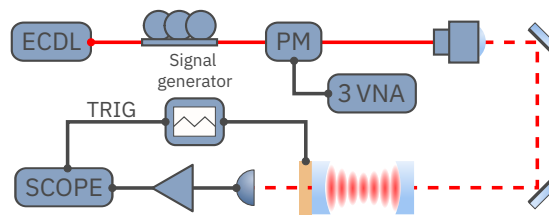


Figure 11.2: Setup for half-wave voltage calibration of phase modulator.

modulator is driven at various input RF power. The signal is then coupled to free-space, indicated in Figure 11.2 as dashed red line, and coupled into a scanning Fabry-Pérot cavity (Thorlabs SA210-12B) with a free spectral range of 10 GHz. The cavity length is then tuned

Chapter 11. Experimental Setup

with a triangle voltage from a signal generator (Thorlabs SA201) which separates the carrier tone from the sidebands. The transmission of the cavity is then observed on a fast scope that is synchronized with the signal generator. From the cavity transmission, the carrier and sideband amplitudes can be extracted and fit to the first sideband ratio

$$\rho_{\text{sb}} = \frac{P_{\text{sb},1}}{P_{\text{car}}} = \frac{J_1(\phi_0)^2}{J_0(\phi_0)^2}, \quad (11.3)$$

where $J_{0,1}$ are Bessel functions of the first kind. The phase modulator was characterized over a wide frequency range from 1 GHz to 19 GHz at a wavelength of $\lambda = 1550$ nm to determine the frequency-dependent V_π . The measured V_π was fit to a linear function

$$V_\pi(\Omega) = V_{\pi,0} + \delta V_\pi \frac{\Omega}{2\pi} \quad (11.4)$$

with $V_{\pi,0} = 4.382$ V and $\delta V_\pi = 0.221$ V/GHz. The oscillations of V_π over this wide frequency

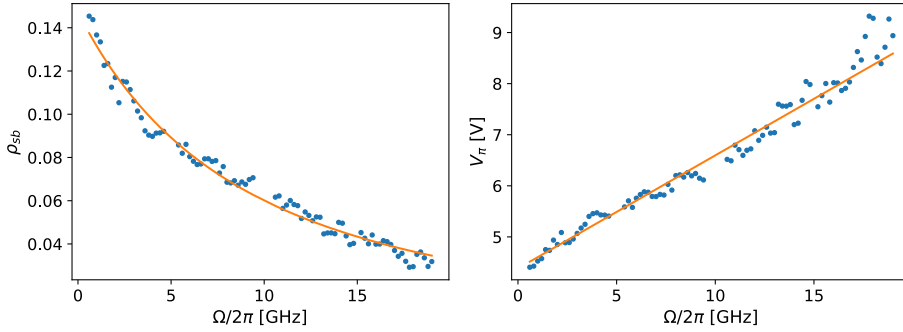


Figure 11.3: First sideband ratio (left) at a modulation power of 10 mW and corresponding V_π as function of modulation frequency Ω .

range are typically ascribed to acoustic resonances in the modulator driven by the piezoelectric effect of lithium niobate. These oscillations are also visible in the measured cavity response (cf. Figure 13.8).

11.1.6 Dynamical Backaction

For dynamical backaction measurements, the RF output of the RX10 photoreceiver is switched from the ESA to port 2 of a Keysight PNA-X vector network analyzer (VNA). The probe sidebands for the observation of OMIA and OMIT are produced by the phase modulator driven by port 3 of the VNA.

11.1.7 Microwave-to-Optical Transduction

For microwave-to-optical transduction measurements, a similar setup to that used for dynamical backaction measurements is used. A Picoprobe 40A ground-signal (GS) microwave probe

11.1. Setup for Microwave-to-optical Transduction

with 10 GHz bandwidth is used to contact the device's microwave port. The device is driven with port 2 of the VNA. The phase reference for signal calibration is again created with the a phase modulator on the input side of the optomechanical device that is driven via port 3 of the VNA.

12 Cavity Optomechanics

12.1 Optical Spectroscopy

The optical resonance is characterized as described in section 11.1. A coupling coefficient $\eta_c = \frac{\kappa_{\text{ex}}}{\kappa} = 0.383$, a loaded quality factor $Q_l = 67,300$ and an intrinsic quality factor $Q_i = 109,000$ at a resonance frequency $\omega_0/2\pi = 196.46 \text{ THz}$ ($\lambda_0 = 1525.97 \text{ nm}$) are calculated from the fit shown in Figure 12.1 (a) to the normalized cavity reflection (see [6])

$$\mathcal{R} = \frac{(\kappa_0 - \kappa_{\text{ex}})/2 - i\Delta}{(\kappa_0 + \kappa_{\text{ex}})/2 - i\Delta}. \quad (12.1)$$

The most noteworthy aspect of the spectrum is the severe blue-shift of over 3 THz compared to the simulated resonance at 193.17 THz. We consistently observe this with photonic crystal cavities, relatively independent of the design, which might either suggest that the literature value of the refractive index of GaP does not match our material (with a discrepancy $\sim 2\%$), or that deviations in the device dimensions with the current etching process have a more significant impact on the optical resonance than expected. Regarding the coupling coefficient, it is usually not possible to infer the coupling coefficient at a fixed coupling with a measurement of the power alone, as one can obtain the same spectrum for an overcoupled and an undercoupled case. However, in this case, the resonance was measured multiple times over the course of many measurements and a decrease in the quality factor was observed. Fits to the respective reflection spectra are shown in Figure 12.1 (b) – instead of the actual data for improved visibility – and it is clear that the extinction decreases with every measurement. This is a clear sign that the cavity was initially very close to critically coupled, and became undercoupled as the quality factor decreased. Additionally, a shift of the resonance frequency of several gigahertz was observed. This is problematic as the detuning may shift over the course of a measurement. The detuning was therefore determined before and after each measurement to ensure consistent results. Frequency shift and quality factor for the measurements shown in Figure 12.1 (b) are shown in (c) and (d).

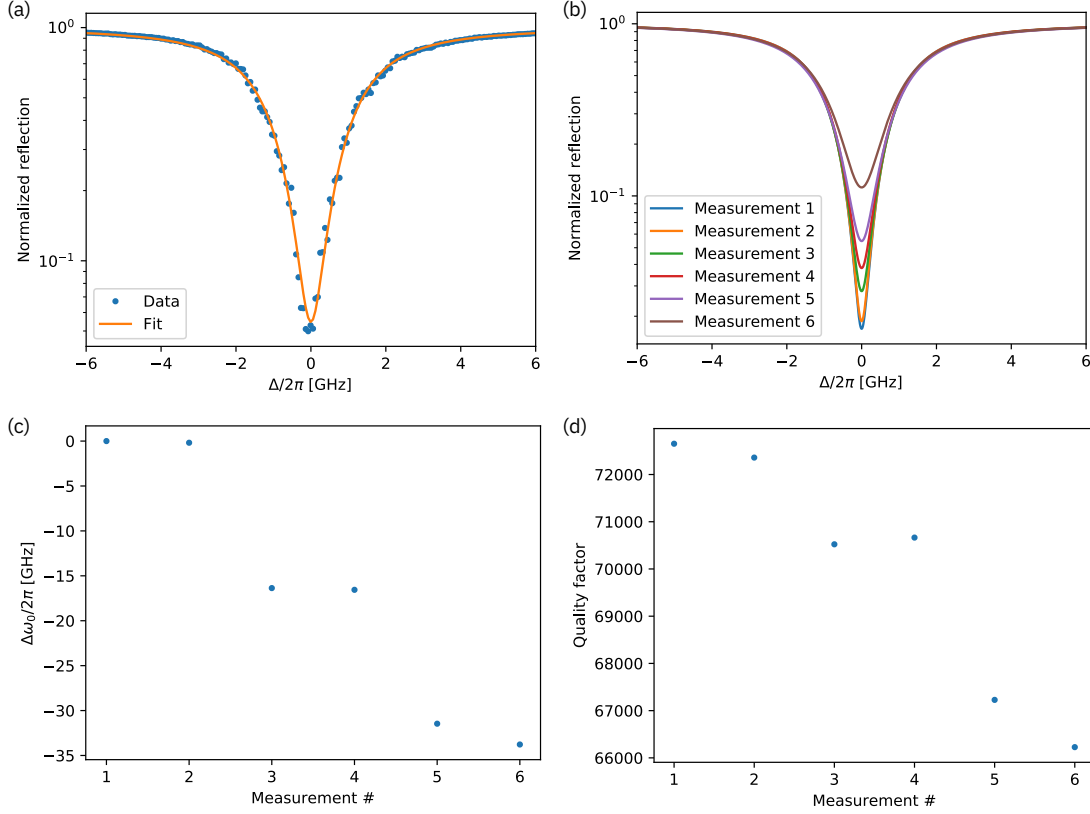


Figure 12.1: Optical cavity resonance measured at low optical power. Data representative of the cavity condition during subsequent measurements with resonance fit is shown in (a). Cavity resonance fits over several measurements (b) reveal a frequency shift (c) and a decrease of the optical quality factor (d).

12.2 Determination of the Vacuum Optomechanical Coupling Rate via a Noise Calibration Measurement

As described in section 3.6 the most accurate way to determine the vacuum optomechanical coupling rate in this case is a noise calibration measurement. This is achieved by weakly modulating the optical pump tone with a known modulation depth at a fixed frequency. The vacuum optomechanical coupling rate g_0 can then be inferred from the resulting spectrum recorded as the output voltage noise spectral density $S_V(\Omega)$ of the photoreceiver with Equation 3.60. It is vital to perform this measurement in the low-cooperativity regime, such that dynamical backaction effects such as cooling or amplification of the mechanical resonator are negligible, and the prerequisite of the fluctuation-dissipation theorem, i.e. that the oscillator is in thermal equilibrium, is fulfilled. In other words it is important to perform the measurement at low power. In order to satisfy this requirement we record the thermal noise spectrum at an optical input power of $P_{\text{in}} = 130 \text{ nW}$, close to our detection threshold for the thermal noise spectrum.

12.2. Determination of the Vacuum Optomechanical Coupling Rate via a Noise Calibration Measurement

We can extract $S_V^{\text{meas}}(\Omega_m)$ and Γ_m by fitting the thermal noise spectrum (without the calibration tone peak) with a sum of Lorentzians for the individual peaks.

Given the high signal-to-noise ratio of this comparatively strong peak, it is justified to extract $S_V^{\text{meas}}(\Omega_{\text{mod}})$ from the resulting spectrum as the peak value of the recorded calibration tone. The effective noise bandwidth (ENBW) can be calculated from the resolution bandwidth of the Gaussian filter used by the electrical spectrum analyzer in this measurement $\text{RBW} = 10 \text{ kHz}$ via the relation

$$\text{ENBW}_{\text{Gauss}} = \frac{1}{2} \sqrt{\frac{\pi}{\ln(2)}} \text{RBW}_{\text{Gauss}} \quad (12.2)$$

as the effective noise bandwidth is defined as the equivalent bandwidth of a rectangular filter function with the same area as the used filter function, whereas the resolution bandwidth (RBW) is defined by the 3 dB-bandwidth (full width at half maximum) of the filter.

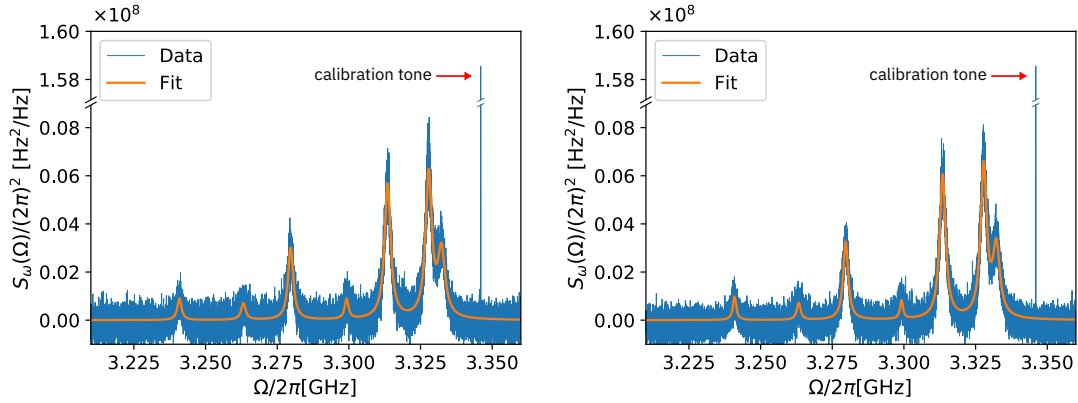


Figure 12.2: Symmetrized frequency noise spectral density $S_\omega(\Omega)$ showing the thermal noise spectrum (blue) recorded at red (left) and blue (right) pump detuning and Lorentzian fit of the mechanical modes (orange).

We measure the thermomechanical spectrum for a blue-detuned pump as well as a red-detuned pump to verify that dynamical backaction is negligible. The extracted g_0 for the four main resonances in Figure 12.2 is shown in Table 12.1. Note that technical noise for the data shown in Figure 12.2 was measured at large optical detuning and subtracted from the measured noise spectrum. Due to an increased reflected power off resonance the calibration spectrum features an increased shot-noise level, and hence the noise floor of the corrected data is slightly negative.

We can find a rough estimation of the effect of dynamical backaction using the values in Table 12.1 to convince ourselves that the effect is negligible in this case. With $\kappa/2\pi = 2.92 \text{ GHz}$, $\kappa_{\text{ex}}/2\pi = 1.12 \text{ GHz}$ and $\Delta/2\pi = -2.70 \text{ GHz}$ (in the red-detuned case) we find in this case a maximum cooperativity of $\mathcal{C} = n_{\text{cav}} \frac{4g_0^2}{\kappa\Gamma} = 6.92 \times 10^{-3}$. In the resolved sideband regime we find an additional backaction cooling of $\Gamma_{\text{opt}} \approx \mathcal{C}\Gamma_m$ [6] (given that $\Delta \approx -\Omega_m$), introducing an acceptable error on Γ_m due to dynamical backaction of $\mathcal{O}(1\%)$, which is consistent with the systematic difference between the values of the red-detuned, and the blue-detuned case.

Table 12.1: Vacuum optomechanical coupling rates g_0 extracted from the measurement shown in Figure 12.2

$\Omega_m/2\pi$	$g_{0,\text{red}}/2\pi$	$g_{0,\text{blue}}/2\pi$
3.280 GHz	$189.5\text{ kHz} \pm 0.8\text{ kHz}$	$193\text{ kHz} \pm 0.8\text{ kHz}$
3.314 GHz	$281.2\text{ kHz} \pm 0.6\text{ kHz}$	$284.7\text{ kHz} \pm 0.6\text{ kHz}$
3.328 GHz	$290.9\text{ kHz} \pm 0.7\text{ kHz}$	$294.4\text{ kHz} \pm 0.7\text{ kHz}$
3.332 GHz	$211.7\text{ kHz} \pm 1.0\text{ kHz}$	$215.1\text{ kHz} \pm 1.0\text{ kHz}$

12.3 Dynamical Backaction

Besides the determination of the vacuum optomechanical coupling rates via a calibrated noise spectrum, the optomechanical coupling in the device was also observed via coherent dynamical backaction to a weak optical probe field. To that end, the cavity was driven at blue and red optical detuning to observe optomechanically induced absorption (OMIA) and optomechanically induced transparency (OMIT), respectively.

12.3.1 Optomechanically Induced Absorption

Optomechanically-induced absorption (OMIA) can be observed for a blue-detuned pump $\Delta \approx \Omega_m$ in the regime of high cooperativity $0 \ll \mathcal{C} < 1$. At $\mathcal{C} > 1$ the device enters the parametric-instability regime. For the devices presented here, this regime is particularly attractive because it is very easily accessible. Residual absorption in the bulk gallium phosphide and/or at the dielectric-air interface via sub-bandgap electronic states leads to a heating of the device which causes a thermorefractive red-shift of the optical frequency. At sufficient power to observe an appreciable backaction effect at room-temperature this leads to an instability of the cavity when pumped at red detuning. At blue detuning however, the device enters a 'thermal lock' where fluctuations of the optical power have less influence on the cavity detuning. Consequently, the optomechanical system can be driven at arbitrary cooperativities and above the parametric-instability threshold. A typical cavity spectrum displaying the OMIA feature is shown in Figure 12.3 (a) with a close-up in (b). The cavity transmission was fit according to Equation 3.41 with a frequency-dependent, separately calibrated modulation depth ϕ_0 (cf. Figure 11.3). Oscillations in the cavity response that are not reflected in the fit are due to acoustic resonances in the phase modulator. It should be noted that the dispersive OMIA feature was not considered for the broadband fit of the cavity detuning. As the dispersive effect of the OMIA feature is very frequency specific and has no influence on the broadband cavity transmission, this is a justified approximation to obtain a stable initial fit. Once the cavity linewidth and detuning are determined, a narrow fit around the mechanical frequency is analyzed (cf. Figure 12.3(b)). In this fit, κ is kept constant, but Δ is kept as a fit parameter, since, as discussed in section 12.1, the detuning is time-dependent due to the drift of the cavity

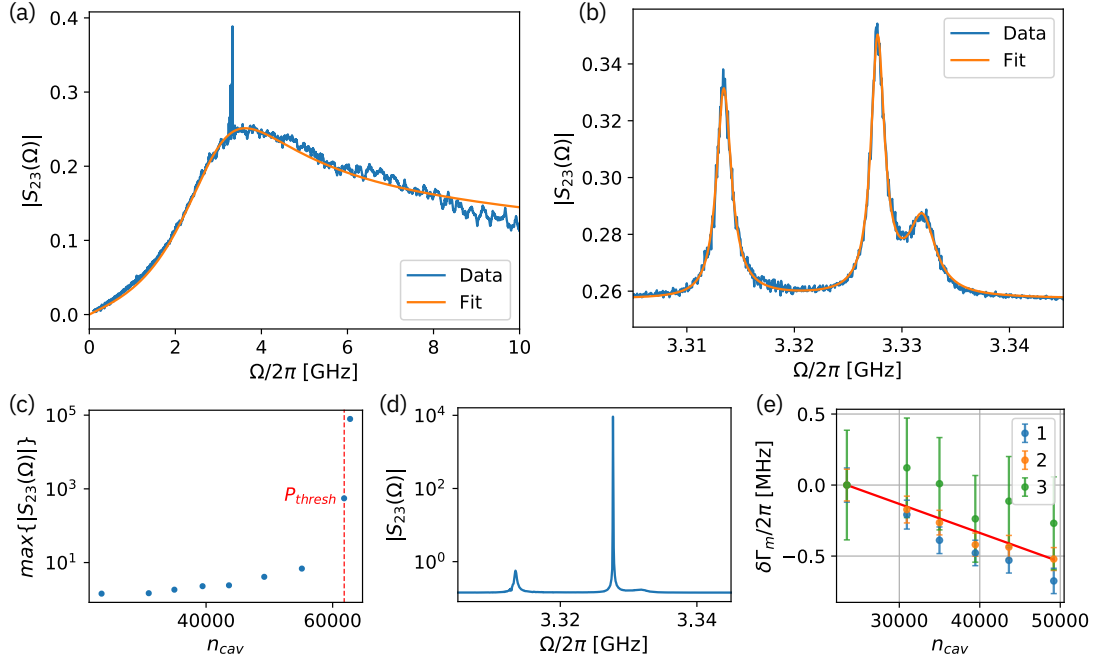


Figure 12.3: Optomechanically induced absorption. (a) Broadband cavity response, (b) dispersive OMIA feature ((a,b) for cooperativity of mode 2 $\mathcal{C} \approx 0.425$), (c) Peak cavity transmission at mode 2 as function of intracavity photon number n_{cav} with threshold for parametric instability indicated as red-dashed line, (d) dispersive OMIA feature of cavity transmission above threshold for parametric instability, (e) shift of mechanical linewidth $\delta\Gamma_m$ due to optomechanical antidamping as function of intracavity photon number n_{cav} for mechanical modes shown in (b) with Equation 12.4 indicated as red line.

resonance. From the fit parameters, the intracavity photon number is inferred as

$$n_{\text{cav}} = P_{\text{in}} \alpha_{\text{IL}} \frac{1}{\hbar \omega_L} \frac{\eta_c \kappa}{\kappa^2/4 + \Delta^2} \quad (12.3)$$

with the input power at the tapered fiber P_{in} and the insertion loss of the tapered fiber to the photonic crystal α_{IL} . It should be noted here that α_{IL} is determined prior to and after the measurement with the laser detuned from the optical resonance by 1 nm, as the reflection close to the optical resonance is determined by the cavity extinction, whereas far off-resonance the photonic crystal can be assumed to be a nearly perfect mirror. This leads to a significant uncertainty in the cavity photon occupation as the insertion loss cannot be monitored simultaneously. However, we can obtain a rough estimate of $g_0 = g/\sqrt{n_{\text{cav}}}$ where g is a fit parameter of Equation 3.42. The extracted coupling rates are shown in column three of Table 12.2. The coupling rates determined in this manner deviate from the values determined by noise calibration by roughly a factor of two. This exceeds the uncertainty that is inferred from that of the insertion loss and the fit parameter variance inferred from the least-squares fit – the 2σ interval of the combined uncertainty is indicated in Table 12.2 as \pm – which might indicate a

systematic error in one of the methods. However, since the noise calibration measurement does not depend on the precise measurement of n_{cav} and does not require a fit with many free parameters, the g_0 derived in this fashion can be assumed to be more reliable. I also note here that the diode laser which was used in this experiment shows a substantial amount of phase noise with oscillations of the laser frequency of ~ 200 MHz, which also leads to an instability of the optical detuning and might present a further source of substantial uncertainty.

The threshold for parametric instability for mode 2 in Equation 3.42 was found to be at $n_{\text{cav}} \approx 61,800$, as indicated in Figure 12.3 (c) by the red dashed line. The cavity transmission above threshold is shown in Figure 12.3 (e). We infer $g_0/2\pi = \sqrt{\mathcal{C} \frac{\kappa \Gamma_m}{4n_{\text{cav}}}}/2\pi \approx 176$ kHz for $\mathcal{C} = 1$ at threshold. Optomechanical anti-damping due to dynamical backaction is also a characteristic of a blue-detuned optomechanical system [6] and can be described via the formula

$$\delta\Gamma_m = g^2 \frac{\omega_m}{\omega} \left(\frac{\kappa}{(\Delta + \omega)^2 + \kappa^2/4} - \frac{\kappa}{(\Delta - \omega)^2 + \kappa^2/4} \right), \quad (12.4)$$

The results for $\delta\Gamma_m$ for the three modes shown in (b) (where 1 corresponds to the lowest frequency mode and 3 to the highest frequency mode) is shown in Figure 12.3 (e). The red line indicates the theoretical prediction from Equation 12.4 which agrees well with the measured mechanical linewidth narrowing.

12.3.2 Optomechanically Induced Transparency

The complementary effect to OMIA, optomechanically induced transparency (OMIT), is observed at red detuning with $\Delta \approx -\Omega_m$. As discussed in the previous section, our gallium phosphide photonic crystal cavities are notoriously unstable at red detuning and high optical power. It is therefore difficult to observe OMIT, as we are restricted to $\mathcal{C} \approx 0.03$. Nonetheless, the effect was clearly observed and the corresponding data is shown in Figure 12.4. The detuning was determined as in subsection 12.3.1 and the fit is shown in Figure 12.4(a). The dispersive feature is shown in panel (b) and the inferred g_0 are displayed in column two of Table 12.2. The results are in agreement with the values inferred from the OMIA measurement within the 2σ uncertainty interval. The excessive noise seen in Figure 12.4 (b) is due to the thermal instability of the cavity at red detuning, which leads, even below the point of bistability, to an increased slope of the optical response compared to the blue-detuned case and therefore to a higher sensitivity to the frequency instability of the laser.

Table 12.2: Vacuum optomechanical coupling rates g_0 extracted from optomechanically induced absorption and transparency measurements.

$\Omega_m/2\pi$	$g_{0,\text{OMIT}}/2\pi$	$g_{0,\text{OMIA}}/2\pi$
3.313 GHz	$108 \text{ kHz} \pm 25 \text{ kHz}$	$117 \text{ kHz} \pm 11 \text{ kHz}$
3.328 GHz	$98 \text{ kHz} \pm 23 \text{ kHz}$	$122 \text{ kHz} \pm 12 \text{ kHz}$
3.332 GHz	$100 \text{ kHz} \pm 24 \text{ kHz}$	$103 \text{ kHz} \pm 10 \text{ kHz}$

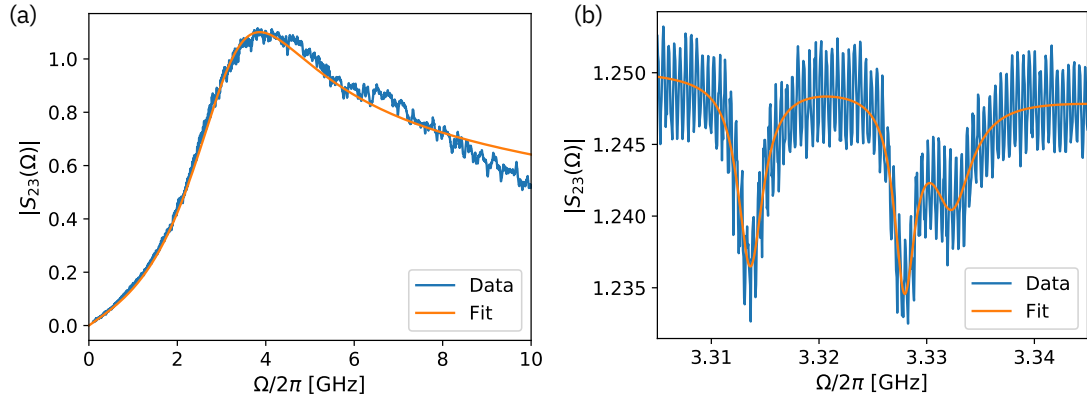


Figure 12.4: Optomechanically induced transparency. Broadband cavity response (a) with fit, and dispersive OMIT feature (b) with fit. (a,b) shown for cooperativity of mode 2 $\mathcal{C} \approx 0.022$.

13 Microwave-to-Optical Transduction

In this chapter, I will show results on classical microwave-to-optical transduction with the design that I introduced earlier. Even though these experiments are performed at room temperature, they still provide valuable insights into the behavior of the device with respect to its frequency response, transduction coherence and microwave coupling.

The setup used here was introduced earlier. As a first experiment, the optomechanical device is operated in the low-cooperativity limit (as before with $\mathcal{C} = 6.92 \times 10^{-3}$) with a red-detuned pump laser.

13.1 Microwave-to-Optical Transduction Spectrum

It is convenient to first analyze the microwave-to-optical signal qualitatively and form some initial conclusions on the spectral response. The microwave-to-optical spectrum is shown in Figure 13.1 (a) together with the thermomechanical noise spectrum in (b). For frequencies > 1 GHz the noise spectrum is dominated by the thermomechanical spectrum of the optomechanical device, which permits us to assign the peaks in the microwave-to-optical spectrum with the mechanical modes of the device that experience large optomechanical coupling. As expected, the transduction process in other parts of the spectrum is suppressed, as there are no strongly optomechanically coupled modes available to mediate the transduction process. Peaks in the thermomechanical spectrum at frequencies < 500 MHz correspond to noise introduced by the measurement setup or to flexural mechanical modes that are only weakly piezoelectrically coupled.

13.2 Continuous-Wave Transduction

The coherence of a transduced microwave tone can be investigated by first analyzing a continuous (CW) signal at a fixed frequency. The microwave tone is produced by the vector network analyzer at port 1. The transduced signal is then captured via the photoreceiver either using a spectrum analyzer (spectrum shown in Figure 13.2), or by the VNA receiver at port 2. In

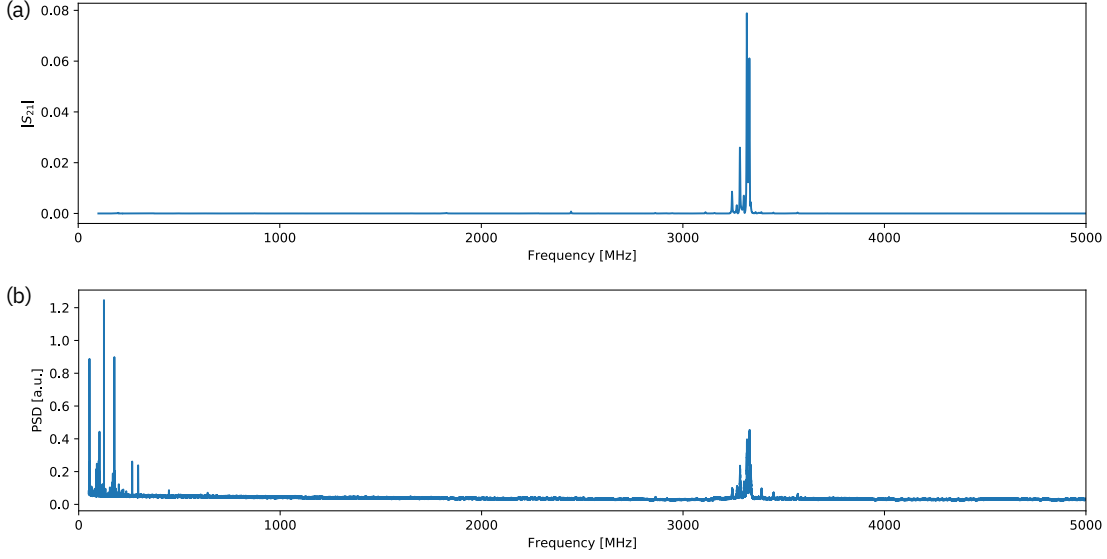


Figure 13.1: Absolute of microwave-to-optical transmission $|S_{21}|$ (a) and thermomechanical spectrum (b) of optomechanical device.

the latter case, the signal is demodulated using the output RF tone of the VNA as phase and amplitude reference. We choose the frequency of the mechanical mode at which we find the

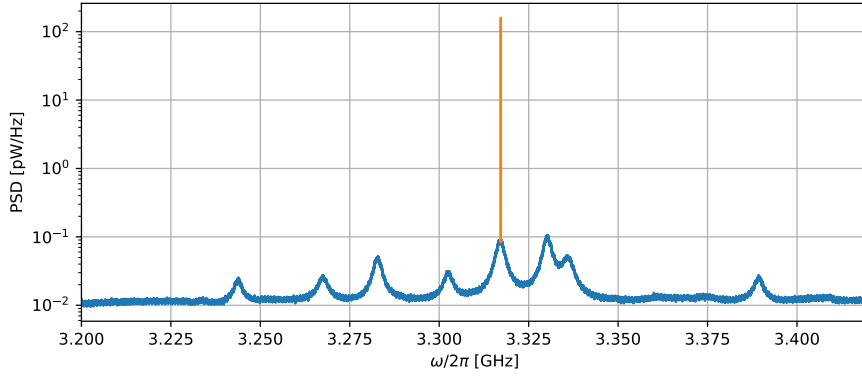


Figure 13.2: Thermomechanical noise spectrum (blue) with 100 μ W CW microwave tone applied at 3.317 GHz (orange).

greatest transduction efficiency at 3.317 GHz for the CW data presented here. The thermomechanical noise spectrum of the device is shown in Figure 13.2 in blue, the transduction sideband generated by the microwave tone applied to the device is highlighted in orange. The transduction tone amplifies the signal from the mechanical mode by ~ 33 dB compared to the thermomechanical signal at a microwave input power of 100 μ W. The transduction sideband therefore dominates the mechanical amplitude compared to thermal fluctuations.

A homodyne measurement of the transduced signal was then carried out with the VNA, illustrated in Figure 13.3 (b), where the demodulated signal is also filtered around the local

oscillator frequency, i.e. the microwave tone produced by the VNA, in this case 3.317 GHz with an IF bandwidth of 10 kHz as indicated in Figure 13.3 (a). For a coherent transduction we would therefore expect the demodulated signal to be a fix point in phase space with small fluctuations around the mean, given by the detection noise and the thermal fluctuations of the device. It is important to note that the VNA signal does not capture the full bandwidth of

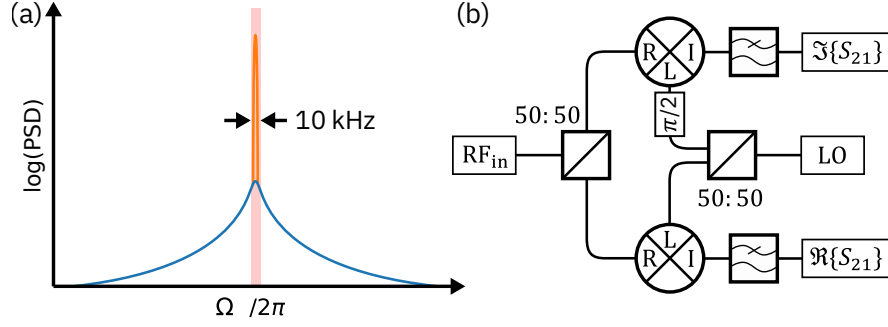


Figure 13.3: Illustration of IF-filtering of VNA (a) and simplified schematic of VNA-internal signal demodulation (b).

the thermal fluctuations, as the IF bandwidth is much smaller than the typical linewidth of the mechanical oscillator. We can therefore not calibrate the variance in phase space with the thermal energy of the oscillator, since that would require, following the fluctuation-dissipation theorem, to consider the full bandwidth of the fluctuations. The root-mean-square output voltage and its fluctuations as recorded by the VNA can be reconstructed from the scattering parameter $S_{21} = \frac{V_{out}}{V_{in}} = \frac{|V_{out}|}{|V_{in}|} e^{i \arg(S_{21})}$ as

$$V_{out} = S_{21} \cdot |V_{in}| = S_{21} \cdot \sqrt{P_{in} Z_0}, \quad (13.1)$$

where $Z_0 = 50 \Omega$ is the reference impedance and P_{in} is the power of the input microwave tone, in the rotating frame of the local oscillator with the phase $\arg(V_{out}) = \arg(S_{21})$ relative to the local oscillator phase. The reconstructed distribution of V_{out} recorded as a time trace with 100,000 points is shown in Figure 13.4 for a microwave input power of $P_{in} = 100 \text{ nW}$ (blue), $P_{in} = 1 \mu\text{W}$ (orange) and $P_{in} = 10 \mu\text{W}$ (green). All signals show a Gaussian distribution around the mean with a variance $\langle \Re\{V_{out}\}^2 \rangle = \langle \Im\{V_{out}\}^2 \rangle = 0.033 \text{ mV}^2$ for $P_{in} = -40 \text{ dBm}$ and $\langle \Re\{V_{out}\}^2 \rangle = \langle \Im\{V_{out}\}^2 \rangle = 0.032 \text{ mV}^2$ for $P_{in} = -20 \text{ dBm}$. The slightly higher variance at -40 dBm input power can be attributed to noise in the detection chain between the photoreceiver and the VNA. The mean values of the transduction, indicated by green arrows in Figure 13.4 show

$$\frac{|V_{out, -20 \text{ dBm}}|^2}{|V_{out, -40 \text{ dBm}}|^2} = 19.92 \text{ dB} \quad (13.2)$$

which indicates a linear increase of the output power with increased input power, as expected. Finally, the relative difference in the mean phase $\langle \phi \rangle = \arg(\langle V_{out} \rangle)$ is found to be

$$\frac{\Delta \phi}{2\pi} = \frac{|\langle \phi \rangle_{-40 \text{ dBm}} - \langle \phi \rangle_{-20 \text{ dBm}}|}{2\pi} \approx 2 \%. \quad (13.3)$$

For $P_{\text{in}} = -40 \text{ dBm} \rightarrow -30 \text{ dBm}$, we find

$$\frac{\Delta\phi}{2\pi} = \frac{|\langle\phi\rangle_{-40 \text{ dBm}} - \langle\phi\rangle_{-30 \text{ dBm}}|}{2\pi} < 0.1 \%. \quad (13.4)$$

Again, the larger deviation at the lower signal level can be attributed to noise in the detection chain from photoreceiver to VNA.

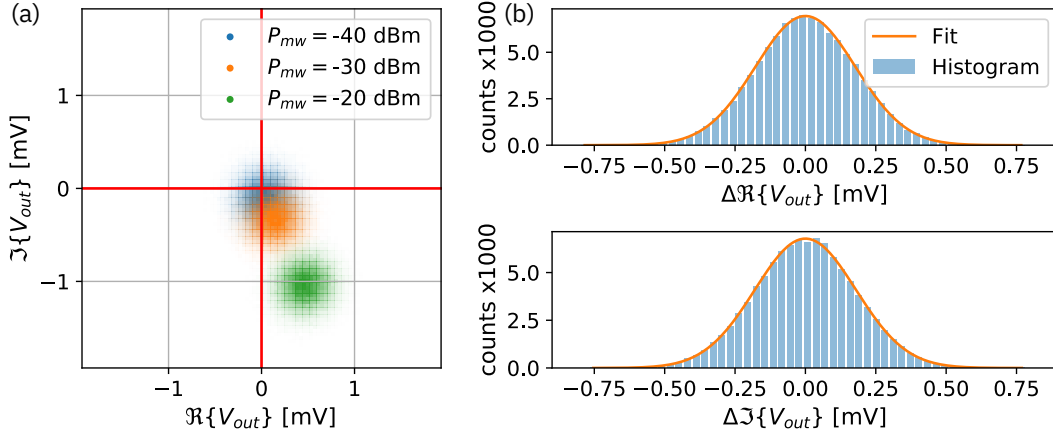


Figure 13.4: (a) Distributions of V_{out} for a various microwave input powers. (b) Noise distribution of -20 dBm -signal with Gaussian fit.

As expected for a coherent state, we find a Gaussian noise distribution around a mean value of the output voltage $\langle V_{\text{out}} \rangle$ which is fixed in phase space. Upon an increase of the drive amplitude $\langle V_{\text{in}} \rangle$, $\langle V_{\text{out}} \rangle$ is displaced linearly from the phase space origin at a fixed phase $\arg(\langle V_{\text{out}} \rangle)$ as shown in Figure 13.7. This is sufficient evidence that the transduction in this case is indeed, and as expected, a coherent process.

13.2.1 Nonlinear Behavior

In the previous section the transduction was shown to be linear up to a driving power of $10 \mu\text{W}$. Notably, the distribution of V_{out} was found to be symmetric and Gaussian around $\langle V_{\text{out}} \rangle$, as shown in Figure 13.4 on the right. If the microwave input power exceeds a threshold between $10 \mu\text{W}$ and $100 \mu\text{W}$ the noise distribution begins to become anisotropic. This effect is clearly visible in Figure 13.5 for drive powers exceeding $100 \mu\text{W}$. The anisotropy can be attributed to a nonlinear response of the mechanical oscillator. Besides the appearance of the phenomenon above a certain power threshold, this hypothesis is also supported by the fact that a nonlinear oscillator, such as a duffing oscillator, no longer follows a circular trajectory in phase space. Consequently, when the signal is demodulated with the local oscillator, which describes a circle in phase space, the resulting IF signal is no longer a pure DC signal, but in an oscillation at the mechanical frequency around the harmonic response. As the signal is sampled at a much lower rate than the oscillation frequency of the mechanical resonator, these oscillations

can not be resolved in time. It is important to note here that, despite the fact that the phase-space image of the transduced tone at high power bears a visual resemblance to a squeezed state, there is no squeezing present, as the variance of the signal is increased for all ϕ at high power. Although nonlinear phenomena are interesting in their own right, for the purpose of

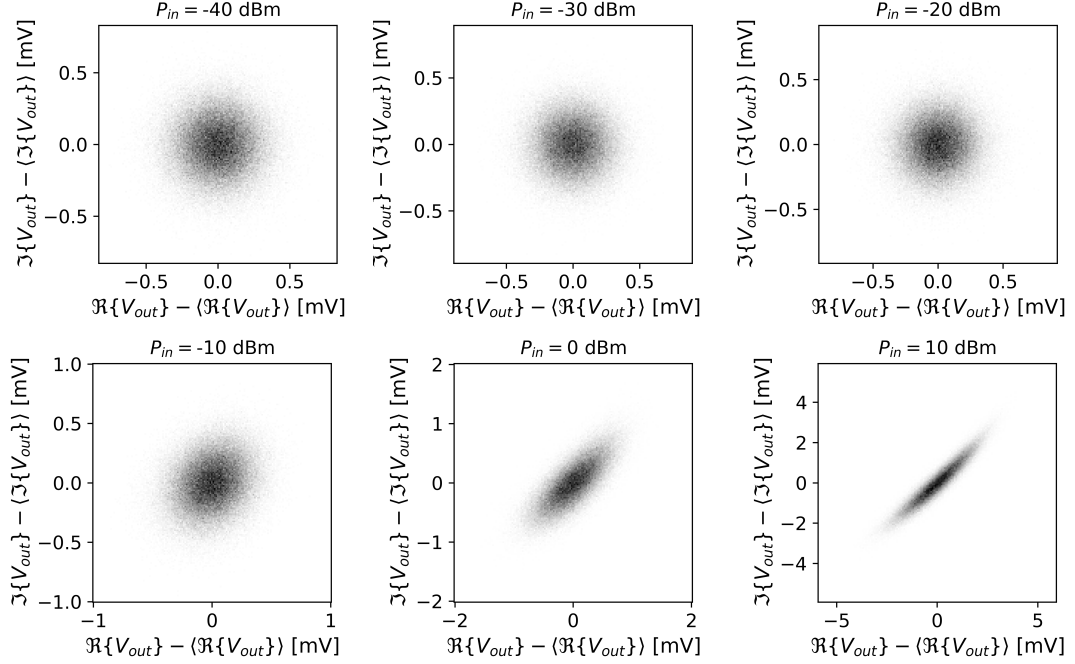


Figure 13.5: Noise distribution of transduced signal in phase space for various microwave drive powers.

microwave-to-optical transduction it is, in the scope of this work, beneficial to put this topic aside and merely find a threshold for the microwave power below which we may still observe a harmonic response. To that end, the signals at different powers were analyzed with respect to the variance $\langle \Re\{V_{out}\}^2 \rangle$ as a function of a phase rotation ϕ performed on the recorded data. As the signal is rotated in phase space, the variance is measured along the real axis, as indicated by the dashed line in Figure 13.6. The results are shown in Figure 13.7 on the right, the absolute of the mean value $|\langle V_{out} \rangle|$ is shown in the figure on the left. While the latter appears to be linear even for high power, it is clear that anisotropy associated with the nonlinear dynamics appears between $10 \mu\text{W}$ and $100 \mu\text{W}$. For $P_{in} \leq 10 \mu\text{W}$ the noise distribution is isotropic and we can assume a linear response. For optimal signal-to-noise ratio all measurements below were carried out for an input power of $10 \mu\text{W}$.

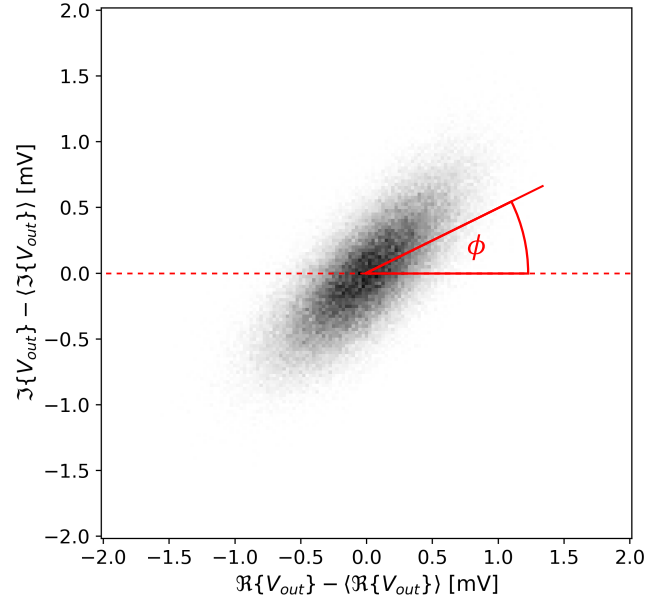


Figure 13.6: Designation of ϕ .

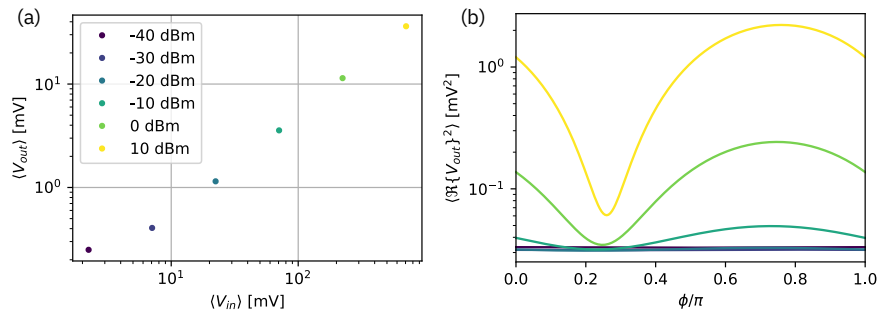


Figure 13.7: Mean output voltage as function of mean input voltage (a) and variance of output voltage measured along real axis over phase ϕ of the signal (b).

13.3 Transduction Calibration and Phase-Coherent Transduction Spectrum

The frequency response of the optomechanical device can give further insight about the mode structure and the microwave coupling of the photonic crystal. Especially, an identification of the experimentally observed modes with the simulated breathing modes is of interest. To that end, the device is now probed with a microwave tone that is swept across a frequency band from 3.22 GHz to 3.35 GHz and the scattering parameter S_{21} is recorded. The measurement configuration is shown in Figure 11.1.

13.3.1 Setup Calibration

Before proceeding to the transduction measurement, it is crucial to perform a calibration measurement of the optical path, to find the global gain factor Γ_D , that is determined by the optical loss in the beam path, amplification in the EDFA, and the optical carrier photon number $|\alpha_0|^2$. A phase-modulated input signal with a known modulation depth can be used to calibrate the signal on the photoreceiver, similar to the procedure used in section 12.2 for the calibration of the thermomechanical spectrum. Port 3 of the VNA is used to drive a lithium niobate phase modulator with a previously calibrated half-wave voltage (see Figure 11.3). We then record S_{23} , the transmission between the driving port of the phase modulator and the photoreceiver. In a first measurement, the broadband response of the cavity is recorded to determine the optical detuning Δ and the cavity linewidth κ . The coupling factor $\eta_c = \frac{\kappa_{\text{ex}}}{\kappa}$ was determined separately with optical spectroscopy. The broadband response is fit to $|S_{23}|$, with

$$S_{23}(\Omega) = \Gamma_D(A_0 A_+^*(\Omega) + A_-(\Omega) A_0^*) e^{-i\Omega\tau + \theta} \quad (13.5)$$

from equation Equation 3.30 where A_0 , A_+ , and A_- are from Equation 3.83. The respective calibration measurements and fits for the subsequent measurements are shown in Figure 13.8 for red detuning (a) and blue detuning (b).

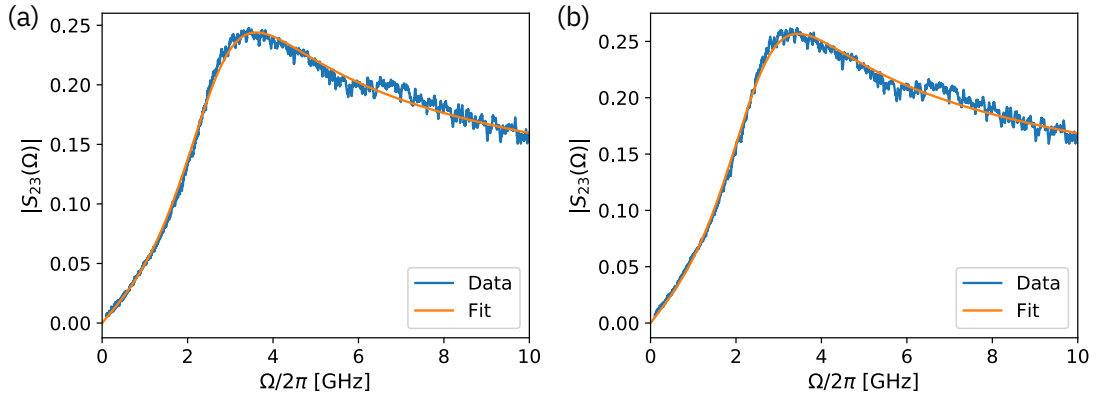


Figure 13.8: Transduction calibration Measurement for red (a) and blue (b) optical detuning.

13.3.2 Frequency Response – Red Detuning

Since this measurement only uses the optomechanical interaction as a readout of the mechanical motion, and the device is operated in the low-cooperativity regime, where dynamical backaction is negligible, as demonstrated by the calibration tone measurement (cf. Table 12.1), it is not critical if we choose blue, or red detuning. For the data shown in Figure 13.9, the laser was red-detuned with $\Delta/2\pi = -2.674$ GHz and the optical linewidth was determined as $\kappa/2\pi = 2.949$ GHz. S_{21} is fit in the complex plane in Cartesian coordinates, instead of directly fitting amplitude and phase of the signal in polar coordinates, since the phase as measured by the VNA is in transmission only well-defined for amplitudes appreciably larger than the signal-to-noise ratio. The measured amplitude and phase of the transduction spectrum is shown in Figure 13.9 on the left together with a fit to Equation 3.77. The model was expanded to a multimode model with eight independent mechanical resonances with individual phases $\phi_m \in \{0, \pi\}$ to account for the phase offset between the mechanical amplitude at the microwave port and the mechanical amplitude at the optical resonance. After fitting, the signal and fit were rotated by multiplication with $e^{-i(\Omega\tau+\theta)}$ to correct for the electronic delay and reveal the characteristic phase-space image of the device. A plot of the latter is shown in Figure 13.9 on the right. The typical circularly shaped spectrum in phase-space is characteristic for the

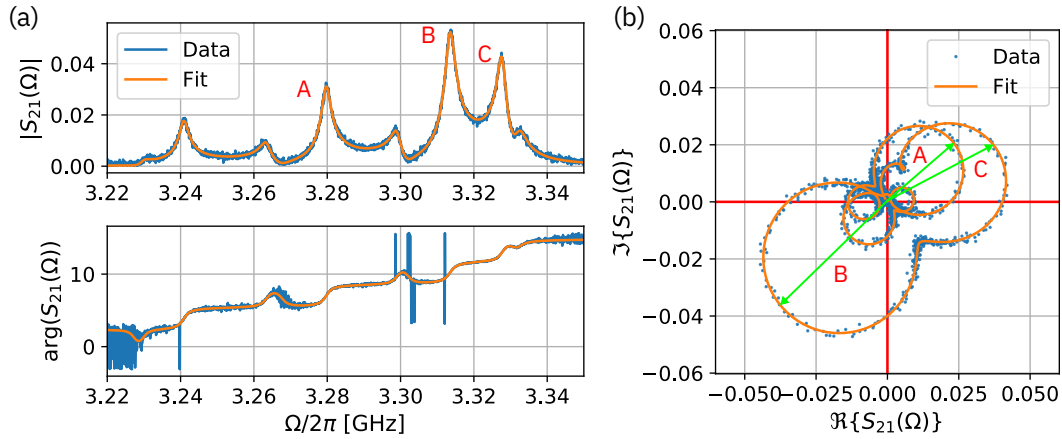


Figure 13.9: Amplitude and phase of microwave-to-optical transduction spectrum (a) and phase-space representation of data (b) with fit to Equation 3.77.

response of a harmonic oscillator. Three dominant mechanical resonances are found (A,B,C), the frequencies, damping and coupling rates of which are listed in Table 13.1. The phasors of the transduced signal at the respective mechanical frequencies are indicated in the right panel of Figure 13.9 as green arrows. The inspection of the phasors of the dominant modes permits to draw conclusions about the nature of the mechanical modes. From the finite-element simulations presented in chapter 5 we can infer that the only modes in this observed frequency range with appreciable coupling to both the microwave field and the optical field are breathing supermodes. From Figure 4.9 we can also infer that among the supermodes, some have an intrinsic phase offset of π between the antinode of the displacement field that couples strongly

13.3. Transduction Calibration and Phase-Coherent Transduction Spectrum

Table 13.1: Transduction fit results.

Mode	$\omega_m/2\pi$ [GHz]	$\Gamma_m/2\pi$ [MHz]	$g_0/2\pi$ [kHz]	$\Gamma_{ex}/2\pi$ [mHz]	ϕ_m [°]
A	3.280	2.562	189.5	2.327	0
B	3.313	2.842	281.2	3.756	π
C	3.328	2.544	211.7	1.712	0

to the microwave port and that which couples to the optical mode, while others have a phase offset of 0. Consequently, we would expect a relative phase offset between the signal that is transduced by the one group with respect to the other. We can identify the observed modes with the first three simulated modes shown in Figure 4.9, which exhibit qualitatively similar optomechanical, and electromechanical coupling. Note that there is an additional rotation of each resonance circle so that they do not appear exactly 180° out of phase. This is due to the response of the optical cavity, which produces a frequency dependent phase rotation of the optical output field. Deviations from the simulated values can be attributed to the sensitivity of the breathing supermodes to variations in the fabrication process, which is amplified by the flat phonon dispersion of the nanobeam waveguide.

13.3.3 Frequency Response – Blue Detuning

As stated above, the transduced signal should not depend on the sign of the detuning, as the signal is in either case given by Equation 3.77. We may verify this statement by analyzing the transduced signal in the blue-detuned case. Data for $\Delta/2\pi = 2.511$ GHz is shown in Figure 13.10. The measurement sequence was performed analogously to the red-detuned case, where the detuning fit is shown in the right panel of Figure 13.8. Amplitude and phase of the scattering parameter S_{21} are shown in the left panel of Figure 13.10 and the phase-space image in the right panel. The inferred values of the mechanical eigenfrequency, the damping and

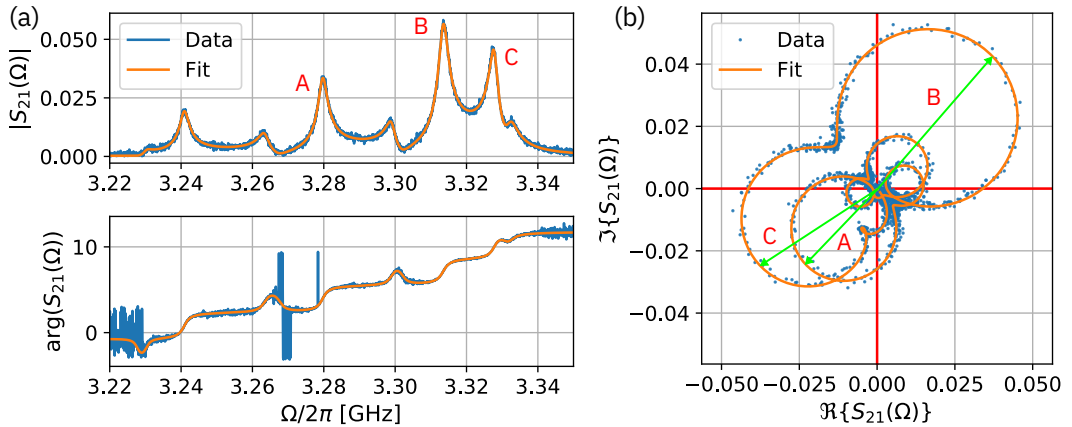


Figure 13.10: Amplitude and phase of microwave-to-optical transduction spectrum (a) and phase-space representation of data (b) with fit to Equation 3.77.

the electromechanical coupling as well as the mechanical phase are displayed in Table 13.2. The fit results agree nearly perfectly with the measurements at red detuning. Note that the

Table 13.2: Transduction fit results for blue detuning.

Mode	$\omega_m/2\pi$ [GHz]	$\Gamma_m/2\pi$ [MHz]	$g_0/2\pi$ [kHz]	$\Gamma_{ex}/2\pi$ [mHz]	ϕ_m [°]
A	3.280	2.562	189.5	2.327	0
B	3.313	2.842	281.2	3.756	π
C	3.328	2.544	290.9	1.712	0

phase-space image shown in panel (d) of Figure 13.10 corresponds exactly to the one shown in Figure 13.9 on the right, with a phase offset. The rotation is due to the arbitrary absolute phase offset θ which depends on the conditions of the detection path and is independent of the device itself.

13.3.4 Inference of the Electromechanical Coupling Rate

Given that the global gain factor Γ_D and the optomechanical coupling rates were determined in separate measurements, the mechanical amplitude β can be inferred and, with knowledge of the input field $\beta_{in} = V_0 e^{-i\omega t}$, the electromechanical coupling rate Γ_{ex} can be inferred. For each detuning, g_0 was determined with a separate noise calibration measurement shown in Figure 12.2. The experimental values of Γ_{ex} listed in Table 13.1 and Table 13.2 are found to be significantly smaller than the coupling rates calculated from the FEM simulations presented in chapter 5. A possible explanation for the smaller coupling is the presence of charge states at the dielectric interface between GaP and air that might partially screen the electric field inside the photonic crystal nanobeam. A more detailed analysis with GaP devices of different surface participation ratio or with electrodes in contact with the GaP beam could potentially shed more light on this discrepancy.

Superconducting Microwave Cavities

Part V

14 Superconducting Nb and NbN Coplanar Waveguide Cavities

In this chapter I will present the results obtained from measurements of Nb and NbN superconducting coplanar waveguide cavities, that were fabricated to benchmark the process for superconducting RF devices in our cleanroom and to investigate whether the fabrication techniques that are used in the fabrication of GaP-on-silicon integrated devices have a detrimental effect on the superconducting devices. A particular concern in that regard was that the high temperature processing steps and exposure during wet etching steps early in the fabrication procedure might deteriorate the quality of the superconducting metal films. In addition, NbN was explored as an alternative platform for superconducting microwave cavities, due to an appreciable kinetic inductance, that allows for tunable, linear microwave cavities, a high transition temperature ~ 13 K which would allow operation at elevated temperatures, and due to its quasi-particle lifetime $\tau_0 \sim 20$ ps [41] which compares very favorably to that of Nb (~ 150 ps) and that of other popular superconductors such as Al (~ 438 ns) [41]. The quasi-particle lifetime might in this case be a decisive factor for the suitability of the material in a microwave-to-optical transducer, as this experiment requires optical pumping, which may introduce quasi-particles into the superconductor. It is then crucial that the quasi-particles decay quickly such that they do not interfere with the microwave device.

14.1 Setup for Measurement of Superconducting Microwave Cavities

Superconducting resonators require first and foremost temperatures below the critical temperature of the superconductor to be characterized. However, typically it is favorable to measure such resonators at as low a temperature as feasible, since the quality factor and coherence time of such devices depend in a complex fashion on the temperature of the bath and the photon occupation of the resonator. The origin of this behavior are saturable absorbers, or two-level systems [81], that are saturated at high power and or temperature, but not at low temperature and power, where they may interact with the photons in the cavity and lead to a frequency instability of the resonator (decoherence) and loss. As quantum measurements

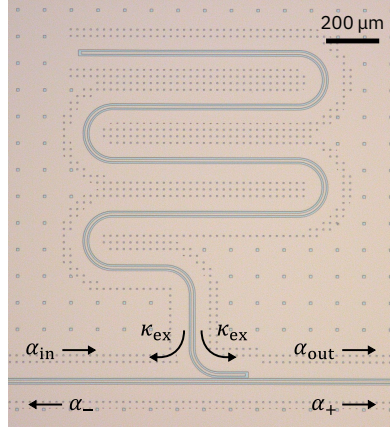


Figure 14.1: Optical micrograph of Nb coplanar microwave cavity coupled to a transmission line in 'notch-type' configuration. Annotation indicates direction of microwave input (α_{in}) and output fields (α_{out}) as well as forwards (α_+) and backwards propagating modes (α_-).

such as dispersive readout of superconducting qubits are performed in this regime, it is useful to understand the limitations of the here presented platform. The superconducting resonators are measured in a Bluefors LD400 dilution refrigerator with fast sample exchange. The setup configuration is shown in Figure 14.2 on the left. The Input signal from the VNA is thermalized to the various stages of the dilution refrigerator as indicated in the drawing. The device output is sent through a circulator that isolates the mixing chamber from thermal noise in the output line, and subsequently through a bandpass filter, an isolator, and another bandpass filter (not shown in the drawing) before being amplified on the 3 K stage by a high-electron-mobility transistor amplifier. The resonators are packaged on a printed circuit board that is connected to the input and output lines of the dilution refrigerator on the mixing chamber. The devices are wire-bonded to the measurement lines on the PCB. Additionally, ground-to-ground connections are bonded between either sides of the coplanar waveguide (shown in right panel of Figure 14.2) to equalize the reference potential.

14.2 Results

The design and fabrication scheme are described above. We use the expression derived in section 1.3:

$$S_{21}(\Omega) = \Gamma_D (1 - \kappa_{\text{ex}} \chi_{\text{mw}}(\Omega)) e^{-i(\Omega\tau + \theta)}. \quad (14.1)$$

to fit the transmission data recorded from a vector network analyzer. I will note here that the data is actually fit to S_{21}^* , as the VNA uses a different phase convention, this, however, does not affect any of the results. We investigated superconducting cavities made from both, Nb and NbN superconducting thin films from two chips each with a center track width of $10\mu\text{m}$ and a gap to ground of $6\mu\text{m}$. An optical micrograph of a typical device is shown in Figure 14.1. A representative transmission dataset is presented in Figure 14.3 as amplitude and phase of the complex scattering parameter S_{21} (a,c), as well as the phase-space image of

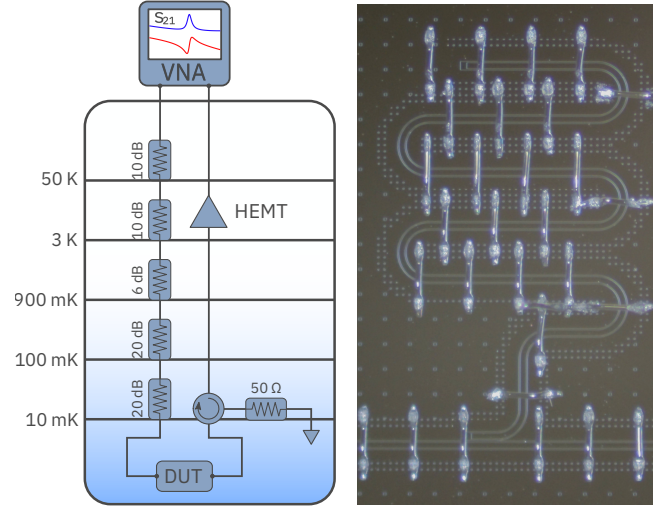


Figure 14.2: Setup for measurement of superconducting microwave cavities at mK temperatures (left) and optical micrograph of bonded coplanar waveguide resonator (right).

the scattering parameter (b,d) for an input power into the fridge of 10 dBm (a,b) and -75 dBm (c,d), which corresponds, after the 86 dB attenuation in the fridge, to an average intracavity photon number – at $\Omega = \Omega_{\text{mw}}$ – of $n_{\text{cav}} = 1.34 \times 10^7$ and $n_{\text{cav}} = 3.46 \times 10^{-2}$, respectively, for the device of which the scattering data is shown in Figure 14.3. The measurement is repeated for input powers from 10 dBm to -75 dBm for the Nb device, and 20 dBm to -90 dBm for the NbN device in 5 dB steps. At each power the frequency Ω_{mw} , coupling rate κ_{ex} , total loss rate κ and intrinsic loss rate κ_0 are extracted from the fit to the complex scattering data, from which the loaded quality factor $Q_L = \Omega_{\text{mw}}/\kappa$, intrinsic quality factor $Q_I = \Omega_{\text{mw}}/\kappa_0$ and coupling quality factor $Q_{\text{ex}} = \Omega_{\text{mw}}/\kappa_{\text{ex}}$ are calculated. The intrinsic decay rate is in this case determined as $\kappa_0 = \kappa - 2\kappa_{\text{ex}}$, as the resonators are measured with ‘notch-type’ transmission line coupling. In this geometry the resonator couples with its coupling rate κ_{ex} equally in the forward direction α_+ and in the backward direction α_- as illustrated in Figure 14.1. Since the output field is only measured in forward direction, the backward propagating waveguide mode is an additional loss channel that must be considered, if the intrinsic cavity loss is of interest. The measured resonance frequency of the coplanar waveguide cavities fabricated from niobium is in good agreement with the design frequency, while for the NbN device presented here we find $\Omega_{\text{mw}}/2\pi = 6.07$ GHz with a design frequency of $\Omega_{\text{mw}}/2\pi = 7.1$ GHz. This deviation of over 1 GHz was expected due to the high kinetic inductance of the superconducting film.

14.3 Nb Resonators

The power-dependent quality factor of the measured Nb resonators is shown in Figure 14.4. The error bars indicate the uncertainty of the parameters that is estimated from the 2σ interval of the standard deviation σ of the fit parameters ω_0 , κ and κ_{ex} , that is propagated through the

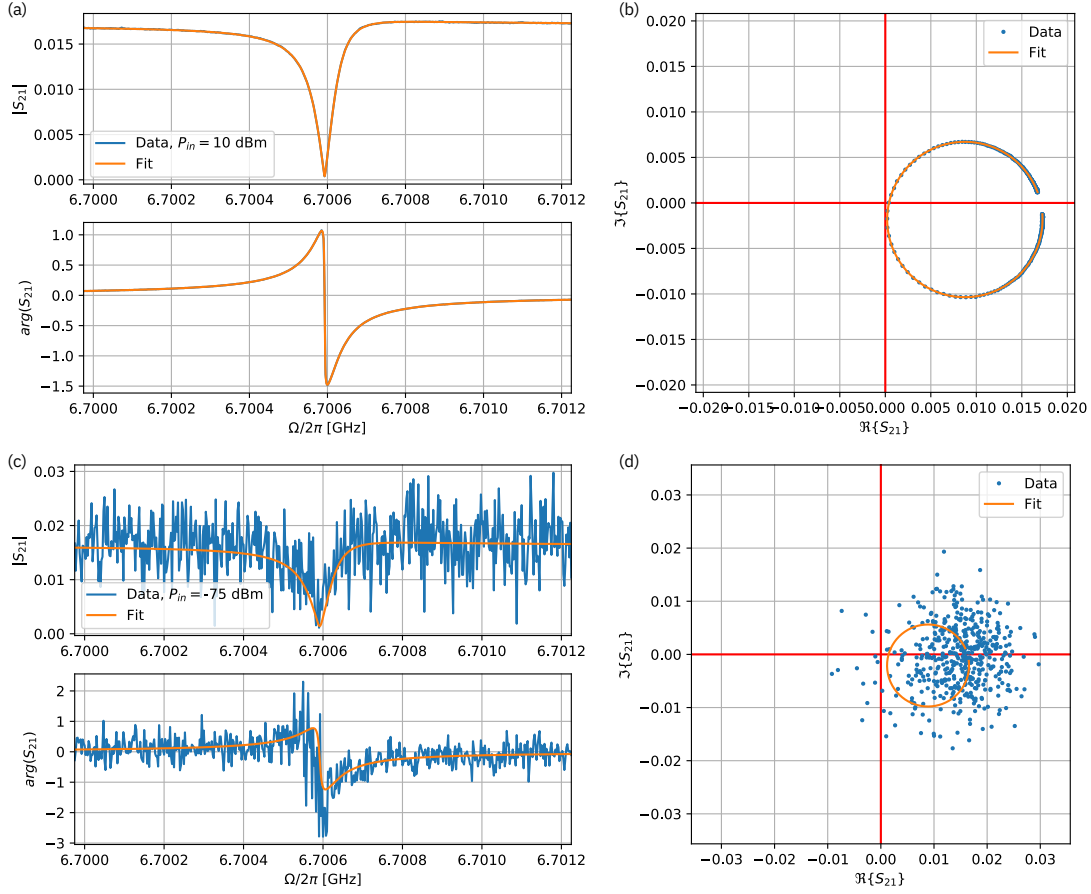


Figure 14.3: Representative complex scattering parameter S_{21} measured at high input power (a,b) and below single-photon level (c,d) (blue) with S_{21} fit (orange).

calculation of Q .

The average intracavity photon number n_{cav} is calculated at $\Omega = \Omega_{\text{mw}}$ as

$$n_{\text{cav}} = \frac{P_{\text{in}}}{\hbar\Omega_{\text{mw}}} \frac{4\kappa_{\text{ex}}}{\kappa^2}. \quad (14.2)$$

A decrease of the intrinsic quality factor is observed as the intracavity photon number is reduced. This is an expected effect that is understood to be due to a bath of two-level systems – or saturable absorbers – that are saturated at high power but no more at power levels approaching the single-photon level [81]. We observe a large uncertainty of the intrinsic quality factor for several devices. This is due to the fact that almost all observed cavities are massively overcoupled with $\kappa_{\text{ex}} \gg \kappa_0$. Consequently, κ_{ex} is afflicted with a large uncertainty. For a given parameter uncertainty of κ ($\delta\kappa$), the uncertainty of $\kappa_0 = \kappa - 2\kappa_{\text{ex}}$ is given as $\delta\kappa_0 = \delta\kappa + 2\delta\kappa_{\text{ex}}$. As a result, even a small $\delta\kappa$ ($\delta\kappa_{\text{ex}}$) creates a large $\delta\kappa_0$. Below single photon level, the signal-to-noise ratio is low, as illustrated by the resonator phase-space image in Figure 14.3 (d). Consequently, for $\kappa_{\text{ex}} \gg \kappa_0$, $\delta\kappa_0$ is in these cases high. The arithmetic mean of the measured intrinsic quality factors for $n_{\text{cav}} < 1$ ($Q_{I,\text{lp}}$) and for $n_{\text{cav}} > 10^6$ ($Q_{I,\text{hp}}$) corre-

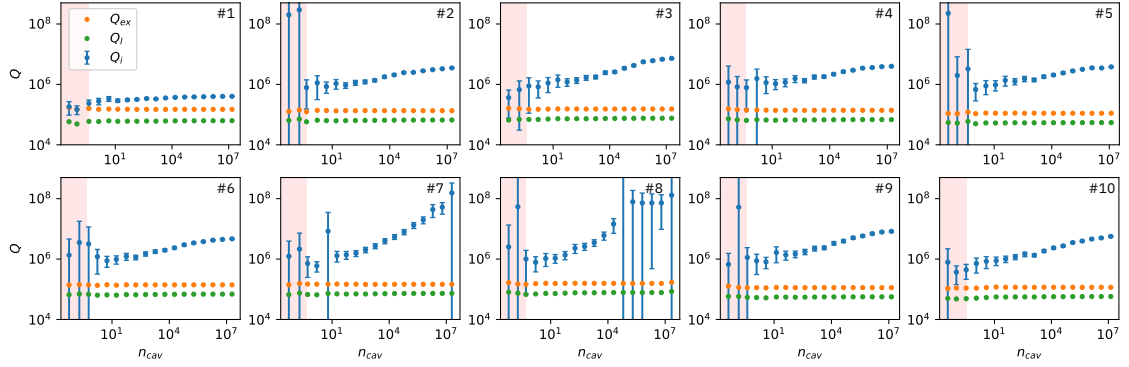


Figure 14.4: Power-dependent quality factor of measured Nb coplanar waveguide cavities. The intrinsic quality factor Q_I is shown in blue, the loaded quality factor Q_L and external quality factor Q_{ex} are shown in green, and orange, respectively. Error bars indicate the 2σ confidence interval. The red-shaded are indicate measurements below the single photon level.

Table 14.1: Intrinsic quality factors of Nb coplanar waveguide cavities as determined from data shown in Figure 14.4 below single photon level $Q_{I,lp}$ and at $n_{cav} > 10^6$ $Q_{I,hp}$ with respective eigenfrequencies Ω_{mw} .

Resonator #	$\Omega_{mw}/2\pi$ [GHz]	$Q_{I,lp}$	$Q_{I,hp}$
1	$6.52 \pm 4.9 \times 10^{-7}$	$1.89 \times 10^5 \pm 2.0 \times 10^4$	$4.00 \times 10^5 \pm 5.8 \times 10^2$
2	$6.71 \pm 3.7 \times 10^{-7}$	$1.65 \times 10^8 \pm 2.2 \times 10^{10}$	$3.29 \times 10^6 \pm 3.0 \times 10^4$
3	$6.86 \pm 4.1 \times 10^{-7}$	$6.40 \times 10^5 \pm 1.7 \times 10^5$	$6.73 \times 10^6 \pm 1.2 \times 10^5$
4	$7.02 \pm 4.2 \times 10^{-7}$	$9.34 \times 10^5 \pm 5.1 \times 10^5$	$3.81 \times 10^6 \pm 4.4 \times 10^4$
5	$7.18 \pm 4.8 \times 10^{-7}$	$7.72 \times 10^7 \pm 1.9 \times 10^{10}$	$3.61 \times 10^6 \pm 4.2 \times 10^4$
6	$6.51 \pm 3.3 \times 10^{-7}$	$2.68 \times 10^6 \pm 2.8 \times 10^6$	$4.46 \times 10^6 \pm 5.2 \times 10^4$
7	$6.70 \pm 3.4 \times 10^{-7}$	$1.36 \times 10^6 \pm 9.64 \times 10^5$	$8.38 \times 10^7 \pm 3.0 \times 10^7$
8	$6.86 \pm 3.5 \times 10^{-7}$	$1.92 \times 10^7 \pm 5.6 \times 10^8$	$9.16 \times 10^7 \pm 3.6 \times 10^8$
9	$7.02 \pm 4.1 \times 10^{-7}$	$1.80 \times 10^7 \pm 5.9 \times 10^8$	$7.70 \times 10^6 \pm 1.7 \times 10^5$
10	$7.17 \pm 4.9 \times 10^{-7}$	$5.33 \times 10^5 \pm 2.4 \times 10^5$	$5.09 \times 10^6 \pm 7.2 \times 10^4$

sponding to the data shown in Figure 14.4 as well as the respective eigenfrequencies are listed in Table 14.1. The uncertainty is derived from the fit uncertainty that is propagated through the mean. We may calculate an average single-photon quality factor $Q_{I,0}$ by considering the data-sets with sufficiently low uncertainty ($2\sigma_Q < Q$). We also discard resonators #1, #7 and #8 as outliers. In this case, we find for the observed devices $Q_{I,lp} = 5.86 \times 10^5 \pm 1.48 \times 10^5$.

14.3.1 TLS Model Fit

Resonator #10 is taken as a representative data set for further analysis. The intrinsic quality factor as a function of the circulating power $P_{circ} = n_{cav}\hbar\Omega_{mw}$ can be modeled as coupling to a

bath of two-level systems [81]. The power-dependent intrinsic quality factor is then given as

$$Q_I(P_{\text{circ}}) = \frac{Q_d(P_{\text{circ}})Q^0}{Q_d(P_{\text{circ}}) + Q^0} \quad (14.3)$$

with

$$\frac{1}{Q_d(P_{\text{circ}})} = \frac{V_f}{Q_d^0} \frac{\coth\left[\frac{\hbar\omega_0}{2k_B T}\right]}{\sqrt{1 + \left(\frac{P_{\text{circ}}}{P'_C}\right)^\beta}}, \quad (14.4)$$

where $1/Q^0$ is a power-independent loss that limits the Q in the case where the TLS are saturated, P'_C is some geometry-dependent critical power and β is a fit parameter [81]. From this fit, which is shown as orange line in Figure 14.5, we can extract an effective loss tangent $\tan(\delta_{\text{eff}}) = V_f/Q_d^0$, where V_f is the fraction of the total volume the electromagnetic field occupies that contains TLS (for example the metal-air, metal-substrate or substrate-air interfaces), and $1/Q_d^0$ is the unsaturated loss tangent of the dielectric due to TLS.

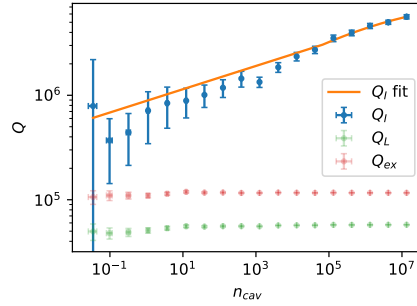


Figure 14.5: Quality factors of device #10 as shown in Figure 14.4 with fit to Equation 14.4.

From the fit we obtain a loss tangent of $\tan(\delta_{\text{eff}}) = (1.58 \pm 0.25) \times 10^{-6}$ and an asymptotic quality factor of $Q^0 = (8.73 \pm 1.33) \times 10^6$. These values compare very favorably to those given by Sage et al. [81] which is an indication that the platform developed during this thesis can be combined with a low-loss platform for microwave devices.

14.4 NbN Resonators

The NbN coplanar waveguide cavities were measured in an identical fashion as the Nb devices. A representative data-set is shown in Figure 14.6. Due to a lower asymptotic intrinsic quality factor below single-photon level and longer averaging, the fitting procedure produced results with significantly lower uncertainty than for the Nb devices. In contrast to the Nb cavities however, a saturation of the quality factor at high power was not observed, as shown in Figure 14.6 on the left. Instead, at high input power a shift in the eigenfrequency was observed (Figure 14.6 right) and at an input power to the fridge exceeding 10 dBm the response of the device became increasingly nonlinear, as seen in the device response shown in Figure 14.7, where the complex scattering parameter S_{21} is shown for an input power of 0 dBm, where

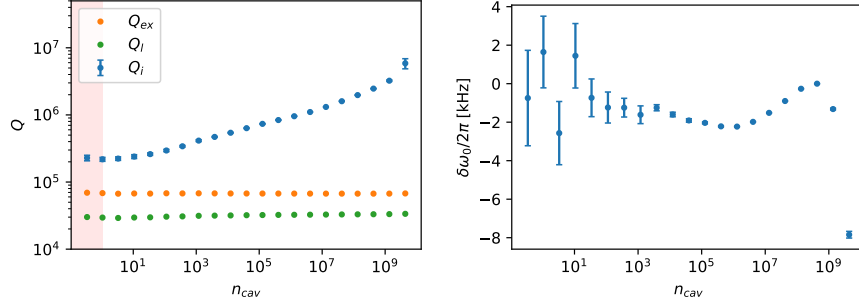


Figure 14.6: Transmission data with fit to section 1.3 (a), quality factors extracted from measurements at different circulating power for Nb (b) and NbN (c) devices.

the device still has a linear response, 10 dBm, the highest power where the linear response fit yielded usable results (the highest photon occupation shown in Figure 14.6), and 20 dBm, the highest power that was recorded, at which point the response of the device is severely nonlinear. Below single photon level, the intrinsic quality factor is determined to be $Q_{I,0} = 2.29 \times 10^5 \pm 1.1 \times 10^4$, a bit more than a factor two worse than for Nb. This is a very encouraging result, as NbN, having a high kinetic inductance and being a compound superconductor, was expected to perform significantly worse than Nb.

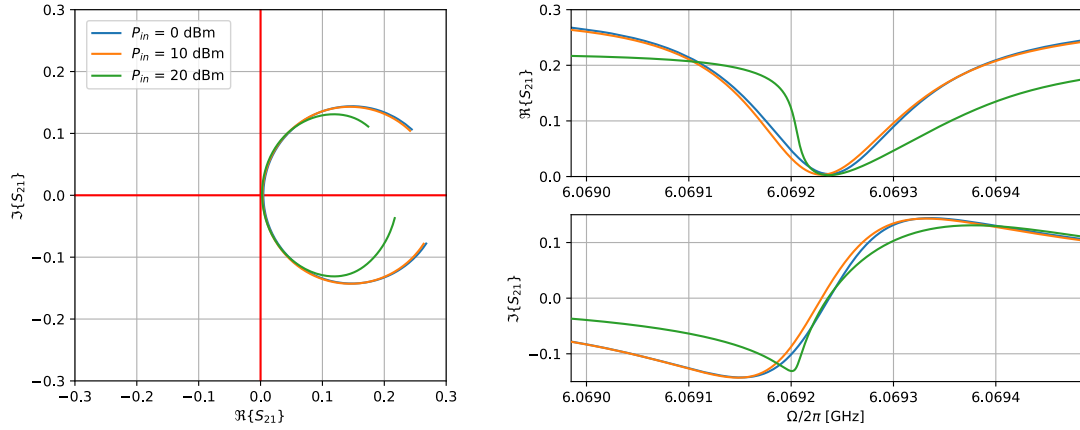


Figure 14.7: Transmission data with fit to section 1.3 (a), quality factors extracted from measurements at different circulating power for Nb (b) and NbN (c) devices.

14.4.1 Kinetic Inductance

The nonlinearity of the NbN cavities can be easily understood in terms of the kinetic inductance of the material. At low power, the inductance is constant and the device behaves similarly to the Nb device with $L = L_0 + L_{k0}$, where L_0 is the geometric inductance and L_{k0} is the kinetic inductance. The current at the antinode of the coplanar waveguide resonator is on

the order of $I \sim \sqrt{P_{\text{circ}}/Z}$, where Z is the resonator impedance. As the power is increased and the current in the waveguide I becomes comparable to the critical current of the NbN I_C , the kinetic inductance can be expressed as a function of the current inside the cavity as

$$L_k(I) \approx L_{k0} \left(1 + \left(\frac{I}{I^*} \right)^2 \right), \quad (14.5)$$

where I^* is a characteristic current on the order of the critical current I_C [102]. It should be noted here that this equation is technically for a DC current through a superconducting loop, but the argument holds for a waveguide section over which the current is approximately constant. With

$$P_{\text{circ}} = P_{\text{in}} \frac{\kappa_{\text{ex}}}{\kappa^2/4 + (\omega - \omega_0)^2} \quad (14.6)$$

being a function of ω , this makes the current I and consequently the kinetic inductance L_k frequency-dependent. This leads at moderate input power to a shift in the eigenfrequency and at high power to the nonlinear response shown in Figure 14.7.

14.5 Conclusion

Superconducting microwave cavities were fabricated and tested using the fabrication techniques employed in the fabrication of GaP optomechanical hybrid devices and the devices were found to exhibit an encouragingly high quality factor at single photon level. This is an important indicator that the employed fabrication techniques, especially the exposure of the superconducting film to high temperature and hydrofluoric acid, has no appreciable detrimental effect on the superconducting devices. This inspires confidence that future superconducting devices that are integrated with the developed hybrid platform may exhibit competitive figures of merit.

Outlook **Part VI**

15 Towards Quantum Optomechanics and Quantum Acoustics

15.1 State of the Art

The results obtained in the scope of this work have demonstrated that GaP is indeed a suitable candidate for a microwave-to-optical link, and simulations have shown that strong coupling with a superconducting qubit should be achievable. The fair agreement between the simulated electromechanical coupling and that measured in the prototype device also indicates that GaP indeed experiences a piezoelectric coupling with a magnitude as we expect, although further research into different device geometries might shed more light onto the discrepancy that is still observed between experiment and simulation.

15.2 Quantum Acoustics

The grand challenge for the next phase of the project is the successful integration of a superconducting qubit with the device and the observation of strong coupling between the mechanical modes and the microwave mode of the qubit.

15.2.1 Dielectric loss in GaP-Transmon Hybrid Devices

Although microwave resonators with an encouragingly high quality factor were tested on this platform, the test was restricted to coplanar waveguide cavities fabricated from Nb and NbN in the absence of the GaP photonic crystal. Although these tests confirm that high microwave quality factors with the thermal budget required for the fabrication of optomechanical hybrid devices, they might not be completely representative as they do not include the effect of the GaP on the microwave mode, and the resonators were fabricated with a designed impedance of $50\,\Omega$. Superconducting qubits typically have a much higher impedance and thus a larger zero-point voltage. Consequently, electric fields at the critical interfaces are stronger for a qubit than they are for a coplanar waveguide cavity, and defects that might be introduced at the interfaces might have a significantly larger impact. In addition, GaP might introduce

significant additional loss to the microwave circuit. First, and of course, GaP is piezoelectric, such that the electric field of the qubit may couple to mechanical modes in the GaP device. While this is the point of this device, it also presents the challenge that the qubit might couple to mechanical modes that it was not designed to couple to. While the device itself is deliberately made such that the phonon density of states is well-controlled in the frequency range of interest, the overall structure might support a number of parasitic modes. For example, in the current device generation, large pads made of GaP are used to suspend the photonic crystal, that might couple strongly to bulk acoustic modes of the substrate. Those pads being large, they might also have a large overlap with the electric field of the qubit. Future devices could address this problem by either replacing the GaP clamp with a non-piezoelectric material, such as a Nb air bridge, or the clamps could be encased in a shielding structure, for example a Nb Faraday cage.

15.2.2 Dielectric Loss due to Defects in GaP

Besides the piezoelectric loss, we also have reason to believe that our GaP film contains a number of local charge states, e.g. unsaturated bonds or defects in the crystal lattice caused by impurities such as carbon. In a recent experiment, fluorescent molecules were placed in close proximity to a GaP waveguide, where we observed a dispersive shift in the molecules' resonance frequencies upon illumination through the GaP waveguide with a laser beam [89]. We attribute this to a short-range interaction between optically excited charge states in the GaP and the fluorescent molecules, as this behavior was not observed for emitters far away from the waveguide, and we observed a correlation between the dispersive shift of two molecules in close proximity, indicating coupling to a common charge state. The defect density that was determined from this experiment is consistent with the background level of carbon during MOVPE growth, or it might be related to the disordered, etched interface between GaP and air. In either case, these defects might present an additional decoherence mechanism for a superconducting qubit. Bulk defects in the GaP might be addressed by increasing the growth temperature even further, although 800 °C is a hard limit in our present reactor. Surface defects may be addressed with passivation techniques developed for other III-V microphotonic devices such as surface passivation by nitridation [40].

15.3 Quantum Optomechanics

A demonstration of optomechanically distributed entanglement between two GaP photonic crystal resonators will be the cornerstone for the viability of this platform as quantum interconnect. A replication of the results obtained by Riedinger et al., both in projecting one mechanical resonator into a quantum state [77] and demonstration of entanglement between two resonators [78] are therefore the next logical steps on this side of the project.

15.4 Improvements to GaP Platform

It is worth discussing at this point how well the developed GaP platform might fare in the planned experiments, and to what extent improvements must be made to obtain significant results. Pulsed measurements of silicon photonic crystal cavities close to the mechanical ground state have revealed that silicon devices experience significant heating effects [66] due to sub-bandgap optical absorption at the silicon-air interface that decay into a thermal population of higher frequency phonons. Inelastic scattering of these phonons into the mechanical mode lead to a delayed heating effect in the oscillator. These defects are similar to what we suspect to be the cause of the aforementioned dispersive shift observed in fluorescent molecules, such that we can expect a similar heating effect to take place in the GaP device. Indeed, this effect has been observed in quantum optomechanical experiments with GaP photonic crystals [93] with time-scales of the delayed heating of $\mathcal{O}(100\text{ ns})$, much faster than a state could be swapped into a superconducting qubit with the current geometry. GaP can therefore be expected to, despite the larger bandgap, suffer from the same challenges found with Si devices. The strategies to improve on potential dielectric loss discussed above, i.e. improved growth and surface treatment, could be applied in this case as well.

We observe a deterioration of the optical quality factor over time. In addition, we observe a substantial shift of the optical frequency, which indicates that, despite a protective alumina coating, an optically induced process still permanently alters the device properties. This is concerning as it indicates chemical processes, such as photo-induced oxidation of the device [100], and the introduction of a potentially even more disordered dielectric-air interface. On the up-side, the photo-induced frequency shift may be used in an entanglement experiment to tune two devices, which may be not entirely identical, into resonance with an initial laser blast at high optical power.

In general, we observe an optical quality factor that allows operation of the device in the resolved-sideband regime where the rotating-wave approximation holds, an important property for single phonon experiments to suppress the beam-splitter (two-mode squeezer) interaction when operating at blue (red) detuning. While the presented devices are in the resolved-sideband regime for near-critical optical coupling, the sideband resolution is relatively low with $\Omega_m/\kappa \approx 1.12$. In addition, the device is sideband-resolved at critical coupling, while an overcoupled cavity is preferable for quantum optomechanical experiments, to enhance the detection efficiency of heralding photons. An improvement of the optical quality factor might therefore be desirable. In GaAs cavities, surface nitridation has proven to enhance the optical quality factor significantly [40], a technique that might be employed here as well.

16 Integration of Superconducting Qubits

Integration of superconducting qubits is, as mentioned before, the next grand challenge for this project. The platform that I presented in this work is designed to accommodate the future integration with superconducting qubits. The specific sequence of the integration

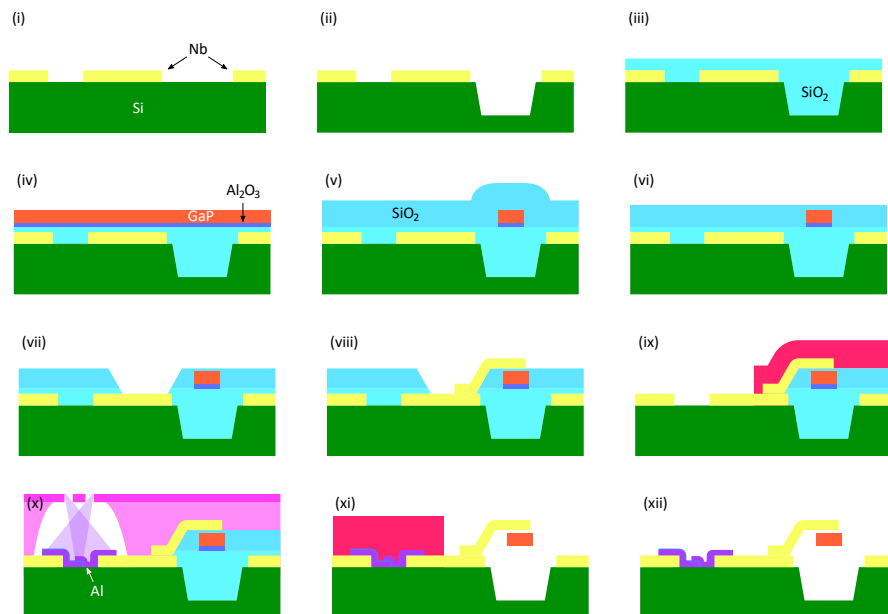


Figure 16.1: Process flow including integration of Josephson junctions. Fabrication of Nb circuit components (i), substrate recess (ii), cladding and planarization (iii), GaP integration with wafer-bonding (iv), photonic circuit integration and cladding (v), cladding planarization (vi), via fabrication (vii), Nb top electrode integration (viii), exposure of qubit circuit components prior to junction evaporation (ix), shadow evaporation and in-situ oxidation of Josephson junctions (x), masking of Josephson junctions and device release (xi), removal of mask (xii).

is important to outline. Josephson junctions fabricated by shadow evaporation and in-situ oxidation of aluminum are the current standard process for most superconducting qubits. Aluminum, unlike Nb, is neither resistant to high temperatures, nor to hydrofluoric acid. In

addition, the junction itself may be sensitive to temperature, which might alter the thin oxide barrier significantly. Therefore, the junction part of the qubit must be integrated after all high-temperature processing steps are completed and must be protected from all subsequent chemical etching processes. Additionally, the optomechanical device must be suspended, which implies an etching step in hydrofluoric acid. The qubits cannot be integrated after the device release, as capillary forces during the resist application would destroy the fragile, suspended structures. This leaves the junction integration step right before the device release. The qubit's shunt capacitor, fabricated in Nb, will then be exposed with a local removal of the SiO_2 dielectric interlayer, and the junctions will be fabricated by shadow evaporation liftoff. Subsequently, the junctions are protected with the mask that is used to also protect the GaP waveguide during release. After removal of the resist mask, the junctions should be unscathed and the released device intact. The fabrication scheme described in Part III and extended to include the fabrication of a Josephson junction is shown in Figure 16.1.

16.1 Transmon Design

A possible design of a transmon qubit is shown in Figure 16.2. The dimensions of the shunt capacitor's pads are chosen to obtain a shunt capacitance according to Equation 5.10 for an appropriate E_J/E_C . Instead of a single junction, the design contains a superconducting quantum interference device (SQUID) to enable frequency tunability of the qubit. Each path of the SQUID contains two symmetric Josephson junctions in series to avoid fabrication of junctions with exceedingly high L_J . The SQUID enables Z control of the qubit as well as frequency-tunability of the microwave mode through an external magnetic field. A drive line for X and Y control is placed on top, capacitive coupling to the readout resonator at the bottom. The photonic waveguide is designed with a 90° -bend to filter TM contributions to the optical waveguide mode and to place the fiber coupler (top left in (a)) off-center with respect to the qubit, which might reduce optical absorption of scattered light by the qubit. A proposed Faraday cage was placed around the clamp of the photonic crystal resonator to reduce parasitic piezoelectric coupling.

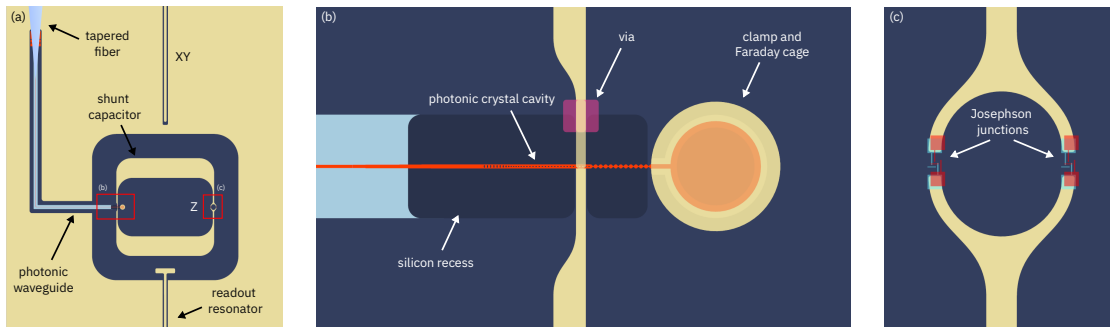


Figure 16.2: Illustration of possible qubit design. Overview of device (a), photonic crystal cavity (b) and SQUID (c) for frequency tunability. Color-scheme same as in Figure 10.1

A Gallium Phosphide Nonlinear Inte- grated Photonics

Besides Microwave-to-optical transduction, I had the opportunity to contribute to a variety of other projects during my PhD. For the sake of completeness, I dedicate the following appendices to my contributions to these projects.

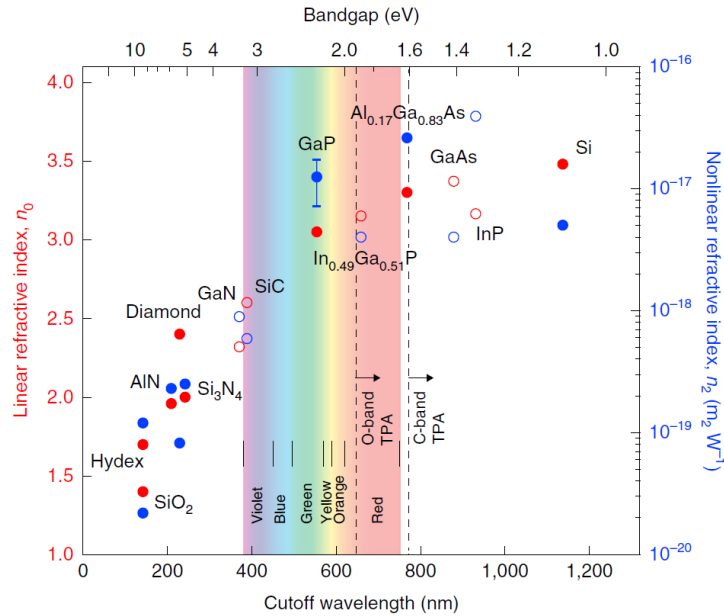


Figure A.1: Linear and nonlinear refractive indices of selected materials for nonlinear photonics (from [100]). Dashed lines indicate cutoff wavelength for two-photon absorption (TPA) and telecom wavelengths in C and O-band.

Gallium phosphide, besides its attractive properties for optical quantum links, is also, and perhaps even more so, an attractive material for nonlinear photonics. It possesses a large nonlinear refractive index ($1.1(3) \times 10^{-17} \text{ m}^2/\text{W}$, see Figure A.1), over one order of magnitude larger than that of Si₃N₄ and a large optical bandgap compared to other phosphide and arsenide III-V semiconductors at $E_g = 2.26 \text{ eV}$. The former permits frequency conversion by four-wave mixing at a substantially lower power threshold compared to materials with larger

bandgap, such as Si_3N_4 , SiO_2 or AlN (assuming similar mode volume and quality factor) while the latter permits stronger optical pumping compared to for example GaAs ($E_g = 1.44 \text{ eV}$) and Si ($E_g = 1.12 \text{ eV}$), since the optical bandgap is much larger than the threshold for two-photon absorption in the telecom C-band (1.62 eV) and O-band (1.97 eV). In addition, the transparency window of GaP extends far in the infrared ($\sim 10.5 \mu\text{m}$ [97]) which opens up the possibility of realizing integrated light sources in the middle-wavelength infrared range. On top of this, GaP also possesses a substantial second order nonlinearity with $d_{14} = 71.8 \text{ pm/V}$ (at $\lambda = 1058 \text{ nm}$) ([61]) which opens up the possibility of efficient frequency conversion by second harmonic generation and parametric down-conversion in integrated devices.

We explored the optical nonlinear properties of GaP in an earlier paper [100] where we demonstrated frequency conversion by both three and four-wave mixing as well as the generation of frequency combs by cascaded four-wave mixing. My contributions to this work was in the design, fabrication and characterization of the optical microresonators. Crucially, the resonators showed an improvement in the optical quality factor of over one order of magnitude compared to previous devices ($Q_0 \sim 2 \times 10^4$) [84].

A.1 Resonator Design

Nonlinear optical effects were shown here with GaP ring resonators. This design enables typically higher quality factors than photonic crystal designs due to larger mode volume and smaller surface participation, and allow for dispersion engineering of the resonator spectrum. A typical design is shown in Figure A.2. A waveguide of width w is closed in a circular loop with radius R . This forms a cavity with physical length $L = 2\pi R$. The free spectral range ν_{FSR} of the resonator is given by the roundtrip time τ_{rt} as $\nu_{\text{FSR}} = 1/\tau_{\text{rt}}$. The latter is given by

$$\tau_{\text{rt}} = \frac{2\pi R}{v_g} \quad (\text{A.1})$$

where $v_g = c/n_g$ is the group velocity (with vacuum speed of light c and group index n_g). The group index can be determined with a numerical simulation of the effective refractive index of the waveguide mode n_{eff} as

$$n_g = n_{\text{eff}} - \lambda_{\text{vac}} \frac{dn_{\text{eff}}}{d\lambda_{\text{vac}}} \quad (\text{A.2})$$

with the vacuum wavelength λ_{vac} . $\frac{dn_{\text{eff}}}{d\lambda_{\text{vac}}}$ is determined numerically with a mode simulation at different wavelengths.

Optical frequency comb generation by cascaded four-wave mixing requires anomalous dispersion of the microresonator to compensate for the frequency shift introduced by cross and self phase modulation [48]. For the devices presented here, the resonator dispersion was simulated with a finite element simulation of the waveguide cross section [100]. The theoretical framework of frequency combs and the details of the dispersion engineering are beyond the scope of this work and are described in great detail elsewhere. Suffice it to say at this point that anomalous dispersion in the wavelength range of interest ($\lambda_{\text{vac}} \sim 1550 \text{ nm}$) is found for 300 nm

thick GaP waveguides for a waveguide width between 400 nm and 700 nm. We found that for waveguide widths $w < 450$ nm the increased participation of the etched waveguide surface leads to excessive optical loss due to scattering and absorption at the etched interface. A good trade-off between optical quality factor and anomalous dispersion is found at a waveguide width of 550 nm. For these dimensions and with a 10 nm thick Al_2O_3 coating (see below) we find $\nu_{\text{FSR}} = 254$ GHz with $n_{\text{eff}} = 2.237$ and $n_g = 3.756$ at $\lambda_{\text{vac}} = 1550$ nm.

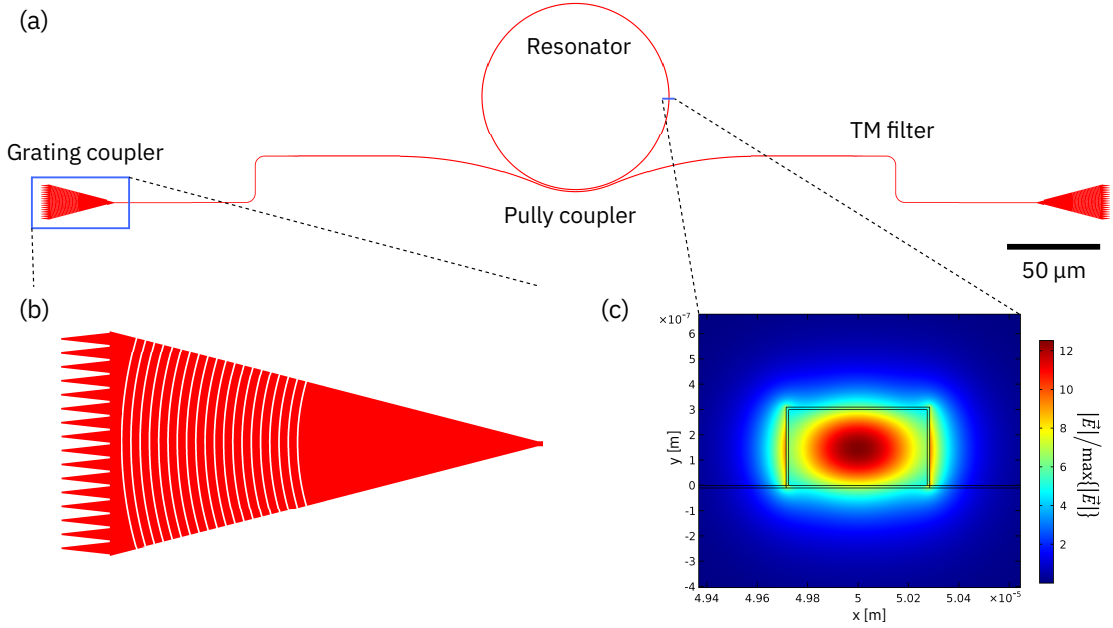


Figure A.2: (a) Design of ring resonator device with pulley coupler. (b) Magnified view of diffraction grating coupler. (c) Simulation of TE waveguide mode cross section in ring resonator. Coloration corresponds to the magnitude of the electric field.

Waveguide Coupling

Light is coupled into the resonator via an evanescently coupled bus waveguide which is connected to a pair of diffraction grating couplers (see Figure A.2(a)). In the design shown here the bus waveguide mode copropagates with the resonator mode over an angle α in a 'pulley' configuration as illustrated in Figure A.3. The coupling can be estimated via a coupled mode model. To that end, the radial effective indices $n_{\text{eff}}R$ of both the resonator and bus waveguide, separated by a gap d are first simulated separately with a finite element method mode simulation to find the bare, uncoupled propagation constants, followed by a simulation of the coupled modes, as function of the bus waveguide width w_{bus} . One finds that the bus waveguide is phase-matched to the resonator waveguide at a narrower width $w_{\text{bus}} < w$. This is due to the larger radius of the bus waveguide in the interaction region, which consequently requires a higher group velocity, i.e. smaller n_{eff} , to be matched to the resonator mode. At the crossing of the bare modes one finds an avoided crossing in the coupled system, as expected,

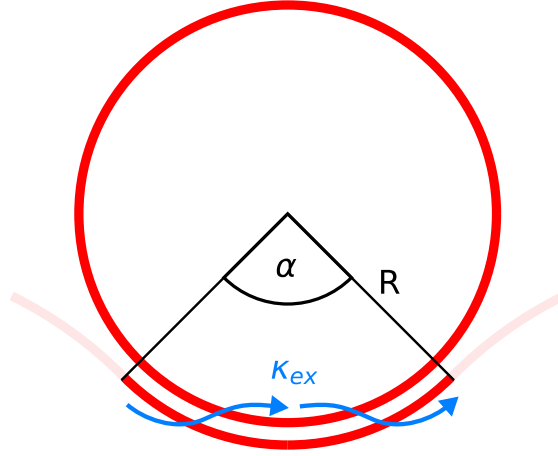


Figure A.3: Resonator geometry in pulley configuration. Bus waveguide couples to resonator waveguide over effective interaction angle α , leading to an external coupling rate κ_{ex} .

the width of which depends on the bus-resonator gap d . The external coupling rate of the resonator κ_{ex} may then be estimated by employing the Rabi oscillation formalism. I credit here Charles Möhl who has derived this method in our group.

The probability of a transition between two coupled energy levels can be found as

$$P_{\text{flip}}(t) = \frac{\Omega_0^2}{\Omega_0^2 + \Delta^2} \sin^2\left(\frac{\Omega}{2} t\right) \quad (\text{A.3})$$

where Δ is the frequency detuning of the coupled modes and Ω_0 is the frequency splitting of the modes at $\Delta = 0$, i.e. in the avoided crossing, and Ω is the frequency splitting at Δ . We may adapt Equation A.3 for two copropagating optical modes by substituting $\Omega t \rightarrow \Delta k x$ where Δk is the difference in propagation constant (phase mismatch) between the coupled modes and $x = \alpha R$ is the length over which the modes interact. We find

$$\Delta k x = \Delta n_{\text{eff}} R \frac{2\pi}{\lambda_{\text{vac}}} \alpha \quad (\text{A.4})$$

where $\Delta n_{\text{eff}} R$ indicates the difference in radial effective index of the symmetric and antisymmetric coupled modes. We may then write

$$P_{\text{flip}}(\alpha) = \frac{\Omega_0^2}{\Omega_0^2 + \Delta^2} \sin^2\left(\frac{\Omega}{2} \alpha\right) \quad (\text{A.5})$$

with

$$\begin{aligned} \Omega &= \Delta n_{\text{eff}} R \frac{2\pi}{\lambda_{\text{vac}}} \\ \Delta &= \Delta n_{\text{eff,bare}} R \frac{2\pi}{\lambda_{\text{vac}}} \\ \Omega_0 &= \sqrt{\Omega^2 - \Delta^2} \end{aligned} \quad (\text{A.6})$$

where $\Delta n_{\text{eff,bare}}R$ is the difference in radial effective refractive index of the uncoupled modes. In the resonator, photons pass the coupling section once every roundtrip. As they pass the coupler, the probability of scattering into the bus waveguide is P_{flip} . Consequently, one finds the rate at which photons leave the resonator system via this channel as

$$\kappa_{\text{ex}} = 2\pi\nu_{\text{FSR}}P_{\text{flip}}. \quad (\text{A.7})$$

An example of a coupler with $d = 320\text{ nm}$ is shown in Figure A.4. The radial effective indices

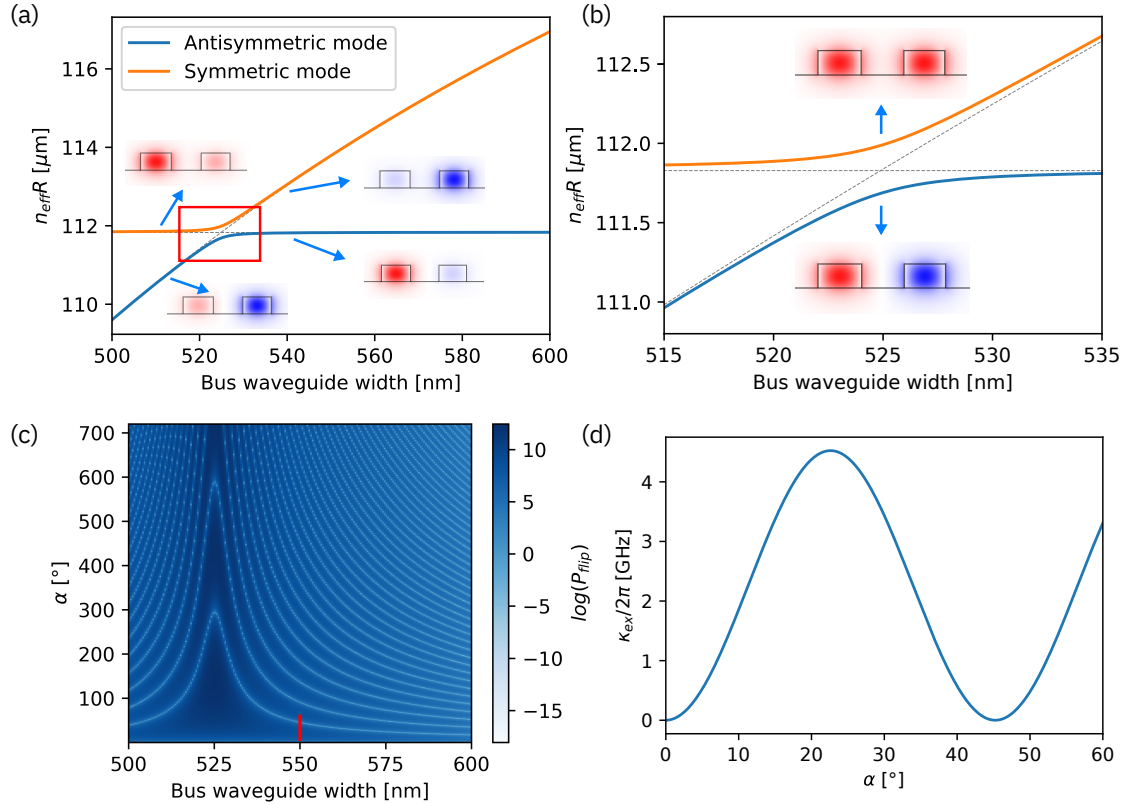


Figure A.4: Mode simulation of evanescent pulley coupler for $d = 320\text{ nm}$. (a) Radial effective mode indices of symmetric and antisymmetric coupled modes with avoided crossing as function of bus waveguide width. Bare modes are indicated as dashed gray lines. Mode profile of coupled modes at large detuning shown as horizontal component of electric field E_y . (b) Magnified view of avoided crossing (indicated by red box in (a)) with mode profile of fully hybridized modes. (c) Probability of Rabi flip P_{flip} as function of bus waveguide width and interaction angle α derived from (a). (d) cross section through (c) at 550 nm bus waveguide width for interaction angle from 0° to 60° (indicated in (c) as red line) indicating predicted external coupling rate κ_{ex} .

of the coupled modes as well as the bare modes (gray dashed) are shown in (a) as function of bus waveguide width. The dashed line ascending from the bottom left to the top right is the bus mode index, which depends, in a small range around the avoided crossing, approxi-

mately linearly on the waveguide width. In addition, the mode confinement is increased at larger widths so that the coupling between bus and resonator waveguides is reduced. In the avoided crossing, the two modes hybridize to form a symmetric (upper) and antisymmetric (lower) mode. The respective mode profiles are also shown as horizontal component of the electric field E_y in (a,b) for illustration. Equation A.5 is plotted in (c) to reveal the familiar Rabi oscillation pattern. The probability is here plotted on a logarithmic scale to improve visibility at large detuning. As expected the maximal contrast is found where bus and resonator waveguides are phase-matched, while at large detuning the contrast is reduced at an increased Rabi frequency. In the device discussed below, the bus waveguide was not phase-matched to the ring resonator at a width of $w_{\text{bus}} = 550 \text{ nm}$. The resulting coupling rate in this case calculated from Equation A.7 is shown in Figure A.4 (c). In this case one finds that, due to the large phase mismatch, one full fringe is covered even at a moderate pulley angle of $\alpha = 45^\circ$. It would in this case be preferable to improve the phase matching to the resonator to allow for a wider pulley angle and a large bus-waveguide gap. The simulation shown in Figure A.4 was carried out for a bus-waveguide gap of $d = 560 \text{ nm}$ in which case the coupling rate is greatly reduced to $\kappa_{\text{ex}}/2\pi \sim 28 \text{ MHz}$ (see Figure A.5).

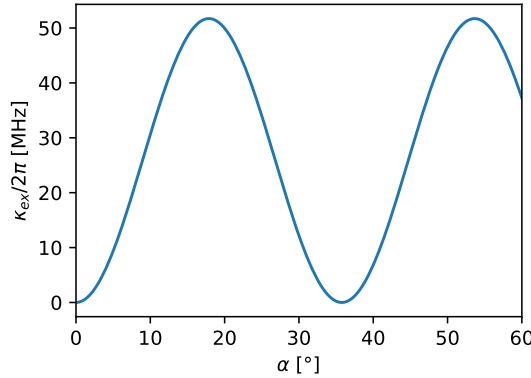


Figure A.5: Coupling rate between ring resonator ($w = 550 \text{ nm}$, $R = 50 \mu\text{m}$, $\nu_{\text{FSR}} = 254 \text{ GHz}$) at $w_{\text{bus}} = 550 \text{ nm}$ as function of pulley angle α .

A.2 Fabrication

The fabrication is identical to that of the photonic crystal cavities described in the main text. Crucially, the GaP waveguides are coated with a 10 nm thick Al_2O_3 layer. On the one hand, this improves the damage threshold of the ring resonator devices to $\sim 50 \text{ W}$ circulating power as the Al_2O_3 acts as oxygen diffusion barrier and therefore inhibits detrimental oxidation effects at the GaP surface that are otherwise observed at high power. On the other hand it was shown that such a coating may passivate the surface recombination layer that occurs at the dielectric-air interface in etched GaAs microresonators [40] which improves the quality factors of the resonator substantially. GaP devices may possess a similar surface recombination layer

that leads to optical loss and a similar passivation effect may also be present in these devices. Apart from the Al_2O_3 coating, which is deposited by atomic layer deposition, the resonators are unclad.

A.3 Resonator Quality

High optical quality factors are a crucial component for the observation of nonlinear effects as the threshold for parametric oscillations in a microresonator (from [100]) is given by

$$P_{\text{th}} \approx \frac{\pi}{4\eta} \frac{V_{\text{eff}}}{\lambda Q^2} \frac{n_g^2}{n_2} \quad (\text{A.8})$$

where η is the resonators coupling factor, V_{eff} its effective mode volume, n_g its group index and n_2 the nonlinear index of the waveguide material. Crucially, the threshold power scales inversely with the square of the resonator quality factor $P_{\text{th}} \propto \frac{1}{Q^2}$. Consequently, the required power for the observation of nonlinear effects can be dramatically improved by increasing the resonator quality factor. My contributions to this project were the design, fabrication and characterization of high quality GaP microresonators. The highest intrinsic quality factors measured in ring resonators with a $50\mu\text{m}$ radius were $Q_0 \sim 6.8 \times 10^5$, a more than one order of magnitude improvement over the previous resonators published from our group [84]. A transmission spectrum showing the best measured device and a fit to the optical cavity response are shown in Figure A.6. This allowed us to observe Kerr frequency combs with a threshold power as low as $P_{\text{th}} = 3\text{ mW}$ [100]. More improvements in the quality factor of GaP resonators could be made by employing more sophisticated passivation techniques such as the ones described by Guha et al. [40], by further improving the sidewall roughness of the etched waveguides with an optimized etching recipe, and by optimizing the coupler design further with larger pulley angles and better phase matching. Furthermore, an improved optical fiber interface of the integrated photonic circuit would allow for operation with even lower injected power and reduce reflections in the bus waveguide.

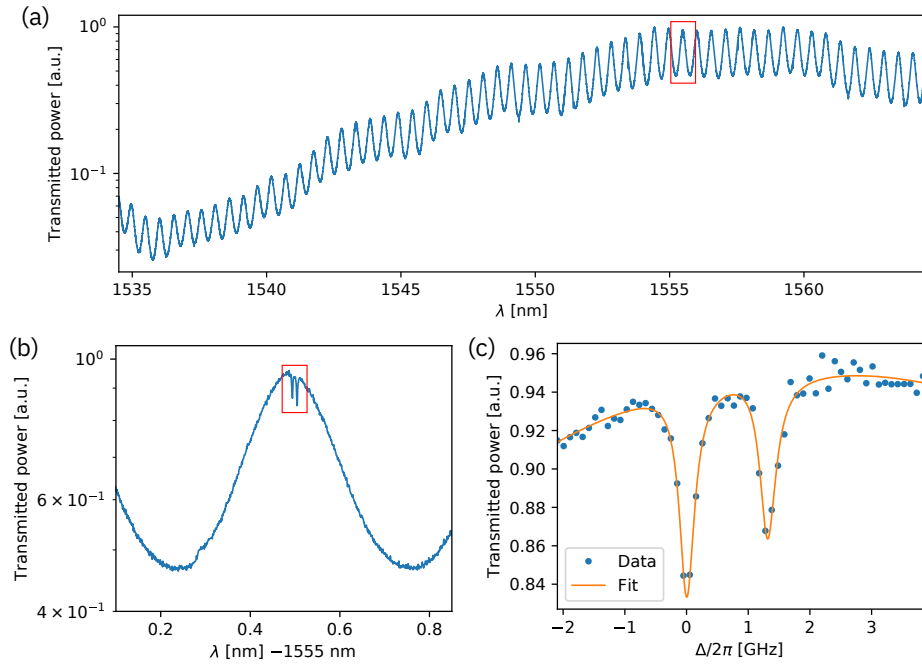


Figure A.6: (a) Transmission spectrum of ring resonator device, red box indicating position of (b). (b) Magnified view of (a) with resonance indicated by red box. (c) Fit of resonance in (b) with intrinsic quality factors $Q_0 = 6.88 \times 10^5$ ($\Delta/2\pi = 0$) and $Q_0 = 6.40 \times 10^5$ ($\Delta/2\pi = 1.3$ GHz).

B Design of Adiabatic Waveguide Coupler

Previous photonic crystal designs in our group implemented the fiber-coupling to the gallium phosphide waveguide via diffraction-grating couplers [83]. While such couplers are suitable for rapid testing of a large number of devices and easy to use in the lab, as they do not require special preparation of the fiber, they are, in the simple single-etch geometry that we use, unsuitable for measurements of photonic crystal cavities in reflection. The main reason for this is that the couplers are very poorly mode-matched to the fiber mode and the waveguide mode. This creates an etalon between the nearly perfectly reflective photonic crystal and the grating coupler that interferes with the output signal of the photonic crystal and may even couple the output field back into the cavity. To overcome this issue, a new technique of

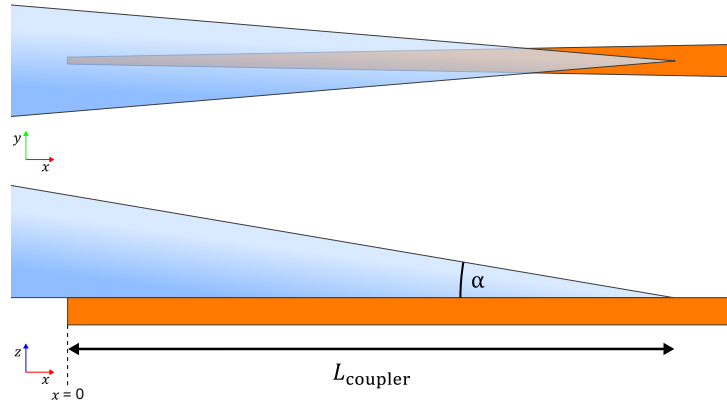


Figure B.1: Adiabatic waveguide coupler design.

fiber-chip coupling was implemented based on an adiabatic transition between the fiber and the waveguide modes, realized with an etched tapered fiber [90]. The coupler is implemented as a waveguide taper with gradually increasing width w_{wg} and effective index of refraction n_{eff} . A fiber with a complimentary taper with decreasing radius r_{fiber} and n_{eff} is brought into contact with the coupler as illustrated in Figure B.1. The increasingly evanescent field of the fiber taper then leads to a hybridization of the fiber mode with the waveguide mode. As the fiber radius

Appendix B. Design of Adiabatic Waveguide Coupler

approaches zero, the mode confinement in the hybridized mode continuously shifts from the fiber to the waveguide as illustrated in Figure B.2 in the mode field plots at the top for various values of x/L_{coupler} . The effective indices of the waveguide mode and the fiber mode

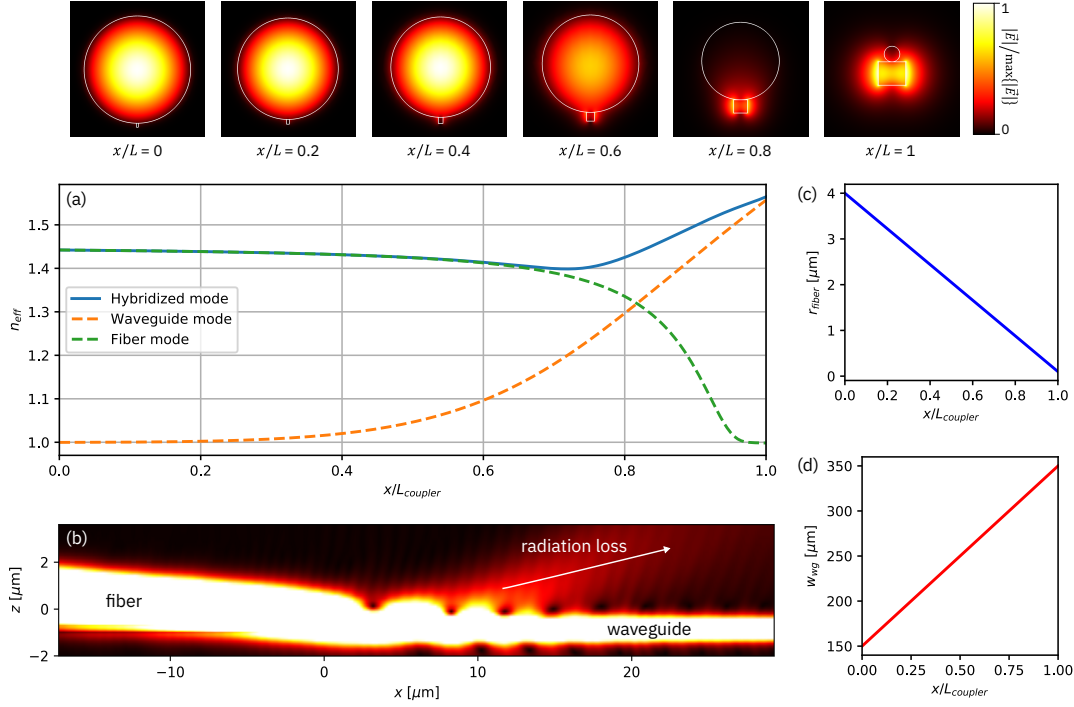


Figure B.2: Effective mode indices of hybridized fiber-waveguide mode (a) as a function of x/L_{coupler} (blue). Simulations of the fiber and waveguide modes are shown as dashed lines. Plots of the hybrid modes' electric field magnitude are shown at the top for various values of x/L_{coupler} . A Fourier transformation at $\lambda_0 = 1550 \text{ nm}$ of the time domain solution of a FDTD simulation of the mode transition is shown in (b) with decreased color range to make radiation loss at the coupler visible. The x -axes of (a) and (b) are not related. Dimensions of the fiber and the waveguide as functions of x/L_{coupler} are shown in (c) and (d), respectively.

as a function of x/L_{coupler} simulated individually are shown as dashed lines in Figure B.2 (a). The hybridized mode is shown as blue line. For $x/L_{\text{coupler}} \leq 0.4$ the mode is mostly confined in the fiber, and n_{eff} of the fiber is relatively constant. For $x/L_{\text{coupler}} > 0.4$, corresponding to $r_{\text{fiber}} < 1650 \text{ nm}$, the mode confinement increasingly shifts from the waveguide to the fiber, as evident from the deviation of the hybrid mode curve in Figure B.2 (a) from the fiber mode towards the waveguide mode, analogous to an avoided crossing between two energy levels of a coupled oscillator system. For $r_{\text{fiber}} \rightarrow 0$ the fiber mode transitions into a free-space mode with $n_{\text{eff}} = 1$. The primary goal to maximize coupling efficiency is for the optical field to move 'adiabatically' through this avoided crossing – that is, slower than the Landau-Zener velocity. The adiabaticity can be tested in a finite-difference time-domain (FDTD) simulation as shown in Figure B.2 (b) by launching an optical pulse through an input port into the fiber on the input (left) side and analyzing the transmission through the waveguide mode on the output

(right) side. For $L_{\text{coupler}} \gg \lambda$ (where λ is the center wavelength of the pulse) the transmission $T(\lambda)$ approaches unity. For $L_{\text{coupler}} \approx 50\mu\text{m}$ a transmission $T(1550\text{nm}) = 69\%$ was achieved in this simulation. The insertion loss of the coupler is dominated by radiation loss at the mode transition as indicated in Figure B.2 (b). The result indicates that the coupling is not yet completely adiabatic, but $50\mu\text{m}$ represent a good trade-off between mechanical stability of the released coupler and coupling efficiency. The major advantage of this coupler implementation compared to diffraction gratings, besides superior coupling efficiency and bandwidth, is that light which is lost in the coupler generally does not couple back into the fiber or the waveguide, but to free-space, eliminating back-reflections in the system.

C Fabrication of Etched Tapered Fibers

The fabrication procedure of sharp fiber tips, initially pioneered for the fabrication of tips for scanning near-field optical microscopy [95], is very straight-forward. A fiber is dipped into hydrofluoric acid or a similar etchant. The etchant attacks the optical fiber and reduces its radius. At the same time, capillary forces create a meniscus at the air-etchant-fiber interface and the etchant creeps up the edges of the fiber. As the etching proceeds the meniscus lowers and a taper forms naturally at the edges of the fiber. This process can be supported by adding a layer of a solvent with low surface tension on top of the etchant which can enhance the formation of the meniscus. In other implementations the etchant slowly evaporates and the taper angle is changed due to the fact that the level of the etchant lowers. The taper angle can be controlled by slowly pulling the fiber from the etchant. Depending on the pulling speed a virtually arbitrarily small taper angle can be achieved. The etching naturally stops at the tip of the fiber. This method can produce very sharp fiber tips with an apex radius $< 50\text{ nm}$. A schematic representation of the etching process is shown in Figure C.1.

C.1 Etching Rig

Pulling of the fiber requires a stage with high precision and the capability of performing small, repeatable steps. In place of a costly precision stage, the advent of consumer 3D printers has provided a cost-effective alternative. In this case, a *Wanhao* Duplicator i3 mini was modified by removing the print-head and replacing it with an aluminum adapter plate. A fiber mounting system was designed and 3D-printed which allows simultaneous etching of eighteen identical tapered fibers. The 3D printer can be programmed with G-code and the stepper motor is capable of retracting the fiber repeatably in $5\text{ }\mu\text{m}$ steps.

A typical fiber tip produced with this method without continuous retraction of the fiber during the etching is shown in Figure C.2. The cladding of the fiber is thinned down additionally to provide more flexibility to the fiber tip and to reduce contact area with the substrate when the fiber is aligned. An optical micrograph of the fiber tip is shown in panel (a), scanning electron micrographs are shown in panels (b-d). The etching process produces a very sharp tip (in this case with an apex $\sim 40\text{ nm}$), but leaves the surface somewhat rough. This is typical

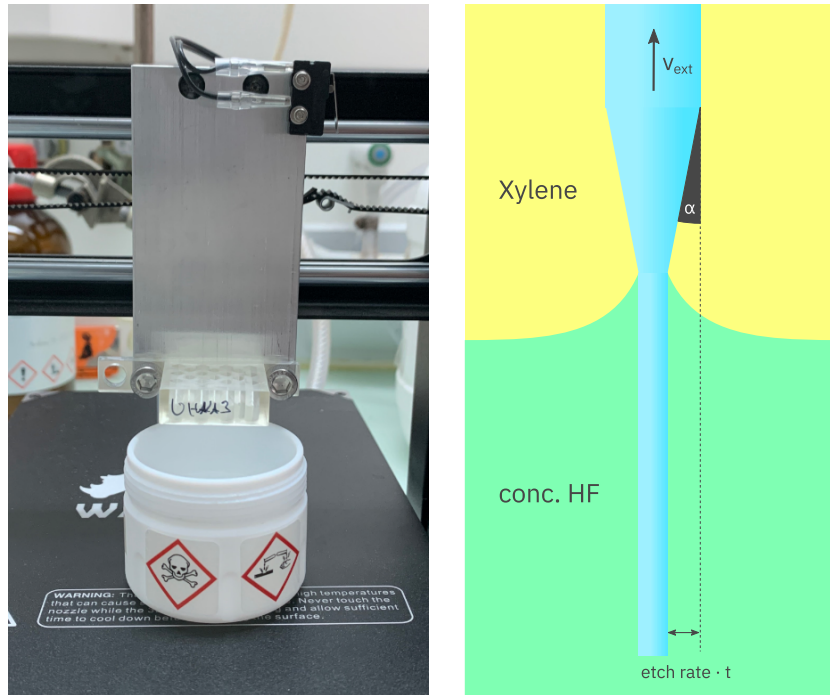


Figure C.1: Fiber etching setup comprising 3D printer (left). White beaker with hazard symbols contains concentrated HF, fibers are dipped into HF with 3D printer stage and held in place with 3D-printed holder (translucent plastic). Schematic of etching process (right).

for etched fiber tips and is primarily due to an initial surface roughness of the fiber that is transferred onto the taper and is amplified due to the reduced fiber diameter. On the other hand the etching in concentrated HF also introduces some additional surface roughness. The roughness has a typical length-scale of $\mathcal{O}(100\text{ nm})$ and is significantly shorter-range than the optical wavelength $\sim 1\text{ }\mu\text{m}$ (in the fiber). It is therefore not expected that scattering due to the surface roughness is a major issue. For future implementations one might strive to improve the fiber's surface finish by reflow of the fiber. This can be achieved by placing the fiber in a ceramic ferrule and heating it with a torch above the glass-transition temperature of SiO_2 . In this implementation concentrated hydrofluoric acid (48 %) was used as etchant and a thin film of Xylene was added as top layer to increase the formation of a meniscus.

C.2 Impact of Differential Etch Rate

Optical fibers typically consist of a core and a cladding. The core guides the light and the cladding provides isolation from the environment. Consequently, the core requires a higher index of refraction than the cladding. This is typically achieved by doping the core with a different material, e.g. Germanium. This has an impact on the etch rate in hydrofluoric acid. In this case, the core of the optical fiber is etched at a rate of $3.447\text{ }\mu\text{m/min}$ while the cladding is etched at a rate of $1.645\text{ }\mu\text{m/min}$ for *Corning* SMF-28 Ultra. This leads to a steeper taper

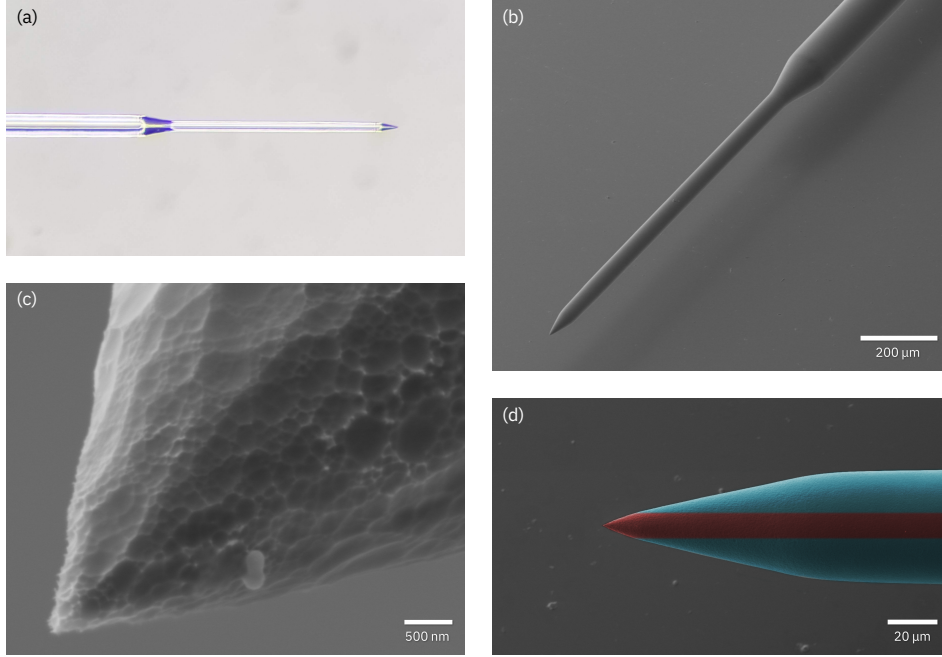


Figure C.2: Optical micrograph of fiber tip etched without continuous retraction (a). Low magnification SEM micrograph of tip (b). Magnified view of etched tip (c) with apex radius of ~ 40 nm and colorized SEM image indicating the cladding (blue) and core (red) of fiber (d).

angle of the fiber at the core as shown in Figure C.2 (d). This must be taken into account when the etching process is designed.

C.3 Etching procedure

In order to produce a tip with an arbitrary taper angle it is necessary to pull the fiber out of the etchant instead of letting the etching self-terminate. When the fiber is dipped into the etchant the interface between HF and the solvent creates a meniscus at the interface of the fiber which pulls the HF up the fiber to a certain degree. The meniscus lowers as the fiber is etched, leading to a linear tapering of the fiber. This self-terminated fiber tip has a pre-defined taper angle which largely depends on the properties of the solvent. In case of Xylene the angle α' of the cladding is 11.86° while the angle of the core is $\alpha = 23.75^\circ$. The relevant parameter here is the core angle, as this is where the mode transition from fiber to waveguide occurs. As the core has an inferred etch rate of $3.447 \mu\text{m}/\text{min}$ we can deduce the speed at which we have to pull to obtain the desired taper angle α .

The tangent of α is given by the ratio of the initial radius of the fiber and the desired length of the taper:

$$\tan(\alpha) = \frac{R_{\text{initial}}}{L}. \quad (\text{C.1})$$

Appendix C. Fabrication of Etched Tapered Fibers

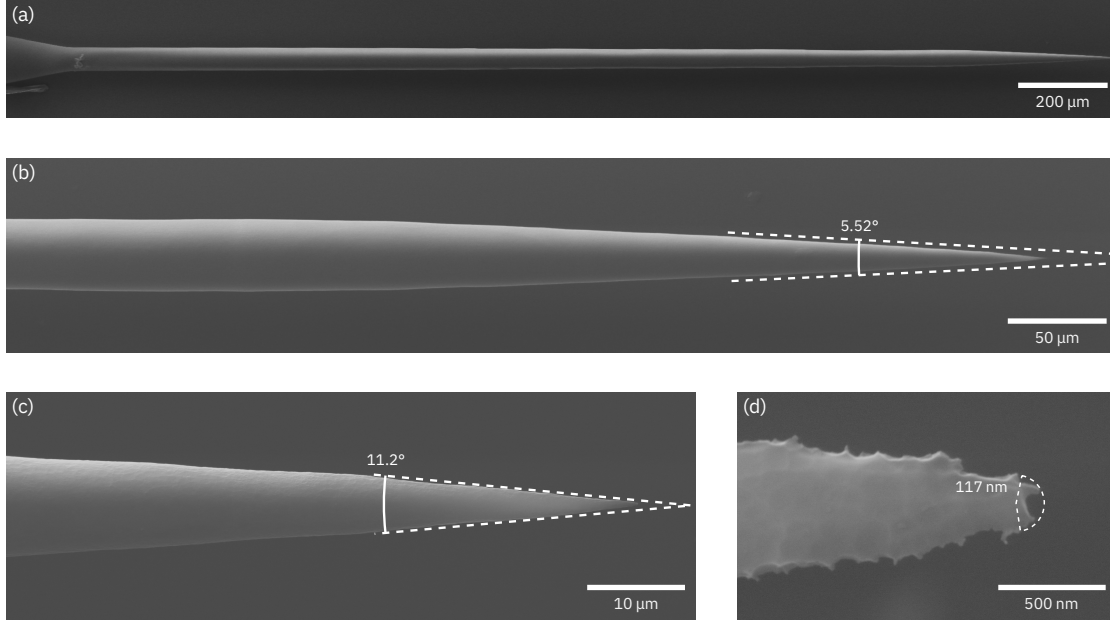


Figure C.3: Tip fabricated by retracting fiber during etching. Low-magnification SEM micrograph (a), view of entire tip (b) with indicated cladding angle $2\alpha_{\text{clad}}$, magnified view of tip (c) with indicated core angle $2\alpha_{\text{core}}$ and micrograph of apex (d) with indicated apex radius.

The total length of the taper at the end of the process is given as the length of the naturally formed taper L_0 , which is assumed to be independent of the pulling speed as the part of the fiber which is immersed in HF should have a constant cross section,

$$L = L_0 + L_{\text{pull}} \quad (\text{C.2})$$

and the additional length L_{pull} , which is given by the elapsed time and the pulling speed, as the part of the fiber which transitions from HF to Xylene stops being etched.

$$L_{\text{pull}} = v_{\text{ext}} \cdot t \quad (\text{C.3})$$

As the taper etching self-terminates after the fiber is fully extracted from the HF the process stops after the elapsed time $t = t_{\text{term}}$ with the condition

$$R_{\text{initial}} = ER \cdot t_{\text{term}} \quad (\text{C.4})$$

with the core etch rate ER . At $t = t_{\text{term}}$ the process self-terminates, hence, the added taper length by pulling the fiber out of the etchant is

$$L_{\text{pull}} = v_{\text{ext}} \cdot t_{\text{term}} = v_{\text{ext}} \frac{R_{\text{initial}}}{ER} \quad (\text{C.5})$$

With a given α we can deduce the required pulling speed from Equation C.1 as

$$L_{\text{pull}} = v_{\text{ext}} \frac{R_{\text{initial}}}{ER} \quad (\text{C.6})$$

$$\Leftrightarrow v_{\text{ext}} = (L - L_0) \cdot \frac{ER}{R_{\text{initial}}} \quad (\text{C.7})$$

$$\Leftrightarrow v_{\text{ext}} = \left(\frac{R_{\text{initial}}}{\tan(\alpha)} - \frac{R_{\text{initial}}}{\tan(\alpha_0)} \right) \cdot \frac{ER}{R_{\text{initial}}} \quad (\text{C.8})$$

$$\Leftrightarrow v_{\text{ext}} = \left(\frac{1}{\tan(\alpha)} - \frac{1}{\tan(\alpha_0)} \right) \cdot ER \quad (\text{C.9})$$

The feed-rate of the 3D printer can be obtained from this equation. A G-code program is most efficiently implemented by defining a constant step size of $5\text{ }\mu\text{m}$ and a resting time that the printer must wait between each step. The resting time is

$$T_{\text{rest}} = \frac{5\text{ }\mu\text{m}}{v_{\text{ext}}} \quad (\text{C.10})$$

C.4 Post Processing

After retraction of the fibers from the HF bath the fiber tips contains both residues of HF and of Xylene that must be removed. The fibers should not be cleaned mechanically as this can break off the fragile fiber tips. Instead, the fibers can be dipped in a water bath and subsequently in a bath of isopropyl alcohol. This can be included into the 3D printer program as a subroutine. In addition, the fiber tips can be dipped into piranha solution to remove all remaining organic residues.

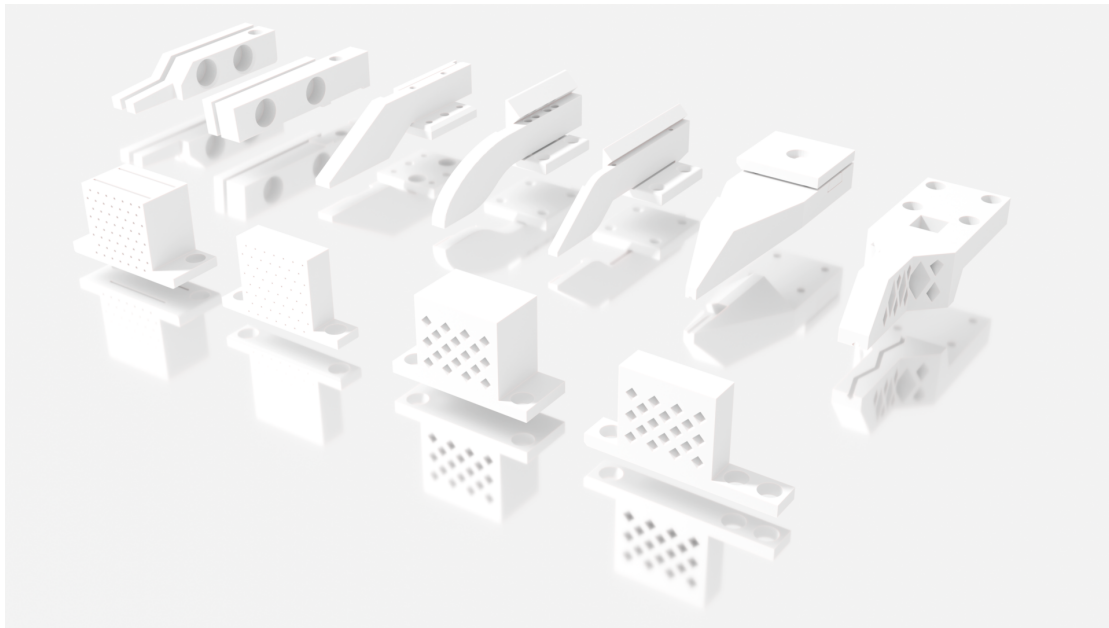


Figure C.4: Various generations of designs of fiber holders for fiber alignment (back) and etching (front).

D Fiber mounting and optical alignment

In order to couple an etched fiber tip to an integrated photonic device it must be mounted to an alignment stage at the correct angle (taper angle). This angle can be determined beforehand for each fiber batch with scanning electron microscopy. The fiber is fixed to an aluminum bracket with epoxy and scotch tape. Various sophisticated, 3D-printed designs have been implemented and are shown in Figure C.4, but none has proven to be as stable as a fixation with Araldite and scotch tape to an aluminum bracket. An image of the installed tapered fiber tip is shown in Figure D.1. The bracket is mounted on a manual goniometer which allows adjustment of the fiber approach angle. The assembly is then mounted to a *SmarAct* slip-stick piezo precision alignment stage that allows the adjustment of the fiber position with < 100 nm accuracy.

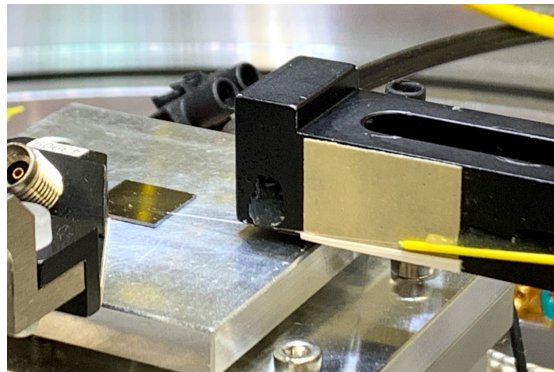


Figure D.1: Fiber mounted on alignment stage for optical measurement.

E Fiber Packaging

Optical coupling of integrated photonic waveguides in a dilution refrigerator is most efficiently achieved by packaging, or 'pig-tailing' the photonic circuits. Similar to wire-bonding, pig-tailing refers to permanently fixing an optical fiber to the optical input port of the photonic circuit. To that end, the coupler is typically immersed in a matrix of optically clear UV-curable adhesive that maintains optical alignment. In coupling architectures such as edge couplers and diffraction grating this is relatively trivial, as the adhesives that are typically used for such applications even improve the mode-matching between chip and fiber facets. An adiabatic coupler however, strongly depends on the refractive index of the surrounding medium being low, that is, the minimum index of refraction of the hybridized mode, as shown in Figure B.2, must be higher than that of the environment, or the coupler will suffer from serious radiation loss. Therefore, the coupler cannot be simply immersed in conventional UV adhesives, which typically have $n > 1.46$, that of glass, while the hybrid mode typically has its mode transition at a lower index than that, since it depends on a significant evanescent optical field. There are two possible solutions. Either, a low-index adhesive can be used, these are typically fluorinated and require an inert atmosphere for curing (i.e. an oxygen-free atmosphere). This increases the complexity of the optical setup as it requires the adhesive to be dispensed and cured in a sealed chamber. Alternatively, an optical fiber with a higher effective refractive index can be used. This is achieved with a stronger doping profile of the core which increases confinement of the optical mode. This is commonly done in optical fibers with high numerical aperture – or high-NA fibers – which are, ironically, designed for improved fiber-chip edge-coupling by improving the mode matching between the fiber mode and the waveguide mode.

E.1 Etching of Ultra-High NA Fibers

Fiber tapers fabricated from *Nufern* UHNA 7 by etching in concentrated HF were explored as an alternative to the use of low-refractive index adhesives. An etched UHNA 7 fiber tip is shown in Figure E.1. The core is in this case found to have a vastly higher etch rate than the cladding, which leads to the formation of a channel in the fiber tip, as seen in the optical micrograph in panel (a) with the cladding forming a thin shell. This is problematic as there is

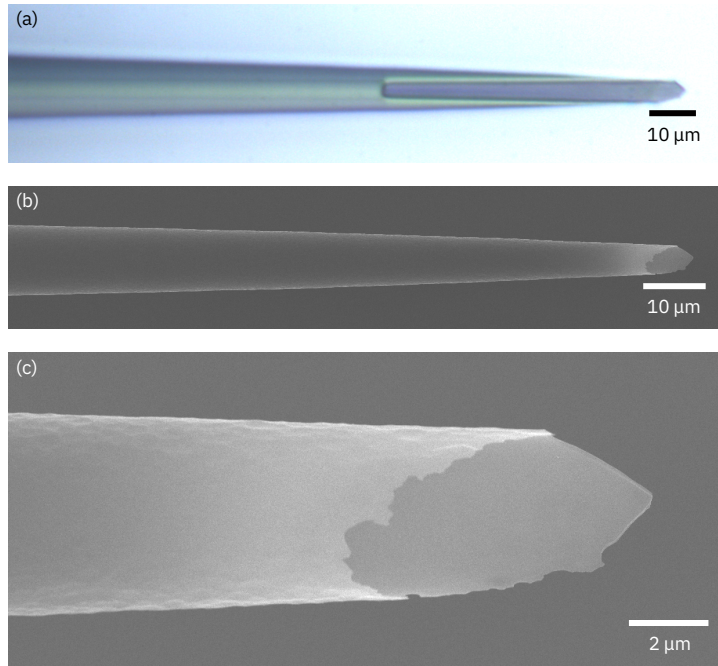


Figure E.1: Fiber tip etched with concentrated HF from *Nufern* UHNA 7 fiber. Optical micrograph (a) and SEM micrographs (b,c)

now a sharp transition of the fiber mode into the hollow-core tip, an unusable result for an adiabatic coupler. We may conclude from this experiment that an adiabatic coupler based on UHNA fibers with an excessively high Ge doping is not feasible for etched fiber tips. Alternative approaches where the tip is formed in a heat-and-pull rig might produce a usable fiber tip.

E.2 Packaging Procedure and UV Curing

Packaging of an adiabatic coupler is a balance act. Firstly, an adhesive must be chosen that has a sufficiently low refractive index. Here, we choose *Norland* NOA81, an un-fluorinated adhesive which has a refractive index matched to that of SiO_2 , as the polymer matrix in which the coupler is embedded. Since NOA81 exhibits an inferior mechanical stability, we use NOA65 as adhesive for a secondary contact point between the fiber and the chip. The primary contact point, i.e. the matrix in which the coupler is embedded, serves to maintain the alignment, while the secondary contact point provides mechanical stability. Secondly, capillary action between the fiber tip and the substrate created by the substrate-liquid-fiber interface can develop substantial forces that may stall the fiber alignment when the epoxy is applied. This may lead one to believe that an adhesive with low viscosity and surface tension is necessary. This, however, complicates the local application of the adhesive, since such adhesives with low surface tension tend to wet the substrate uncontrollably and even extend to the device, rendering it useless.

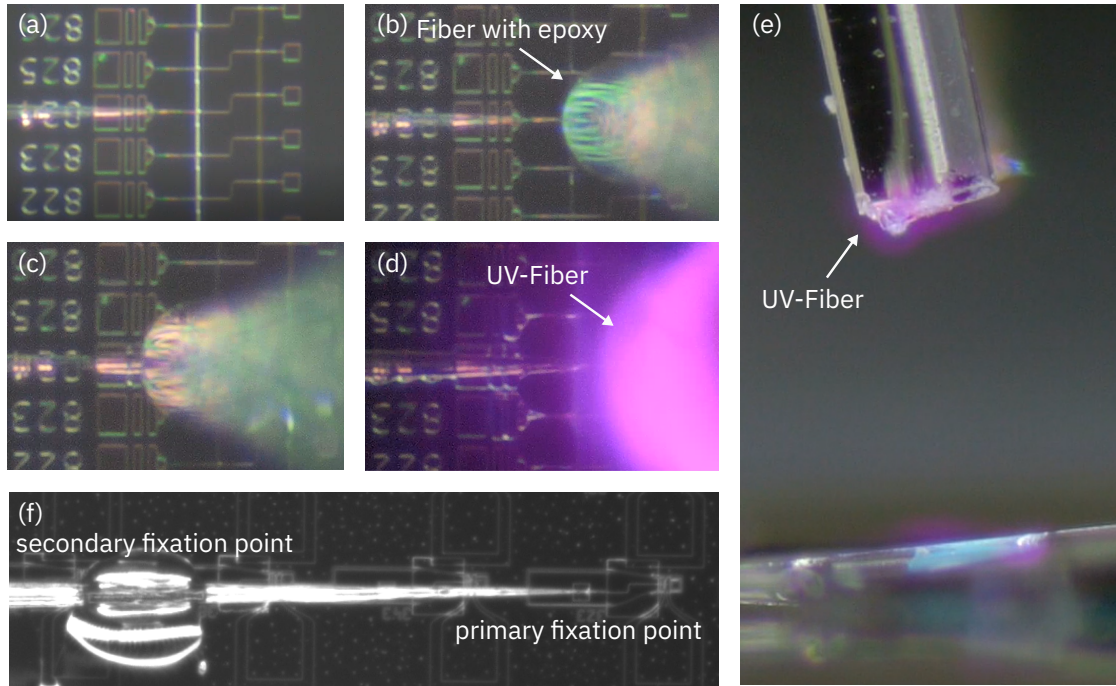


Figure E.2: Fiber packaging procedure. Fiber tip with thin coating of NOA81 is aligned to coupler (a) and cured (d,e). Secondary fixation point with NOA65 is applied with auxiliary fiber (b,c) and cured (d,e). Packaged fiber is shown in (f).

E.2.1 Primary Fixation

The primary fixation points serves to maintain coupling between fiber and waveguide during the packaging procedure. Due to capillary action, it is impossible to fix the fiber, in contact with the substrate, to the waveguide, away from the coupler, without also wetting the coupler with adhesive. Therefore, it is the better strategy to completely embed the coupler in adhesive. This requires the adhesive to have appropriate optical properties, such as a low refractive index and high optical clarity. In addition, the adhesive must be applied such that capillary forces do not destroy the coupler – a $\sim 50\mu\text{m}$ long suspended structure with $\sim 1\mu\text{m}$ gap to the substrate. The best strategy to achieve that is to dip the tapered fiber tip into an adhesive droplet and pull it out while in contact with the substrate – as one would remove excessive paint from a brush. Then, with a thin epoxy coating, the fiber is first aligned in plane through the top alignment microscope, while the taper is not in contact with the coupler, cf. Figure E.2 (a). When aligned, the fiber is brought into contact and coupling is optimized. Subsequently, the adhesive is cured locally with a UV fiber, cf. Figure E.2 (d,e).

E.2.2 Secondary fixation

Once the primary fixation is cured, a second fiber is dipped into an adhesive droplet. This method, while seeming crude, has proven to be the only method with which a sufficiently

Appendix E. Fiber Packaging

small volume $\sim 500\text{pl}$ can be dispensed repeatably. The adhesive application procedure is shown in Figure E.2 (b,c). In the shown image sequence, the adhesive was applied directly to the coupler on-top of the primary fixation point. We have since found that it is preferable to introduce the secondary fixation further away from the coupler, as shown in Figure E.2 (f). As before, the adhesive is cured with a UV fiber. With this method, we could maintain optical coupling after removing the fiber from the alignment mechanism, and even when the sample was cooled to liquid nitrogen temperatures $\sim 80\text{K}$. However, we have observed an increased optical insertion loss and more work in this direction is needed to perfect the procedure. Fluorinated adhesives with even lower refractive index might improve the process further.

Bibliography

- [1] S. Abel, F. Eltes, J. E. Ortmann, A. Messner, P. Castera, T. Wagner, D. Urbonas, A. Rosa, A. M. Gutierrez, D. Tulli, et al. Large pockels effect in micro-and nanostructured barium titanate integrated on silicon. *Nature materials*, 18(1):42–47, 2019.
- [2] V. Ambegaokar and A. Baratoff. Tunneling between superconductors. *Physical Review Letters*, 10(11):486, 1963.
- [3] R. W. Andrews, R. W. Peterson, T. P. Purdy, K. Cicak, R. W. Simmonds, C. A. Regal, and K. W. Lehnert. Bidirectional and efficient conversion between microwave and optical light. *Nature Physics*, 10(4):321–326, 2014.
- [4] G. Arnold, M. Wulf, S. Barzanjeh, E. Redchenko, A. Rueda, W. J. Hease, F. Hassani, and J. M. Fink. Converting microwave and telecom photons with a silicon photonic nanomechanical interface. *Nature communications*, 11(1):1–7, 2020.
- [5] P. Arrangoiz-Arriola, E. A. Wollack, Z. Wang, M. Pechal, W. Jiang, T. P. McKenna, J. D. Witmer, R. Van Laer, and A. H. Safavi-Naeini. Resolving the energy levels of a nanomechanical oscillator. *Nature*, 571(7766):537–540, 2019.
- [6] M. Aspelmeyer, T. J. Kippenberg, and F. Marquardt. Cavity optomechanics. *Reviews of Modern Physics*, 86(4):1391, 2014.
- [7] K. C. Balram, M. Davanço, J. Y. Lim, J. D. Song, and K. Srinivasan. Moving boundary and photoelastic coupling in GaAs optomechanical resonators. *Optica*, 1(6):414–420, 2014.
- [8] K. C. Balram, M. I. Davanço, J. D. Song, and K. Srinivasan. Coherent coupling between radiofrequency, optical and acoustic waves in piezo-optomechanical circuits. *Nature photonics*, 10(5):346–352, 2016.
- [9] Y. Baumgartner. *A CMOS-Compatible Hybrid III-V/Si Photonic Platform for High-Speed Transceivers*. PhD thesis, ETH Zurich, 2020.
- [10] C. H. Bennett, G. Brassard, C. Crépeau, R. Jozsa, A. Peres, and W. K. Wootters. Teleporting an unknown quantum state via dual classical and einstein-podolsky-rosen channels. *Physical review letters*, 70(13):1895, 1993.

Bibliography

- [11] C. H. Bennett, G. Brassard, S. Popescu, B. Schumacher, J. A. Smolin, and W. K. Wootters. Purification of noisy entanglement and faithful teleportation via noisy channels. *Physical review letters*, 76(5):722, 1996.
- [12] C. H. Bennett, D. P. DiVincenzo, J. A. Smolin, and W. K. Wootters. Mixed-state entanglement and quantum error correction. *Physical Review A*, 54(5):3824, 1996.
- [13] A. Bienfait, K. J. Satzinger, Y. Zhong, H.-S. Chang, M.-H. Chou, C. R. Conner, É. Dumur, J. Grebel, G. A. Peairs, R. G. Povey, et al. Phonon-mediated quantum state transfer and remote qubit entanglement. *Science*, 364(6438):368–371, 2019.
- [14] F. Bloch. Über die Quantenmechanik der Elektronen in Kristallgittern. *Zeitschrift für physik*, 52(7-8):555–600, 1929.
- [15] J. Bochmann, A. Vainsencher, D. D. Awschalom, and A. N. Cleland. Nanomechanical coupling between microwave and optical photons. *Nature Physics*, 9(11):712–716, 2013.
- [16] R. Camley, B. Djafari-Rouhani, L. Dobrzynski, and A. Maradudin. Transverse elastic waves in periodically layered infinite and semi-infinite media. *Physical Review B*, 27(12):7318, 1983.
- [17] J. Chan. *Laser cooling of an optomechanical crystal resonator to its quantum ground state of motion*. PhD thesis, California Institute of Technology, 2012.
- [18] J. Chan, T. M. Alegre, A. H. Safavi-Naeini, J. T. Hill, A. Krause, S. Gröblacher, M. Aspelmeyer, and O. Painter. Laser cooling of a nanomechanical oscillator into its quantum ground state. *Nature*, 478(7367):89–92, 2011.
- [19] J. Chan, A. H. Safavi-Naeini, J. T. Hill, S. Meenehan, and O. Painter. Optimized optomechanical crystal cavity with acoustic radiation shield. *Applied Physics Letters*, 101(8):081115, 2012.
- [20] Y. Chu, P. Kharel, W. H. Renninger, L. D. Burkhardt, L. Frunzio, P. T. Rakich, and R. J. Schoelkopf. Quantum acoustics with superconducting qubits. *Science*, 358(6360):199–202, 2017.
- [21] Y. Chu, P. Kharel, T. Yoon, L. Frunzio, P. T. Rakich, and R. J. Schoelkopf. Creation and control of multi-phonon fock states in a bulk acoustic-wave resonator. *Nature*, 563(7733):666–670, 2018.
- [22] M. Churaev, S. Honl, R. N. Wang, C. Mohl, T. Liu, J. C. Skehan, J. Riemensberger, D. Caimi, J. Liu, P. Seidler, et al. Hybrid Si₃N₄-LiNbO₃ integrated platform for electro-optic conversion. In *CLEO: Science and Innovations*, pages STh1F–3. Optical Society of America, 2020.
- [23] A. N. Cleland. *Foundations of nanomechanics: from solid-state theory to device applications*. Springer Science & Business Media, 2013.

-
- [24] L. Czornomaz. *Hybrid InGaAs/SiGe technology platform for CMOS applications*. PhD thesis, Université de Grenoble Alpes.
- [25] N. Daix, E. Uccelli, L. Czornomaz, D. Caimi, C. Rossel, M. Sousa, H. Siegwart, C. Marchiori, J. Hartmann, K.-T. Shiu, et al. Towards large size substrates for III-V co-integration made by direct wafer bonding on Si. *APL materials*, 2(8):086104, 2014.
- [26] M. H. Devoret, A. Wallraff, and J. M. Martinis. Superconducting qubits: A short review. *arXiv preprint cond-mat/0411174*, 2004.
- [27] R. Dixon. Photoelastic properties of selected materials and their relevance for applications to acoustic light modulators and scanners. *Journal of Applied Physics*, 38(13): 5149–5153, 1967.
- [28] L.-M. Duan, M. D. Lukin, J. I. Cirac, and P. Zoller. Long-distance quantum communication with atomic ensembles and linear optics. *Nature*, 414(6862):413–418, 2001.
- [29] M. Eichenfield, J. Chan, R. M. Camacho, K. J. Vahala, and O. Painter. Optomechanical crystals. *Nature*, 462(7269):78–82, 2009.
- [30] F. Eltes. *Barium titanate Pockels modulators integrated with silicon photonic circuits*. PhD thesis, ETH Zurich, 2019.
- [31] J. Eppele, C. Sanchez, T. Chung, K. Cheng, and K. Hsieh. Dry etching of GaP with emphasis on selective etching over AlGaP. *Journal of Vacuum Science & Technology B: Microelectronics and Nanometer Structures Processing, Measurement, and Phenomena*, 20(6):2252–2255, 2002.
- [32] L. Fan, C.-L. Zou, R. Cheng, X. Guo, X. Han, Z. Gong, S. Wang, and H. X. Tang. Superconducting cavity electro-optics: a platform for coherent photon conversion between superconducting and photonic circuits. *Science advances*, 4(8):eaar4994, 2018.
- [33] G. Floquet. Sur les équations différentielles linéaires à coefficients périodiques. In *Annales scientifiques de l'École normale supérieure*, volume 12, pages 47–88, 1883.
- [34] M. Forsch, R. Stockill, A. Wallucks, I. Marinković, C. Gärtner, R. A. Norte, F. van Otten, A. Fiore, K. Srinivasan, and S. Gröblacher. Microwave-to-optics conversion using a mechanical oscillator in its quantum ground state. *Nature Physics*, 16(1):69–74, 2020.
- [35] W. Fu, M. Xu, X. Liu, C.-L. Zou, C. Zhong, X. Han, M. Shen, Y. Xu, R. Cheng, S. Wang, et al. Ground-state pulsed cavity electro-optics for microwave-to-optical conversion. *arXiv preprint arXiv:2010.11392*, 2020.
- [36] W. Fu, M. Xu, X. Liu, C.-L. Zou, C. Zhong, X. Han, M. Shen, Y. Xu, R. Cheng, S. Wang, et al. Cavity electro-optic circuit for microwave-to-optical conversion in the quantum ground state. *Physical Review A*, 103(5):053504, 2021.

Bibliography

- [37] S. M. Girvin. *Circuit QED: Superconducting Qubits Coupled to Microwave Photons*, volume 96 of *Quantum Machines: Measurement and Control of Engineered Quantum Systems: Lecture Notes of the Les Houches Summer School*. Oxford University Press, Oxford, 2011.
- [38] D. Glowacka, D. Goldie, S. Withington, H. Muhammad, G. Yassin, and B. Tan. Development of a NbN deposition process for superconducting quantum sensors. *arXiv preprint arXiv:1401.2292*, 2014.
- [39] M. Gorodetsky, A. Schliesser, G. Anetsberger, S. Deleglise, and T. J. Kippenberg. Determination of the vacuum optomechanical coupling rate using frequency noise calibration. *Optics express*, 18(22):23236–23246, 2010.
- [40] B. Guha, F. Marsault, F. Cadiz, L. Morgenroth, V. Ulin, V. Berkovitz, A. Lemaître, C. Gomez, A. Amo, S. Combrié, et al. Surface-enhanced gallium arsenide photonic resonator with quality factor of 6×10^6 . *Optica*, 4(2):218–221, 2017.
- [41] T. Guruswamy, D. J. Goldie, and S. Withington. Nonequilibrium superconducting thin films with sub-gap and pair-breaking photon illumination. *Superconductor Science and Technology*, 28(5):054002, 2015.
- [42] X. Han, C. Xiong, K. Y. Fong, X. Zhang, and H. X. Tang. Triply resonant cavity electro-optomechanics at X-band. *New Journal of Physics*, 16(6):063060, 2014.
- [43] X. Han, K. Y. Fong, and H. X. Tang. A 10-ghz film-thickness-mode cavity optomechanical resonator. *Applied Physics Letters*, 106(16):161108, 2015.
- [44] X. Han, C.-L. Zou, and H. X. Tang. Multimode strong coupling in superconducting cavity piezoelectromechanics. *Physical review letters*, 117(12):123603, 2016.
- [45] X. Han, W. Fu, C. Zhong, C.-L. Zou, Y. Xu, A. Al Sayem, M. Xu, S. Wang, R. Cheng, L. Jiang, et al. Cavity piezo-mechanics for superconducting-nanophotonic quantum interface. *Nature communications*, 11(1):1–8, 2020.
- [46] X. Han, W. Fu, C.-L. Zou, L. Jiang, and H. X. Tang. Microwave-optical quantum frequency conversion. *Optica*, 8(8):1050–1064, 2021.
- [47] W. Hease, A. Rueda, R. Sahu, M. Wulf, G. Arnold, H. G. Schwefel, and J. M. Fink. Bidirectional electro-optic wavelength conversion in the quantum ground state. *PRX Quantum*, 1(2):020315, 2020.
- [48] T. Herr. Solitons and dynamics of frequency comb formation in optical microresonators. Technical report, EPFL, 2013.
- [49] A. P. Higginbotham, P. Burns, M. Urmey, R. Peterson, N. Kampel, B. Brubaker, G. Smith, K. Lehnert, and C. Regal. Harnessing electro-optic correlations in an efficient mechanical converter. *Nature Physics*, 14(10):1038–1042, 2018.

-
- [50] J. Holzgrafe, N. Sinclair, D. Zhu, A. Shams-Ansari, M. Colangelo, Y. Hu, M. Zhang, K. K. Berggren, and M. Lončar. Cavity electro-optics in thin-film lithium niobate for efficient microwave-to-optical transduction. *arXiv preprint arXiv:2005.00939*, 2020.
 - [51] S. Hönl, H. Hahn, Y. Baumgartner, L. Czornomaz, and P. Seidler. Highly selective dry etching of GaP in the presence of $\text{Al}_x\text{Ga}_{1-x}\text{P}$ with a $\text{SiCl}_4/\text{SF}_6$ plasma. *Journal of Physics D: Applied Physics*, 51(18):185203, 2018.
 - [52] W. Jiang, R. N. Patel, F. M. Mayor, T. P. McKenna, P. Arrangoiz-Arriola, C. J. Sarabalis, J. D. Witmer, R. Van Laer, and A. H. Safavi-Naeini. Lithium niobate piezo-optomechanical crystals. *Optica*, 6(7):845–853, 2019.
 - [53] W. Jiang, C. J. Sarabalis, Y. D. Dahmani, R. N. Patel, F. M. Mayor, T. P. McKenna, R. Van Laer, and A. H. Safavi-Naeini. Efficient bidirectional piezo-optomechanical transduction between microwave and optical frequency. *Nature communications*, 11(1):1–7, 2020.
 - [54] J. D. Joannopoulos, S. G. Johnson, J. N. Winn, and R. D. Meade. Molding the flow of light. *Princeton Univ. Press, Princeton, NJ [ua]*, 2008.
 - [55] S. G. Johnson, M. Ibanescu, M. Skorobogatiy, O. Weisberg, J. Joannopoulos, and Y. Fink. Perturbation theory for maxwell's equations with shifting material boundaries. *Physical review E*, 65(6):066611, 2002.
 - [56] P. Jurcevic, A. Javadi-Abhari, L. S. Bishop, I. Lauer, D. F. Bogorin, M. Brink, L. Capelluto, O. Günlük, T. Itoko, N. Kanazawa, et al. Demonstration of quantum volume 64 on a superconducting quantum computing system. *arXiv preprint arXiv:2008.08571*, 2020.
 - [57] M. Kjaergaard, M. E. Schwartz, J. Braumüller, P. Krantz, J. I.-J. Wang, S. Gustavsson, and W. D. Oliver. Superconducting qubits: Current state of play. *Annual Review of Condensed Matter Physics*, 11:369–395, 2020.
 - [58] J. Koch, M. Y. Terri, J. Gambetta, A. A. Houck, D. Schuster, J. Majer, A. Blais, M. H. Devoret, S. M. Girvin, and R. J. Schoelkopf. Charge-insensitive qubit design derived from the cooper pair box. *Physical Review A*, 76(4):042319, 2007.
 - [59] M. S. Kushwaha, P. Halevi, L. Dobrzynski, and B. Djafari-Rouhani. Acoustic band structure of periodic elastic composites. *Physical review letters*, 71(13):2022, 1993.
 - [60] O. Landry, J. A. W. van Houwelingen, A. Beveratos, H. Zbinden, and N. Gisin. Quantum teleportation over the swisscom telecommunication network. *JOSA B*, 24(2):398–403, 2007.
 - [61] D. R. Lide. *CRC handbook of chemistry and physics*, volume 85. CRC press, 2004.
 - [62] G. S. MacCabe, H. Ren, J. Luo, J. D. Cohen, H. Zhou, A. Sipahigil, M. Mirhosseini, and O. Painter. Phononic bandgap nano-acoustic cavity with ultralong phonon lifetime. *arXiv preprint arXiv:1901.04129*, 2019.

Bibliography

- [63] G. S. MacCabe, H. Ren, J. Luo, J. D. Cohen, H. Zhou, A. Sipahigil, M. Mirhosseini, and O. Painter. Nano-acoustic resonator with ultralong phonon lifetime. *Science*, 370(6518): 840–843, 2020.
- [64] P. Magnard, S. Storz, P. Kurpiers, J. Schär, F. Marxer, J. Lütolf, T. Walter, J.-C. Besse, M. Gabureac, K. Reuer, et al. Microwave quantum link between superconducting circuits housed in spatially separated cryogenic systems. *Physical Review Letters*, 125(26):260502, 2020.
- [65] T. P. McKenna, J. D. Witmer, R. N. Patel, W. Jiang, R. Van Laer, P. Arrangoiz-Arriola, E. A. Wollack, J. F. Herrmann, and A. H. Safavi-Naeini. Cryogenic microwave-to-optical conversion using a triply-resonant lithium niobate on sapphire transducer. *arXiv preprint arXiv:2005.00897*, 2020.
- [66] S. M. Meenehan, J. D. Cohen, G. S. MacCabe, F. Marsili, M. D. Shaw, and O. Painter. Pulsed excitation dynamics of an optomechanical crystal resonator near its quantum ground state of motion. *Physical Review X*, 5(4):041002, 2015.
- [67] M. Mirhosseini, A. Sipahigil, M. Kalaei, and O. Painter. Superconducting qubit to optical photon transduction. *Nature*, 588(7839):599–603, 2020.
- [68] D. Nelson and E. Turner. Electro-optic and piezoelectric coefficients and refractive index of gallium phosphide. *Journal of Applied Physics*, 39(7):3337–3343, 1968.
- [69] D. Niepce, J. Burnett, and J. Bylander. High kinetic inductance NbN nanowire superinductors. *Physical Review Applied*, 11(4):044014, 2019.
- [70] S. E. Nigg, H. Paik, B. Vlastakis, G. Kirchmair, S. Shankar, L. Frunzio, M. Devoret, R. Schoelkopf, and S. Girvin. Black-box superconducting circuit quantization. *Physical Review Letters*, 108(24):240502, 2012.
- [71] A. D. O’Connell, M. Ansmann, R. C. Bialczak, M. Hofheinz, N. Katz, E. Lucero, C. McKenney, M. Neeley, H. Wang, E. M. Weig, et al. Microwave dielectric loss at single photon energies and millikelvin temperatures. *Applied Physics Letters*, 92(11):112903, 2008.
- [72] A. D. O’Connell, M. Hofheinz, M. Ansmann, R. C. Bialczak, M. Lenander, E. Lucero, M. Neeley, D. Sank, H. Wang, M. Weides, et al. Quantum ground state and single-phonon control of a mechanical resonator. *Nature*, 464(7289):697–703, 2010.
- [73] J. Orcutt, H. Paik, L. Bishop, C. Xiong, R. Schilling, and A. Falk. Engineering electro-optics in SiGe/Si waveguides for quantum transduction. *Quantum Science and Technology*, 5(3):034006, 2020.
- [74] D. M. Pozar. *Microwave engineering*. John wiley & sons, 2011.
- [75] L. Qiu, I. Shomroni, P. Seidler, and T. J. Kippenberg. Laser cooling of a nanomechanical oscillator to its zero-point energy. *Physical Review Letters*, 124(17):173601, 2020.

-
- [76] P. T. Rakich, P. Davids, and Z. Wang. Tailoring optical forces in waveguides through radiation pressure and electrostrictive forces. *Optics express*, 18(14):14439–14453, 2010.
- [77] R. Riedinger, S. Hong, R. A. Norte, J. A. Slater, J. Shang, A. G. Krause, V. Anant, M. Aspelmeyer, and S. Gröblacher. Non-classical correlations between single photons and phonons from a mechanical oscillator. *Nature*, 530(7590):313–316, 2016.
- [78] R. Riedinger, A. Wallucks, I. Marinković, C. Löschnauer, M. Aspelmeyer, S. Hong, and S. Gröblacher. Remote quantum entanglement between two micromechanical oscillators. *Nature*, 556(7702):473–477, 2018.
- [79] A. Rueda, F. Sedlmeir, M. C. Collodo, U. Vogl, B. Stiller, G. Schunk, D. V. Strekalov, C. Marquardt, J. M. Fink, O. Painter, et al. Efficient microwave to optical photon conversion: an electro-optical realization. *Optica*, 3(6):597–604, 2016.
- [80] A. H. Safavi-Naeini, T. M. Alegre, J. Chan, M. Eichenfield, M. Winger, Q. Lin, J. T. Hill, D. E. Chang, and O. Painter. Electromagnetically induced transparency and slow light with optomechanics. *Nature*, 472(7341):69–73, 2011.
- [81] J. M. Sage, V. Bolkhovskiy, W. D. Oliver, B. Turek, and P. B. Welander. Study of loss in superconducting coplanar waveguide resonators. *Journal of Applied Physics*, 109(6):063915, 2011.
- [82] K. J. Satzinger, Y. Zhong, H.-S. Chang, G. A. Peairs, A. Bienfait, M.-H. Chou, A. Cleland, C. R. Conner, É. Dumur, J. Grebel, et al. Quantum control of surface acoustic-wave phonons. *Nature*, 563(7733):661–665, 2018.
- [83] K. Schmeing. *Integrated Gallium Phosphide Photonics*. PhD thesis, École Polytechnique Fédérale de Lausanne, 2019.
- [84] K. Schneider, P. Welter, Y. Baumgartner, H. Hahn, L. Czornomaz, and P. Seidler. Gallium phosphide-on-silicon dioxide photonic devices. *Journal of Lightwave Technology*, 36(14):2994–3002, 2018.
- [85] K. Schneider, Y. Baumgartner, S. Hönl, P. Welter, H. Hahn, D. J. Wilson, L. Czornomaz, and P. Seidler. Optomechanics with one-dimensional gallium phosphide photonic crystal cavities. *Optica*, 6(5):577–584, 2019.
- [86] M. Seifried. *III-V on Silicon Photonics for CMOS-Embedded On-Chip Light Sources*, volume 8. ETH Zurich, 2018.
- [87] M. Seifried, G. Villares, Y. Baumgartner, H. Hahn, M. Halter, F. Horst, D. Caimi, C. Caër, M. Sousa, R. F. Dangel, et al. Monolithically integrated CMOS-compatible III–V on silicon lasers. *IEEE Journal of Selected Topics in Quantum Electronics*, 24(6):1–9, 2018.
- [88] M. Shen, J. Xie, C.-L. Zou, Y. Xu, W. Fu, and H. X. Tang. High frequency lithium niobate film-thickness-mode optomechanical resonator. *Applied Physics Letters*, 117(13):131104, 2020.

Bibliography

- [89] A. Shkarin, D. Rattenbacher, J. Renger, S. Hönl, T. Utikal, P. Seidler, S. Götzinger, and V. Sandoghdar. Nanoscopic charge fluctuations in a gallium phosphide waveguide measured by single molecules. *arXiv preprint arXiv:2012.02991*, 2020.
- [90] A. Sipahigil, R. E. Evans, D. D. Sukachev, M. J. Burek, J. Borregaard, M. K. Bhaskar, C. T. Nguyen, J. L. Pacheco, H. A. Atikian, C. Meuwly, et al. An integrated diamond nanophotonics platform for quantum-optical networks. *Science*, 354(6314):847–850, 2016.
- [91] M. Soltani, M. Zhang, C. Ryan, G. J. Ribeill, C. Wang, and M. Loncar. Efficient quantum microwave-to-optical conversion using electro-optic nanophotonic coupled resonators. *Physical Review A*, 96(4):043808, 2017.
- [92] L. Steffen, Y. Salathe, M. Oppliger, P. Kurpiers, M. Baur, C. Lang, C. Eichler, G. Puebla-Hellmann, A. Fedorov, and A. Wallraff. Deterministic quantum teleportation with feed-forward in a solid state system. *Nature*, 500(7462):319–322, 2013.
- [93] R. Stockill, M. Forsch, G. Beaudoin, K. Pantzas, I. Sagnes, R. Braive, and S. Gröblacher. Gallium phosphide as a piezoelectric platform for quantum optomechanics. *Physical review letters*, 123(16):163602, 2019.
- [94] Y. Sun, D. Law, S. Visbeck, and R. Hicks. Kinetics of tertiarybutylphosphine adsorption and phosphorus desorption from indium phosphide (001). *Surface science*, 513(2): 256–262, 2002.
- [95] D. R. Turner. Etch procedure for optical fibers, Sept. 4 1984. US Patent 4,469,554.
- [96] C. Wang, C. Axline, Y. Y. Gao, T. Brecht, Y. Chu, L. Frunzio, M. Devoret, and R. J. Schoelkopf. Surface participation and dielectric loss in superconducting qubits. *Applied Physics Letters*, 107(16):162601, 2015.
- [97] M. J. Weber. *Handbook of optical materials*, volume 19. CRC press, 2002.
- [98] R. Weil and W. O. Groves. The elastic constants of gallium phosphide. *Journal of Applied Physics*, 39(9):4049–4051, 1968.
- [99] S. Weis, R. Rivière, S. Deléglise, E. Gavartin, O. Arcizet, A. Schliesser, and T. J. Kippenberg. Optomechanically induced transparency. *Science*, 330(6010):1520–1523, 2010.
- [100] D. J. Wilson, K. Schneider, S. Hönl, M. Anderson, Y. Baumgartner, L. Czornomaz, T. J. Kippenberg, and P. Seidler. Integrated gallium phosphide nonlinear photonics. *Nature Photonics*, 14(1):57–62, 2020.
- [101] J. D. Witmer, J. A. Valery, P. Arrangoiz-Arriola, C. J. Sarabalis, J. T. Hill, and A. H. Safavi-Naeini. High-Q photonic resonators and electro-optic coupling using silicon-on-lithium-niobate. *Scientific reports*, 7(1):1–7, 2017.

- [102] M. Xu, X. Han, W. Fu, C.-L. Zou, and H. X. Tang. Frequency-tunable high-Q superconducting resonators via wireless control of nonlinear kinetic inductance. *Applied Physics Letters*, 114(19):192601, 2019.
- [103] Y. Xu, A. Sayem, L. Fan, C.-L. Zou, S. Wang, R. Cheng, W. Fu, L. Yang, M. Xu, and H. Tang. Bidirectional interconversion of microwave and light with thin-film lithium niobate. *Nature communications*, 12:4453, 2021.



Moosstr. 3, 8803,
Rüschlikon



+41 78 404 46 57



[Linkedin](#)

Simon Hönl

Curriculum vitae



Date of birth November 25th, 1992

Nationality German (B-permit)

Research engineer with strong background in III-V semiconductor integrated photonic circuits and microfabrication.

Excellent teamwork and communication skills. Creative and innovative approach to problem-solving.

Professional Experience

2017 - 2021

IBM Research Europe – Zurich, Rüschlikon, Switzerland

Doctoral candidate, Science & Technology

- **Managing** my own research project as well as a master thesis research project
- **Responsible for development cycle** (design, fabrication, characterization) of novel, award-winning III-V microwave-to-optical converters for superconducting quantum computers [1]
- **Collaboration** with other IBM and international research teams resulting in several high-impact, peer-reviewed publications [2,3,4]
- **Design** of integrated photonic circuits and nano-electromechanical devices
- **Nanofabrication** of ultra low-loss III-V integrated photonic circuits for micro-resonator frequency combs and quantum transduction, including III-V growth by MOVPE (GaP, GaAs, InGaP), fabrication of low-loss superconducting circuits on silicon, hybrid integration of III-V on silicon by direct wafer-bonding.
- **Characterization** of integrated photonic circuits by fiber-optic spectroscopy and high-speed RF vector network analysis.

University of Konstanz, Germany

2016 - 2017

Research assistant, AG Weig, Nanomechanical Systems

- **Nanofabrication** of vertical GaAs micromechanical resonator arrays
- **Characterization** of micromechanical resonators with free-space optical interferometry [5]

2015

Research assistant, AG Schmidt-Mende, Hybrid Nanostructures

- **Fabrication** of bulk-heterojunction organic solar cells

Education

2017 - 2021

Doctoral Studies, Photonics

Doctoral studies at **IBM Research Europe – Zurich** with affiliation École Polytechnique Fédérale de Lausanne (EPFL). IBM supervisor: Dr. Paul Seidler, Academic supervisor: Prof. Dr. Tobias Kippenberg (thesis title: *Microwave-to-Optical Transduction with Gallium Phosphide Electro-Optomechanical Devices*).

Master, Physics (1.3)

M.Sc. at the **University of Konstanz** with focus on nanotechnology.

Master thesis (title: *Mechanical Dynamics and Coupling Phenomena in Inverted Tapered Gallium Arsenide Nanowires*) in the group of Prof. Dr. Eva Weig.

2014 - 2016

Bachelor, Physics (1.7)

B.Sc. at the **University of Konstanz**.

Bachelor thesis at the ENS Paris (title: *Study of Gyrase from Mycobacterium Tuberculosis in a Single Molecule Assay*) in the group of Dr. Vincent Croquette.

2011 - 2014

German Abitur (1.8)

Otto-Hahn Gymnasium Furtwangen, Germany

2011

Awards

IBM Outstanding Technical Achievement Award (OTAA)

For innovations in “Integrated gallium phosphide photonics for quantum transduction” (2021)

Interests

Music (violin, cello, guitar), photography (for example [IBM website](#)), videography (production of [video](#) for EU network) mountain biking, organization of group events, CGI (blender)

Soft Skills

Languages

- German (native)
- English (full professional proficiency)
- French (limited working proficiency)

Communication

- Communication course (Raymond Fein)
- Conference presentations (CLEO 2018, CLEO 2020)
- Technical writing workshop

Leadership

- Supervision of PhD and master students
 - Representative of doctoral students in European training network
 - Management of development cycle of hybrid photonic integrated circuits
-

Programming

- Python: Analysis of optical and RF signals, numerical simulation of quantum systems, lithography mask design
- Matlab: Analysis of optical and RF signals, numerical simulations (in combination with COMSOL Multiphysics), programming of hardware interface with data acquisition devices
- G-code: direct programming of 3D printer for micro-positioning

Electronic data processing

- MS Office (PowerPoint, Excel, Word), LaTeX

Simulation

- Finite element method (FEM): COMSOL Multiphysics, Ansys HFSS, Sonnet
- Finite difference time domain (FDTD): Ansys Lumerical
- Simulation Program with Integrated Circuit Emphasis (SPICE)

Nanofabrication

- Epitaxial growth (MOVPE)
- Lithography: Electron beam lithography, direct laser writing, UV contact lithography
- Material deposition: PVD (sputtering, evaporation), PECVD, ALD
- Dry etching: ICP-RIE (developed process [\[7\]](#)), RIE, ion milling
- Wet etching
- Chemical-mechanical planarization (CMP)

Metrology

- Scanning electron microscopy (SEM), Focused ion beam milling (FIB)
- Atomic force microscopy (AFM)
- Energy-dispersive X-ray spectroscopy (EDX)
- Photo-luminescence spectroscopy (PL)
- X-ray diffraction analysis (XRD)

Characterization

- Vector network analysis: characterization of electro-optomechanical devices and superconducting microwave devices at GHz frequencies
- Fiber-optics: characterization of integrated photonic circuits with direct/heterodyne/homodyne optical spectroscopy

Prototyping

- Computer-aided design (CAD) and 3D printing of setup components

Technical Skills

List of Publications

- [1] **Hönl, Simon**, Youri Popoff, Daniele Caimi, Alberto Beccari, Tobias J. Kippenberg, and Paul Seidler. "Microwave-to-optical conversion with a gallium phosphide photonic crystal cavity." *arXiv preprint arXiv:2105.13242* (2021).
- [2] Tikan, Alexey, Johann Riemensberger, Kenichi Komagata, **Simon Hönl**, Mikhail Churaev, Connor Skehan, Hairun Guo et al. "Emergent nonlinear phenomena in a driven dissipative photonic dimer." *Nature Physics* 17, no. 5 (2021): 604-610.
- [3] Shkarin, Alexey, Dominik Rattenbacher, Jan Renger, **Simon Hönl**, Tobias Utikal, Paul Seidler, Stephan Götzinger, and Vahid Sandoghdar. "Nanoscopic charge fluctuations in a gallium phosphide waveguide measured by single molecules." *Physical Review Letters* 126, no. 13 (2021): 133602.
- [4] Wilson, Dalziel J., Katharina Schneider, **Simon Hönl**, Miles Anderson, Yannick Baumgartner, Lukas Czornomaz, Tobias J. Kippenberg, and Paul Seidler. "Integrated gallium phosphide nonlinear photonics." *Nature Photonics* 14, no. 1 (2020): 57-62.
- [5] Doster, Juliane, **Simon Hönl**, Heribert Lorenz, Philipp Paulitschke, and Eva Maria Weig. "Collective dynamics of strain-coupled nanomechanical pillar resonators." *Nature communications* 10, no. 1 (2019): 1-5.
- [6] Schneider, Katharina, Yannick Baumgartner, **Simon Hönl**, Pol Welter, Herwig Hahn, Dalziel J. Wilson, Lukas Czornomaz, and Paul Seidler. "Optomechanics with one-dimensional gallium phosphide photonic crystal cavities." *Optica* 6, no. 5 (2019): 577-584.
- [7] **Hönl, Simon**, Herwig Hahn, Yannick Baumgartner, Lukas Czornomaz, and Paul Seidler. "Highly selective dry etching of GaP in the presence of $\text{Al}_x\text{Ga}_{1-x}\text{P}$ with a $\text{SiCl}_4/\text{SF}_6$ plasma." *Journal of Physics D: Applied Physics* 51, no. 18 (2018): 185203.
- [8] Schneider, Katharina, Pol Welter, Yannick Baumgartner, **Simon Hönl**, Herwig Hahn, Lukas Czornomaz, and Paul Seidler. "Optomechanics with one-dimensional gallium phosphide photonic crystal cavities." In *Quantum Nanophotonics*, vol. 10359, p. 103590K. International Society for Optics and Photonics, 2017.

[Google scholar](#)

List of Conference Presentations

CLEO, San Jose, CA, USA (virtual conference) 11th – 15th May 2020, *Monolithic integration of GaP on superconducting circuits for applications in quantum computing* (contributed talk)

OMT-HOT 2020 annual conference; Saanen, Switzerland, 19-23 January 2020 (contributed talk)

HOT2019 Network Conference, Ascona, Switzerland, 7th – 11th July 2019, *A Platform for Hybrid Integration of Acoustic and Photonic Devices with Superconducting Qubits* (poster presentation)

OMT-HOT 2019 annual conference; Saanen, Switzerland, 20-24 January 2019 (contributed talk)

CLEO, San Jose, CA, USA 13th – 18th May 2018, *GaP-On-Insulator as a Platform for Integrated Photonics* (contributed talk)

OMT-HOT 2018 annual conference; Saanen, Switzerland, 15-18 January 2018 (poster presentation)

SPIE Europe, Strasbourg, France 22nd – 26th April 2018, *Gallium phosphide microresonator frequency combs* (poster presentation)